UNIVERSITEIT VAN PRETORIA
UNIVERSITY OF PRETORIA
YUNIBESITHI YA PRETORIA
Department of Materials Science and Metallurgical Engineering

Development of a validated thermal model for the Slow-Cool Process of Waterval Converter Matte

Lambert Petrus van Sittert de Villiers

Submitted in partial fulfilment of the requirements for the degree

M. Eng. (Metallurgical Engineering) 2013

In the Department of Materials Science and Metallurgical Engineering

Faculty of Engineering, Built Environment and Information Technology,

University of Pretoria, South Africa

Promoter: Prof. JPR De Villiers

July 2013

Abstract

The Anglo American Platinum Converter Plant produces a copper-nickel sulphide converter matte which is slow-cooled in ingots over several days. During the process, the formation of alloy platelets, containing the majority of the PGM's and Au, occurs. The alloy forms a magnetic fraction in the bulk matte which can be liberated when the matte is crushed and milled. The alloy platelets are then separated via a magnetic separation process in the Magnetic Concentration plant. The quality of the converter matte is dependent on the reaction and cast temperatures, bulk matte composition and cooling rate of each ingot, which define the microstructure of the slow-cooled matte that is produced as the final product of the ACP process.

The current mould size used in the ACP slow-cool aisle is ~10 tonnes (maximum 14.84t), designed for 2 full ingots to be poured from every tap from a full ladle with a capacity of ~20t. This is the ideal situation, however, during normal plant operation ladles develop a build-up of material on the inside (or skull) that reduces the ladle active volume. This results in a large number of half ingots being produced, and, given the smaller ingot size, suboptimal cooling conditions arise and subsequently poor quality Waterval Converter Matte (WCM) is produced because of rapid cooling.

In an attempt to match the converter blow size, the ladle size and the slow-cool mould size in future, a larger mould size of 15 ton was specifically constructed to determine if the smelter converted matte can be cast into the larger mould size. Therefore a larger size ingot of 15t with a maximum capacity of 20.6t was also used as part of the trials in order to determine if cooling rates in the larger sized ingot necessitated longer cooling times, and would therefore negatively affect the platinum pipeline and working inventory. The data obtained from these trials were then used to develop and validate a CFD model, specifically developed to simulate the cooling process.

From the heat loss data it was calculated that the bulk of the heat lost from the ingots is through the top surface. After the first 12 hours of cooling, approximately 89% of the heat lost from the ingot is via the top surface and this increases to 96% after 24 hours. It can therefore be concluded that the cooling rates of the ingots can be easily manipulated by changing the thermal insulation of the lid that is placed over the ingot after casting.

Acknowledgements

Several people contributed to this work and I would acknowledge all with the following summary:

- The operational personnel and metallurgical staff at ACP for their help with the test work and data collection, especially Me. Bernadette Mdluli. Dr. Greg Georgalli, for his help with the FactSage® modelling and general arrangements for the experiments on the plant.
- The staff at the Anglo American Research Laboratories, more especially the Mineralogical Research department for the help with the analysis and interpretation of data. I would like to acknowledge the following people; specifically Mr Tshepo Mohlotja for the help with the sample preparation, Me. Lesley Andrews & Me. Yolanda Scharneck for the help with mineralogical analysis and Mr Robert Schouwstra for the help with the general arrangements and mineralogical data interpretation.
- The Anglo American Platinum Technology department, specifically Dr Lloyd Nelson and Mr Rodney Hundermark for their input in the interpretation and documentation of the results.
- Mr Thomas Kingsley, CFD Analyst at HATCH for the help with the CFD model setup.
- The University of Pretoria, Department of Material Science and Metallurgical Engineering staff, specifically Prof Johan de Villiers, Prof Andrie Garbers-Craig and Mr Markus (MW) Erwee, thank you for your support and guidance.
- Thank you to Anglo American Platinum for allowing me the time and opportunity to complete this work.

Then finally to my wife Ulanda for your support and my Heavenly Father for the grace on my life!

This thesis has not been submitted in part or as a whole for another degree at any other institution. I further declare that the work presented here is authentic and original unless clearly indicated otherwise.

_____

Signed: L.P. v S. de Villiers

Table of Contents

7.5 Data Correlations

List of Figures

List of Tables

List of Abbreviations

AAP	Anglo American Platinum Limited
ACP	Anglo Converting Process
RBMR	Rustenburg Base Metal Refinery
BSE	Backscattered Electron
CFD	Computational Fluid Dynamic
CSIR	Council for Scientific and Industrial Research in South Africa
DO	Discrete Ordinate Model
ECD	Equivalent Circle Diameter
FC	Final Concentrate
MCP	Magnetic Concentration Plant
NCM	Nickel Copper Matte
PFM	Polokwane Smelter Furnace Matte
PGM	Platinum Group Metal
PWL	Piece Wise Linear Functions
PWP	Piece Wise Polynomial Functions
QEM-SCAN	Quantitative Evaluation of Minerals by Scanning Electron Microscopy
QEM-SEM	Quantitative Evaluation of Mineralogy by Scanning Electron Microscope
RTE	Radioactive Transfer Equation
SCFM	Slag Cleaning Furnace Matte
Th.S	Theoretical Sulphur
UFM	Union Smelter Furnace Matte
Veref	Vereeniging Refractories
WCM	Waterval Converter Matte
WVS	Waterval Smelters
XRF	X-Ray Fluorescence

1. Introduction

The slow cooling of converter matte or “the slow-cool process” as used by Anglo American Platinum Limited (AAP) is a very specific process step for the concentrating of precious metals and used by AAP. The quality of the converter matte has a direct impact on the downstream process efficiencies and must therefore be carefully controlled to ensure optimal process performance. The quality of the slow-cooled converter matte is determined by chemistry, process temperatures and the cooling rate of the matte after casting. The chemistry of the final converter matte is controlled by the converter feed blend, that consists of furnace matte produced at the various smelting operations and the converter operating process conditions. By manipulating these parameters a converter matte of specific quality is produced which is cast into a specifically sized mould for the slow-cool process.

During the slow-cooling of the converter matte, the Platinum Group Metals (PGM) concentrates in a relatively small volume of magnetic Ni-Cu-Fe alloy. The rate of cooling will have a direct bearing on the available time for crystallisation and texture of the final product. In order to optimise the plant operations, the size of the slow cooled cast ingots had to be increased from 10t to 20t. The exact impact of this change on the converter matte cooling rate during slow-cooling, alloy platelet size, plant inventory and other aspects product quality was unknown.

This investigation aimed to develop a validated thermal model of the slow-cool process for various sized cast ingots simulating the solidification energy transformations and heat losses during the cool down process within the critical temperature ranges.

In order to obtain detailed mineralogical data and to accurately determine the various compositional zones within the cast ingots, a cross sectional plane was core drilled in each ingot in order to map these distinct zones within the ingots both from a chemical and mineralogical perspective. This has not been done before and provided the necessary data to improve the understanding of the size and shape of these zones. The data obtained from the test work was also then correlated to the specific mineralogical and chemical analyses obtained from the cast ingots in order to extrapolate the impact, if any, on the increase in the size of the slow-cooled mould and its effect on the slow-cool process and product quality. Furthermore, a better understanding of the influence on product quality at faster cooling rates during the slow-cool process will enable further optimisation of the process and the reduction of working inventory and less lockup of PGM’s in the slow-cool isle.

1.1 Anglo American Platinum Operations Description

AAP operates various mines in both the Eastern and Western limbs of the Bushveld Igneous Complex and also one open pit operation at Mogalakwena mine, close to Mokopane. Concentrate, produced in 17 different concentrators and combined with other concentrates received from joint-venture operations and third parties, are smelted at three smelting complexes, namely the Mortimer, Waterval and Polokwane Smelters as indicated in Figure 1.1-1, with red circles.

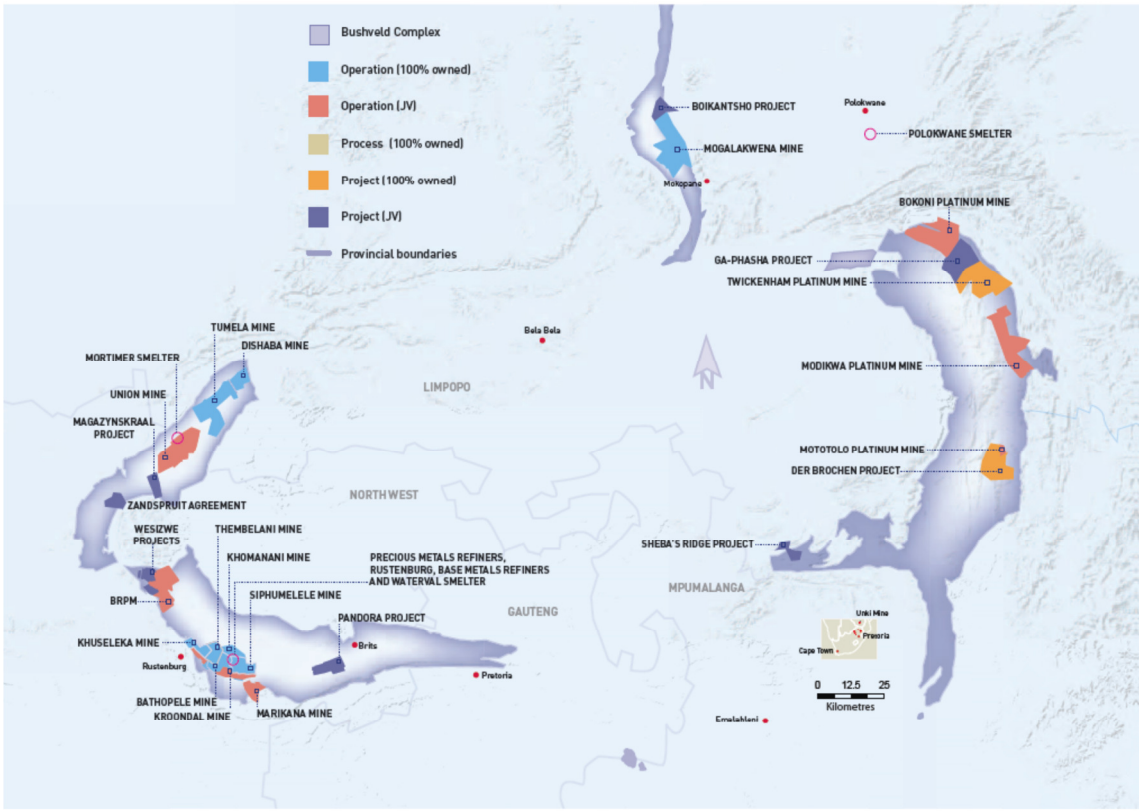

Figure 1.1-1: Location of the Anglo American Platinum Ltd Operations (S&SD annual Report 2010)

Concentrates are smelted in six-in-line furnaces at the smelters, resulting in the production of furnace matte. The furnace matte is then treated using the Anglo Platinum Converting Process (ACP), which takes place at the Waterval Smelter complex in Rustenburg. The matte tapped from the converter, termed Waterval Converter Matte (WCM), is then slow-cooled, crushed and dispatched to Rustenburg Base Metal Refiners (RMBR) for further processing. Slag from the ACP is returned to Waterval Smelter for re-smelting in the Slag Cleaning Furnace (SCF) in order to recover the remaining Platinum Group Metals (PGMs) and nickel oxide via a reductive smelting process. Slag from the SCF is then milled and floated in a concentrator situated at Waterval Smelter.

At RBMR, the precious metals are separated from the base metals via magnetic separation in the Magnetic Concentration Plant (MC Plant). From here the magnetic fraction is transferred to the Precious Metals Refinery (PMR) and the non-magnetic portion is transferred to the RBMR for leaching and electro-winning.

The basic process flow for the total Anglo American Platinum production pipeline (from mine to market) is shown in Figure 1.1-2.

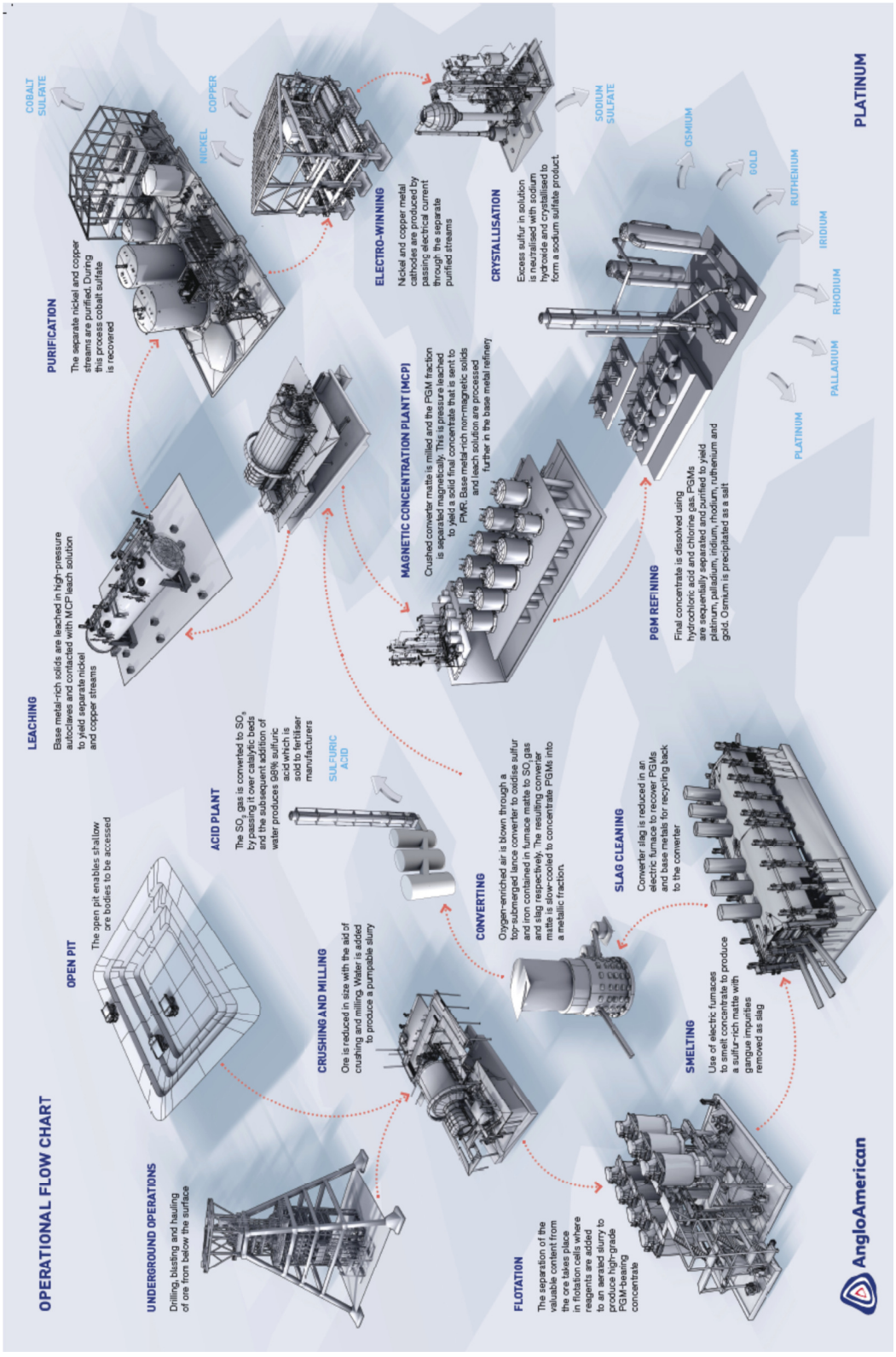

Figure 1.1-2: Anglo Platinum process route (Anglo Annual S& SD report 2010)

For ease of reference, the AAP smelter process flow is described and a schematic of the Waterval Smelter flowsheet is provided in Figure 1-3. The Mortimer and Polokwane Smelter flowsheets are simpler and only comprise of the drying, primary furnace, offgas, slag and matte handling unit operations.

In the late 1990's AAP embarked on a smelter modernisation project, primarily to reduce site emissions to below the regulatory limit of 20 tons per day SO_2, but also to increase the converting capacity in line with future projected production profiles. To achieve these requirements the Peirce Smith converters were replaced with a single large Ausmelt converter and a new acid plant. This was the first time that an Ausmelt furnace had been used for converting, but it had the advantages of being a very robust furnace and was fully enclosed giving good gas capture, thus meeting both production and environmental requirements.

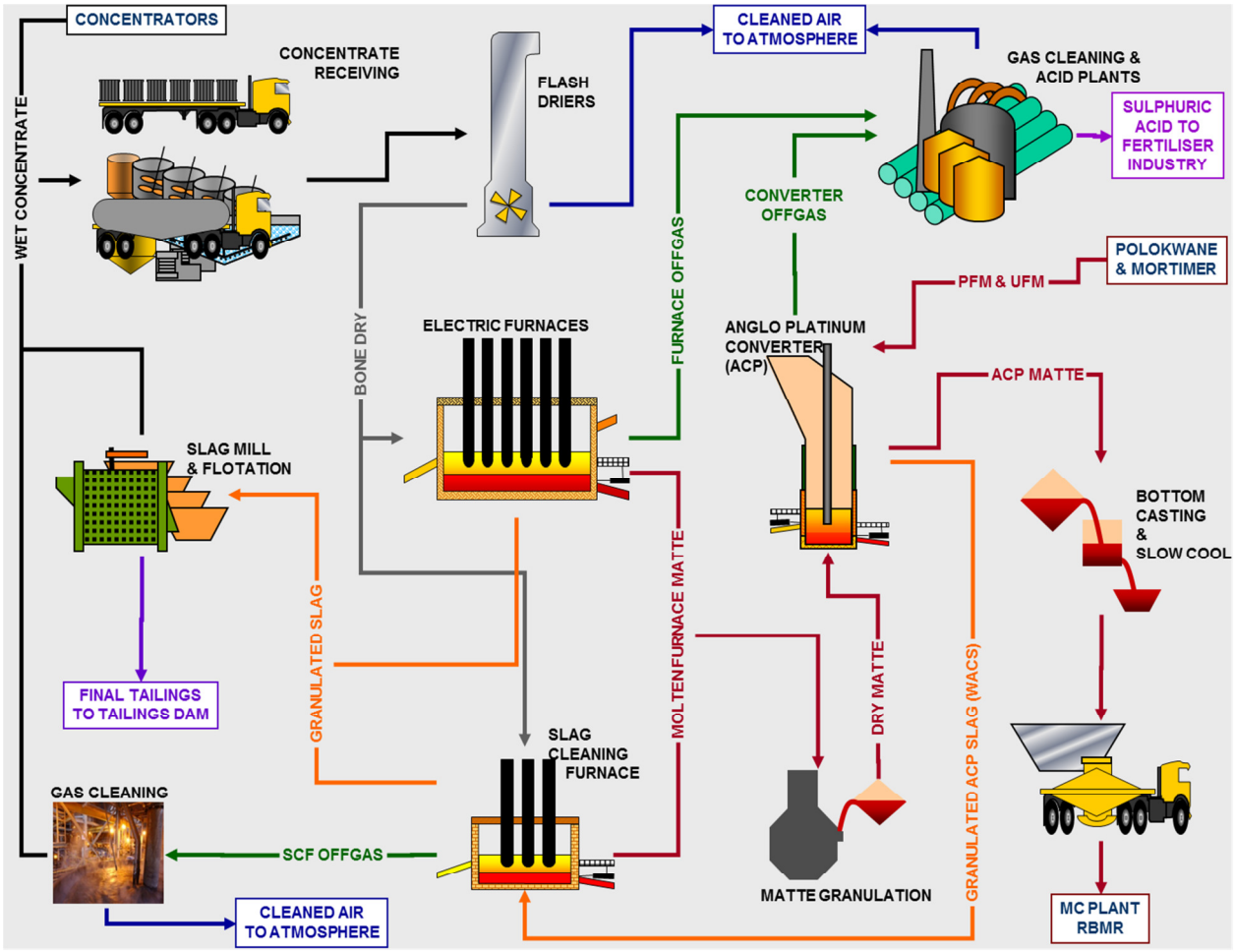

Figure 1.1-3: Schematic of process flow at Waterval Smelter (Jacobs 2006)

In the ACP the electric furnace matte (containing ~40%Fe) from all of the AAP primary furnaces is injected down the converter lance and converted with oxygen enriched air to produce a high grade product matte. The continuous process converts furnace matte directly down to ~3 percent Fe continuously while feeding. The high grade molten matte is tapped and slow-cooled before being sent to the Base Metals Refinery, while the slag is tapped and granulated, then dried for feeding into the SCF. The SO_2 rich process offgas from the ACP is cooled in the boiler uptake then transferred to the acid plant.

The quality of converter matte product and the consistency with which it is achieved ensures that the correct alloy content in the WCM facilitates the optimum PGM separation in the downstream operations. The quality of matte is controlled by measuring the oxidation state of the slag as well as the SiO_2 content. The oxygen injection is controlled to achieve the desired oxidation state, which ensures the required Fe and S levels in the product matte. Converter matte produced contains three main phases: nickel sulphide, copper sulphide and a magnetic alloy, typically 60% nickel and the balance copper and iron. The PGM's and Ag are collected in the alloy phase and the quantity and quality of the alloy phase produced is dependent on the chemical composition of the matte and the cooling rate of the slow-cooled converter matte.

The quantity and size of alloy platelets formed within the WCM during the slow cooling process has a direct impact on the downstream process efficiency of the Magnetic Concentration Plant (MC Plant) situated within the RBMR. At the MC Plant the WCM is milled down to -45µm, to liberate the alloy platelets, which is then separated as a magnetic fraction via magnetic separators. If the alloy platelets are not of sufficient size, it will result in recovery losses within the MC Plant and bypass the system to the Base Metal refining section. If excessive quantities (normally controlled ~12%) of platelets are produced it will be detrimental to the primary leaching capacity of the MC Plant and also have a negative impact on operating costs.

2. Literature Review

2.1. Process fundamentals – Converter Operations

The Waterval Converter Matte (WCM) contains three phases: nickel sulphide (Ni_3S_2 –type phase), copper sulphide (Cu_2S –type phase) and a metallic alloy (Cu-Ni-Fe alloy). The affinity of PGMs for the metallic alloy phase is very high and this ensures the concentration of virtually all the precious metals in the alloy phase after solidification. The metallic alloy phase is magnetic and allows for magnetic separation of the PGM rich fraction from the base metals sulphide fraction. This is a key differentiator of the AAP process flow from its competitors where the converter matte is quenched and the PGMs are recovered as a residue from the RBMR process.

The texture of slow-cooled matte is very important and therefore the alloy grains/platelets that are formed during the slow-cool process need to be of sufficient size and quantity in order to be effectively liberated during the milling process at the MC Plant and subsequent magnetic separation process from the sulphide fraction, but not so large as to form alloy platelets that are shattered during subsequent milling.

During the converter operation most of the iron and a large percentage of sulphur is removed from the furnace matte to produce a sulphur deficient converter matte. The quantity of alloy formed in the converter matte is controlled by the sulphur level that is the more sulphur in the matte, the less alloy and vice versa (Hill, 1995). Available data also indicate that the alloy grain sizes increases as the sulphur content decreases (Schouwstra, 2003).

It is of interest to understand the mechanisms employed in the converter in order to control the sulphur, and hence alloy content, in the WCM. During converter operation, as oxygen is blown into the molten bath, the sulphur content of the molten matte decreases as sulphur and iron are oxidised according to the following reaction:

Reaction 1:

$2FeS_{matte} + 2O_2 + 2SiO_{2\ flux} = 2FeO.SiO_{2\ slag} + 2SO_2$ + energy (ΔH = -988.5KJ per mol FeS @1350°C)

During the oxidation of iron sulphide (FeS) in the furnace matte, FeO is formed and fluxed with silica to form a fayalite slag ($2FeO.SiO_2$) and small amounts of magnetite.

The factors controlling the reaction are:

For sulphur removal: Temperature

Oxidation from the air flow rate and oxygen enrichment (pO_2/pSO_2)

For iron removal: Temperature

Oxidation from the air flow rate and oxygen enrichment (pO_2/pSO_2)

SiO_2 Concentration in the slag

The converter slag chemistry is vital for Fe removal from the feed matte as the SiO_2 activity in the slag drives the FeO across the matte/slag interface, therefore the equilibrium concentration of FeO in slag will depend on the SiO_2 concentration of the slag. Figure 2.1-1 illustrates the formation of a FeO-SiO_2 slag, in the typical converter slag operating region with 26-35% SiO_2. Details of the slag chemistry for sulphide smelting and converting slags are also discussed in detail by Mackey, 1982.

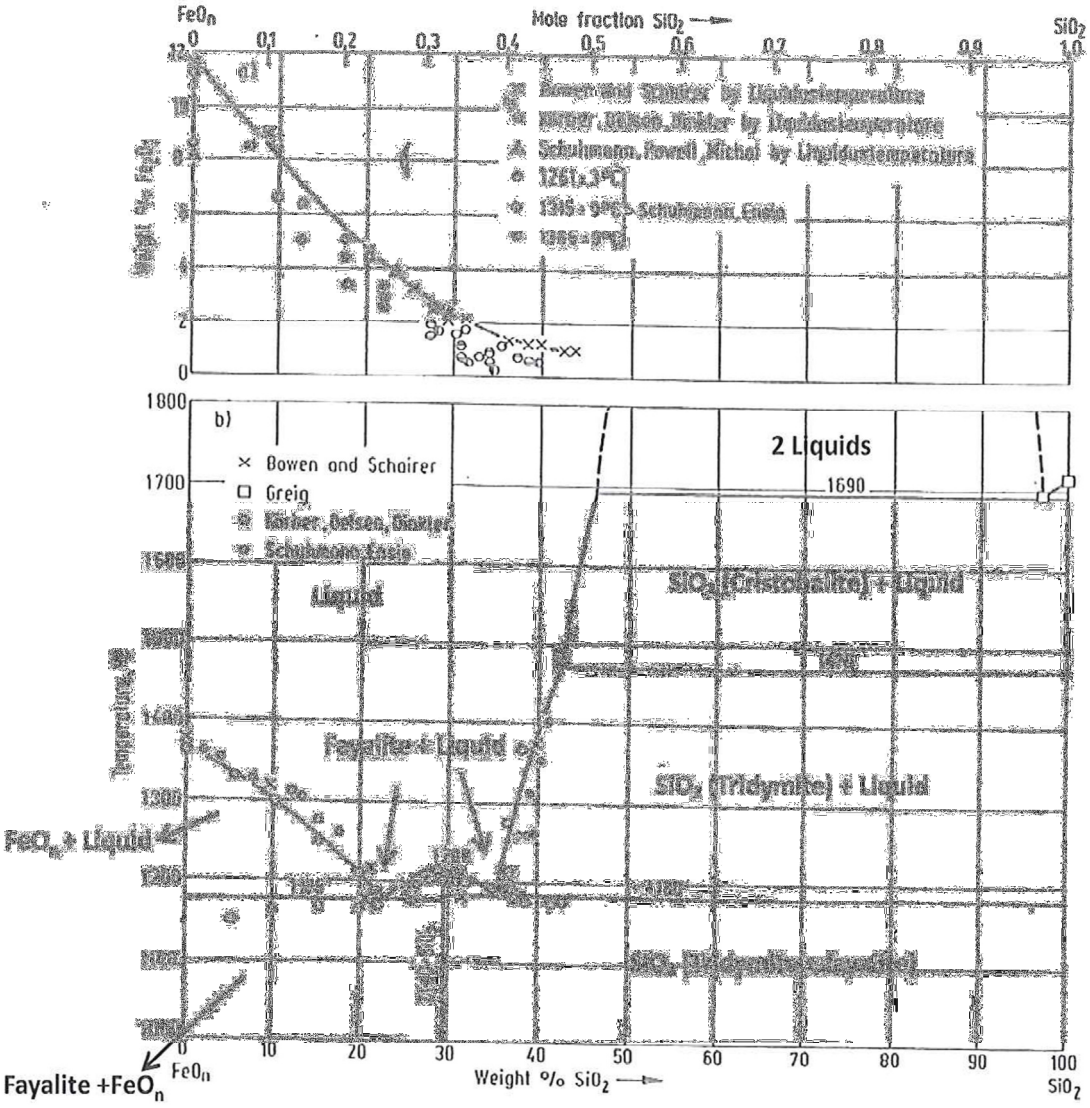

Figure 2.1-1: FeO-SiO_2 system (Stahleisen, 1981)

This equilibrium will, together with temperature and available oxygen, drive the Fe removal from the matte. Therefore the slag composition influences the rate of S removal indirectly. If the activity of SiO_2 is low in the slag (on the left hand side of figure 2.1-1), there will be a tendency for FeO to be further oxidised in the slag phase. The combination of low SiO_2 slags and low converter temperatures (<1220^{o}C) produces high magnetite (Fe_3O_4) levels and low alloy contents in WCM (Taylor, 1997). The recommended SiO_2 content in converter slag is 26 – 35% according to (Badcock, 1993).

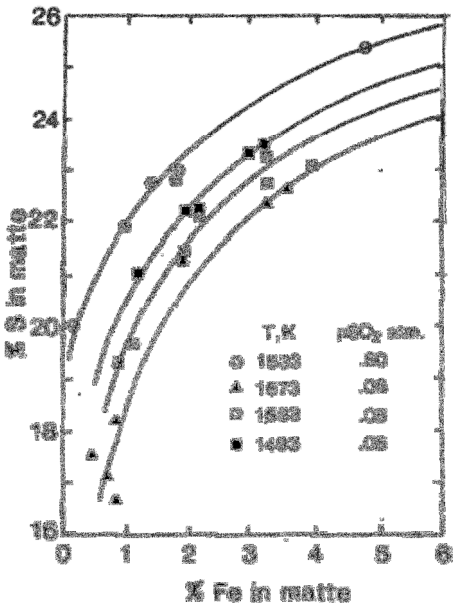

Figure 2.1-2: Relationship between %Fe and % S in converter matte at varying pSO_2 and temperatures (Taylor, 1997)

For a given matte, high converting temperatures (>1260°C) at a specific pSO_2 will lead to lower %S contents in WCM and increased alloy formation, as shown in Figure 2.1-2. On the other hand, low converting temperatures (<1220°C) will produce higher sulphur WCM with reduced alloy contents and increased magnetite formation. Converting at temperatures below 1200°C produces insufficient alloy to collect PGM's and Au (Badcock, 1993) as is evident in the microstructure due to the formation of PGM Sulphides, e.g. Ni-Fe-Ru-S and significant increases in magnetite (Fe_3O_4) formation. The formation of Fe_3O_4 is detrimental on the quality of WCM because it (Taylor, 1997):

- Becomes concentrated with the magnetic fraction in the MC Plant and lowers grade
- Reduces leaching efficiency of final concentrate (FC) in the MC Plant
- Either increases insoluble residue on atmospheric dissolution of FC, or increases the iron content of liquor when pressure leaching is employed.

In the traditional Peirce Smith (PS) converter operation, a batch process, a specific Fe level in matte was targeted to indicate the endpoint of each converter blow so as to ensure the correct sulphur content of the converter matte (WCM). The objective of this operation was to produce WCM which is at equilibrium at >1200°C with an alloy content of 8% and minimal corrosion on the refractory lining (Hill, 1995). Therefore, the concentration of free SiO_2 in slag will determine the equilibrium Fe content in matte at a given temperature. Thus the rate at which Fe is removed from the matte bath during a blow is determined by the SiO_2 content; however the S removal is not directly influenced by the SiO_2 slag concentrations. This suggests that there is a relationship between the target alloy content of the WCM (which is firmly related to the S content) and the target Fe content of the WCM which will change with

varying SiO_2 levels. There is, however, one limiting step in the Peirce Smith Converter (PS) operation with respect to the amount of SiO_2 that is added as flux, and this is the rate of refractory wear resulting from highly acidic (siliceous) slags. Excess quantities of SiO_2 will also result in alloy contents in the range of 13-15% (Hill, 1995) which will result in increased magnetic fraction and thus mass pulls in the MC Plant, resulting in capacity constraints and recovery losses.

The ACP was commissioned in 2003, mainly to replace the PS converters due to environmental reasons, whereby the ACP provided better sulphur fixation and reduced secondary emissions. In the ACP, furnace matte is oxidised with oxygen-enriched air which is blown through a partially-submerged top injected lance into the molten bath. The air-oxygen mixture is combined with the furnace matte, coal, and silica as it enters the bath as schematically shown in Figure 2.1-3. As the oxygen and air pass into the liquid bath, the contained oxygen reacts selectively with components in the furnace matte, primarily FeS. The FeS is converted to FeO and combines with SiO_2 to form a molten slag (as per reaction 1) that is intermittently tapped out of the furnace, while the sulphur is oxidised to sulphur dioxide and leaves the furnace in the off-gas. The slag process temperature is approximately 1300 - 1350°C with matte tapped at ~1250°C. Heat to sustain the process is generated by the oxidation of S and Fe (exothermic nature of Reaction 1), with supplemental energy provided by the combustion of coal for accurate control of process temperatures.

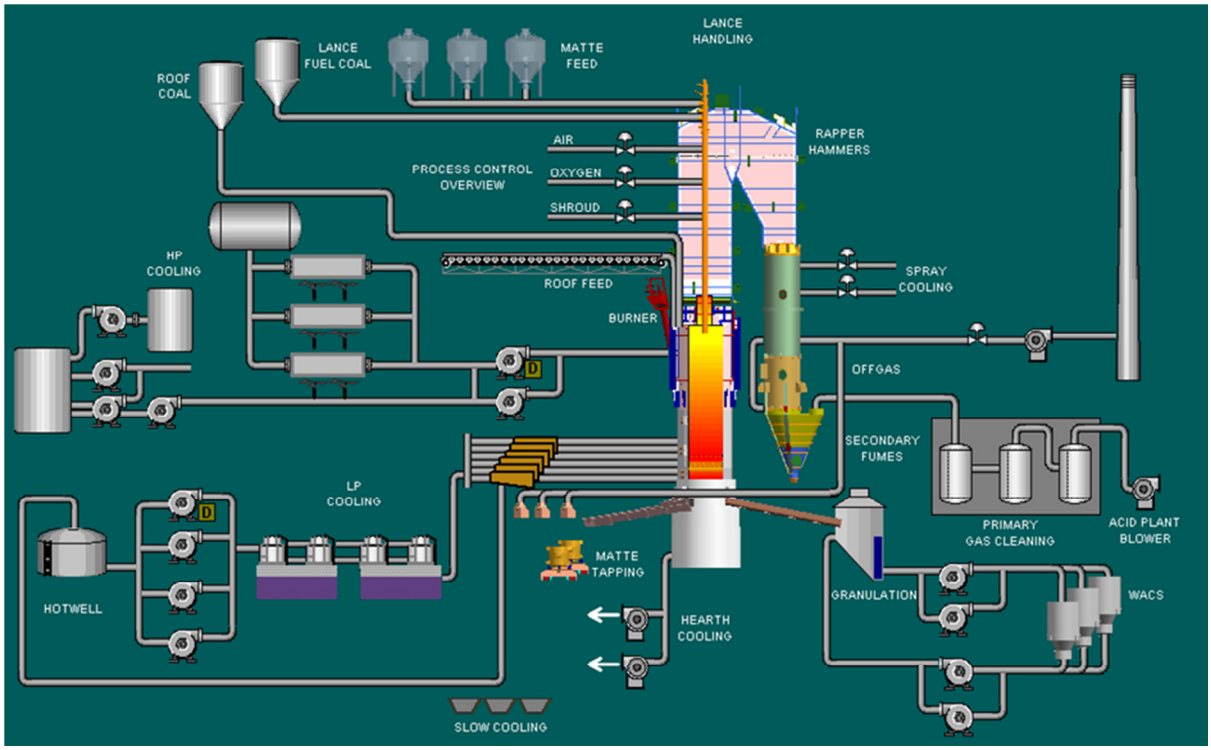

Figure 2.1-3: Schematic drawing of the ACP converter and key auxiliary equipment (Metskill, 2007)

The ACP crucible contains water cooled sidewall copper coolers within the slag zone, and has thus eliminated the refractory wear problem traditional to the Peirce Smith converter. However, this resulted in another constraint which is the fact that both slag and matte are tapped from the converter through separate tapholes of approximately 40mm diameter. Therefore the slag composition and temperature are controlled to achieve a specific viscosity so as to facilitate the tapping process and minimise the possibility of slag foaming. This is achieved by controlling the basicity or $(Fe+MgO+CaO)/(SiO_2 + Al_2O_3)$/ ratio in the slag such that the viscosity of the slag can be minimised and this is achieved at a basicity of ~1.6 -1.75 as shown in Figure 2.1-4. The data presented in Figure 2.1-4 was generated in FactSage® for a typical ACP slag at 1350°C, by varying the SiO_2 and calculating the basicity with only Fe/SiO_2 ratio. It is evident that the calculated liquid viscosity decreases with increasing basicity but the % solids in the slag will then increase as the % spinel increases causing the bulk viscosity to be at a minimum, at a basicity of ~1.6. In practice however, some minor amounts of MgO, CaO and Al_2O_3 enter the converter slag via the combustion coal and silica flux, moving the minimum viscosity point slightly higher on the basicity scale. This effect of viscosity of slag as a function of Fe was also described in detail by Eric, 2004.

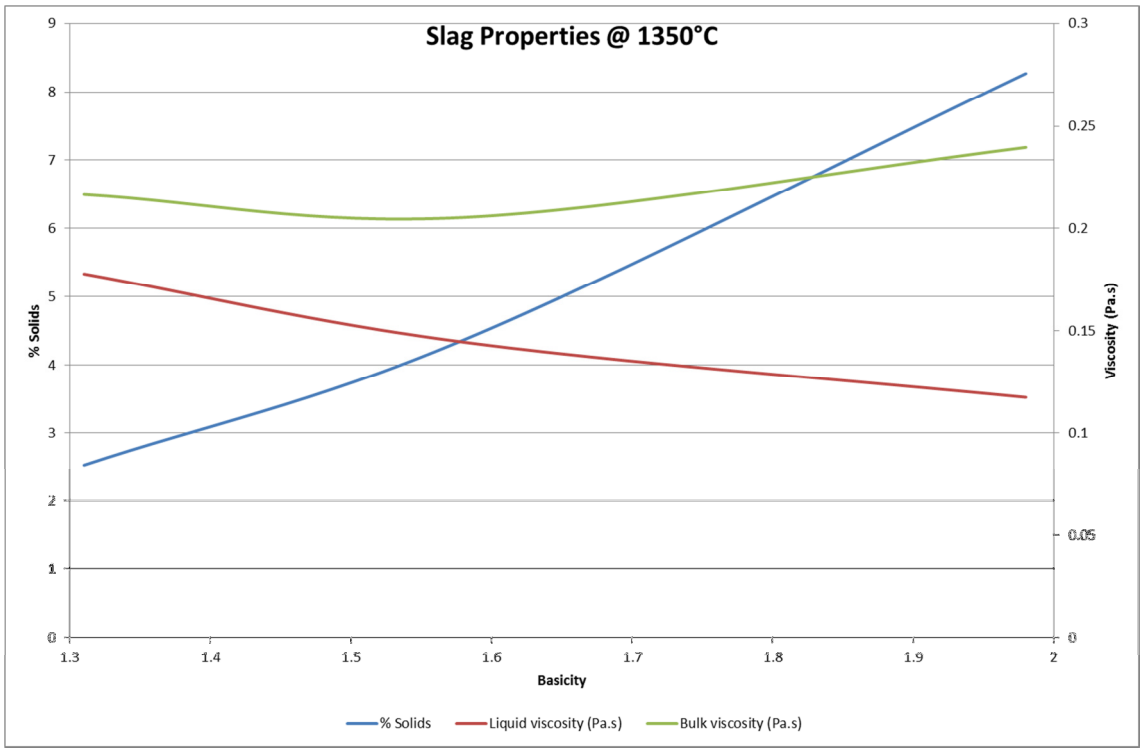

Figure 2.1-4: Effect of basicity on viscosity as calculated in FactSage® for a typical ACP slag with basicity defined as Fe/SiO_2

If the basicity is too high (Low SiO_2 and high FeO), the bath can become over oxidised in order to achieve the appropriate Fe in WCM and this can result in the formation of too much magnetite (Fe_3O_4) in the slag causing it to become viscous (as explained) and will also result in an over oxidised slag and poor WCM quality (Mackey, 1982). High magnetite content may also react with the sulphur in furnace matte and cause the slag to foam, as a result of a combination of high viscosity slag and excessive gas evolution from the reactions, which is a major safety and operational concern. Limited amounts of magnetite are generated and are used as a control variable to create build-up on the converter hearth for protection. Once formed, due to its high melting point of ~1594^oC, the magnetite is then very slowly dissolved into the slag. If the basicity is too low, this is an indication of excessive SiO_2 addition, which also causes the viscosity to increase due to the effect of a polymerised SiO_2 chain network forming or the presence of solid silica (Trydymite).

ACP is a continuous process with furnace matte fed continuously whilst slag and matte are tapped intermittently through separate tapholes positioned at different heights. This arrangement makes the direct sampling of the converter matte from the bath difficult and therefore the slag analysis is used to infer the matte Fe content. Whilst oxidising FeS , other metal sulphides also present in the matte get oxidised and report to the converter slag as metal losses. From the Ellingham diagram in Figure 2.1-5, for a given temperature, Fe is most easily oxidised thereafter, cobalt, nickel and then copper. For this reason, the %Ni in the slag is used to infer %Fe in the matte.

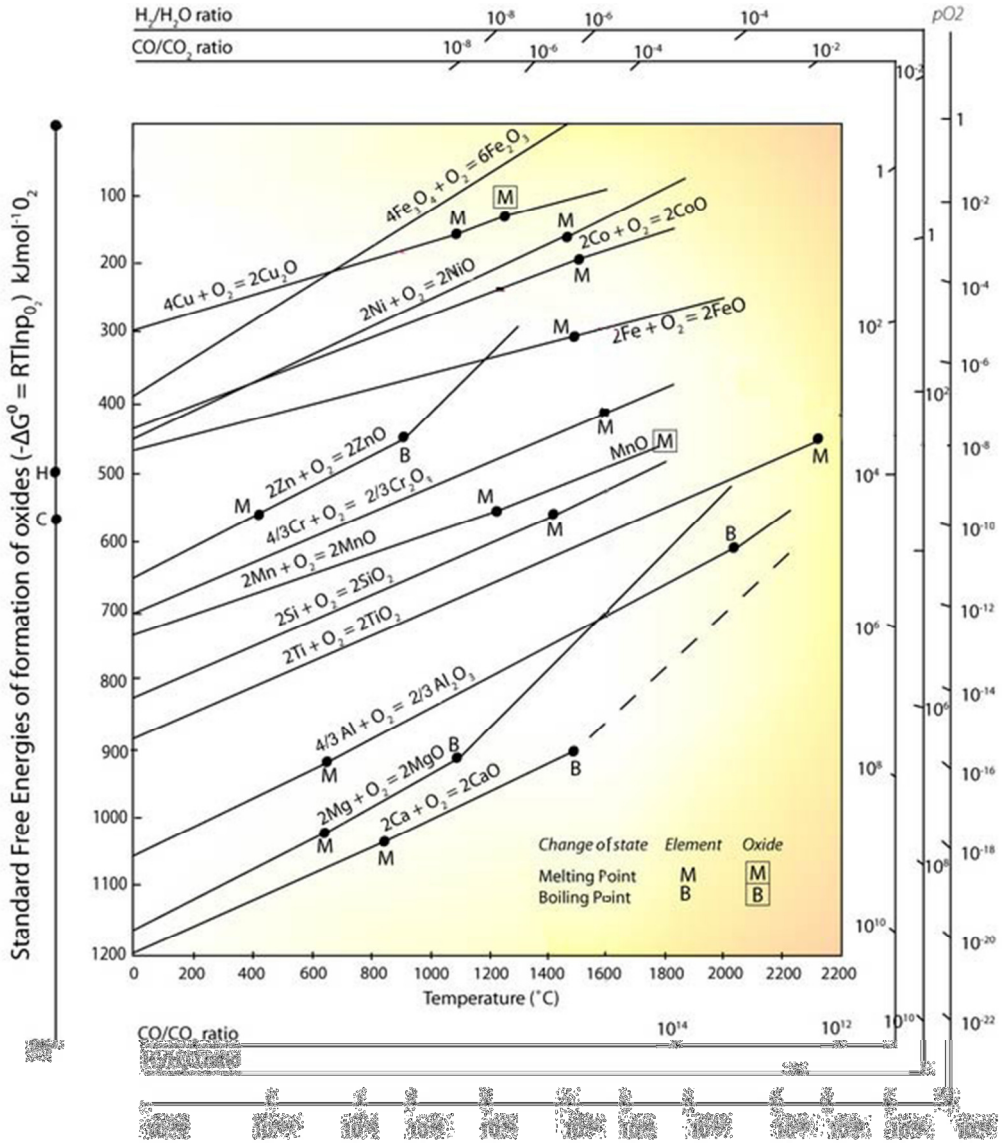

Figure 2.1-5: Ellingham diagram for metal oxides *(http://www.doitpoms.ac.uk/tlplib/ellingham_diagrams/ellingham.php)*

Reaction 2 below shows the oxidation of Ni into the slag. This is similar for Co and Cu.

Reaction 2:

$Ni_3S_{2Matte} + 3½\ O_2 = 3NiO_{Slag} + 2SO_2 + energy$ (ΔH = -1030.1KJ per mol Ni_3S_2 @1350°C)

Since nickel is oxidised after iron (as per reaction 2 above and illustrated in the Ellingham diagram, figure 2.1-5), the amount of nickel present in the slag can be used to determine the amount of oxidation which has taken place in the molten bath and hence the amount of iron removed from the matte. Generally, 3% Ni in slag will result in ~3% Fe in converter matte depending on the slag basicity and operating temperature. Figure 2.1-6 shows the data correlations for the distribution of the metals Cu, Ni and Co between matte and slag versus the % Fe in matte. This plot was generated from actual plant data and illustrates the fact that metal losses to slag increases exponentially under more oxidising conditions.

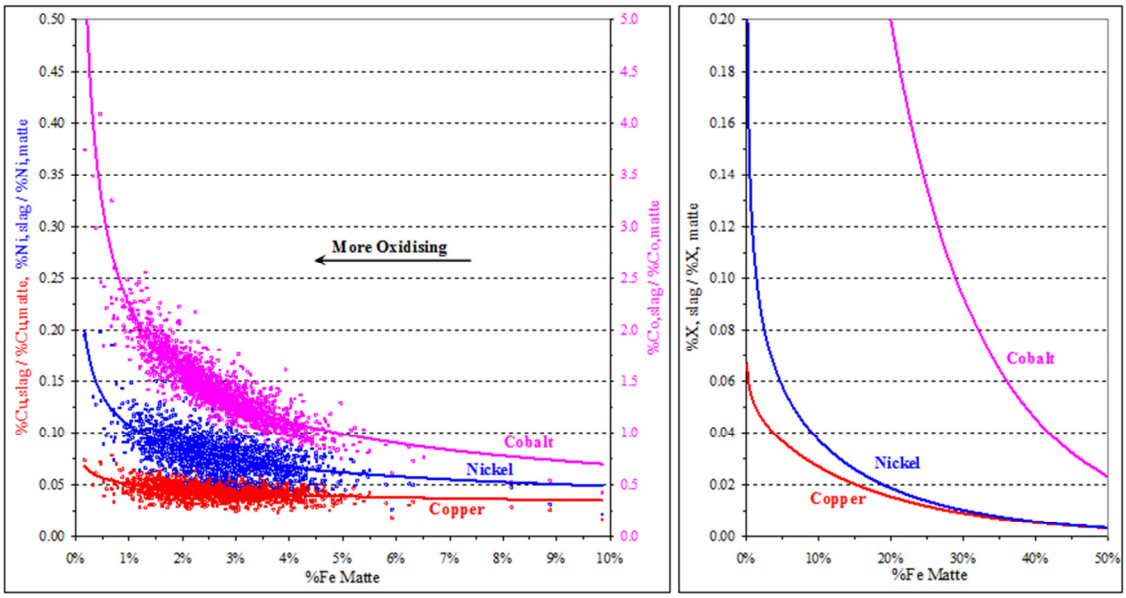

Figure 2.1-6: Nickel / Cobalt and Copper in slag/matte versus Iron in matte (Matthew, 2009)

The major difference between the ACP and Peirce Smith (PS) operations in terms of blow endpoint control is that in the PS converter the matte is directly converted and the %Fe in converter matte can be measured directly and oxygen is then adjusted accordingly before casting. In the ACP operation however, most of the converting reactions take place as the mixture of furnace matte blend of Polokwane furnace matte (PFM), Mortimer furnace matte (UFM) and Waterval furnace matte (WFM), oxygen and coal exits the lance within the slag bath. Therefore it is of utmost importance, for operational control purposes, to predict the matte composition during each blow. The endpoint prediction is currently done based on empirical data and modelling. The slag analysis is done intermittently (every ~10 - 15min) during each blow and the matte composition is predicted from this analysis. A final matte sample is only taken after WCM tapping to finally confirm the quality of WCM before casting and therefore cannot be adjusted after tapping.

To summarise, maximising the PGM recovery and overall process efficiency depend on being able to control both Fe and S levels in matte independently during the converting process (Taylor, 1997).

2.2. Process fundamentals – Slow Cooling Process

WCM is tapped from the converter after the operations personnel are satisfied that the slag analysis received predicts that the WCM Fe content is within specification. The matte is tapped into 20t ladles (provided no build-up is present in the ladle) at temperatures ranging between 1250°C - 1300°C (Figure 2.2-1). The molten matte is then cast into the slow-cooled moulds (current mould size ~10t) and cooled for a period of 3 days and various phases form in the slow-cooled matte. The cast matte consists of mainly 3 phases:

- nickel sulphide (Ni_3S_2),
- copper sulphide (Cu_2S, normally djurleite-bornite $Cu_{1.96}S$ and $CuFeS_4$ respectively (Schouwstra, 2003) and
- magnetic alloy (typically 60% nickel with the balance Cu and Fe which collects >99% of the PGM's) (Taylor, 1997).

After casting, a lid is placed over the mould in order to reduce the radiation heat loss via the top surface of the ingot. The matte is then cooled from 1050°C to 475°C at a relatively constant rate over a period of 3 days. The rate of cooling determines the size of the individual phases in the WCM and in general, the slower the cooling the larger the phases, providing the chemical composition is correct (Taylor, 1997). Essentially the quality of the alloy is controlled in the converter (as explained above) while the quality in terms of size of the final WCM i.e. separability of alloy influenced by the slow cooling process. The other factors that also influence the WCM quality are levels of magnetite, pentlandite and ferrosilicate slag present in the matte and these are also negatively influencing recoveries and mass pull at the MC Plant (Hill, 1995). Historic slag and matte temperatures from the ACP plant data are shown in Figure 2.2-1.

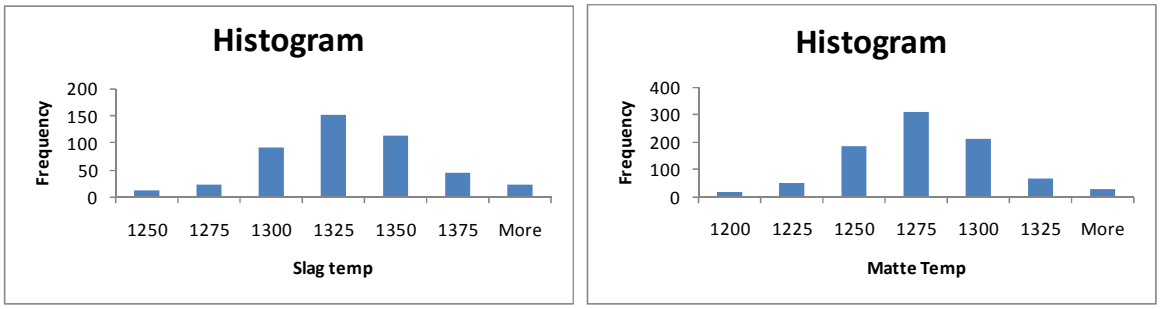

Figure 2.2-1: Slag and matte tap temperatures (°C) from plant data Feb – May 2011

2.3. Cooling Rate

The purpose of slow cooling the converter matte is to allow sufficient grain growth of the alloy components so as to achieve satisfactory liberation of the phases during milling. The process is affected by the matte chemistry, the initial casting temperature, rate of cooling and the final temperature before chilling. When matte is cast it must have sufficient heat to ensure that any chilled solidified matte on the sides of the mould is re-melted (Badcock, 1993). A minimum temperature of 1050°C is required at the start of the slow cooling process; therefore it is recommended that the matte is cast at 1150°C and that the mould temperature is pre-heated to ~200°C before casting. Chilled and solidified material on the edges of the mould results in losses of PGMs to the Nickel Copper matte (NCM) at the RBMR. Low casting temperatures are mineralogically indicated by small Cu_2S crystals and Cu_2S/alloy intergrowths.

The preferred rate of cooling is from 1050°C to 500°C in three days (72hrs). Most of the heat is lost via the top surface of the ingot (primarily through the lid that is placed over the ingot after the casting) and it is therefore vitally important the lid is placed over the mould as soon as the matte is poured. Mattes containing up to 5% Fe are completely molten above 925°C and, as the matte cools, Cu_2S starts to precipitate at ~920°C. This is followed by primary alloy at ~700°C, depending on the exact chemical composition of the remaining melt. It is also possible for Os-Ir-(Pt) to precipitate above 700°C and act as a nucleus for the primary alloy. Ni_3S_2 separates at ~605°C and the eutectic which contains all the above phases is reached at ~580°C.

The eutectic temperature and alloy composition may vary based on the specific conditions as a result of the initial melt composition and temperature and this was studied separately by three authors. The eutectic temperatures, the eutectic composition of the alloy phase are shown in Table 2.3-1.

Table 2.3-1: Comparison of the composition (in %wt) of the eutectic point and the eutectic alloy composition from three separate investigations.

		Eutectic Composition			Alloy Composition	
Investigator	Temperature	%Ni	%S	% Cu	%Ni	%Cu
Koster and Mulfinger (1940)	580 °C	63	23	14	79	21
Kullerud *et al. (*1969)	572±5 °C	67	21	12	-	-
Sploure *et al.* (1960)	575 °C	-	-	10	80	20

Finally there is a phase transformation of Ni_3S_2 from β to β' at ~520°C (Badcock, 1993). The solidification process is later explained in more detail (Section 2.5) for different compositions of matte, as the sequence of phase formation may vary as a result of composition.

The primary alloy and eutectic alloy start as small particles at their precipitation temperatures and gradually coalesce to larger particles. The coalescence is vital to form particles >20 - 30 µm for recovery in the magnetic separators (Schouwstra, 2002). If the cooling rates are too rapid at these stages, the primary alloy has a "shattered appearance" and the eutectic alloy is left as widely disseminated fine particles in the Ni_3S_2 matrix and recovery will be negatively affected. To promote liberation, the shape of the base metal alloy plates is of importance with euhedral plates easily liberated whereas anhedral (irregular) plates result in composite alloy-sulphide particles (intergrowths), (Schouwstra, 2003). The phase transformation temperature at 520°C is important because it induces a strain in the WCM matrix and facilitates subsequent breaking (Badcock, 1993).

Other phases in the converter matte include, but are not limited to, magnetite in the upper section of the ingots, native copper (abundant in gas cavities), silver (exhibiting a preferred association with the copper-iron sulphide) and PGE alloys (Schouwstra, 2003).

2.4. Effect of Ni:Cu ratio

The concentrates smelted in the six-in-line furnaces have Ni:Cu ratios varying from >0.72 to <2.01 therefore it is of the utmost importance to measure and control blending throughout the operations in order to ensure WCM that is within optimal Ni:Cu ratio of 1.5 – 1.8 (Wright, 1998). This is further complicated by the addition of SCF Matte (SCFM) which is also Ni - rich (with a high Ni:Cu ratio) and will therefore elevate the Ni:Cu ratio in WCM. This can be seen from the analysis summary in Table 2.4-1 and Figure 2.4-1, showing the Ni:Cu ratio of furnace mattes and WCM based on 2009-2010 data and the variation as a result of the SCF operation.

Table 2.4-1: Average Ni:Cu ratios for Waterval, Polokwane, Union and Slag Cleaning Furnace mattes based on actual plant operational data between 2006 and 2010.

	Ni/Cu -WFM	Ni/Cu - PFM	Ni/Cu - UFM	Ni/Cu - SCFM
Ave	1.70	1.62	1.64	2.33
Std dev	0.14	0.10	0.08	0.24
Min	1.2	1.31	1.32	1.5
Max	2.2	1.88	1.84	2.9

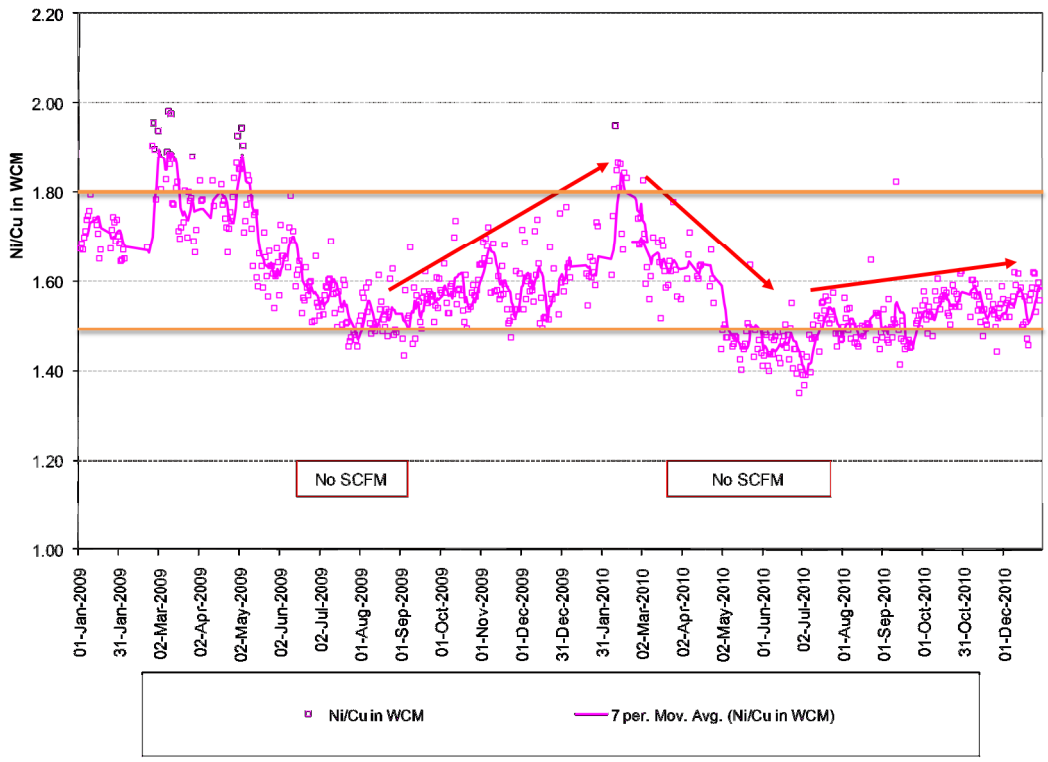

Figure 2.4-1: Ni:Cu ratio in WCM based on actual operational analysis for the period Jan 2009 – Feb 2011 (WCM assays 2009-2011)

The effect of the Ni:Cu ratio on the quality and crystallisation path of Ni-Cu mattes have been investigated in detail by various authors. Theoretical Sulphur (Th.S) is used to describe the %S deficiency in a matte containing a metallic phase versus the amount of sulphur that such a matte would normally contain under equilibrium conditions with only sulphide phases present. Therefore if Cu, Ni and Fe are present in a matte in their sulphide forms as Cu_2S, Ni_3S_2 and FeS, then there is 100% Th.S. (Badcock, 1993). Therefore the lower the %Th.S the greater the quantity of alloy present in a specific matte. From modelling work done by Taylor (1997) it was concluded that the theoretical %S will decrease with an increase in the Ni:Cu ratio (for specific Fe contents) and is also illustrated in Figure 2.4-2.

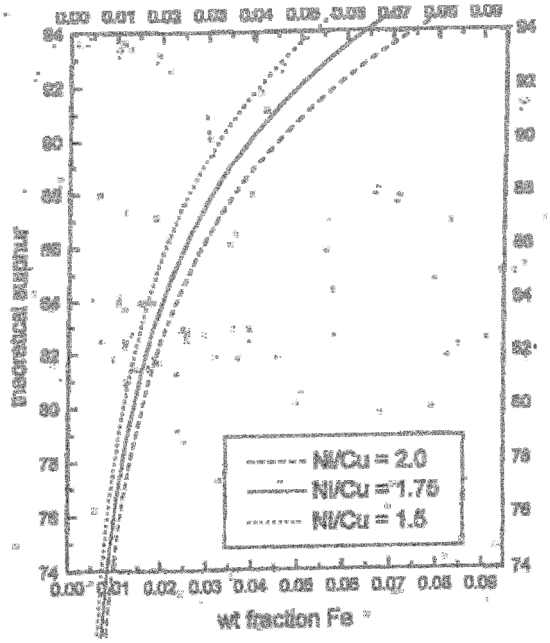

Figure 2.4-2: Simulated theoretical %S content for different Ni:Cu ratios (Badcock, 1997)

The effect of Ni:Cu ratio is relatively small and subtle compared with the changing theoretical sulphur (Th.S) and therefore the control of %S (as described in 2.1) is seen to be more important than the control of the Ni:Cu ratio (Badcock, R.F.W., Bodenstein, J.J., 1997).

Actual historical operational data for the ACP converter is shown in Figures 2.4-3 and 2.4-4 for the calculated theoretical sulphur and the actual %Fe and %S in WCM produced.

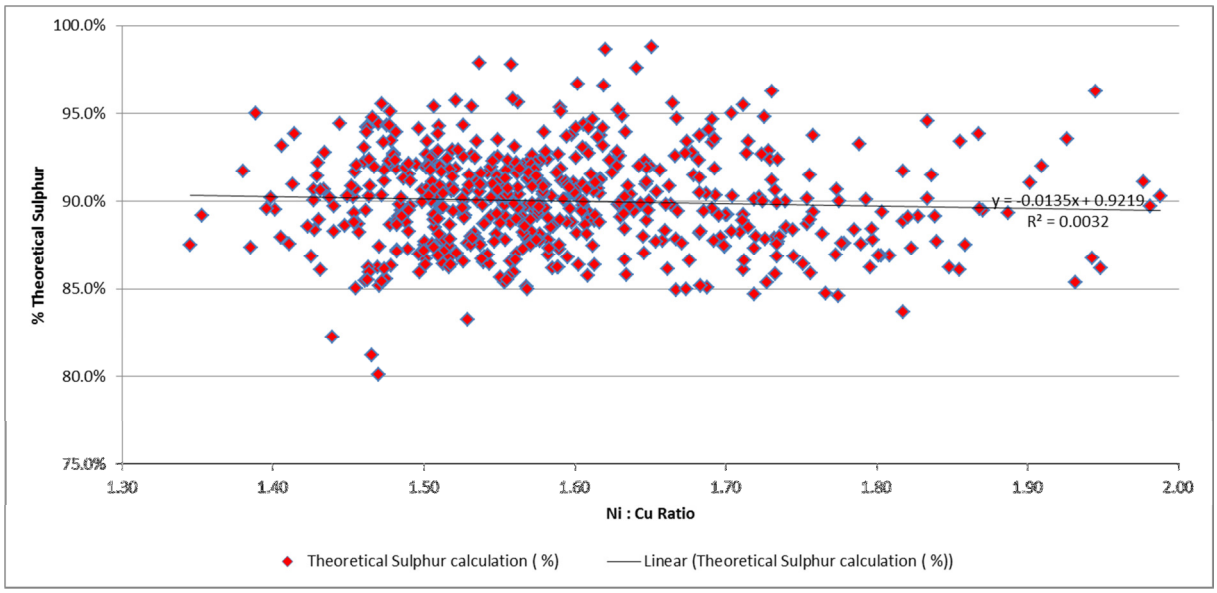

Figure 2.4-3: % Theoretical Sulphur vs. Ni:Cu Ratio in WCM based on actual operational analysis for the period Jan 2009 – Feb 2011 (WCM assays 2009-2011)

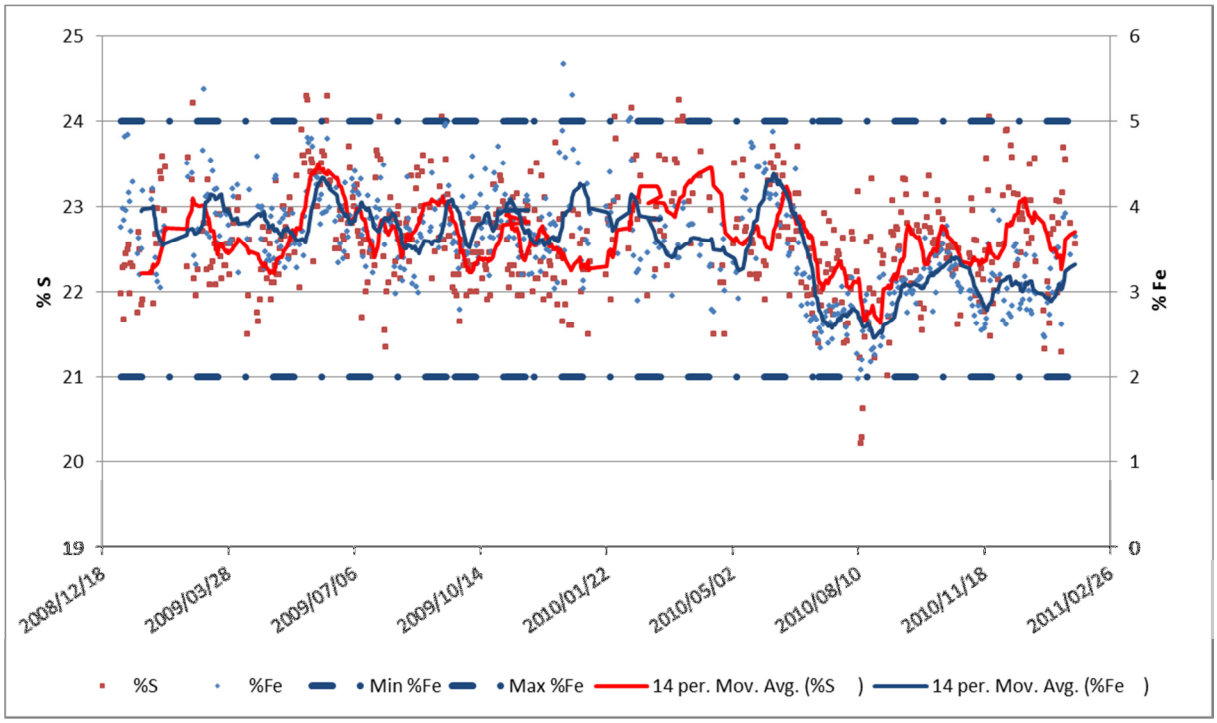

Figure 2.4-4: % S and %Fe in WCM based on actual operational analysis for the period Jan 2009 – Feb 2011 (WCM assays 2009-2011)

Investigations indicate that high nickel to copper ratios in mattes are characterised by lesser amounts of copper-iron sulphides, lesser alloy-sulphide intergrowths and a basal section of the ingot containing large alloy platelets (Schouwstra, 1999). Low nickel to copper ratio mattes are fairly rare but from the data available, these mattes will be characterised by an abundance of copper-iron sulphides, fine grained alloy plates and abundant sulphide-plate intergrowths. However during mid-2010 (as shown in Figure 2.4-1) for a period the SCF was not in operation and a drastic deterioration in WCM quality was observed which proved to be related to low Ni:Cu ratios.

2.5. Theoretical aspects regarding solidification and phase formation

The liquidus temperatures and phase formation sequences of slow-cooled matte can be described using the Cu-Ni-S phase diagram as an approximation (Bruwer, 1996). The Cu-Ni-S system has been investigated and described by numerous authors and this can be used to extrapolate the slow-cooled fractional crystallisation sequence of converter matte. This system however excludes Fe but gives a simple explanation of the various possible crystallisation paths based on varying Cu:Ni ratios and S contents. Bruwer (1996) described four possible crystallisation paths that are dependent on the %S and Cu:Ni ratio of the molten matte. There is a certain critical %S that will cause solidification and fractioning of the liquid at the eutectic point, E4 (as shown in Figure 2.5-1). Higher %S will cause crystallisation of alloy only at the eutectic point, E4 and lower %S will result in the crystallisation of alloy before E4. This critical %S is shown by the straight line between Cu_2S and E4 (with point 4 from Sproule *et al.*, 1960) in Figure 2.5-1. The critical %S is dependent on the Cu:Ni ratio of the bulk sample composition of the liquid during fractioning.

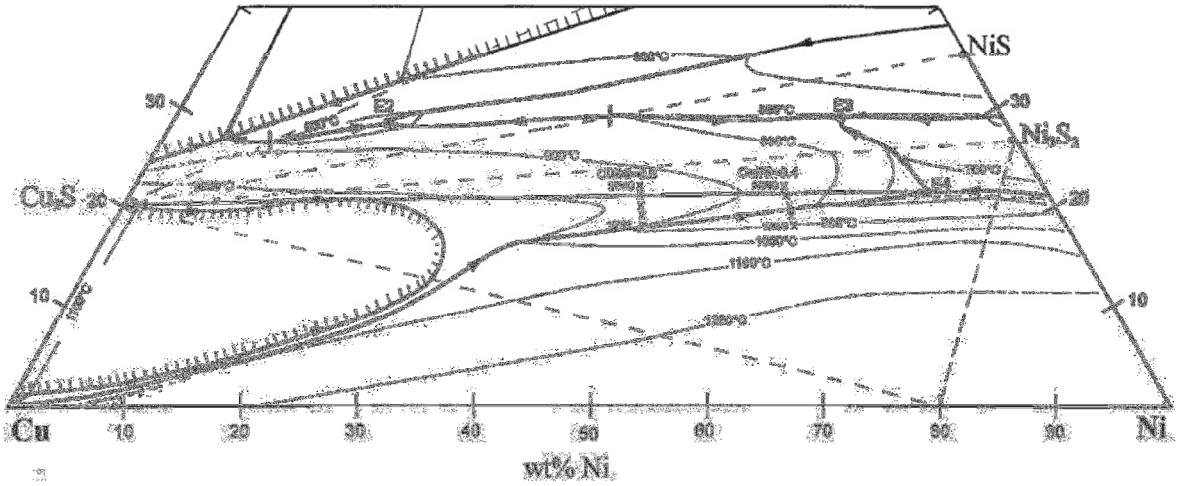

Figure 2.5-1: Examples of possible converter matte compositions (shown as x) with varing Cu:Ni ratios of 0.8 and 0.4 and %S ranging from 18% - 22% as projected on the Cu-Ni-S phase diagram (Bruwer, 1996). The Eutectic point E4 is from Sproule et al. (1960)

Using the stoichiometric Cu_2S phase as the composition of primary Cu_2S and the eutectic point from Sproule *et al.* (1960) as E4, the theoretical crystallisation paths expected for matte with different %S and a constant Cu:Ni ratio are illustrated in Figures 2.5-2 to 2.5-5.

Path 1 – as shown in Figure 2.5-2: For example a matte containing <18wt %S and with a Cu:Ni ratio of 0.6, plots in the initial alloy phase field and therefore alloy will be the first phase to crystallise. The liquid composition will change, following a straight line through the alloy and matte composition, until it reaches the alloy- Cu_2S phase boundary at point d. From point d to E4, Cu_2S will also crystallise and alloy- Cu_2S-liquid will co-exist until the E4 is reached. At E4, Ni_3S_2 will then also start to crystallise together with alloy and Cu_2S until all the liquid is solidified. Mattes containing <18wt %S (with Cu:Ni ratio = 0.8) or <19.5wt %S (Cu:Ni ratio of =0.4) as shown in Figure 2.5-1 will also follow this crystallisation path.

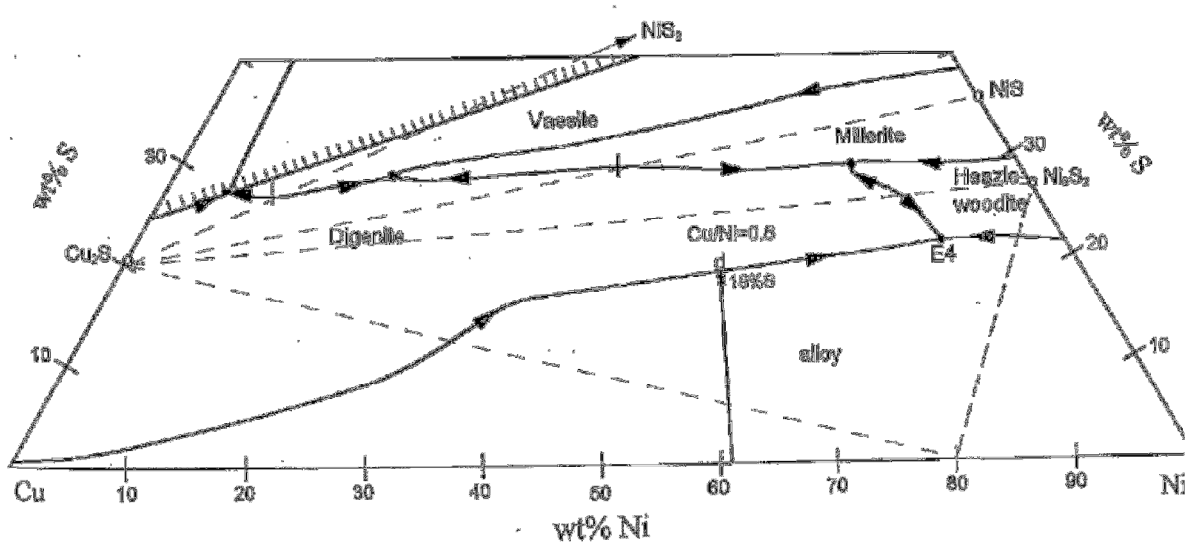

Figure 2.5-2: The crystallisation path of a matte with a 18wt %S (shown as x) and Cu:Ni ratio of 0.6 as projected on the Cu-Ni-S phase diagram (Bruwer, 1996). The Eutectic point E4 is from Sproule et al. (1960)

Path 2 - as shown in Figure 2.5-3: For example a matte with a composition of 20wt %S and a Cu:Ni ratio of 0.6 will crystallise Cu_2S and follow a path with a straight line from Cu_2S through the point "x" representing the matte composition until it reaches the Cu_2S-alloy phase boundary at point "a". From point "a", alloy will start to crystallise together with Cu_2S and Cu_2S-alloy-liquid will coexist until the eutectic composition is reached (E4). At this point (E4) Ni_3S_2 will also start to crystallise and the temperature will stay constant at the eutectic temperature until the matte is solidified, before the bulk temperature will reduce further as cooling takes place. This crystallisation path will be followed with mattes of composition 18-21wt %S at a Cu:Ni ratio of 0.8 or 19.5%-21.3wt %S with a Cu:Ni ratio of 0.4 as shown in Figure 2.5-1.

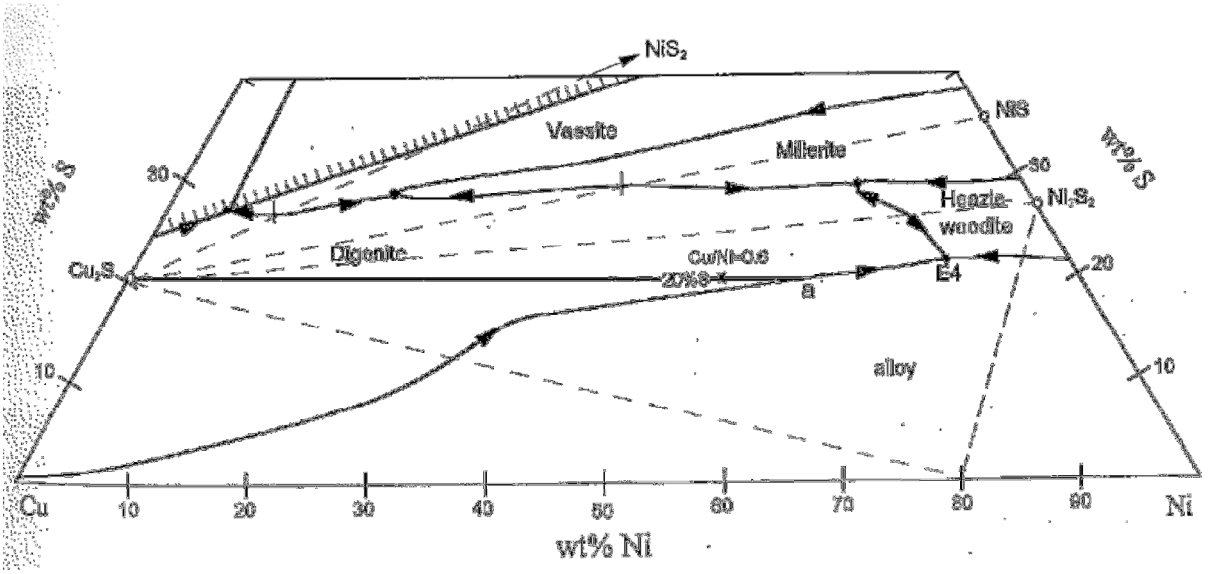

Figure 2.5-3: The crystallisation path of a matte with a 20%S (shown as x) and Cu:Ni ratio of 0.6 as projected on the Cu-Ni-S phase diagram (Bruwer, 1996). The Eutectic point E4 is from Sproule et al. (1960)

Path 3 - as shown in Figure 2.5-4: For example using a 21.2wt %S at a Cu:Ni ration of 0.6 the matte will crystallise Cu_2S first and this will co-exist with liquid until the eutectic composition is reached at point E4. At this point Ni_3S_2 and alloy will also start to crystallise until the matte has solidified before the bulk temperature will decrease further. Mattes with the compositions 21wt %S and Cu:Ni ratio of 0.6 or 21.3wt %S and Cu:Ni ratio of 0.4 will also follow this crystallisation path as shown in Figure 2.5-1.

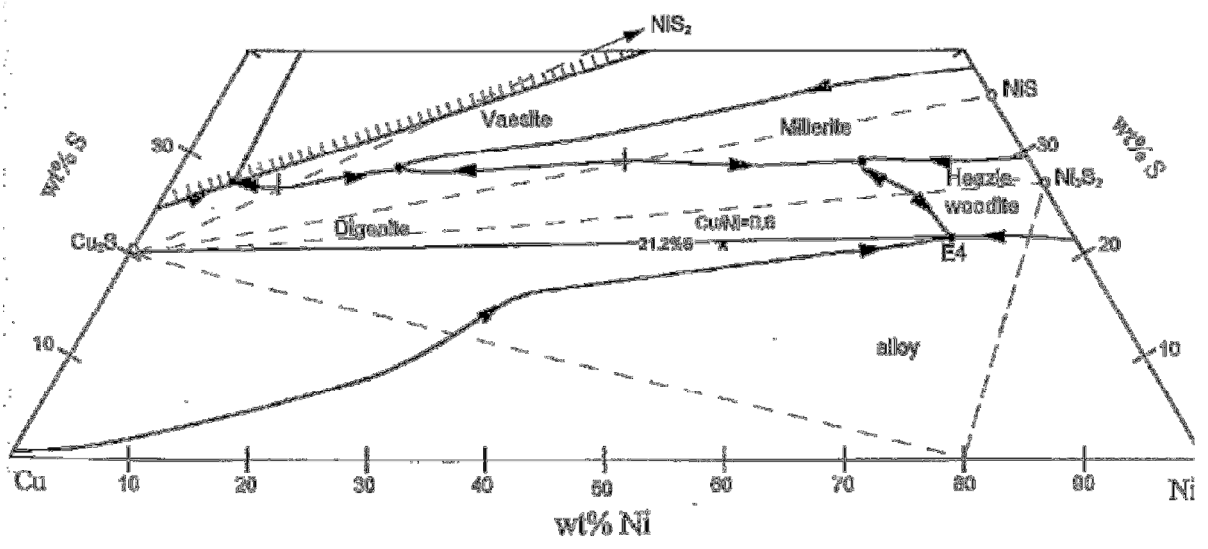

Figure 2.5-4 : The crystallisation path of a matte with a 21.2%S (shown as x) and Cu:Ni ratio of 0.6 as projected on the Cu-Ni-S phase diagram (Bruwer, 1996). The Eutectic point E4 is from Sproule et al. (1960)

Path 4 - as shown in Figure 2.5-5: For example for a matte with >22wt %S and Cu:Ni ratio of 0.6, Cu_2S will crystallise first from the Cu_2S point on the phase diagram following a straight line through the eutectic point "x" until it reaches the phase boundary at point "h". From point h following the phase boundary to point E4, Cu2S and Ni_3S_2 will jointly precipitate from the liquid. At the eutectic point, all liquid is depleted when Cu_2S, Ni_3S_2 and alloy are jointly precipitated. At the eutectic point alloy will then also start to crystallise until all the liquid is depleted before the bulk temperature will reduce. This crystallisation path will also be followed by mattes with the compositions >21wt %S and Cu:Ni ratio of 0.8 or >21.3wt %S and Cu:Ni ratio of 0.4 as shown in figure 2.5-1.

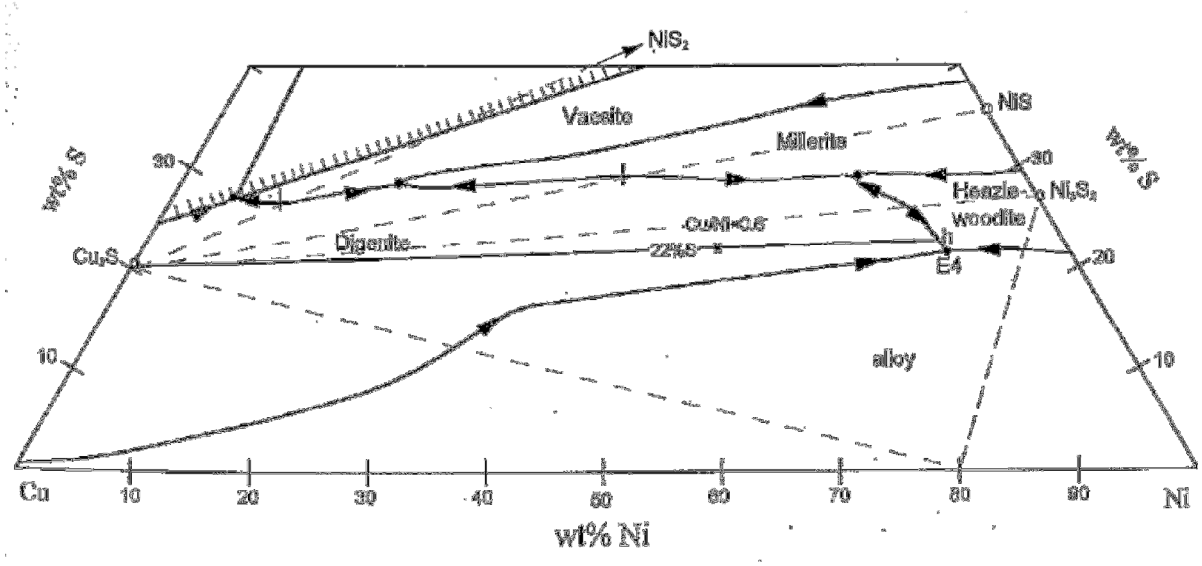

Figure 2.5-5: The crystallisation path of a matte with a 22%S (shown as x) and Cu:Ni ratio of 0.6 as projected on the Cu-Ni-S phase diagram (Bruwer, 1996). The Eutectic point E4 is from Sproule et al. (1960)

Thyse et al., 2013, examined the effect of end point composition of the ternary system Ni-Cu-S by using MTDATA phase diagram software, and quantified the liquidus temperature range, at fixed Fe and Co concentrations. It was concluded that the liquidus temperature range is lowered when the Fe and Co concentration decreases in the bulk matte. Moreover, it has also shown that variations in starting compositions of oxygen-free matte alter the path of solidification towards the eutectic and confirms the work done by Bruwer, 1996.

2.6 Previous studies on the slow cooling of WCM ingots

In 1994 four plant trials were conducted at the Waterval Smelter where WCM ingots, half the normal size, ingots were cast into the 28t size mould that was used at the time. Therefore two ingots with the same chemical composition each was cast and cooled (Figure 2.6-1), one with a lid on and one without (Bruwer, 1998).

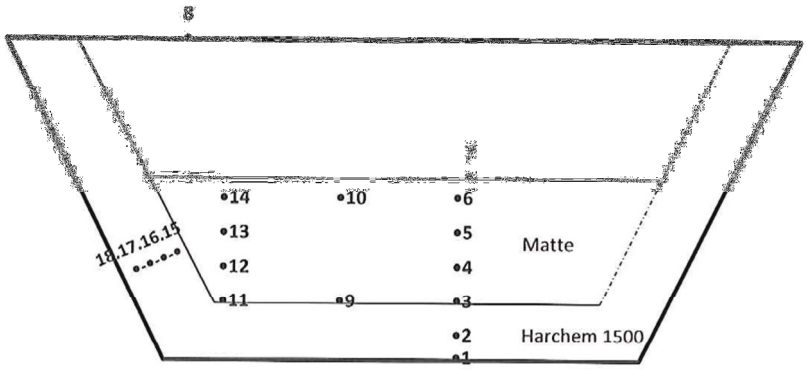

Figure 2.6-1: Thermocouple positions in matte (numbers 3-6, and 9-14) and in refractory lining (numbers 1, 2, and 15-18). The vertical spacing of the matte thermocouple tips were 110mm (Bruwer, 1998).

The chemical compositions of the two different sets of ingots are shown in Table 2.6-1, obtained from spoon samples.

Table 2.6-1: Cooling conditions and chemical analysis for four trial ingots from spoon samples obtained from two separate converter blows (Bruwer, 1998).

	%Cu	%Ni	%Fe	%S	Cooling Time (hours) to reach ~580°C (Eutectic point)
Test 1 - No lid (5) Test 1 - With lid (6)	27.7	47.1	1.9	20.6	24 26
Test 2 - No lid (7) Test 2 - With lid (8)	26	45.9	2.35	21.7	16 30

The key observations from the tests can be summarised by the following:

- The initial mould temperatures of the ingots without lids were hotter than that of the ingots that were cooled with lids.
- There was a much larger thermal gradient from top to bottom in the ingots that were cooled without lids.
- Comparison of the thermal profiles of the two sets of ingots indicates that the "hot" zone in the ingots occurs at different positions. The "hot" zone for ingots with lids were located more to the centre of the ingot and for those without lids, the hot zone were positioned at the bottom centre of the ingot.
- For the macro element analysis, the two ingots without lids had Ni enrichment at the bottom and the two ingots with lids had Ni enrichment in the centre.
- No conclusions were made regarding the platelet size of the alloy formed and from the chemical compositions it was also not conclusive if the faster cooling was detrimental to the WCM quality.

Several laboratory scale tests were also conducted to determine the influence of composition and cooling rates on WCM (Bruwer, 1998)[8]. The tests were conducted by taking 400g samples from chilled cast WCM and adjusting the chemistry by adding different proportions of metals and synthetic metal sulphide. The samples (with %S of 21.5%, 21.75%, 22%, 22.25% with a constant Ni:Cu ratio of 1.5 and %Fe of 2.8%wt) were then heated in an inert atmosphere and cooled down at different rates for comparison. The major observations from these tests can be summarised by the following:

- It was found that samples with lower sulphur content contained more alloy and that it consisted of larger, irregularly shaped grains. Therefore mattes with low sulphur will probably also contribute to losses in the MC Plant. It was concluded that a WCM matte with 22% S contained ~9% alloy, which is the closest to the design capacity of the MC Plant.

- Matte samples with similar compositions were also subjected to various cooling profiles and it was found that the cooling rates between 700°C - 500°C have an effect on the alloy grain shape. Cooling rates of ~10°C/h (0.167°C/min) were detrimental to the texture, whereas rates of ~4°C/h (0.067°C/min) did not have an effect on texture.

In practice however, on the plant scale environment there are large differences in the cooling rates in various parts of the ingot e.g. in the 800°C - 500°C temperature interval the cooling rates typically varies between ~14.4 °C/h (0.24°C/min) at the top to as low as ~3.6°C/h (0.06°C/min) at the bottom. The faster cooling rates in practice do not seem to have detrimental effect on the alloy formation and therefore the natural cooling process is far more complex than anticipated and cannot be simulated by small scale laboratory tests (Bruwer, 1998)[8].

In 2001 work was done on the thermal analysis on three different sized ingots (4t, 8t and 16t) where the three ingots were cast in identical shapes and cooled down using the same cooling profile as shown in Table 2.6-2 (Poushkarova, 2001). From the chemical analysis it was concluded that the ingots varied considerably in terms of macro and micro segregation. From the analysis it was concluded that the "hot" zone occurred at different levels for the different sized ingots. The hot zone in the 4t ingot appeared close to the bottom of the ingot, in the 16t ingot the hot zone was closer to the middle of the ingot and for the 8t ingot the hot zone was between the middle and the bottom of the ingot.

Table 2.6-2: Experimental cooling profile used (Poushkarova, 2001)

Temperature Range (°C)	Time interval (hours)	Time (cumulative hours)	Cooling Rate (°C/hour)	Cooling Rate (°C/minute)
1200 – 700	6	6	83	1.4
700 – 500	48	54	4	0.07
500 - ambient	12	66	42	0.7

To simulate the heat transfer, a computer model (ProCast) was developed by the Council for Scientific and Industrial Research (CSIR) in South Africa to simulate the cooling profiles of WCM (Pain, 1997). The model was designed by using the data from the temperature measurements done by Bruwer, 1998[10] and the cooling boundary conditions and material properties used is summarised in Tables 2.6-3 and 4. The thermal conductivity of matte, film coefficient on the matte surface and matte mould interface coefficient were calculated by means of an inverse modelling method from a 2d thermal analysis model.

Table 2.6-3: Material properties and boundary conditions calculated and used for the 2D thermal model as developed by the CSIR

Material	Temperature (°C)	Thermal Conductivity (W/m/K)	Latent Heat of fusion (KJ/Kg)	Density (Kg/m^3)	Cp (KJ/kg/K)
WCM	300	7.1	140	6500	
WCM	500	11.5	140	6500	
WCM	620				0.568 (linear)
WCM	700	7.0	140	6500	
WCM	920	6.3	140	6500	
WCM	960	7.0	140	6500	
WCM	1380				0.674 (linear)
Harchem 1500 (Hot face refractory material)	All temps	1.05		2250	0.88
Harcast 1300 (cold face refractory material)	500	0.91		2250	0.88
Harcast 1300 (cold face refractory material)	1000	0.97		2250	0.88
Civil Concrete	All	1.37		2100	0.88

** Matte liquidus temperature 920°C and solidus temperature 610°C

Table 2.6-4: Matte and mould interface coefficient and matte surface coefficient as calculated by the CSIR

Matte Surface film coefficient (as determined by inverse module)				Matte/mould interface coefficient (as determined by inverse module)	
Temperature (°C)	$W/m^2/K$ (With cover)	W/m2/K (Without cover)	Emissivity	Temperature (°C)	W/m/K
500	9.7	37	0.94	500	414
700	9.8	37	0.94	700	1850
900	21	37	0.94	900	10000

The model developed by the CSIR was done with some of the very first finite element modelling packages available. The model did not predict the initial faster cooling rates just after casting and also did not include and simulate differences in chemical compositions and the influence of this on material properties with temperature throughout the ingot. Most of the WCM material properties finally used in the model was also calculated by means of trial and error using the model because of the limited data available. It was concluded from the model that the removal of the lid has a drastic effect on the cooling rate of the matte as the heat transfer mechanisms are mainly radiation and convection to air. (Bruwer, 1998)[7]

Further work was also done by Sheng, 1998, on the mathematical modelling of smelting of nickel matte in an electric furnace where the thermal conductivity of matte used was 17 W/m/K and density 4500 kg/m^3.

3. Experimental Design

3.1 Plant Trials

3.1.1 Background

As described above, the ACP produces a sulphide converter matte which is slow-cooled in ingots over several days. During the process, the formation of alloy platelets, containing the majority of the PGM's and Au, occurs. The alloy forms a magnetic fraction in the bulk matte which can be liberated when the matte is crushed and milled. The alloy platelets are then separated via a magnetic separation process in the MC Plant. The quality of the converter matte is dependent on the reaction and cast temperatures, bulk matte composition and cooling rate of each ingot, which defines the microstructure of the slow-cooled matte that is produced as the final product of the ACP process.

The current mould size used in the ACP slow-cool aisle is ~10 tonnes (maximum 14.84t), designed for 2 full ingots to be poured from every tap from a full ladle with a capacity of ~20t. This is the ideal situation, however, during normal plant operation ladles develop a build-up of material on the inside (or scull) that reduces the ladle active volume. This results in a large number of half ingots being produced, and, given the smaller ingot size, suboptimal cooling conditions arise and subsequently poor quality WCM is produced because of rapid cooling.

In an attempt to match the converter blow size, the ladle size and the slow-cool mould size in future, a larger mould size of 15 tons was specifically constructed to determine if the smelter can convert and cast into the larger mould size. Therefore a larger size ingot of 15t with a maximum capacity of 20.6t was also used as part of the trials in order to determine if cooling rates in the larger sized ingot necessitated longer cooling times, and would therefore negatively affect the platinum pipeline and working inventory. The data obtained from these trials was then used to validate a CFD model, specifically developed to simulate the cooling process.

3.1.2 Experimental Design

The plant trials were designed to measure the cooling rates in various locations of three different sized ingots for the duration of the cooling process. Three test ingot moulds were prepared with the dimensions as presented in Table 3.1-1 and Figure 3.1-1.

Table 3.1-1: Geometry calculations for the three different sized moulds used

	Units	Test 1 - Ingot B (9.7t)	Test 2 - Ingot C (5.5t)	Test 3 - Ingot A (14.7t)
Radius B (mould upper surface radius)	m	1.0940	1.0940	1.2525
Radius A (mould lower surface radius)	m	0.7391	0.7391	0.8049
Radius at upper surface of ingot	m	1.0047	0.9043	1.1717
Slant Angle of cone (Deg)	degrees	20	20	24.09
Total mould depth (Height of mould = frustrum height)	m	0.975	0.975	1.001
Ingot Height	m	0.73	0.45	0.82
Feeboard height	m	0.25	0.52	0.18
Surface area A (Mould Lower base area)	m^2	1.72	1.72	2.04
Ingot lower base area relative % size increase	%	0%	0%	19%
Surface area ingot top (Ingot Upper base area)	m^2	3.17	2.57	4.31
Ingot upper surface area relative % size increase	%	23%	0%	68%
Surface area B (Mould Upper base area)	m^2	3.76	3.76	4.93
Ingot side surface area	m^2	5.68	5.36	6.81
Ingot side circumference surface area relative % size increase	%	6%	0%	27%
Total mould Surface area	m^2	11.45	11.45	14.05
Total Ingot Surface area	m^2	10.57	9.64	13.16
Ingot total surface area relative % size increase		10%	0%	36%
Total cone volume (full mould)	m^2	3.77	3.77	4.60
Mould Frustrum volume	m^3	2.61	2.61	3.38
Total cavity volume on top of mould	m^3	0.85	1.64	0.83
Ingot volume	m^3	1.76	0.97	2.55
Calculated SG of WACM	ton/m^3	5.695	5.695	5.695
Max Mass of full ingot	t	14.8	14.8	19.3
Normal mass of ingot	t	10.00	5.50	14.50
% Underfill	%	48%	170%	33%
Ratios:				
Ingot - Total volume : Total surface area		0.17	0.10	0.19
Ingot - Upper base area : Total Surface area		0.30	0.27	0.33
Ingot - Upper base area : Total volume		1.81	2.66	1.69
Ingot - Top : bottom radius		1.36	1.22	1.46

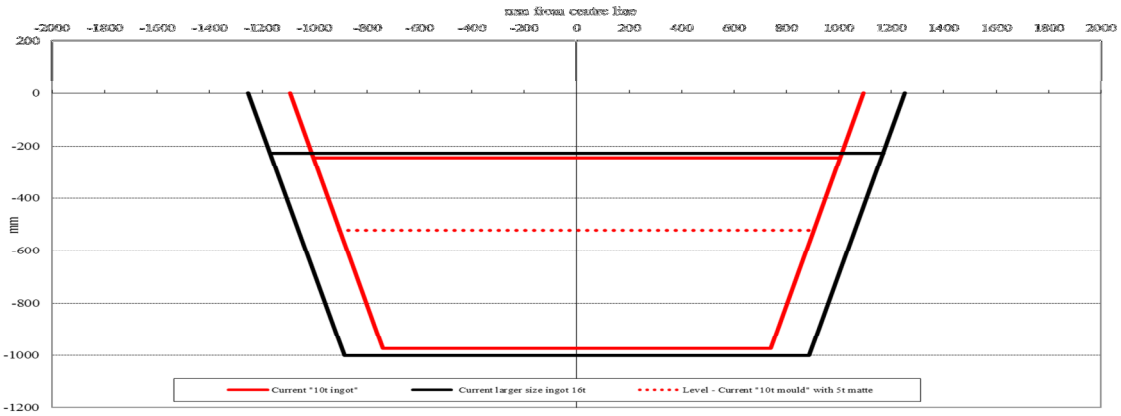

Figure 3.1-1: Schematic representation of ingot cavity and fill dimensions with the zero on the vertical axis on ground level and on the horizontal axis through the centre line of the mould.

After tapping the matte into a 20t ladle, the matte was cast (Figure 3.1-2) into the mould and a rig containing the thermocouples (Figure 3.1-3) was placed into the molten WCM (Figure 3.1-4). The thermocouples were then connected to digital data recorders (Figure 3.1-5) and the lid placed over the mould for the slow cooling process to commence.

Figure 3.1-2: Casting of WCM from a 20t ladle via a bottom caster into the refractory lined mould

Figure 3.1-3: Empty mould with the prepared thermocouple rig positioned over it. The steel thermocouple holders were coated with a refractory to prevent reaction between the steel and the WCM

Figure 3.1-4: Molten WCM in a mould with the thermocouple rig positioned in the molten material. In the background of the picture (left) a typical lid positioned over a mould is visible.

Figure 3.1-5: Two of the four channel digital recorders used for data collection

The thermocouples were positioned as illustrated in Figure 3.1-6 – 3.1-8, similar to the work done in 1998 by J Bruwer which was also reported by Schouwstra, 2005.

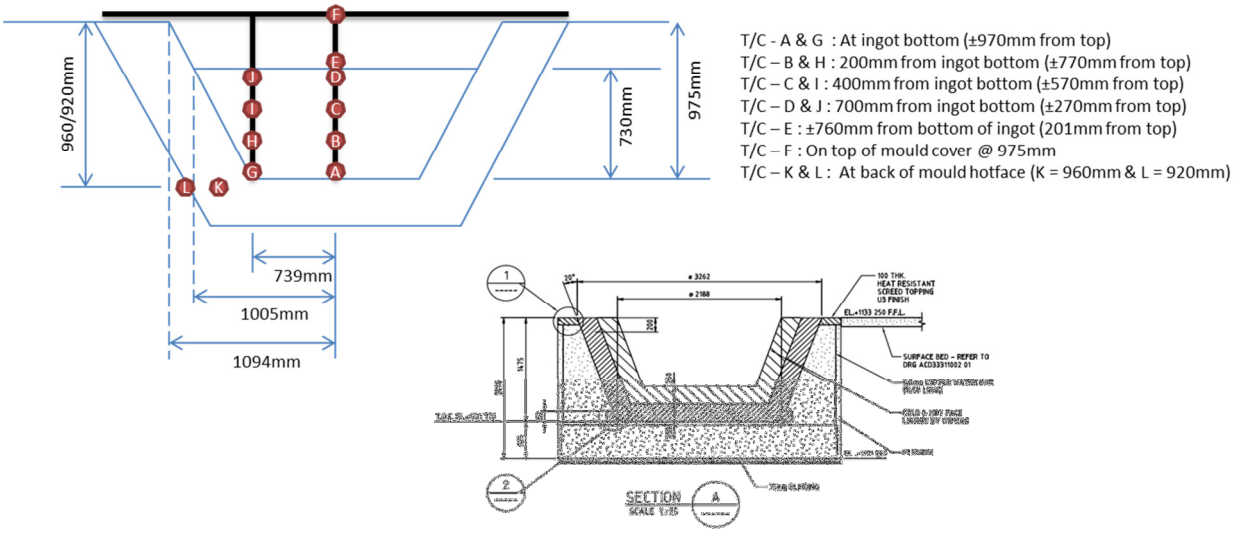

Figure 3.1-6: Thermocouple locations in 10t mould

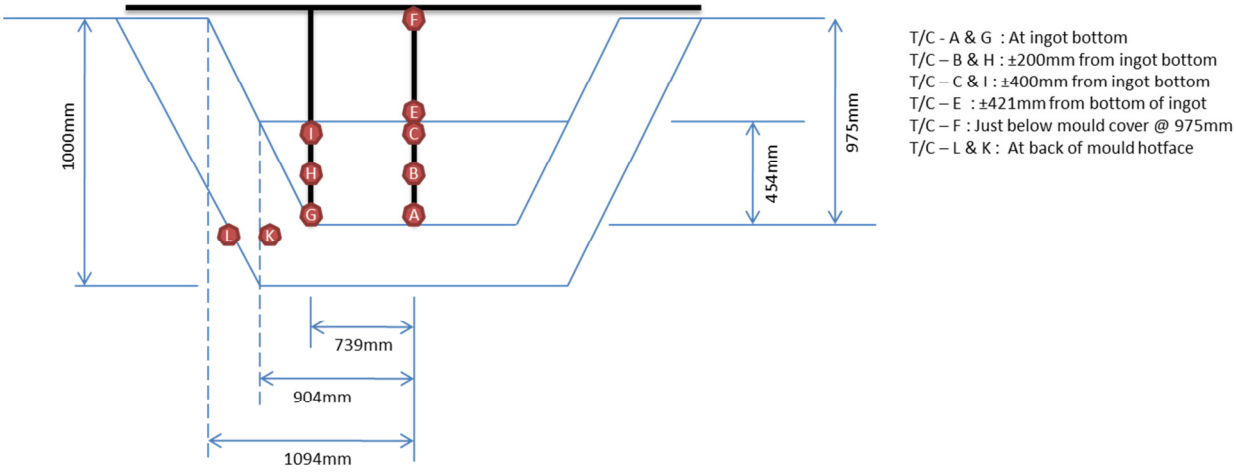

Figure 3.1-7: Thermocouple locations in current ACP 10t mould but with a 5t cast

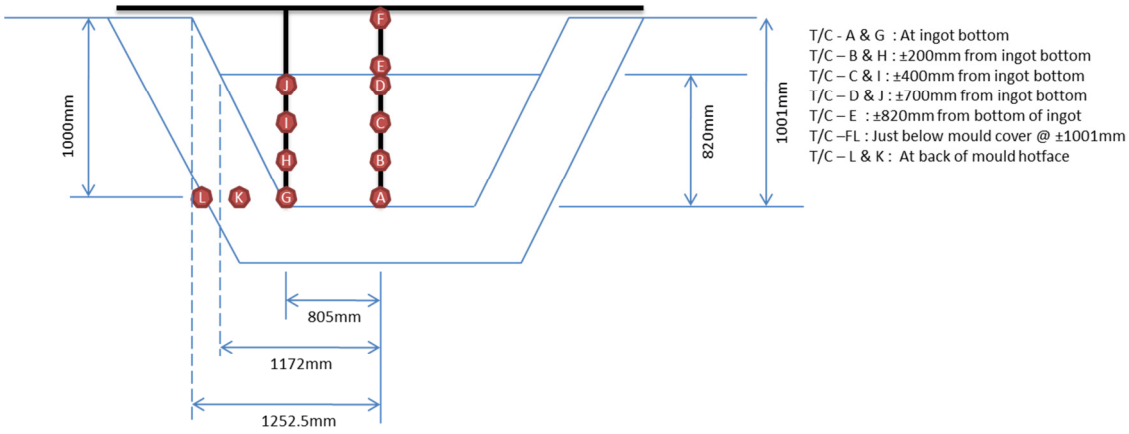

Figure 3.1-8: Thermocouple locations in current ACP 20t mould but with a 15t cast

The data for each tap and cast was recorded on a separate log sheet and is summarised in Table 3.1-2. During each tap three lollipop samples were taken from the converter matte launder at the start, midway through and at the end of each tap. Each time that a sample was taken the matte tapping temperature was measured and recorded. The average chemical analysis from these samples was used to calculate the bulk chemical composition for each specific tap. A fourth matte sample was taken directly after casting the matte into the mould as a reference sample. Furthermore tap and cast temperatures together with time sequences were also recorded on the log sheets.

Table 3.1-2: Log sheet of tap and cast data

SLOW COOL AISLE WCM DATA LOG SHEET AND CHECK LIST- PLANT TRIAL									
TRAIL NUMBER:	1			2			3		
DATE:	30-Jun-11			21-Jul-11			04-Aug-11		
TIME:	~16H45			~11H50			~14H00		
BLOW NUMBER	C02-110630-05			C02-110721-04A			C02-110804-06		
MATTE TAPPING	START	MID	END	START	MID	END	START	MID	END
TAP TEMPERATURE	1249	1254	1257	1273	1288	1291	1293	1291	1291
MATTE CASTING									
MOULD SURFACE T BEFORE CASTING	95			101.4			78.4		
1ST INGOT DATA	START	MID	END	START	MID	END	START	MID	END
MATTE CASTING TEMP	1047	1054	1054						
TIME OF CAST START	17:44:00 PM	TIME OF CAST END	17:49:00 PM	11:55:00	TIME OF CAST END	12:05:00	14:33:00	TIME OF CAST END	14:40:00
START TC TEMPS	@ 18:20								
A	968			350.8			1049.5		
B	972			939.1			1048.1		
C	974			928.5			1037.2		
D	959						1048.8		
E	809			989.6			819.7		
F	47.3	@18:35		25.5			23.2		
G	972			998			1052.3		
H	972			109.4			1050.6		
I	971			1065.4			1052.4		
J	966						1051.1		
K	133.7			116.8			61.5		
L	121.3			118.2			40.2		
LADLE DATA									
EMPTY LADLE MASS	19			15.4			21.6		
LADLE MASS AT START OF CAST	41.2			39.8			37.1		
LADLE MASST AT END OF CAST	31.5			34.3			22.4		
INGOT MASS BY DIFF	9.7			5.5			14.7		
TAP MASS	22.2			24.4			15.5		
LID ON TIME	18:28:00 PM			12:50:00			15:10:00		
MEASURED INGOT HEIGHT (DIST FROM FULL)	~190			~577			~250		
2ND INGOT DATA	START	MID	END	START	MID	END	START	MID	END
MATTE CASTING TEMP	1041	995	950				N/A		
TIME OF CAST START	18:06:00 PM			12:17:00	TIME OF CAST END	12:20:00			

The three test ingots were cast from matte produced under normal converter operations with a blend of feed material from Polokwane Smelter, Mortimer Smelter and Waterval Smelter. The WFM also included matte produced from the Slag Cleaning Furnace. The matte produced was typical of the converter matte produced during normal operation and it was aimed to achieve the following specifications:

- Ni:Cu Ratio = 1.5 – 1.8 (Wright, 1998)
- %S ~ 21%
- % Fe = 3–3.8% (Taylor, 1997). Collection efficiency of matte peaks around 3.5% Fe (Badcock, 1993)
- %SiO_2 in slag 28%-30% (Taylor, 1997) – Basicity ~ 1.75
- Converter operating temperature >1250^{o}C
- Matte tapping temperature ~ 1250^{o}C (J Hill, 1995)
- Matte casting temperature > 1150^{o}C (Badcock, 1993)
- Lid on temperature > 1050^{o}C (Badcock, R.F.W. ,1993)
- Cooling process for a 10 ton ingot as currently practised at the ACP
    - Cooling in mould 52hrs with lid on
    - Cooling in mould 20 hrs without lid
    - 24 hrs air cooling out of mould

After air cooling of the ingots, core drilling was done according to the profile schematically shown in Figure 3.1-9. The Figure 3.1-10 shows a picture of an ingot after core drilling.

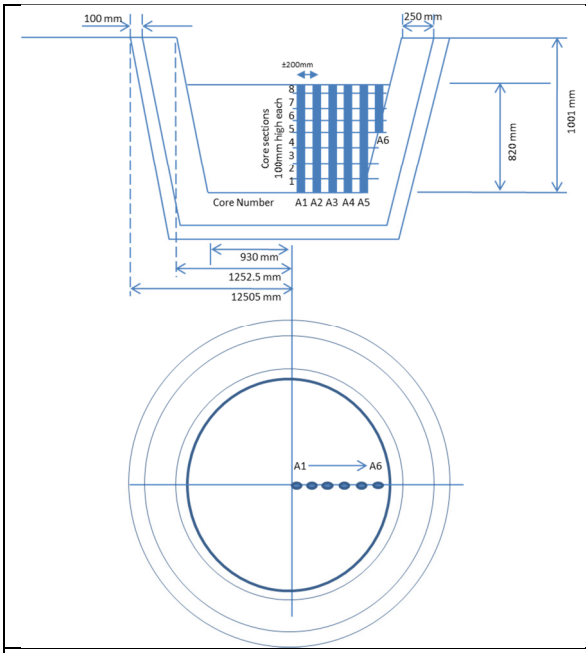

Figure 3.1-9: Schematic representation of the core drilling done on ingot A, test 3. It also shows the core numbering pattern used for the experiments

Figure 3.1-10: Photo showing the 6 core holes in the 15t ingot after drilling

3.2 Sample Preparation and Analysis

The cores from each of the three ingots were then separately cut in half (Figure 3.2-1) and divided into 100mm sections (Figure 3.2-3). Each section was then individually numbered (Figure 3.1-9 and Figure 3.2-3) and prepared for both mineralogical and chemical analysis. The samples were crushed to -3mm and split into 16 even portions by means of a rotary splitter (Figure 3.2-4). One portion of the sample was then used for chemical analysis and further milled and prepared. A second portion of the sample was then prepared for the mineralogical analysis by preparing sample cups where the samples were mixed with resin, placed under vacuum and left to set. These samples were then polished and placed in the QEM-SEM sample holder for mineralogical analysis (Figure 3.2-2).

Figure 3.2-1: Diamond blade saw used to cut the drill cores in sections for analysis

Figure 3.2-2: Polished samples loaded into the sample holder ready for the QEM-SEM

Figure 3.2-3: Drill cores laid out in a sample tray, marked out and numbered

Figure3.2-4: Sample splitter used during sample preparation

Figure3.2-5: QEM-Scan machine used for bulk modal mineralogical analysis

Figure 3.2-6: Showing the loaded samples for QEM

Figure 3.2-5 shows the SEM used for bulk modal scanning of the samples and the scanning was done at 61x magnification, scanned on point spacing every 3µm and line spacing every 250µm. The sample was set up with a 30mm diameter scanning pattern (Figure3.2-6), with a total of 413 fields over the sample surface.

4. Data Analysis

4.1 Chemical Analysis

Three ingots of different masses were cast as described in the experimental design section and the bulk chemical analysis for each are shown in tables 4.1-1 and 4.1-2. For the purposes of the test work it was aimed to produce similar type converter mattes with ~3% Fe, but this was achieved only for test 1 and 3. The WCM in Test 2; however had a Fe content of 4.7% which was out of the desired specification but still within the limits of acceptable quality according to plant standards. From the data it was also expected that for test 2 and 3, higher quantities of alloy plates would be produced, compared to test 1, as shown in the theoretical alloy calculation. The low theoretical % alloy of 8.4% predicted for test 1 can be ascribed to the relatively low %Fe and high %S in the matte. The theoretical %S and %alloy for test 2 and 3 were similar but, because of different reasons, test 3 had both low %Fe and %S, resulting in a higher theoretical sulphur deficiency and therefore a higher expected % alloy. The data from test 2 suggests that the slightly higher %Fe and % Ni in the matte will result in the higher predicted % alloy. The Ni:Cu ratio in tests 1 and 2 were within the required range of 1.5 – 1.8 (Wright, 1998); however, the test 3 ratio was well below this value at 1.41 which could lead to an abundance of copper- iron sulphides, fine grained alloy platelets and abundant sulphide-plate intergrowths (Schouwstra, 1999).

Table 4.1-1: Bulk chemical composition of the three ingots obtained from tap samples, and an average of three samples that was taken during each tap.

	Cu	Fe	Ni	S	Total	Ni/Cu	PGM/ (Cu+Ni)	Theoretical	Theoretical	Theoretical % Sulphur
	%	%	%	%	Ni+Cu+Fe+S	ratio	ratio	% alloy	% S	@100%
Test 1-9.7t	28.7	3.3	44.7	22.4	99.1	1.56	34.5	8.4	88%	25.4
Test 2 - 5.5t	26.9	4.7	45.0	21.5	98.1	1.67	51.5	11.8	83%	25.9
Test 3 - 14.7t	31.0	3.0	43.8	20.9	98.8	1.41	37.5	12.7	82%	25.5

The bulk precious metal analysis for the three tests is shown in Table 4.1-2 and indicated that the ingot in test 2 also had a significant higher Pt, Pd, Rh, Ir, Ru contents and Pt:Pd ratio than test 1 and test 3. The PGM: Base metal ratio was also significantly higher for test 2.

Table 4.1-2: Bulk chemical composition of the Precious Metals of the three ingots obtained from tap samples, and is an average of three samples that was taken during each tap.

	Pt	Pd	Au	Rh	Ir	Ru	Pt/Pd
	ppm	ppm	ppm	ppm	ppm	ppm	Ratio
Test 1-9.7t	1230	694	53	191	67	296	1.77
Test 2 - 5.5t	1870	876	60	289	112	490	2.14
Test 3 - 14.7t	1340	823	65	212	72	295	1.63

As described in the experimental design, the cores from each ingot were sliced up in 100mm sections, samples prepared and then analysed. The detailed schematic drawings with dimensions showing the core layouts for each ingot are shown in detail in Appendix 1. Figures 4.1-1, 4.1-2, 4.1-5, 4.1-6, 4-19 and 4.1-10 show the schematic and actual layout of the cores for each of the three ingots that correspond to the sequence of the chemical analysis shown for the base and precious metals in the graphs below.

Test 1, Ingot B, 10t - Chemical analysis data

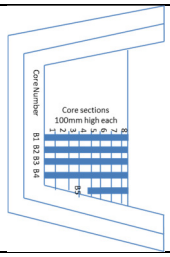

Figure 4.1-1: Core layout for Test 1, Ingot B, 10t. The schematic is in the specific orientation to correspond with the graphs below.

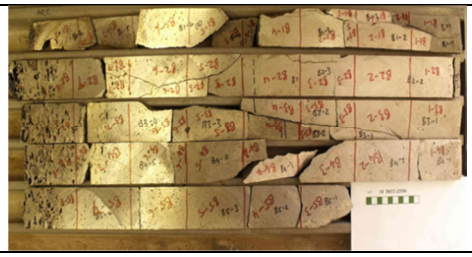

Figure 4.1-2: Picture of the cores that were sliced in half. The picture is a mirror image of the core layout as schematically shown in Figure 4.1-1 because of the angle of the original photo but is marked accordingly.

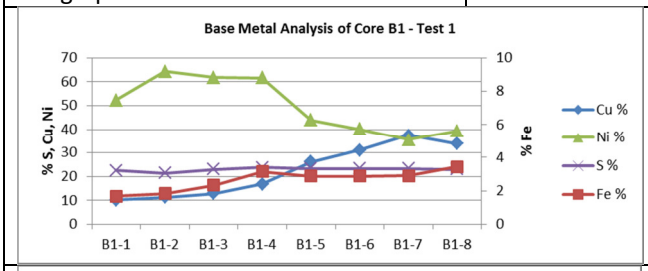

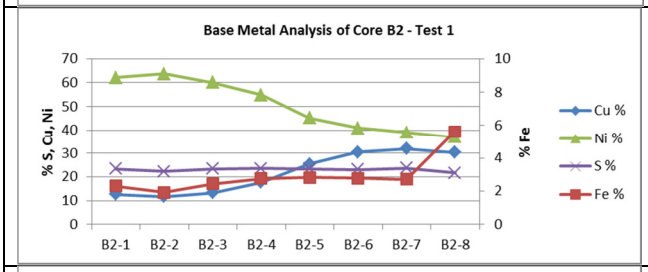

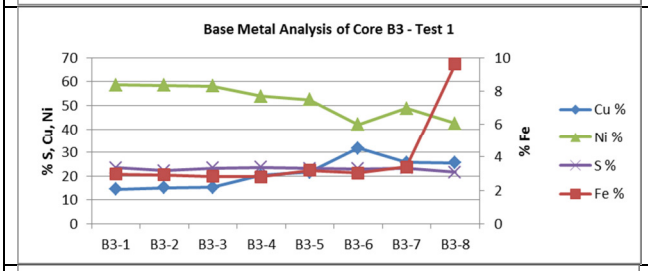

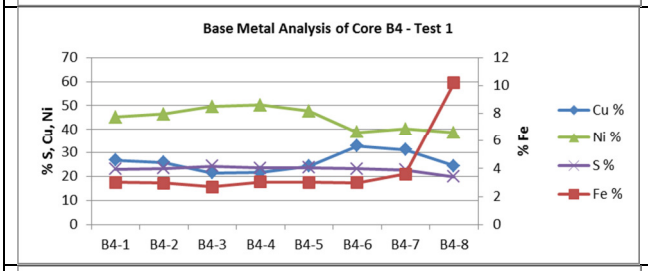

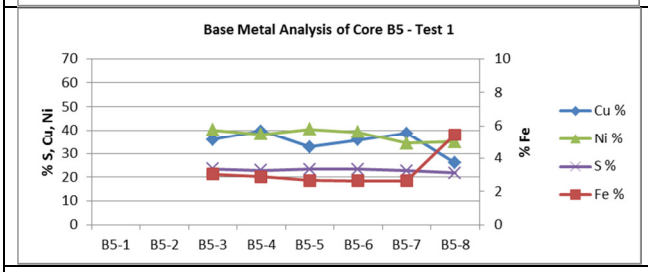

Figure 4.1-3 Graphs for Test 1, Ingot B, 10t – showing the **Base Metal Analysis** per drill core for each 100mm section from the bottom of the ingot at position 1 to the top of the ingot at position 8 (left to right on the x-axis).

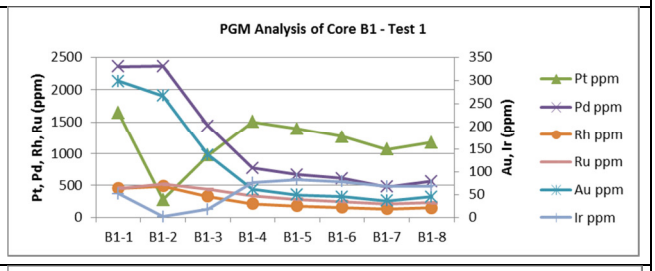

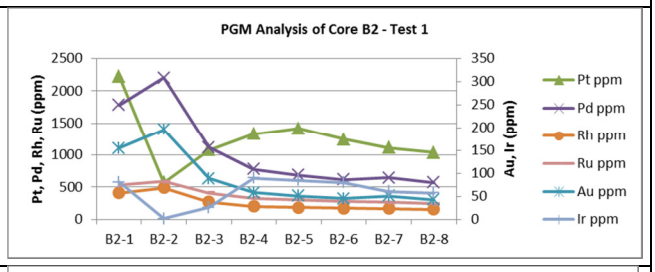

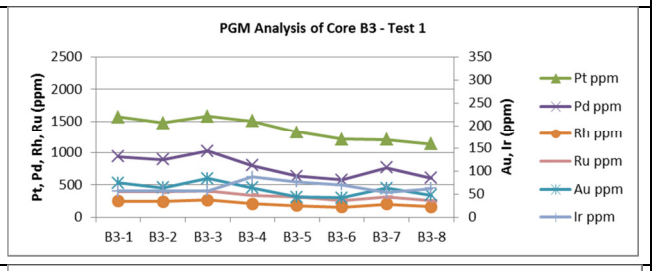

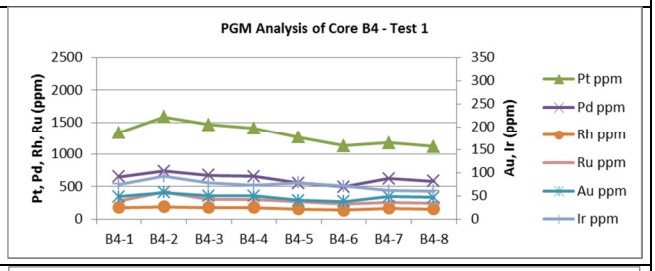

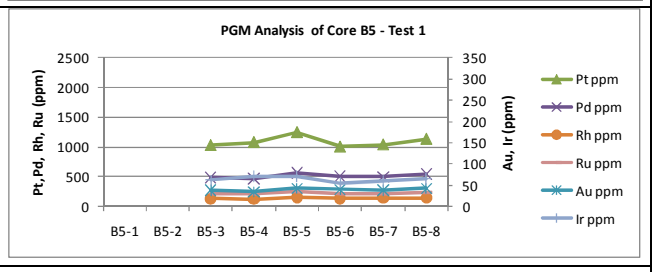

Figure 4.1-4 Graphs for Test 1, Ingot B, 10t – showing the **Precious Metal Analysis** per drill core for each 100mm section from the bottom of the ingot at position 1 to the top of the ingot at position 8 (left to right on the x-axis).

The graphs for Test 1 for Cores 1 to 5 indicate the following general trends:

- The S and Fe contents stay constant throughout the ingot except for cores B2 to B5 where an elevated amount of Fe is seen only in the top layer of the ingot (slice 8) and this can be due to magnetite formation.
- The composition of Ni and Cu also vary as expected, with higher levels of Cu observed in the upper sections of the ingot, as copper sulphides would solidify first. The Ni content in the core section of the ingot is higher than the outer sections as expected, as the nickel sulphides solidify last.
- For the PGE the normal trend of increasing Pd, Au, Rh and Ru towards the base-centre of the ingot is observed
- Pt and Ir show the usual trend of decreasing quantities towards the base of the ingot.
- Samples B1-1 and B2-1 however show a reversal of the two points described above and is as a result of the chill zone that normally forms at the bottom of the ingot.
- There is almost no Ru, Rh, Pd and Pt in the outer core (B5) visible

Test 2, Ingot C, 5t - Chemical analysis data

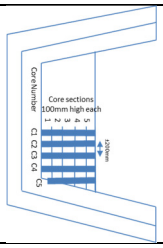

Figure 4.1-5: Core layout for Test 2, Ingot C, 5t. The schematic is in the specific orientation to correspond with the graphs below.

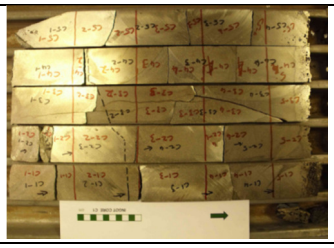

Figure 4.1-6: Picture of the cores that were sliced in half. The picture is upside down with core 5 on top and core 1 at the bottom compared to the core layout as schematically shown in Figure 4.1-5 because of the angle of the original photo but is marked accordingly.

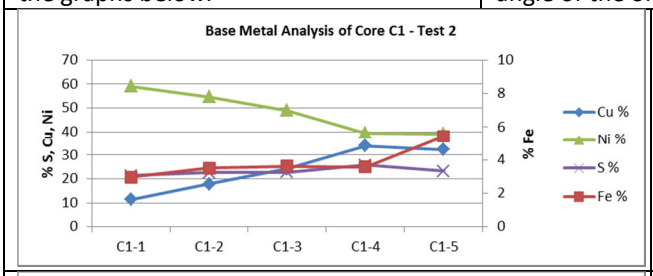

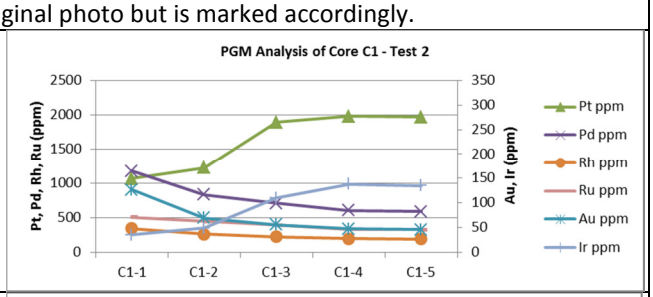

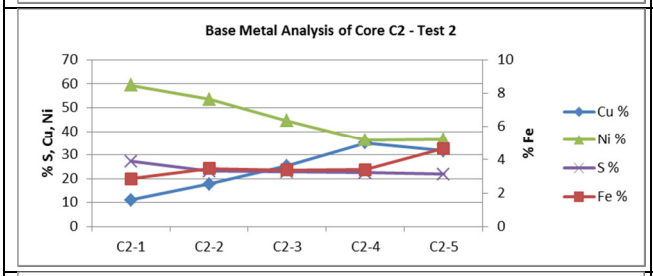

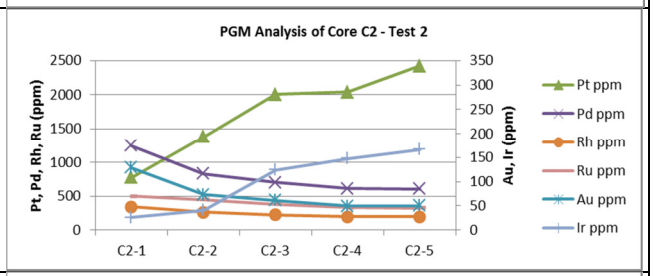

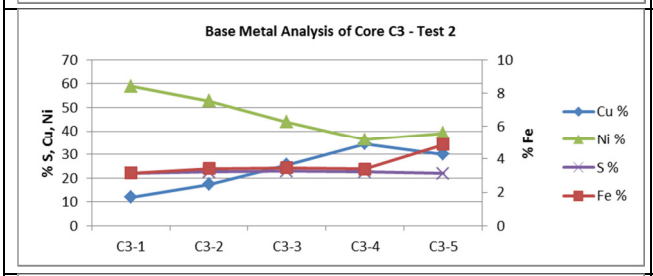

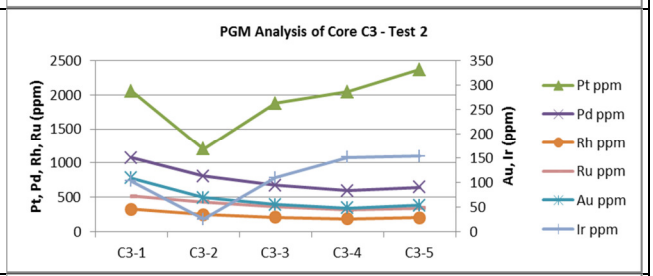

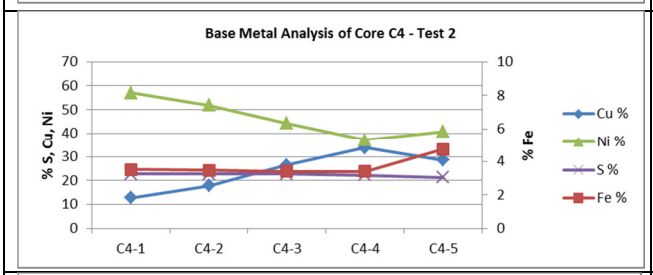

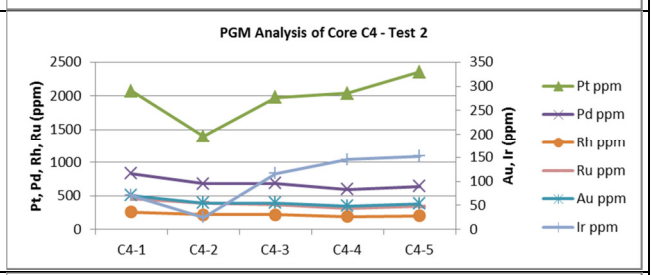

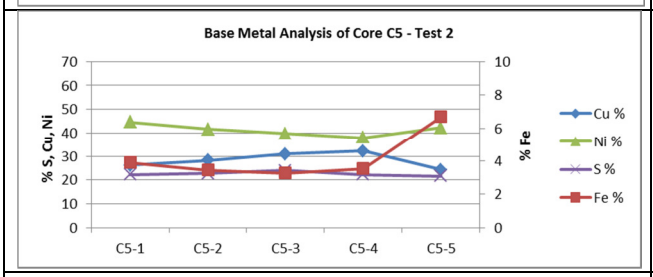

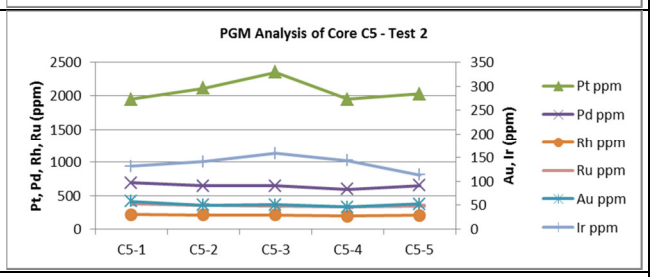

Figure 4.1-7 Graphs for Test 2, Ingot C, 5t – showing the Base Metal Analysis per drill core for each 100mm section from the bottom of the ingot at position 1 to the top of the ingot at position 5 (left to right on the x-axis).

Figure 4.1-8 Graphs for Test 2, Ingot C, 5t – showing the Precious Metal Analysis per drill core for each 100mm section from the bottom of the ingot at position 1 to the top of the ingot at position 5 (left to right on the x-axis).

The graphs for Test 2 for Cores 1 to 5 indicate the following general trends:

- The S and Fe contents stay constant throughout the ingot
- The composition of Ni and Cu also vary as expected, with higher levels of Cu observed in the upper sections of the ingot. The Ni content in the core section of the ingot is higher than the outer sections as expected. The outer core (Core C-5) shows a relatively constant analysis for both Cu and Ni, possibly indicating that this area in the ingot solidified rapidly with little fractional crystallisation taking place.
- For the PGE the normal trend of increasing Pd, Au, Rh and Ru towards the base-centre of the ingot is observed
- Pt and Ir shows the usual trend of decreasing quantities towards the base of the ingot
- Again the PGM analysis for the outer core (C5) shows a fairly constant analysis for all PGE's and therefore possibly showing signs of rapid cooling without fractional crystallisation.

Test 3, Ingot A, 15t - Chemical analysis data

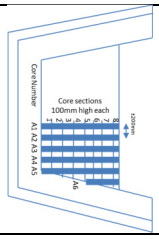

Figure 4.1-9: Core layout for Test 3, Ingot A, 15t. The schematic is in the specific orientation to correspond with the graphs below.

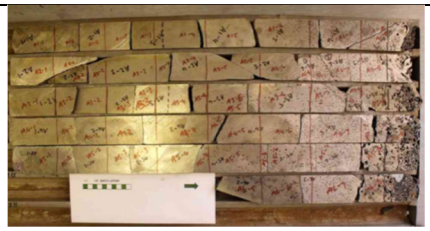

Figure 4.1-10: Picture of the cores that were sliced in half. The picture is laid out exactly the same as the core layout schematically shown in Figure 4.1-9 and is marked accordingly.

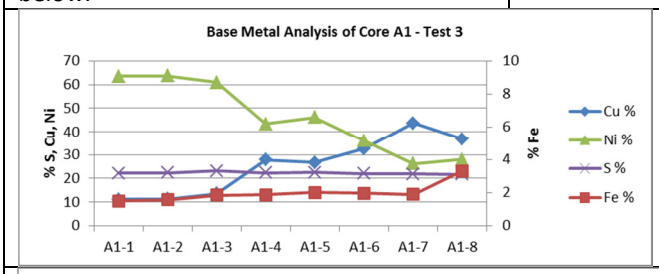

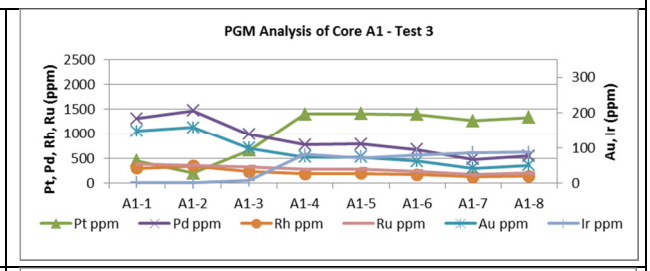

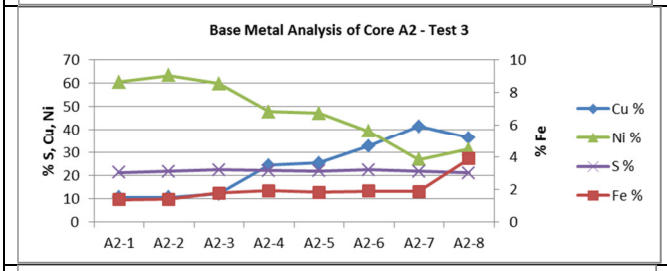

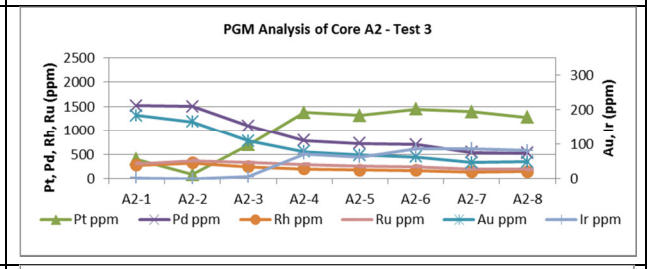

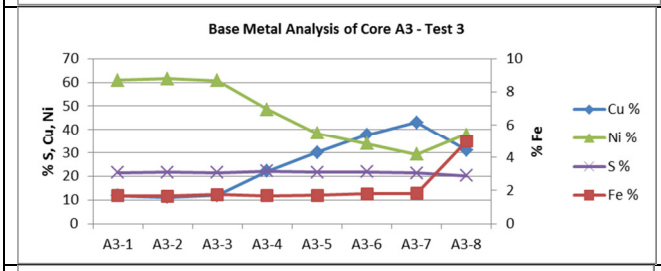

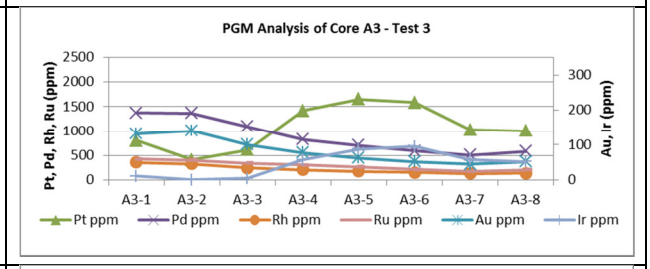

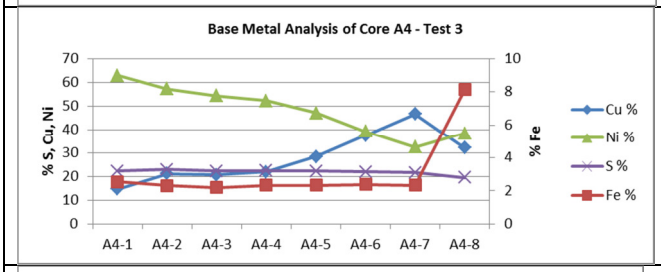

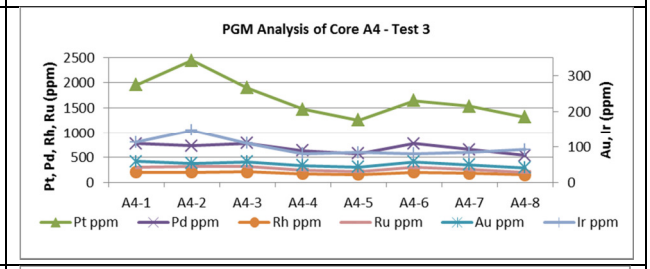

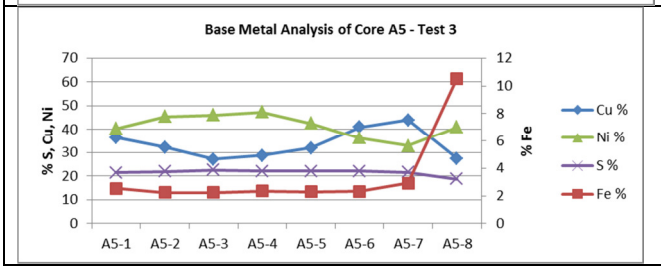

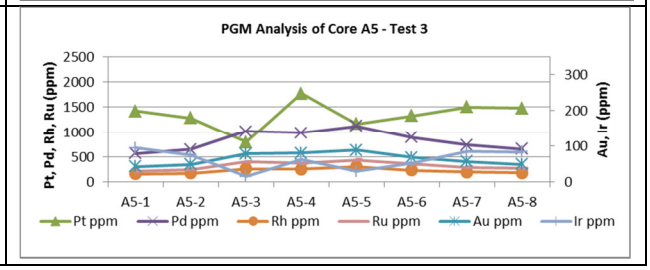

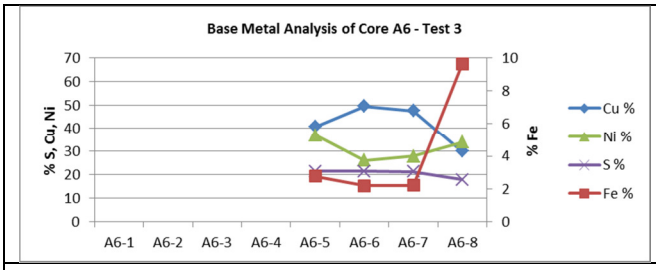

Figure 4.1-11 Graphs for Test 3, Ingot A, 15t – showing the Base Metal Analysis per drill core for each 100mm section from the bottom of the ingot at position 1 to the top of the ingot at position 8 (left to right on the x-axis).

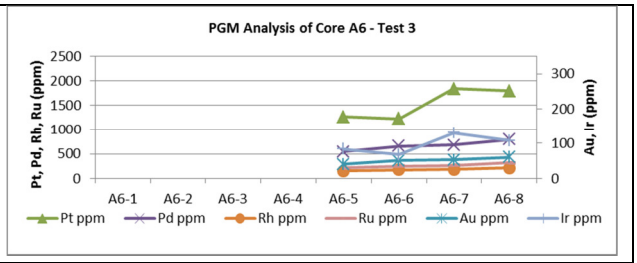

Figure 4.1-12 Graphs for Test 3, Ingot A, 15t – showing the Precious Metal Analysis per drill core for each 100mm section from the bottom of the ingot at position 1 to the top of the ingot at position 8 (left to right on the x-axis).

The graphs for Test 3 for Cores 1 to 8 indicate the following general trends:

- The S and Fe contents stay constant throughout the ingot except for cores A3 to A6 where an elevated amount of Fe is seen only in the top layer of the ingot (slice 8) and this can be due to magnetite formation.
- The composition of Ni and Cu also vary as expected, with higher levels of Cu observed in the upper sections of the ingot. The Ni content in the core section of the ingot is higher than the outer sections as expected.
- For the PGE the normal trend of increasing Pd, Au, Rh and Ru towards the base-centre of the ingot is observed
- Pt and Ir shows the usual trend of decreasing quantities towards the base of the ingot
- The short core (Core 6) on the edge of the ingot shows very little variation in base and precious metal analysis, indicating rapid cooling with little or no fractional crystallisation.

4.2 Comparative Mineralogical Data

The mineralogical analysis was done by means of bulk modal scanning on a QEM-SEM as described under the experimental design (Section 3.2) and the data are summarised and compared below based on the three major mineralogical species present in the ingots. These major phases are nickel sulphides [heazlewoodite (Ni_3S_2)], copper sulphides [bornite (Cu_5FeS_4 or $Cu_5S_3.FeS$), djurleite ($Cu_{1.97}S$) or digenite (Cu_9S_5) (depending on the temperature)] and Base Metal Alloy (BMA). The colour scale in the figures below is just for illustration purposes and was applied relatively for each major component present where green indicates the "highest" amounts present, yellow is "mid-range" and red the "lowest" region.

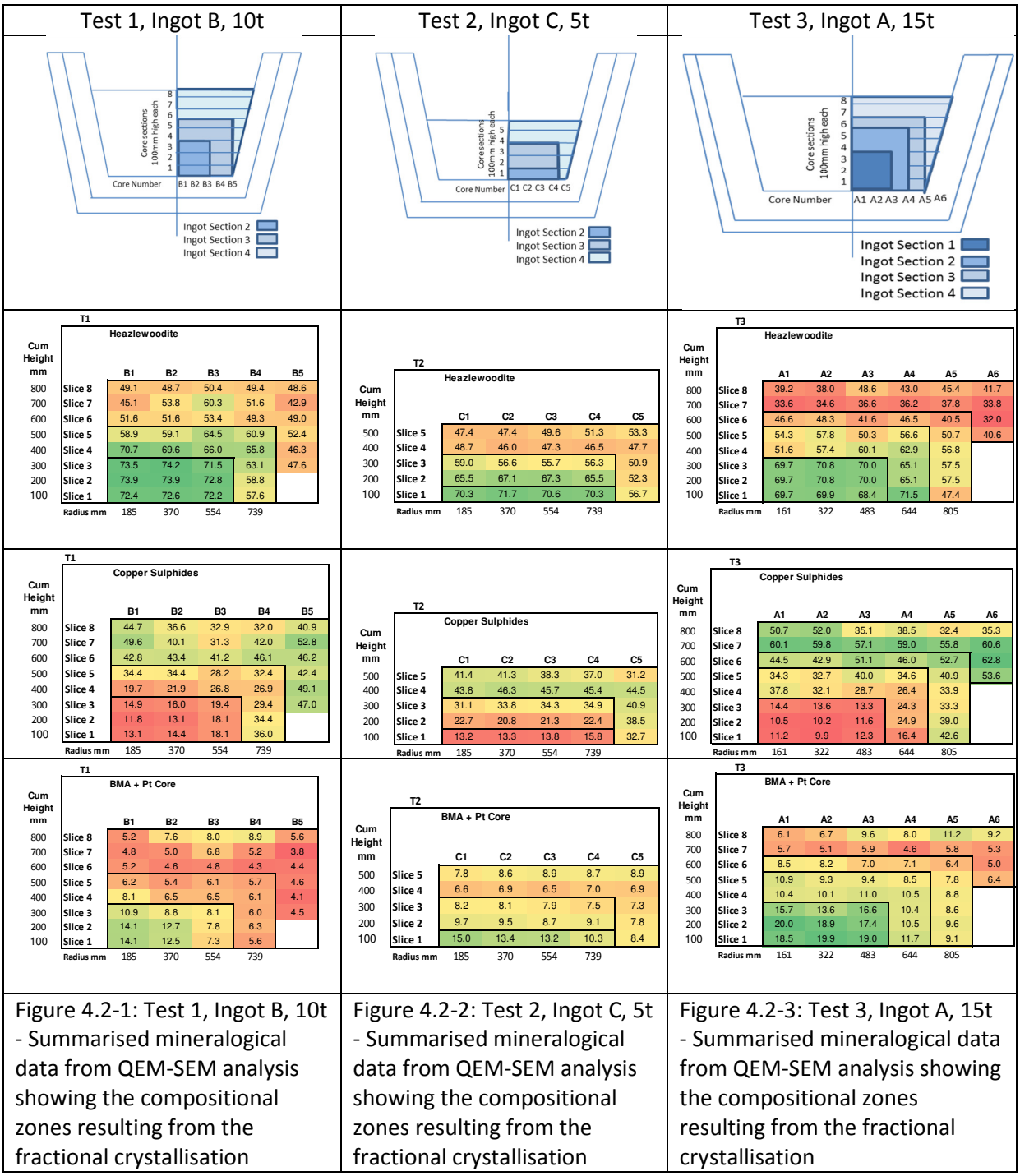

Figure 4.2-1: Test 1, Ingot B, 10t - Summarised mineralogical data from QEM-SEM analysis showing the compositional zones resulting from the fractional crystallisation

Figure 4.2-2: Test 2, Ingot C, 5t - Summarised mineralogical data from QEM-SEM analysis showing the compositional zones resulting from the fractional crystallisation

Figure 4.2-3: Test 3, Ingot A, 15t - Summarised mineralogical data from QEM-SEM analysis showing the compositional zones resulting from the fractional crystallisation

Each of the ingots was then divided into sections depending on the relative amounts of BMA with the general rule applied being:

- Section 1: BMA & Pt core ~ > 15 % (green)
- Section 2: BMA & Pt core between ~ 9% – 15% (yellow)
- Section 3: BMA & Pt core between ~ 6% - 9% (yellow)
- Section 4: BMA & Pt core between ~ < 6% (red)

The ingot in test 3 was significantly bigger and had a distinct higher BMA content in the core (>15%), therefore it was divided into four sections, while the other two smaller ingots for test 1 and 2 only had 3 sections each, as schematically shown in the Figures above. The outer sections (Section 4) of all the ingots shows higher amounts of copper sulphides, mostly bornite (Cu_5FeS_4 or Cu_5S_3.FeS) or djurleite ($Cu_{1.97}S$) and this decreases towards the cores (section 1 and 2). This is in line with the expected fractional solidification as described in section 2.5. The centre of each ingot is nickel rich and the nickel sulphide is present as heazlewoodite (Ni_3S_2). The detailed mineralogical data for all the drill cores, showing all the phases present in each ingot, is summarised in Appendix 2.

4.3 QEM SEM Micrographs

For completeness a few micrographs were taken of the centre two cores of ingot A, 15t, test 3 (Figure 4.3-1 to 4.3-8). The same samples used for the mineralogical analysis on the QEM-SEM were used to show the phases present under different magnifications. From these photos the following is evident:

- Magnetite is only visible in the top section of the ingot and confirms the increase in Fe from the chemical analysis in this zone
- On a relative comparison basis, larger amounts of copper sulphides are visible at the top of the ingot and larger amounts of nickel sulphides at the bottom of the ingot
- A vast amount of BMA is visible at the bottom of the ingot without Pt cores.

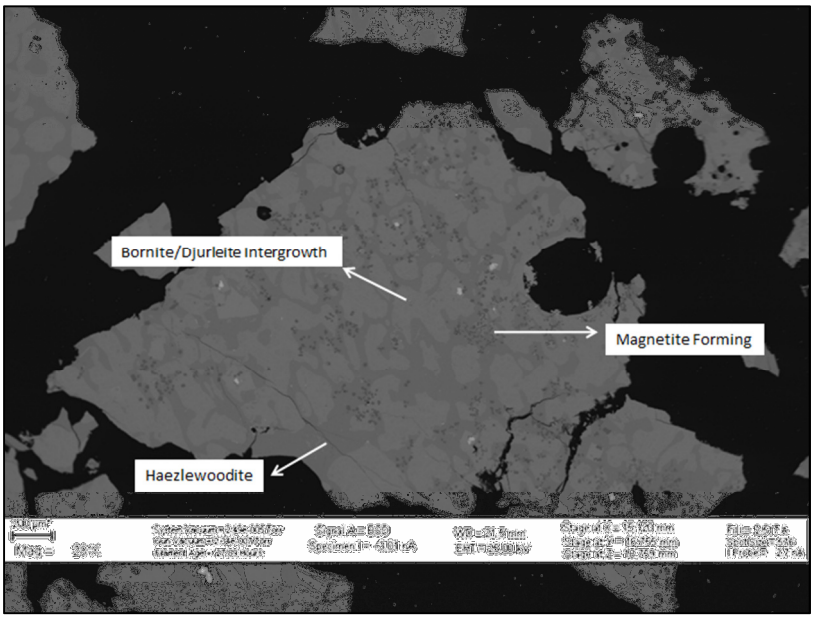

Figure 4.3-1:

Sample A1-8, at 200µm magnification, showing a sample from the top section of ingot A, where magnetite is visible with different Copper Sulphides [Bornite (Cu_5FeS_4 or $Cu_5S_3.FeS$) or Djurleite ($Cu_{1.97}S$)] and Nickel sulphide [Heazelwoodite (Ni_3S_2)]

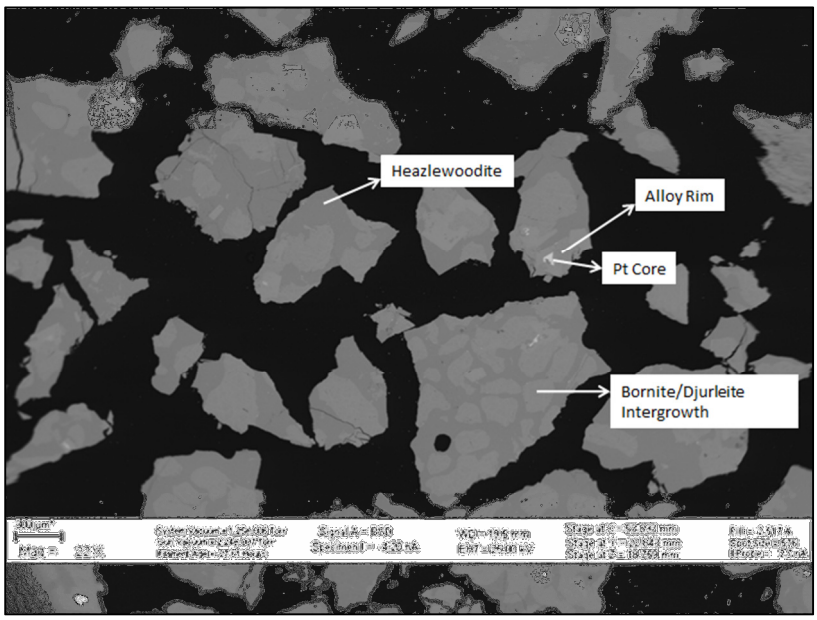

Figure 4.3-2:

Sample A1-6, at 300µm magnification, showing a visible Pt core surrounded by BMA and also Copper Sulphides [Bornite (Cu_5FeS_4 or $Cu_5S_3.FeS$) or Djurleite ($Cu_{1.97}S$)] and Nickel sulphide [Heazelwoodite (Ni_3S_2)]

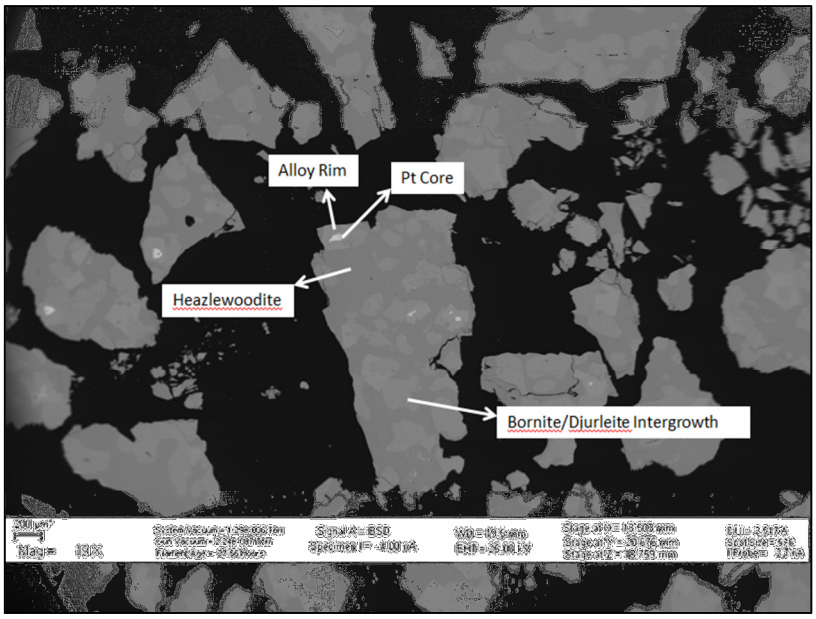

Figure 4.3-3:

Sample A1-5, at 200µm magnification, showing visible Pt cores surrounded by BMA and also Copper Sulphides [Bornite (Cu_5FeS_4 or $Cu_5S_3.FeS$) or Djurleite ($Cu_{1.97}S$)] and Nickel sulphide [Heazlewoodite (Ni_3S_2)]

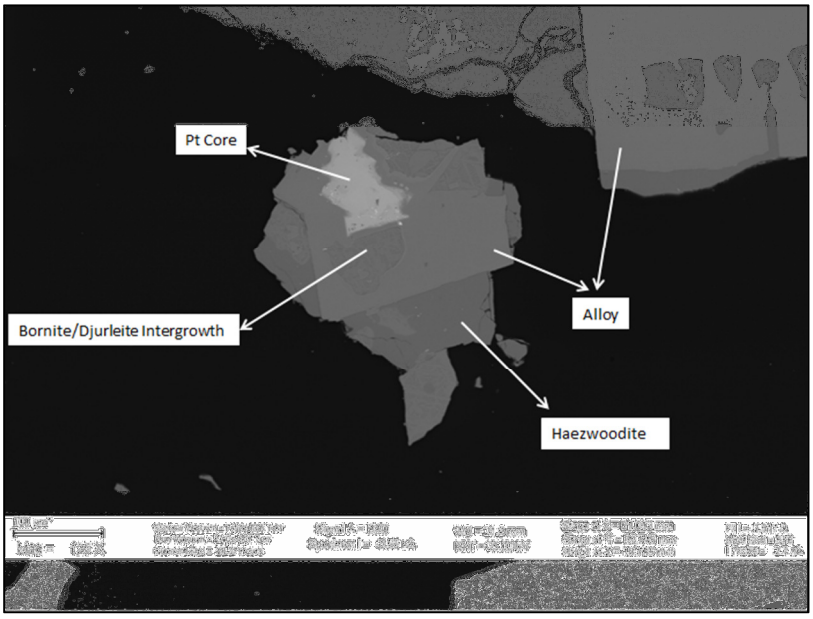

Figure 4.3-4:

Sample A2-4, at 100µm magnification, showing a large Pt core associated with large alloy platelets.

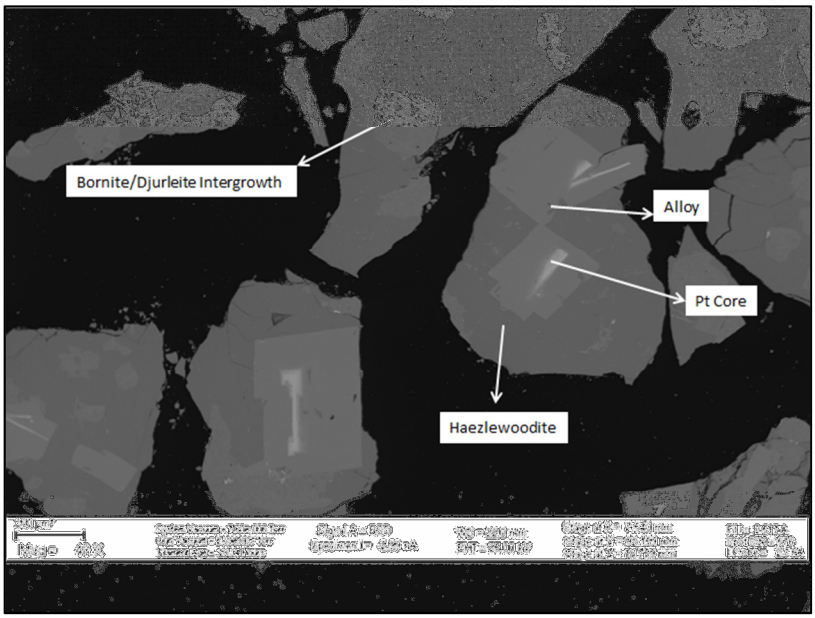

Figure 4.3-5:

Sample A2-3, at 200µm magnification, showing a Pt core and BMA fairly low down in the ingot, with more Nickel sulphide [Heazlewoodite (Ni_3S_2)] than Copper Sulphides [Bornite (Cu_5FeS_4 or $Cu_5S_3.FeS$) or Djurleite ($Cu_{1.97}S$)] present.

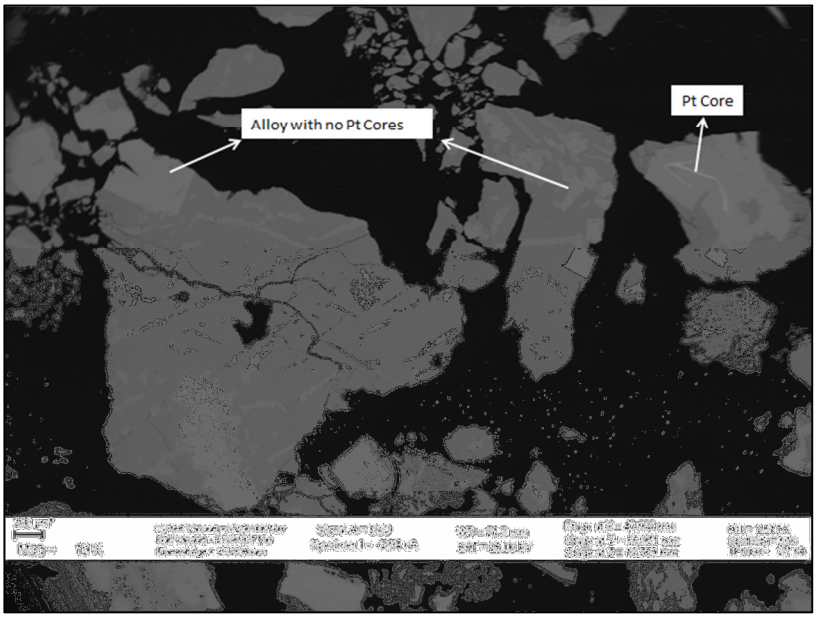

Figure 4.3-6:

Sample A2-2, at 200µm magnification, showing BMA with no Pt cores as expected low down in the ingot core.

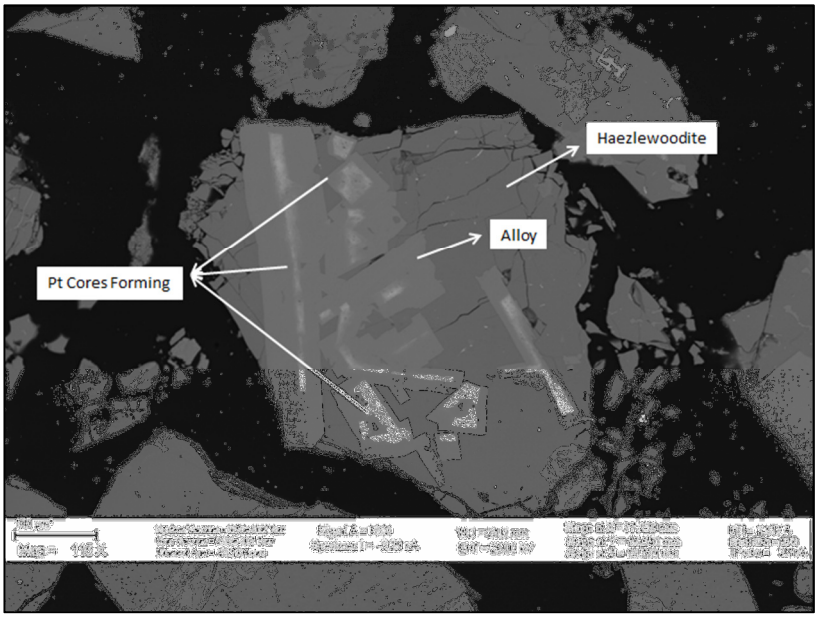

Figure 4.3-7:

Sample A2-1, at 200µm magnification, showing vast amounts of BMA an Pt cores

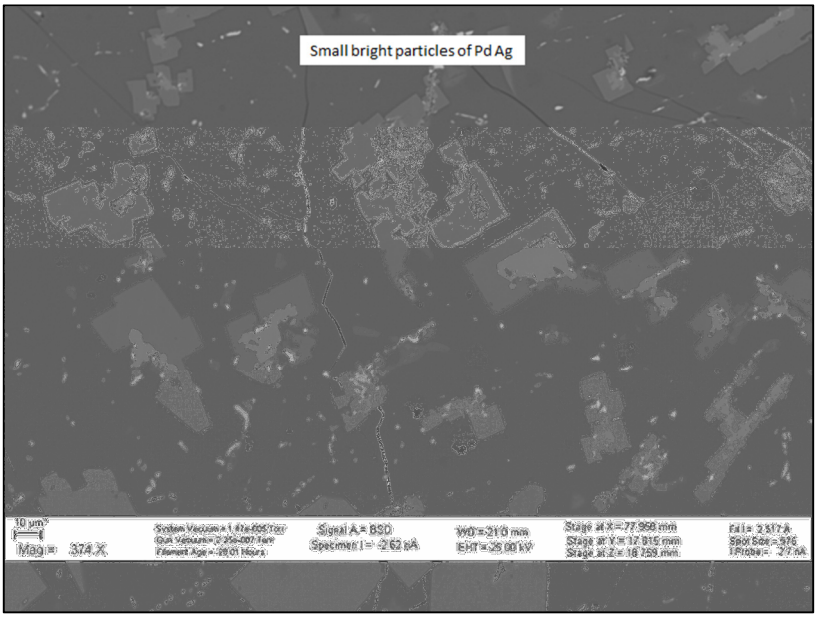

Figure 4.3-8:

Sample A2-1, at 10µm magnification, showing finely dispersed Pd and Au particles within the BMA low down in the ingot

4.4 Platelet Size Comparison

The platelet sizes have a direct impact on the recovery of the alloy fraction from the bulk WCM in the Magnetic Concentration Plant (MC Plant) and is therefore of the utmost importance to the operations, as described in the process overview section. Alloy platelets smaller than 25µm are considered eutectic and normally do not recover well (Schouwstra, 2002) because it cannot be properly liberated during the milling process.

The centre core of each of the ingots (A1, B1 and C1) was analysed on the QEM-SCAN instrument using an automated sparse phase liberation measurement to identify and characterise the particles of interest in a specific sample block. The technique identifies and maps mineral particles with a set of Backscattered Electron (BSE) image intensity using set grey levels. Only BSE bearing phases were targeted and the BSE threshold on 119 was set to map only alloy bearing phases. The size of each particle was then measured and calculated based on the equivalent circle diameter (ECD). This method uses the calculated diameter of a circle that would have an area equivalent to that of the sectional area of a grain measured. The measured alloy sizes for the three sets of samples A1, B1 and C1 are shown in Tables 4.4-1 to 4.4-3 and Figures 4.4-1 to 4.4-6. The size comparison should not be viewed as absolute size values but more as comparative values because the technique of measuring the relative platelet sizes can be influenced by the platelet orientation on the scanned surface. It is believed that the actual size distribution curves will show a slightly coarser distribution and can be obtained by magnetic separation and screen size analysis test work.

From the data, the larger 15t ingot, in test 3, has the lowest number of <25µm platelets (21%) and also the largest amount of >400µm platelets at 14% (double that of the 10t ingot and 3.6 times that of the 5t ingot). The smallest 5t ingot, in test 2, had the largest amount of <25µm particles at 27% and also the lowest amount of >400µm platelets at 4%. It is observed that the 10t and 15t ingots, in tests 1 and 3 respectively, with similar %Fe as shown in tables 4.1-1 and 4.1-2, have the lower <25µm platelet size fraction, which is significant and may indicate that the change to a larger ingot can be beneficial in terms of BMA, and hence PGM, recovery.

ECD Size of Alloy	A1-1	A1-2	A1-3	A1-4	A1-5	A1-6	A1-7	A1-8	Alloy Size Distribution (%)	Cum Alloy Size Distribution (%)
<25µm	5.0	5.4	8.9	26.6	30.7	33.0	34.4	26.9	21%	21%
25 µm - 100 µm	10.4	8.9	9.3	5.2	14.3	16.7	17.5	28.0	14%	35%
100 µm - 200 µm	15.4	11.4	18.7	16.4	29.0	27.0	26.7	30.5	22%	57%
200 µm - 400µm	32.6	32.1	44.2	42.3	25.3	23.0	20.6	13.8	29%	86%
>400 µm	36.6	42.2	18.9	9.5	0.7	0.3	0.8	0.8	14%	100%

Table 4.4-1: Distribution of alloy sizes in drill core A1, T3 - 15t

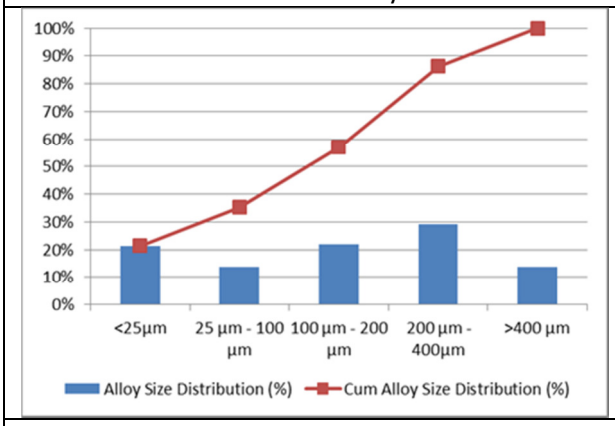

Figure 4.4-1: Total and cumulative alloy size distribution for drill core A1, T3 - 15t

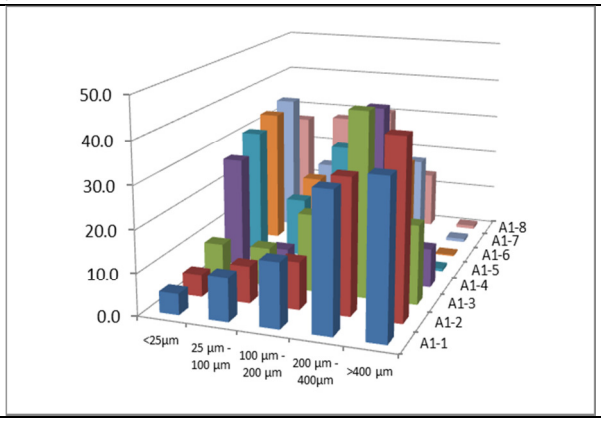

Figure 4.4-2: Individual section alloy size distribution for drill core A1, T3 - 15t

ECD Size of Alloy	B1-1	B1-2	B1-3	B1-4	B1-5	B1-6	B1-7	B1-8	Alloy Size Distribution (%)	Cum Alloy Size Distribution (%)
<25µm	14.0	8.6	14.7	31.8	34.3	34.5	33.2	32.8	25%	25%
25 µm - 100 µm	16.4	15.7	18.8	29.4	21.1	27.3	29.9	48.1	26%	51%
100 µm - 200 µm	15.9	16.9	33.5	30.8	24.3	23.3	23.1	17.7	23%	75%
200 µm - 400µm	22.3	38.5	31.0	7.2	19.7	14.9	12.7	1.4	18%	93%
>400 µm	31.4	20.3	2.0	0.8	0.6	0.0	1.1	0.0	7%	100%

Table 4.4-2 - Distribution of alloy sizes in drill core B1, T1 - 10t

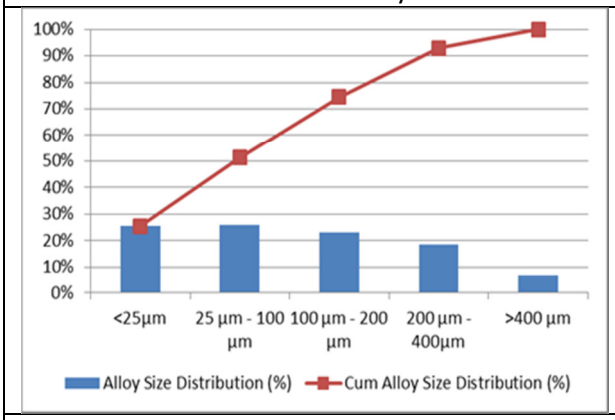

Figure 4.4-3: Total and cumulative alloy size distribution for drill core B1, T1 - 10t

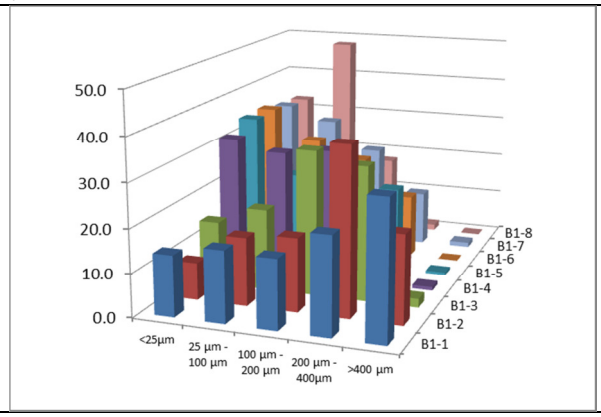

Figure 4.4-4: Individual section alloy size distribution for drill core B1, T1 - 10t

ECD Size of Alloy	C1-1	C1-2	C1-3	C1-4	C1-5	Alloy Size Distribution (%)	Cum Alloy Size Distribution (%)
<25µm	7.6	22.9	27.0	38.2	39.3	27%	27%
25 µm - 100 µm	10.8	14.9	15.5	16.3	31.8	18%	45%
100 µm - 200 µm	22.9	35.1	33.2	27.3	21.7	28%	73%
200 µm - 400µm	42.3	26.4	22.7	17.8	7.2	23%	96%
>400 µm	16.4	0.7	1.6	0.4	0.0	4%	100%

Table 4.4-3 - Distribution of alloy sizes in drill core C1, T2 – 5t

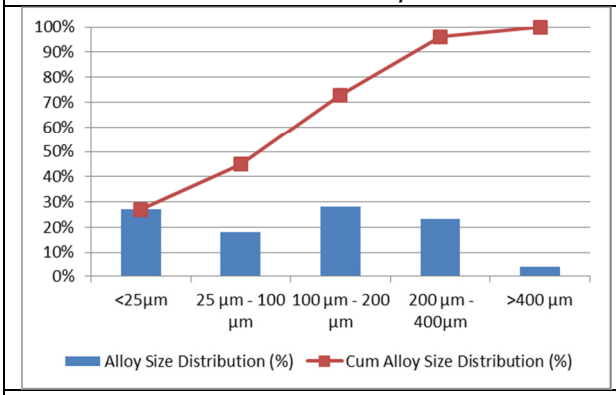

Figure 4.4-5: Total and cumulative alloy size distribution for drill core C1, T2 – 5t

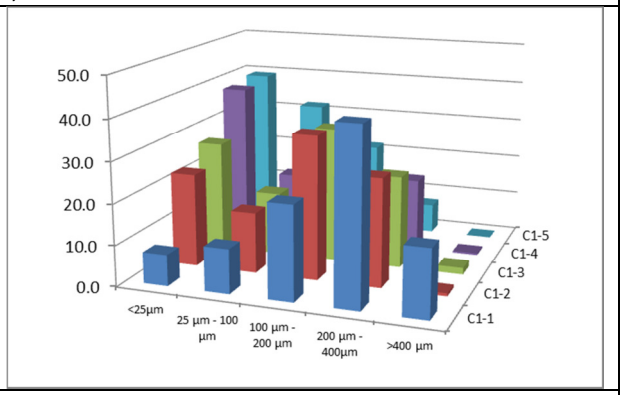

Figure 4.4-6: Individual section alloy size distribution for drill core C1, T2 – 5t

The ratio of <25µm: total alloy present, is 0.25, 0.27 and 0.21 respectively for the 10t, 5t and 15t ingots as shown in Figure 4.4-6. This indicates that although the 15t ingot had a significantly faster cooling rate (cooling rates will be described in the next section), the <25 µm fraction is still lower than the 10t ingot that followed the expected normal cooling rate. This observation is significant and might indicate that cooling rates can be increased without compromising product quality relating to the minimum platelet size required for magnetic separation. Lastly an observation was made that for both the 5t and 15t ingots, the fraction +25µm-100 µm was significantly lower than the other size fractions and that these two ingots also had the faster cooling rates.

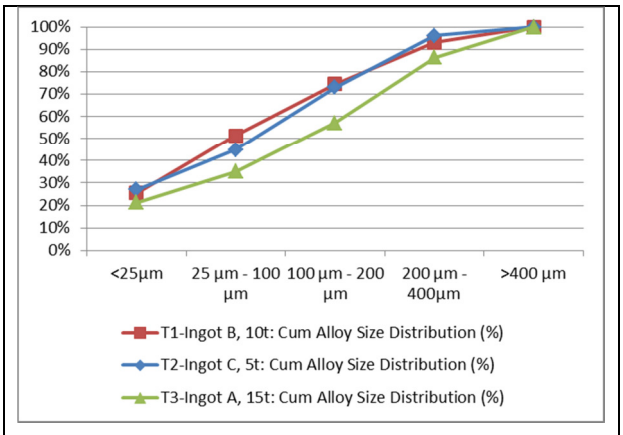

Figure 4.4-7: Comparison of the cumulative alloy platelet size distribution for drill cores B1, C1 and A1

4.5 Cooling curves and cooling rates of various tests:

The temperatures of the ingots after casting were measured by placing thermocouples at various positions throughout the ingots and refractory as schematically shown in Figures 3.1-2 to 3.1-4. The thermocouples were placed in similar positions to earlier work done in 1995 by Bruwer, but not published, on a 30t ingot (the work was later also published in Schouwstra, 1995). These measurements were done for the previous Waterval Smelter process flow-sheet, when the Peirce Smith converters were still operational and 30t WCM moulds were used. The cooling curve is included in Figure 4.5-4 but it must be noted that the temperatures were only recorded from ~900°C and therefore the initial period of rapid cooling was not included as part of the work. The cooling curves for the Test 1 to 3 ingots, based on the measured temperatures over a period of 92 hours, are shown in Figures 4.5-1 to 4.5-3. Larger views of Figures 4.5-1 to 4.5-3 are included in Appendix 5, Figures 7.5-1.7, 7.5-2.7 and 7.5-3.7. After casting the molten metal into the prepared moulds, the thermocouples were placed in position and then the lid placed over the ingot for a period of ~52hrs. The lid was then removed and the ingot left to cool for another 20 hours before the ingot was removed from the mould and then left to air cool for another 20 hours.

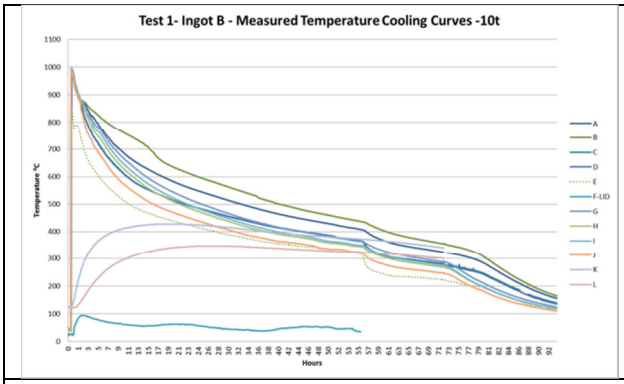

Figure 4.5-1: Measured cooling curves for test 1, 10t ingot B.

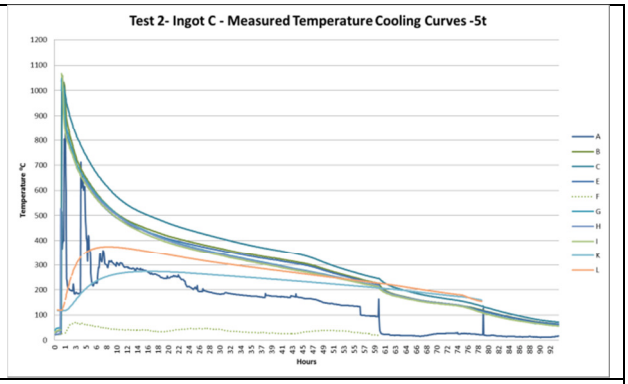

Figure 4.5-2: Measured cooling curves for test 2, 5t ingot C. Problematic thermocouples: A, D, H, J which did not record properly and the data was excluded from any analysis

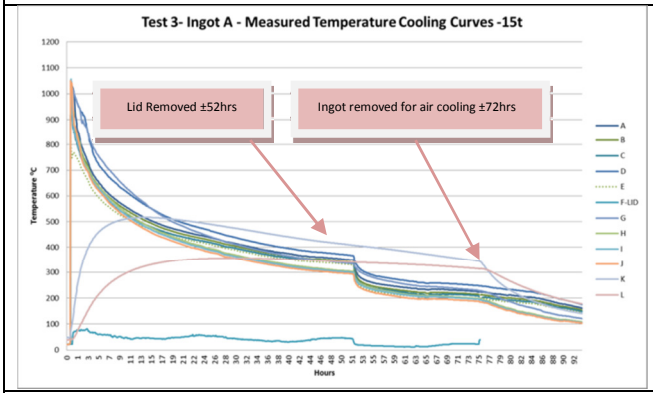

Figure 4.5-3: Measured cooling curves for test 3, 15t ingot A.

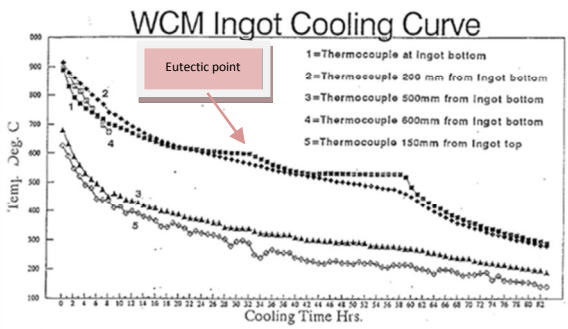

Figure 4.5-4: Cooling curve obtained from internal work done in 1995 by J Bruwer on a 30t ingot of Peirce Smith converter matte cooling.

The data from the four cooling curves were compared to show the time intervals between certain important temperatures, at which certain solidification reactions take place, and is shown in Table 4.5. The selected temperature intervals were specifically selected values for a specific WCM composition and are only used to illustrate the difference in cooling times and may vary in practice as a result of matte composition. The data shows that the original 30t ingots used to take ~36 hours to reach its eutectic temperature compared to the 10t ingot which reaches this in ~27 hours. This is significantly longer than the 5t and 15t ingots that only took ~7-8hours to reach their eutectic temperatures due to extremely fast cooling during the initial few hours. This was expected for the 5t ingot due to its high ratio between the upper ingot surface area: ingot volume of 2.66 from Table 3.1-1. The fast cooling of the 15t ingot was unexpected and can be explained by:

(1) It is believed that the refractory lining of the mould was not adequately cured before the experiment commenced; and/or

(2) The lid refractory lining might have been compromised which may have contributed to the faster cooling rate.

Because of the faster cooling rates measured during the three tests conducted, the constant temperature observed when approaching the eutectic temperature (as seen in Figure 4.5-4), was not visible on the cooling profiles.

Table 4.5: Comparison of cooling times between specific solidification milestones between the data from the three tests conducted and the work done Bruwer, 1997 and again reported on by Schouwstra, 1995.

	Cooling Time (Hours)			
	Test 1 10t ingot	Test 2 5t ingot	Test 3 15t ingot	Schouwstra 1995, 30t
~ 920°C - Solidification starts, Cu_2S starts to precipitate	1.07	0.8	0.27	0.1
~ 700°C – Alloy starts to form	15.14	3.34	3.34	12
~ 605°C – Ni_3S_2 starts to form	23.60	6.00	6.54	32
~580°C – Eutectic point is reached, final solidification	27.54	6.94	7.87	36
~ 520°C - Ni_3S_2 transitions from ß to ß’	36.60	9.67	12.20	59

4.5.1 Cooling rate comparison

From the literature it is stated (Taylor, 1997) that an average cooling rate of ~0.18°C/min would be ideal and this rate was plotted for comparison (Figures 4.5-5 and 4.5-6) versus the actual cooling rates of thermocouple A and B for the three tests conducted and the data reported by Schouwstra, 1995. Unfortunately the A thermocouple for test 2 malfunctioned during the test and the data was excluded from the comparison. The cooling rates were calculated for each temperature interval where significant phase changes approximately take place. From Figure 4.5-6 it is clear that the cooling rates for tests 2 and 3, at all temperature ranges, were significantly higher than the ~0.18°C/min recommended, and also higher than those achieved in test 1 or as reported by Schouwstra, 1995. This may therefore suggest that non-ideal solidification conditions existed in test 2 and 3, but from the chemical, mineralogical analysis and platelet size comparison it seems that the faster cooling rate of the 15t ingot did not have a negative effect on the alloy and platelet formation.

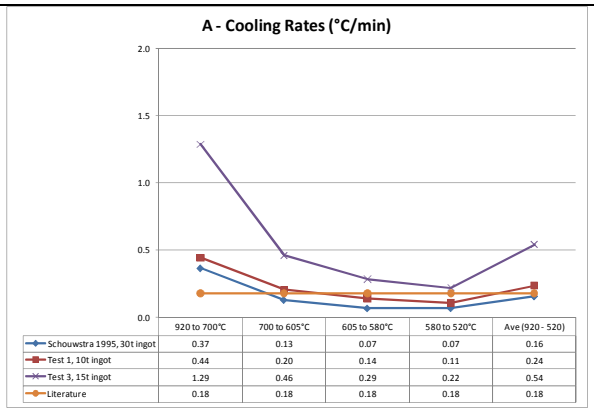

	920 to 700°C	700 to 605°C	605 to 580°C	580 to 520°C	Ave (920 - 520)
Schouwstra 1995, 30t ingot	0.37	0.13	0.07	0.07	0.16
Test 1, 10t ingot	0.44	0.20	0.14	0.11	0.24
Test 3, 15t ingot	1.29	0.46	0.29	0.22	0.54
Literature	0.18	0.18	0.18	0.18	0.18

Figure 4.5-5: Cooling rate comparison between the various tests from thermocouple A, at the bottom centre of each ingot

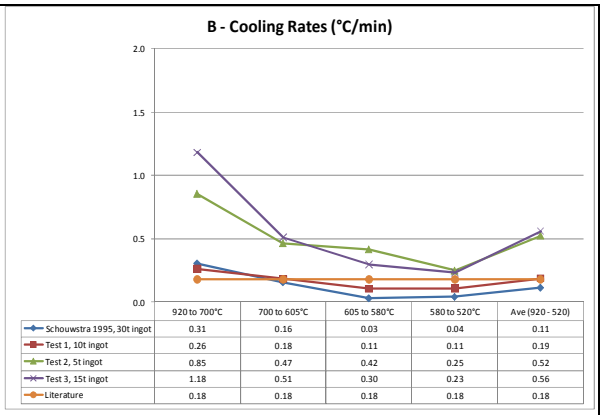

	920 to 700°C	700 to 605°C	605 to 580°C	580 to 520°C	Ave (920 - 520)
Schouwstra 1995, 30t ingot	0.31	0.16	0.03	0.04	0.11
Test 1, 10t ingot	0.26	0.18	0.11	0.11	0.19
Test 2, 5t ingot	0.85	0.47	0.42	0.25	0.52
Test 3, 15t ingot	1.18	0.51	0.30	0.23	0.56
Literature	0.18	0.18	0.18	0.18	0.18

Figure 4.5-6: Cooling rate comparison between the various tests from thermocouple B, that was positioned in the centre of the ingot, 200mm from the bottom of each ingot

4.6 FactSage® simulations and data

Based on the mineralogical data as presented in Section 4.2, for each section identified in each ingot, the bulk chemical composition was calculated from the chemistry results shown in Section 4.1. These calculated average bulk chemical compositions are presented separately for each section of each ingot in Appendix 3. Equilibrium cooling conditions for each section of each ingot, based on the bulk chemical composition, was simulated using the standard FactSage® v.6.2 modelling software with the associated databases, to calculate the predicted mineralogical phases, enthalpy of formation (H) and specific heat capacity (Cp) in the temperature range of 1323K to 673K which is applicable for the solidification of WCM. The FTmisc solution database (FTmisc53Soln.sda) was used in all the calculations with the specific models for the S-Cu-Fe-Ni system and the list of references used for the databases are also summarised in Table 4.6-1.

List of Databases used:	List of References
Liquid sulphide, [FTmisc-MAT2] – all compositions from pure metal to pure sulphur	[4012] P. Waldner and A.D.Pelton, "Thermodynamic Assessment of the Fe-Ni-S System", Metall. and Mat. Trans., 35B, 897-907 (2004).
Beta Ni2S, [FTmisc-M3S2] – non-stoichiometric (Ni,Cu,Fe)2S1+x solution	[4013] P. Waldner and A.D. Pelton, "Thermodynamic Modeling of the Ni-S System", Z. Metallkunde, 95, 672-681 (2004).
Digenite/Bornite, [FTmisc-Dgnt] – Cu2+xS-NiS-FeS solid solution.	[4015] P. Waldner and A.D. Pelton, "Thermodynamic Modeling of the Fe-S System", J. Phase Equilibria and Diffusion, 26, 23-38 (2005).
Fcc, [FTmisc-FCCS] – Cu-Fe-Ni-Co-Cr-Mn-S fcc solution	[4018] P. Waldner, internal reports, to be published. [4019] Y.-B. Kang, "Critical evaluations and thermodynamic optimizations of the Mn-S and the Fe-Mn-S systems", Calphad Journal, 34, 232-244 (2010).

Table 4.6-1: List of models used in FactSage® 6.2 to model the Cu-Fe-Ni-S quaternary system (www.factsage.com)

For each section the equilibrium mass fraction present over the temperature range 673K to 1323K was calculated and plotted showing the solidification and crystallisation sequence graphically (see Appendix 3). From the calculated Cp values, the polynomial fit function in Microsoft Excel was used, to generate a series of polynomial functions that described the Cp curve for each section of each ingot. This data is presented for each section of each ingot in Appendix 3.

The major mineralogical components present in the WCM for each section within the ingot are nickel sulphide [heazlewoodite (Ni_3S_2)], copper sulphides [bornite (Cu_5FeS_4 or Cu_5S_3.FeS) or djurleite ($Cu_{1.97}S$) or digenite (Cu_9S_5) (depending on the temperature/composition as described in Section 2.5 and Figure 2.5-6)] and Base Metal Alloy (BMA). The major Cu-S phases present, as calculated in FactSage®, were then grouped together as if in solid solution and together with nickel sulphide and the Base Metal Alloy compared to the actual calculated bulk mineralogical composition for each section of each ingot. This data is presented in Tables 4.6-2 to 4.6-4, where the FactSage® data is compared with the actual mineralogical analysis, as validation of the FactSage® model. The FactSage® calculated values generally agree well with the actual mineralogical analysis, but in all three cases the amount of BMA at the ingot core (section 1 and 2) is under predicted by between 4% and 8%. This is as expected due to the fractional crystallisation with a higher concentration of alloy formed at the ingot core which was not catered for in the modelling, resulting in an over prediction of %S in the core of the ingot.

Table 4.6-2: Test 1, Ingot B, 10t: FactSage® prediction of mineralogical data versus actual average calculated QEM SEM analysis for each section in the ingot.

Test 1, Ingot B, 10t:	% Heazlewodite	% Bornite/ Digenite/ Djurleite	% Alloy
Section 2			
B1-1 to B1-3, B2-1 to B2-3, B3-1 to B3-3	73	15	11
FactSage® Data	79	13	7
Section 3			
B1-4 to B1-5, B2-6, B2-4 to B2-5, B3-4 to B3-5, B4-1 to B4-5	63	29	6
FactSage® Data	71	26	4
Section 4			
B1-6 to B1-8, B2-6 to B2-8, B3-6 to B3-8, B4-6 to B4-8, B5-3 to B5-8	47	43	7
FactSage® Data	59	38	4

Table 4.6-3: Test 2, Ingot C, 5t: FactSage® prediction of mineralogical data versus actual average calculated QEM SEM analysis for each section in the ingot.

Test 2, Ingot C, 5t:	% Heazlewodite	%Bornite/ Digenite/ Djurleite	% Alloy
Section 2			
C1-1, C2-1, C3-1, C4-1	71	14	13
FactSage® Data	83	12	5
Section 3			
C1-2 to C1-3, C2-2 to C2-3, C3-2 to C3-3, C4-2 to C4-3	62	28	9
FactSage® Data	70	25	5
Section 4			
C1-5 to C1-5, C2-4 to C2-5, C3-4 to C3-5, C4-4 to C4-5, C5-1 to C5-5	50	41	8
FactSage® Data	59	38	4

Table 4.6-4: Test 3, Ingot A, 15t: FactSage® prediction of mineralogical data versus actual average calculated QEM SEM analysis for each section in the ingot.

Test 3, Ingot A, 15t:	% Heazlewodite	%Bornite/ Digenite/ Djurleite	% Alloy
Section 1			
A1-1 to A1-3, A2-1 to A2-3, A3-1 to A3-3	70	12	18
FactSage® Data	79	12	9
Section 2			
A1-4 to A1-5, A2-4 to A2-5, A3-4 to A3-5, A4-1 to A4-5	59	30	10
FactSage® Data	66	28	6
Section 3			
A1-6, A2-6, A3-6, A4-6, A5-1 to A5-6	49	43	8
FactSage® Data	54	41	5
Section 4			
A1-7 to A1-8, A2-7 to A2-8, A3-7 to A3-8, A4-7 to A4-8, A5-7 to A5-8, A6-5 to A6-8	39	51	7
FactSage® Data	43	49	8

4.7 CFD Model and Model Parameters

4.7-1 Setup of the CFD Model

The ingot casting and slow-cool process is explained in detail in the literature review and experimental design section. Based on this, a three dimensional Fluent, Computational Fluid Dynamic (CFD) model was developed using the ANSYS® v13 software package to simulate the cooling profiles within an ingot from the time after a cast is complete in the mould until all phase transformations have taken place. The model geometry was set up in ANSYS® v13, Design Modeller as shown in Figure 4.7-1.1, with the different components within the model indicated in separate colours. Also visible are the circled crosses which indicate the positions of the point monitors where the thermocouple temperatures were simulated from within the model. Figures 4.7-1.2 to 4.7-1.4 illustrates the different sections within each ingot as derived from the zones identified with similar composition by means of mineralogical analysis as described in Section 4.2. The exact size and number of sections identified was dependent on the original ingot geometry and areas identified from the mineralogical data. The mesh was created with the standard Meshing v.13 software included in the ANSYS® v.13 Workbench package and consisted of ~76,000 nodes and ~167,904 elements.

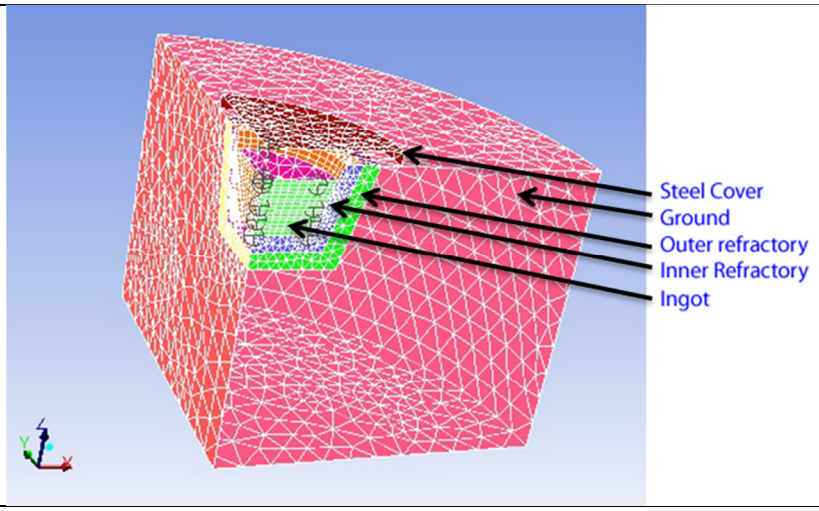

Figure 4.7 – 1.1: Schematic representation of the typical geometry for the CFD model showing the different components

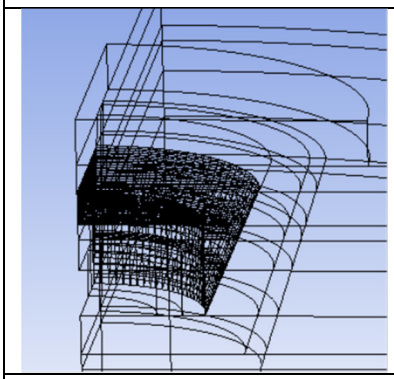

Figure 4.7 – 1.2: Meshing shown for section 4 of the ingot

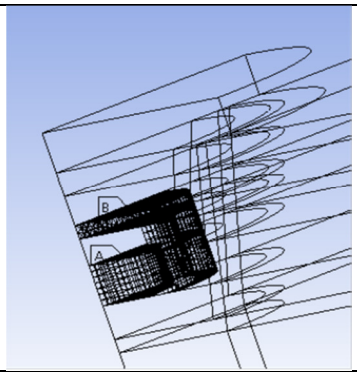

Figure 4.7 – 1.3: Meshing shown for sections 1 and 3 of the ingot

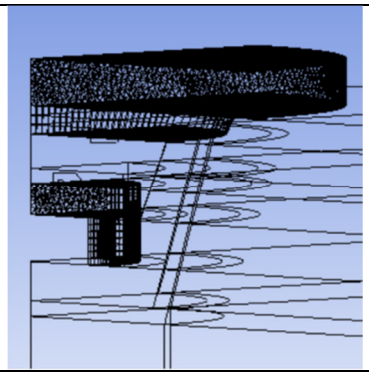

Figure 4.7 – 1.4: Meshing shown for section 2 in the ingot, the air above the ingot and the hood section

A three dimensional transient heat flux model was set up to simulate the cooling of the WCM over time with the relevant heat losses. Transient simulations require real time information to determine the time intervals at which the CFX-Solver calculates the flow field (Quoting some sections from the ANSYS® 13.0, help files). Transient behaviour can be caused by the initially changing boundary conditions of the flow, as in start-up, or it can be inherently related to the flow characteristics, so that a steady state condition is never reached, even when all other aspects of the flow conditions are unchanging.

ANSYS® FLUENT solves the energy equation in the following form:

$$\frac{\partial}{\partial t}(\rho E) + \nabla \cdot \left(\overline{v}\,(\rho E + p)\right) = \nabla \cdot \left(k_{eff}\,\nabla T - \Sigma_j h_j\,\overline{J}_j + \left(\bar{\bar{\tau}}_{eff}\,\overline{v}\right)\right) + S_h \qquad \text{(Equation 4.7-1)}$$

where k_{eff} is the effective conductivity (k + k_t), where k_t is the turbulent thermal conductivity, defined according to the turbulence model being used, and $\overline{J}_j$ is the diffusion flux of species j. The first three terms on the right-hand side of Equation 4.7–1 represent energy transfer due to conduction, species diffusion, and viscous dissipation, respectively (with the stress tensor $\bar{\bar{\tau}}_{eff}$ and the velocity vector $\overline{v}$). S_h includes the heat of chemical reaction, and any other volumetric heat sources defined.

In Equation 4.7–1,

$$E = h - \frac{p}{\rho} + \frac{v^2}{2} \qquad \text{(Equation 4.7–2)}$$

where sensible enthalpy h is defined for ideal gases as, pressure p, density ρ *and velocity* v

$$h = \Sigma_j \mathrm{Y}_j \mathrm{h}_j \qquad \text{(Equation 4.7-3)}$$

(and for incompressible flows as)

$$h = \Sigma_j \mathrm{Y}_j \mathrm{h}_{j+\frac{p}{\rho}} \qquad \text{(Equation 4.7–4)}$$

In Equation 4.7–3 and Equation 4.7–4, Y_j is the mass fraction of species j and

$$h_j = \int_{T_{ref}}^{T} C_p, j dT \qquad \text{(Equation 4.7–5)}$$

where T_{ref} is 298.15 K.

The Discrete Ordinate (DO) model for the radiation heat transfer calculations was used to solve for the radiation heat transfer component. The DO model solves the Radiative Transfer Equation (RTE) for a finite number of discrete solid angles, each associated with a vector direction $\bar{s}$ fixed in the global Cartesian system (*x,y,z*).

The RTE for an absorbing, emitting, and scattering medium at position in the direction is

$$\frac{dI\,(\vec{\gamma},\vec{s})}{ds} + (a + \sigma_s)\, I\,(\bar{r}\,,\bar{s}) = an^2\,\frac{\sigma T^4}{\pi} + \frac{\sigma_s}{4\pi}\int_0^{4\pi} I\,(\bar{r}\,,\,\bar{s}^t)\,\Phi(\bar{s}\,.\,\bar{s}^t)\,d\Omega^t \qquad \text{(Equation 4.7–6)}$$

where

$\bar{r}$= position vector

$\vec{s}$ = direction vector

$\bar{s}^t$ = scattering direction vector

$\bar{s}$ = path length

a = absorption coefficient

n = refractive index

σ_s = scattering coefficient

σ = Stefan-Boltzmann constant (5.669 x 10^{-8} W/m^2-K^4)

I = radiation intensity, which depends on position and direction

T = local temperature

Φ = phase function

Ω^t = solid angle

$(a + \sigma_s)$ is the optical thickness or opacity of the medium. The refractive index n is important when considering radiation in semi-transparent media.

The DO model considers the RTE in the direction $\bar{s}$ as a field equation.

Thus, Equation 4.7–6 is written as

$$\nabla\,.\,(I\,(\bar{r}\,,\bar{s})\;\bar{s}) + (a + \sigma_s)\, I\,(\bar{r}\,,\bar{s}) = an^2\,\frac{\sigma T^4}{\pi} + \frac{\sigma_s}{4\pi}\int_0^{4\pi} I\,(\bar{r}\,,\,\bar{s}^t)\,\Phi(\bar{s}\,.\,\bar{s}^t)\,d\Omega^t \qquad \text{(Equation 4.7–7)}$$

Each component in the model was then assigned specific physical and thermal properties according to the tables in Appendix 4. The initial temperature of all the materials was set at 300K except for the ground, inner/outer refractory and ingot temperature. For these components, the actual starting temperatures from the experimental data were used as initial temperatures for each simulation.

The physical material properties data for each component in the model is shown in Appendix 4 and were obtained from various sources and can be summarised by:

- Properties for air: from the Fluent database. The air gap below the lid (above the ingot) was assumed to only have radiation and conduction heat transfer components with no convection. This was done as part of the model simplification. For the air section above the lid, convection was included with the assumption of the heat transfer coefficient (*h*) over a plate for an air flow of 2m/s (Holman, 2010 (p11)).
- Properties for ground: from Hollman, 2010 (p645), the physical properties of low density structural concrete was used for the entire section.
- Properties of refractory: from the Intocast data sheet (Intoval T1500 – inner refractory for the hot-face and Intoval C1400 EHS - outer refractory material). The data for density, Cp and thermal conductivity (at temperatures above 800°C) were used for the castable hot/cold face mould linings. The thermal conductivity data for temperatures below 800°C was obtained from the Vereeniging Refractories (Verref) data sheet and a refractory with similar composition to the castable was chosen (A5 brick – with similar chemical composition to the castable). The reason for using the Verref data was because it was temperature based over the range of temperatures expected in the model and the Intocast data sheet only stated thermal conductivity for one specific temperature in the datasheet, making thermal conductivities <1000°C inaccurate. This data was then used to populate the Piece Wise Linear (PWL) functions in the Fluent software (Appendix 4, table 3).
- The WCM bulk density was calculated from the ingot geometry and actual ingot weights measured during the trials as shown in Table 3.1-1. The Cp curve for each section of each ingot was derived from the FactSage® data modelling, as discussed in Section 4.6. Polynomial functions were then fitted for each section of the ingot data and combined as a Piece Wise Polynomial (PWP) function in the Fluent software. These functions are shown on the individual ingot section graphs (Appendix 3).
- The thermal conductivities for the different sections of the ingot was calculated using the chemical analysis for each section based on the molar fractions of the major elements Fe, Ni, S and Cu and is presented in Appendix 4. This resulted in the matte thermal conductivity ranging between 85,8 – 151.4 W/m-K and was consistently used throughout the temperature range whilst modelling the cool down of the ingot. These high thermal conductivities enabled the model to follow the actual high cooling rates in the first part of the cooling profile but also then resulted in the predicated cooling rates for the latter part being faster than the measured rate. A further improvement to the model can be made by varying the matte thermal conductivity with temperature., but limited published data is available on this subject.

In order to simplify the Fluent cooling model without compromising the accuracy of the results, the following assumptions were made for model simplification:

- The lid, used as a radiation shield, is in practice only placed over the ingot after casting (one or 2 ingots depending on the size of the tap) and following the removal of the bottom caster ladle. This process normally takes 30 – 40 minutes to complete from the starting time of the cast. During modelling, it was assumed that at time zero, the lid was already over the ingot. For each model, the WCM temperature was then set to the actual measured temperature at the time of each cast. The implication of this is that the ingot heat loss during the first hour of cooling will be greater in practice than modelled. Because this time period is relatively small versus the total cooling time of 48hrs, as modelled, it was assumed not to have had a significant impact on the end result of the modelling.
- The lid that is placed over the ingot has three slots to enable the placement of the hanger bars into the ingot after casting. The model assumes no slots in the lid and also no impact of the hanger bars on the cooling of the ingot. The lid is also lined with ceramic wool on the lower side that faces the radiation surface of the ingot which protects the steel plate when it is placed over the ingot after casting. To accommodate these physical differences, the heat transfer coefficient used in the model was manipulated to accommodate these physical effects as shown in Appendix 4, Table 2, but kept constant for all three cases during the modelling.
- The model also assumes that the air cavity above the ingot (below the lid) has no convective heat transfer component and only radiation and conductive heat transfer mechanisms were modelled for this zone. However, the air above the lid (bulk ambient air) does take convective heat transfer into account and it was assumed that an average air movement of 2m/s was prevalent in the slow-cool aisle.
- It was also assumed that from time zero no fluid flow or change of density takes place within the WCM ingot with only internal conductive heat transfer. This might significantly under estimate the heat losses from the ingot at temperatures above 900°C.
- During modelling, perfect contact between the refractory mould hot-face and the ingot sides were maintained throughout the first 48 hours of modelling.

Simulations for the various sized ingots were performed for ingot cooling over a period of 48 hours. The detailed plots of the actual temperature measurements versus the modelled temperatures are shown in Figures 4.7-2.2 to 4.7-5.5 (for Test 1), Figures 4.7-7.2 to 4.7-7.5 (for Test 2) and Figures 4.7-9.2 to 4.7-9.5 (for Test 3), with each time the measured temperature plotted in a darker colour and the modelled temperature shown in the same but lighter colour for a specific thermocouple. The calculated temperature data from each point monitor simulating a thermocouple temperature was then correlated with the actual measured temperature data for each thermocouple as validation of the model. The correlation coefficient (R^2) for each thermocouple is shown in Tables 4.7-2.1 to 4.7-4.1 for each ingot. A second correlation was also done for each ingot starting with the data after 1 hour of cooling to see if the effect of the lid on slowing the cooling rate has any significant effect on the applicability of the model and this data is also shown for each test in the second part of Tables 4.7-2.1 to 4.7-4.1.

4.7-2 Temperature data analysis – Test 1, Ingot B, 10t:

The thermocouple layout for Test 1 is shown in Figure 4.7-2.1, and the temperature trends with both the measured and modelled cooling profiles are shown in four separate graphs in Figures 4.7-2.2 to 4.7-2.5 where the thermocouples are grouped together based on location within the ingot.

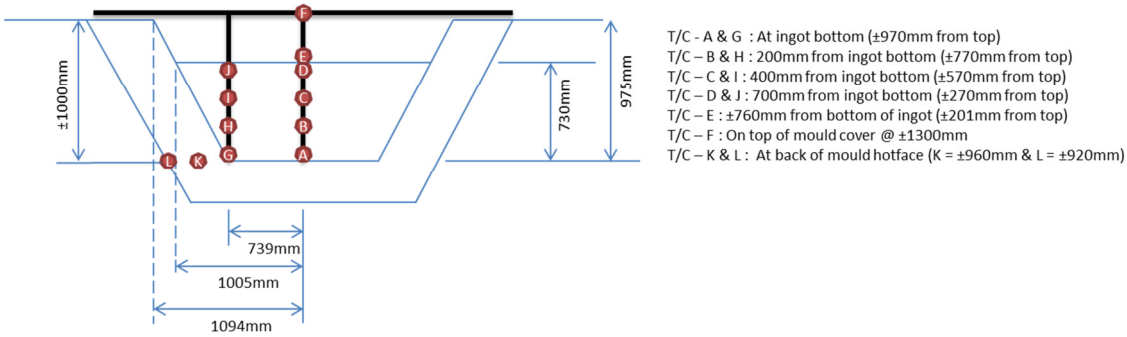

Figure 4.7-2.1: Test 1 – Ingot B, 10t thermocouple layout

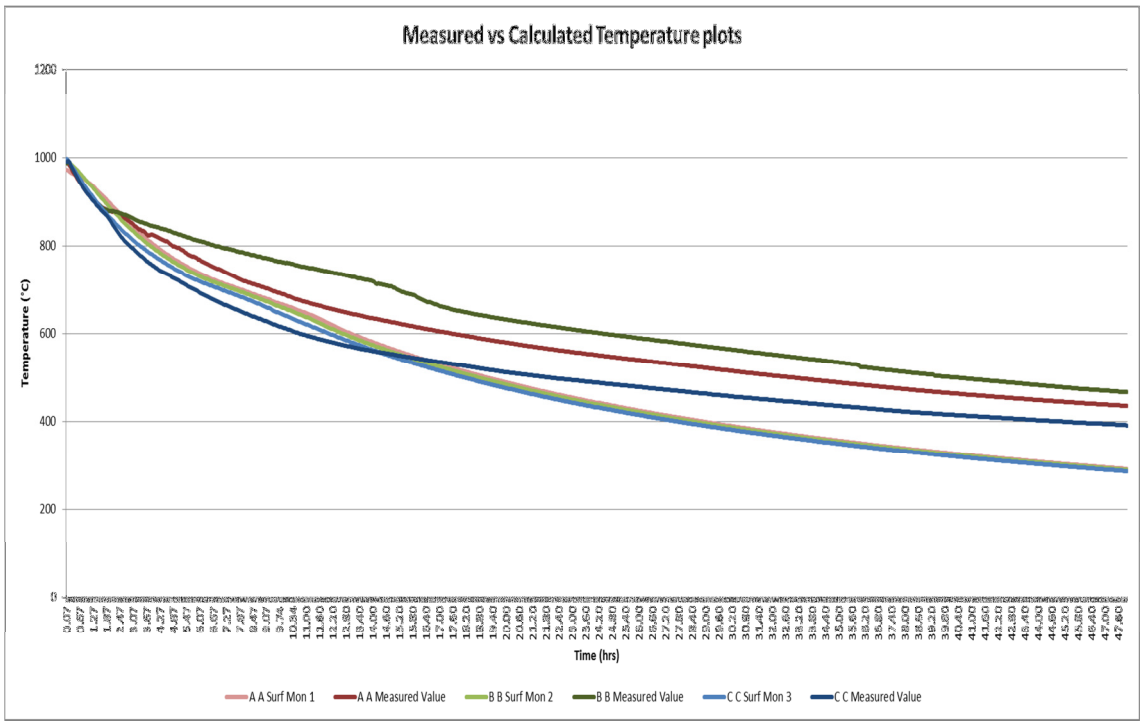

Fig 4.7-2.2: Temperature plots for thermocouples A to C for measured (Measured value) and modelled values (Surf Mon)

In all the temperature profile graphs the lighter colour refers to the surface monitor data which was created at a specific point within the Fluent model which corresponds to the approximate position of the actual thermocouple tip used during measurement. The darker colour each time shows the actual measured temperature profile for each thermocouple. In Figure 4.7-2.2, the modelled and measured temperature profiles for thermocouples A (Dark and light red) and C (dark and light blue) follows the measured values fairly well down to the ~580 °C @ ~15.5hours, from there the modelled cool down rates are slightly faster than the measured values. The reason for the B thermocouple deviating from the rest in the manner it did cannot be explained and might be as a result of an instrument problem. For the centre line thermocouples the modelled temperature ended up ~100°C below the actual measured temperature after 48hrs. This can be as a result of the constant thermal conductivity assumed for WCM. For all the modelled temperature profiles, at ~700 to 600°C, there is a slight change in the slope as a result of the change in the Cp values modelled from FactSage® as the eutectic point is approached and is shown in Appendix 3, Figure 7.3-1. The correlations done for thermocouples A to C indicate a $R^2 > 0.99$, as shown in Table 4.7-2.1.

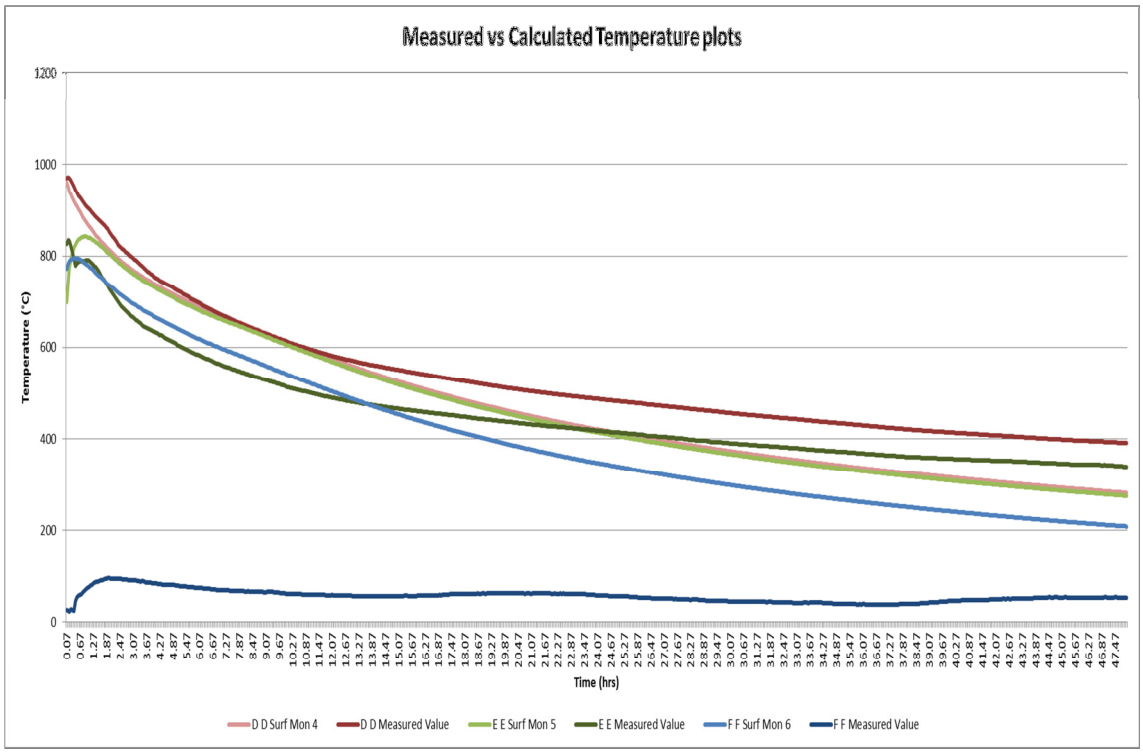

Fig 4.7-2.3: Temperature plots for thermocouples D to F for measured and modelled values

The modelled and measured cooling down profiles for thermocouple D (light and dark red in Figure 4.7-2.3) follows a similar trend to A to C (Figure 4.7-2.2), with the modelled temperatures decreasing slightly faster than the measured after ~15hrs of cooling. The difference in the measured and modelled trends for thermocouples E and F can be explained by:

E: The exact height of the matte in the mould was very difficult to control and therefore it is very difficult to confirm the exact thermocouple tip position relative to the ingot top surface. From the interpretation of the measured data, it is possible that the thermocouple tip could just have been immersed in the top layer of the ingot and not above the surface as planned.

F: The thermocouple on the top of the lid showed a relatively small temperature increase (~80 – 100°C) vs. the modelled thermocouple reaching ~800°C after 1 hour. This was due to the fact that the model assumed a modified thermal conductivity for the lid and the assumption that there were no slots cut into the lid. The data for thermocouple F is only shown in this graph Fig 4.7-2.3 but was excluded for the correlation data.

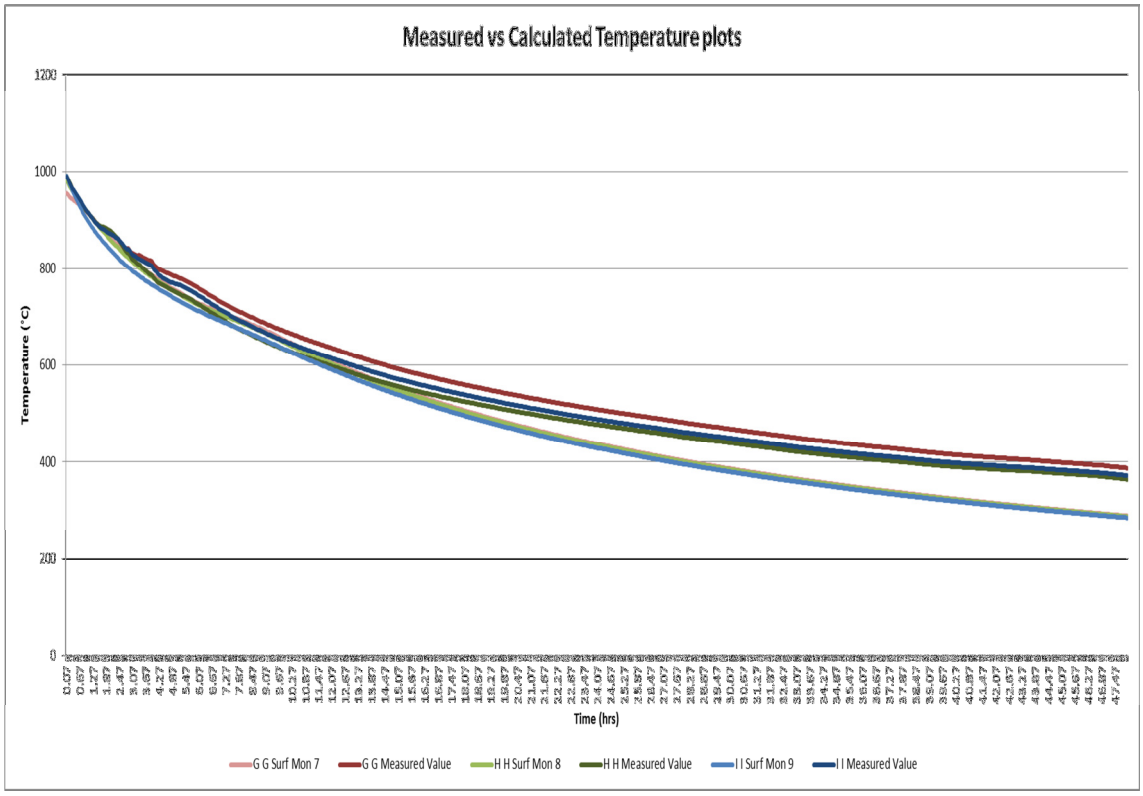

Fig 4.7-2.4: Temperature plots for thermocouples G to I for measured and modelled values

The measured vs. modelled cool down profiles for thermocouples G to I, in Figure 4.7-2.4, follows each other very closely for the first ~15hours of the cool down. After this the modelled temperatures (lighter colours) decrease slightly faster than the measured values (in the darker colours) and end ~100°C lower after 48 hours. The slightly erratic measurements between 1 – 4 hours cannot be explained and is believed to be an instrument error. The correlations done for thermocouples A – C indicate a $R^2 > 0.99$, as shown in Table 4.7-2.1.

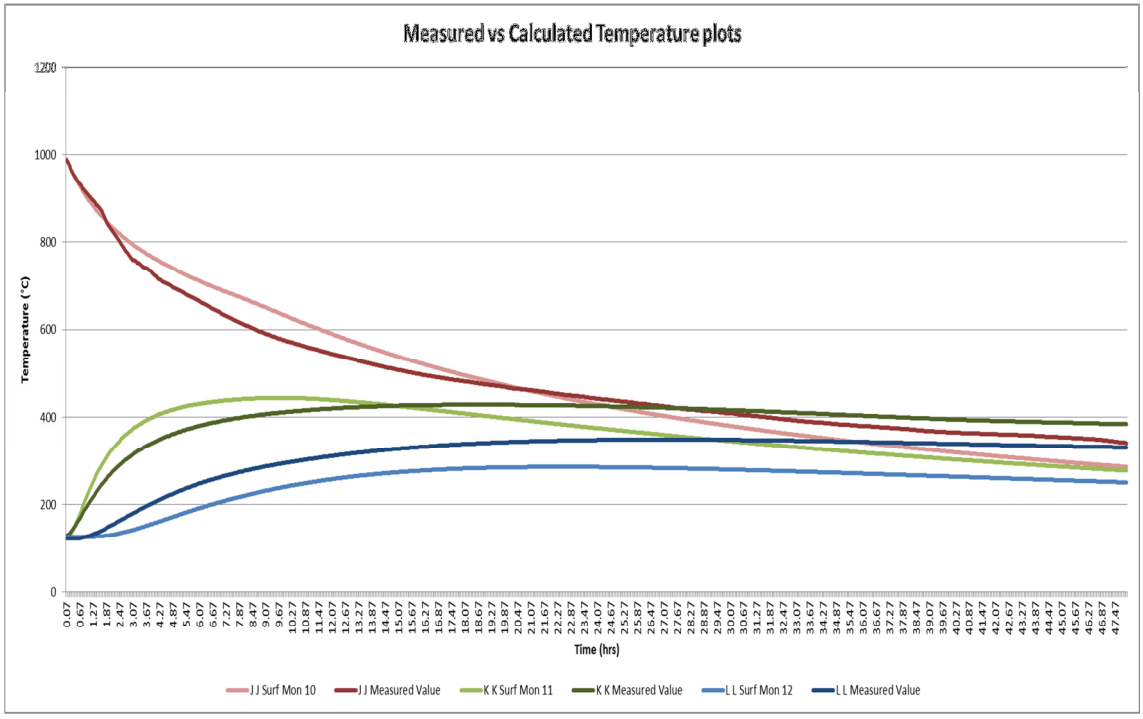

Fig 4.7-2.5: Temperature plots for thermocouples J to L for measured and modelled values

For thermocouple J, Figure 4.7-2.5, the measured and modelled temperatures correlate well for the time period with $R^2 = 0.987$, but the modelled temperatures (light red) ends ~50°C below the measured value after 48 hours. Thermocouples K and L were located within the refractory material. The modelled temperatures for thermocouple K (light green) showed a faster initial temperature increase compared to the measured temperature (dark green) and then after ~15 hours the modelled temperatures started decreasing slightly whilst the measured temperatures stayed almost constant. This might be related to the constant thermal conductivity selected for the WCM. For thermocouple L however, the initial measured (dark blue) temperature increase was faster than the modelled (light blue) and can be attributed to the thermal conductivity of the refractory material. The data shows a correlation for K, $R^2 = 0.544$ and L, $R^2 = 0.98$, as presented in Table 4.7-2.1.

Table 4.7-2.1: 10t ingot B, Test 1, data correlation for the modelled temperature data with the measured thermocouple temperatures with all the data and then also with the data excluding the data for the first hour of cooling.

Correlation Geom 3_8_48hr

	A Surf Mon 1	B Surf Mon 2	C Surf Mon 3	D Surf Mon 4	E Surf Mon 5	G Surf Mon 7	H Surf Mon 8	I Surf Mon 9	J Surf Mon 10	K Surf Mon 11	L Surf Mon 12
A Measured Value	0.997259										
B Measured Value		0.994067									
C Measured Value			0.988445								
D Measured Value				0.989413							
E Measured Value					0.97251						
G Measured Value						0.998327					
H Measured Value							0.995176				
I Measured Value								0.997632			
J Measured Value									0.986537		
K Measured Value										0.544327	
L Measured Value											0.98049

Correlation Variance Geom 3_8_48hrs_ after 1hr

	A Surf Mon 1	B Surf Mon 2	C Surf Mon 3	D Surf Mon 4	E Surf Mon 5	G Surf Mon 7	H Surf Mon 8	I Surf Mon 9	J Surf Mon 10	K Surf Mon 11	L Surf Mon 12
A Measured Value	0.997751										
B Measured Value		0.99362									
C Measured Value			0.989588								
D Measured Value				0.989468							
E Measured Value					0.98246						
G Measured Value						0.998593					
H Measured Value							0.995204				
I Measured Value								0.99731			
J Measured Value									0.987413		
K Measured Value										0.356273	
L Measured Value											0.979583

There is no significant difference between the correlations done with all the data points from the start of the test and those done starting 1 hour after the start of the test, except for thermocouple K, where the correlation after 1 hour is substantially lower that the correlation done that includes all the data points

The contour temperature profile plots for the 10 t ingot, showing the modelled temperature contours at different time intervals with varying temperature scales, is graphically shown in Figures 4.7-2.6 to 4.7-2.11. The temperature scale was varied for the contour graphs as the temperature zones were more clearly visible, but for completeness the contour graphs with a fixed temperature scale are also shown in Appendix 6, Figure 7.6-1.1 to 7.6-1.6.

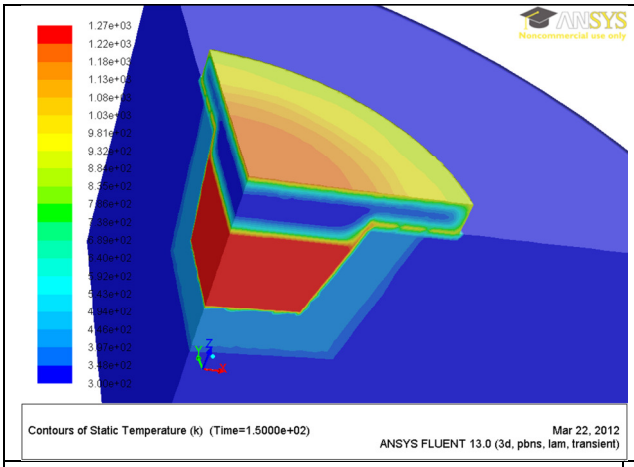

Figure 4.7-2.6: Static temperature profile showing the 10t ingot B, Test 1 after - 1min

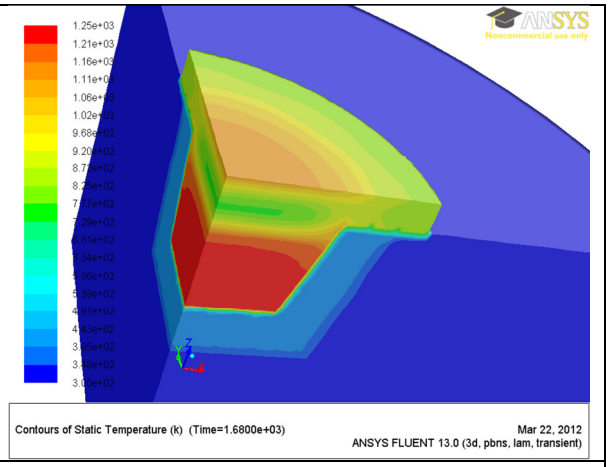

Figure 4.7-2.7 : Static temperature profile showing the 10t ingot B, Test 1 after - 1hr

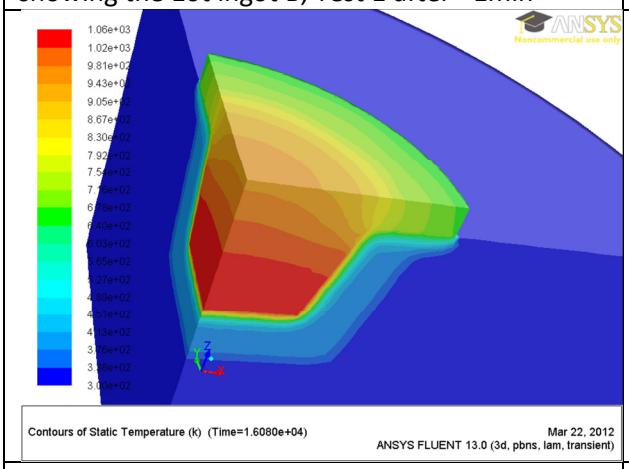

Figure 4.7-2.8: Static temperature profile showing the 10t ingot B, Test 1 after - 5hrs

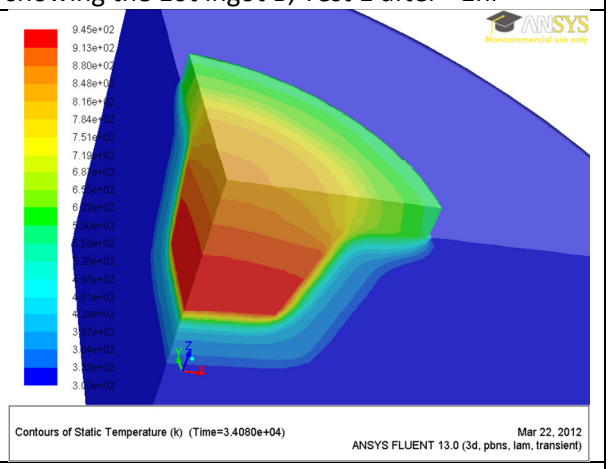

Figure 4.7-2.9: Static temperature profile showing the 10t ingot B, Test 1 after - 10hrs

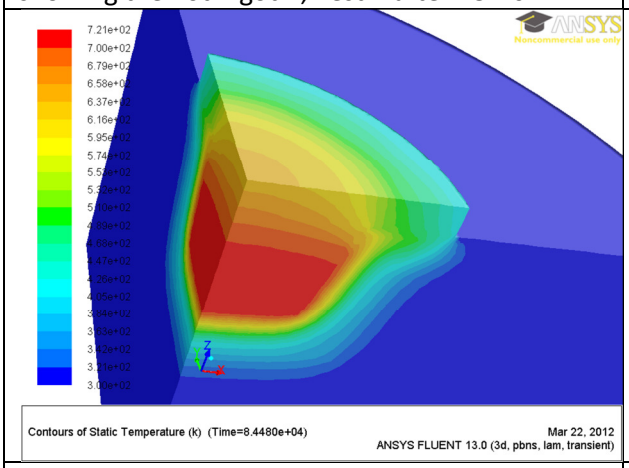

Figure 4.7-2.10: Static temperature profile showing the 10t ingot B, Test 1 after - 24hrs

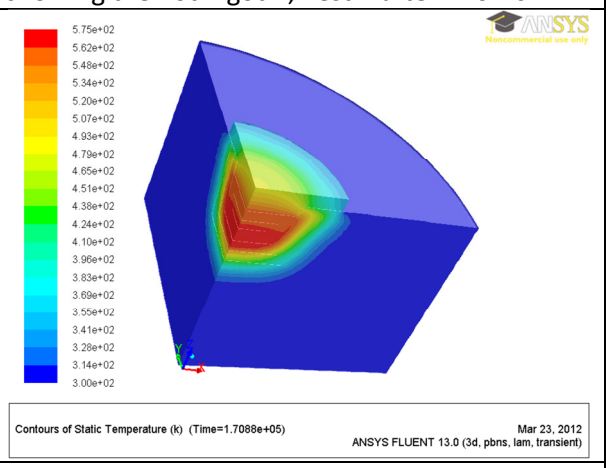

Figure 4.7-2.11: Static temperature profile showing the 10t ingot B, Test 1 after - 48hrs. (showing specifically a wider zoom to include the complete meshed section)

4.7-3 Temperature data analysis – Test 2, Ingot C, 5t:

The thermocouple layout for Test 2 is shown in Figure 4.7-3.1, and the temperature trends with both the measured and modelled cooling profiles are shown in four separate graphs in Figure 4.7-3.2 to 4.7-3.5 where the thermocouples are grouped together based on location within the ingot.

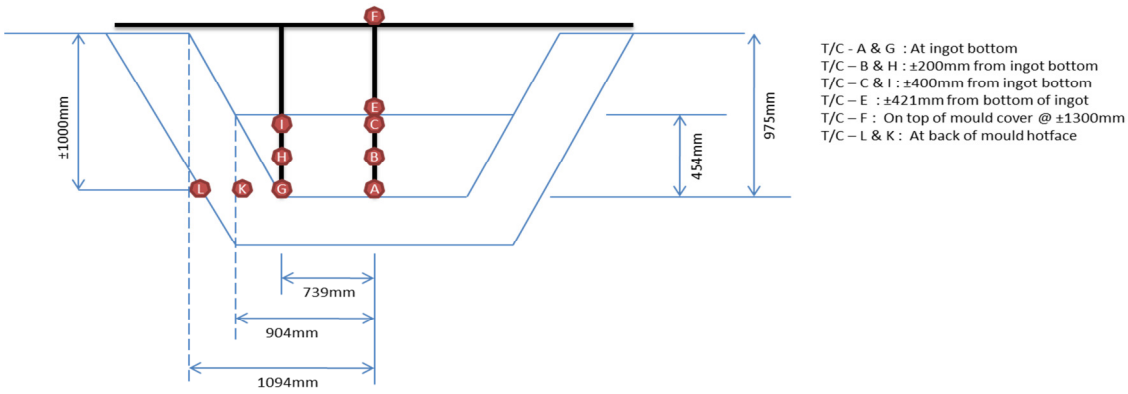

Figure 4.7-3.1: Test 2 – Ingot C, 5t thermocouple layout

Unfortunately some thermocouples malfunctioned during test 2 and not all the data could be used to perform the data correlations. The failed thermocouples are believed to be as a result of a failure in the refractory coating applied over the thermocouple rig before insertion into the molten matte which then caused the steel rig and thermocouples to be directly exposed to the molten WCM. The problematic thermocouples A and H which did not record properly were therefore excluded from any analysis. Because of the small ingot size, thermocouple positions D and J were not used in test 2.

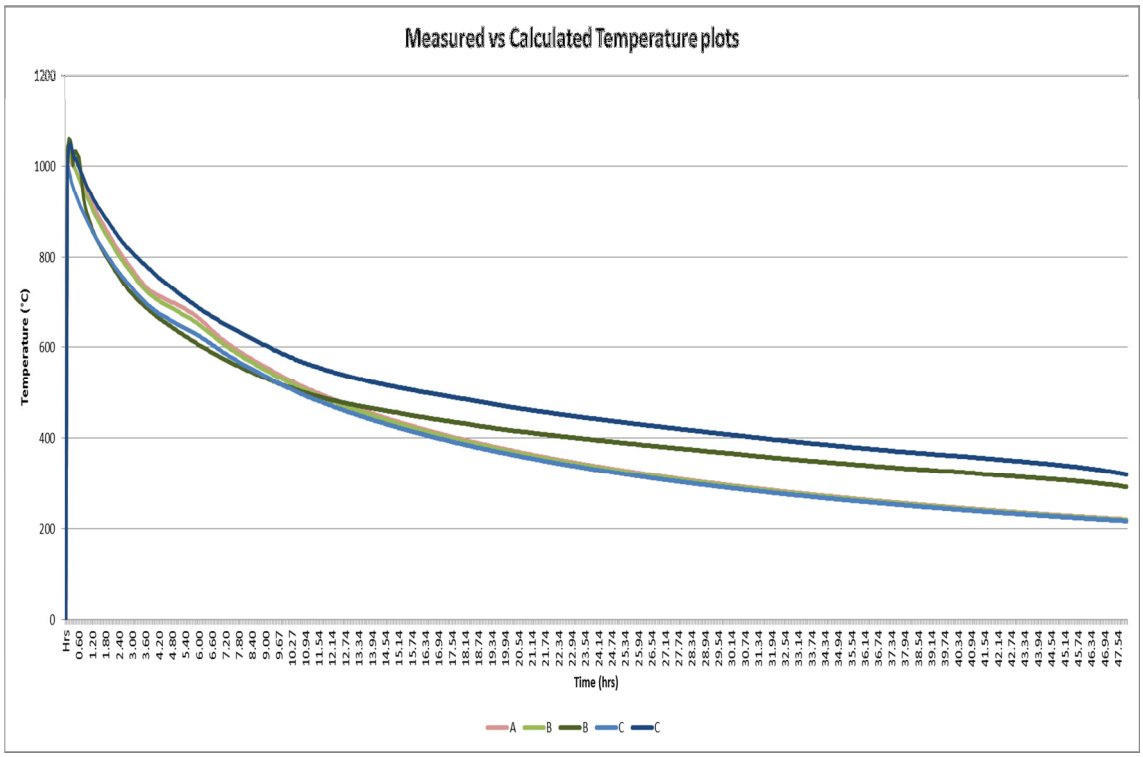

Fig 4.7-3.2: Temperature plots for thermocouples A to C for measured and modelled values (thermocouple A failed to record data)

In all the temperature profile graphs the lighter colour refers to the surface monitor data which was created at a specific point within the Fluent model which corresponds to the approximate position of the actual thermocouple tip used during measurement. The darker colour each time shows the actual measured temperature profile for each thermocouple. From Figure 4.7-3.2, the data recorded for thermocouple B (dark green line) shows some erratic behaviour in the first hour, which cannot be explained. It then showed a dramatic drop in temperature, where after it followed the expected cooling profile and ended ~100°C above the modelled temperature (light green line) after 48 hours. The cooling down profile for the measured (dark blue line) and modelled (light blue line) temperature of thermocouple C follows almost exactly the same cooling profile up to ~15hrs of cooling after which it starts to move apart slightly to end up ~120°C apart after 48 hours of cooling. All the modelled temperature profiles shows a slight deviation from the normal cooling profile from ~700°C to 600°C as a result of the phase changes as the eutectic point is approached as modelled in FactSage® and shown in Appendix 3, Figure 7.3-2. The data correlations for thermocouples B and C shows a R^2>0.99 as per Table 4.7-3.1.

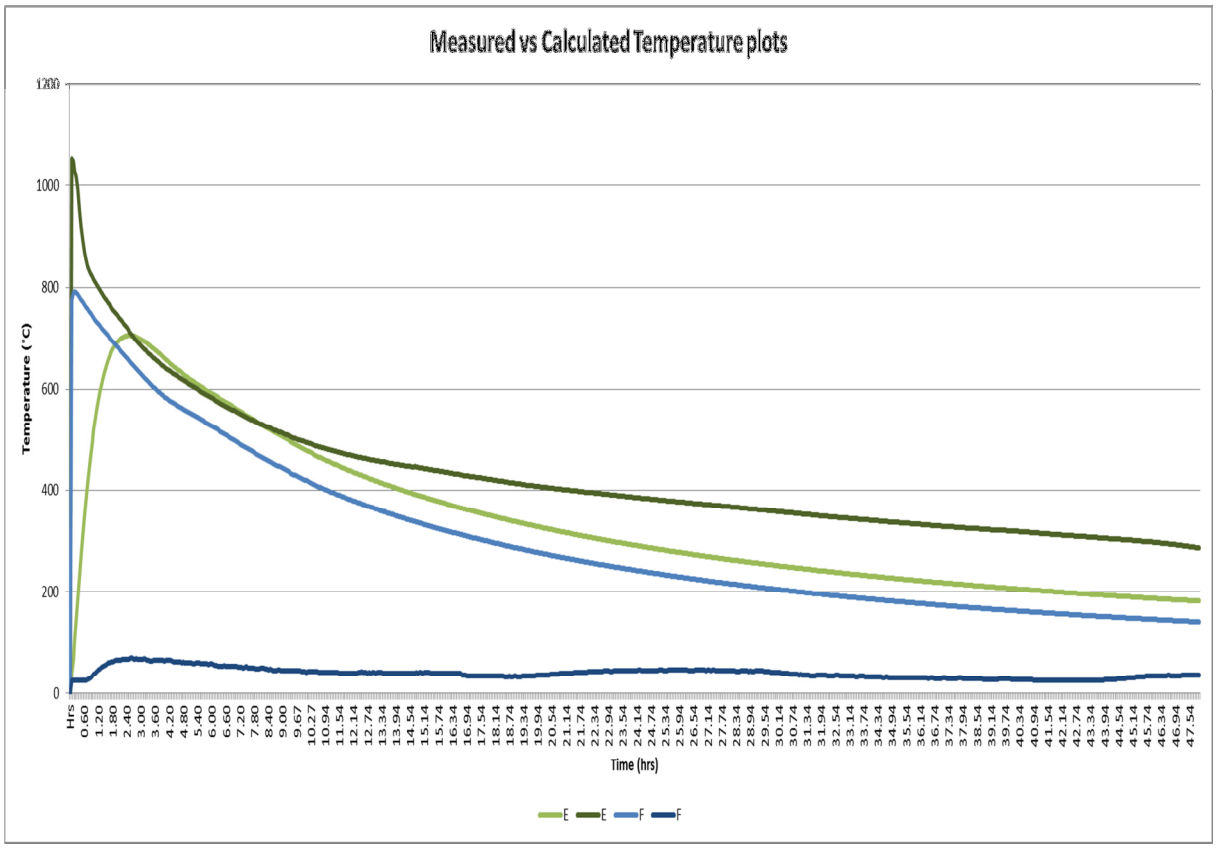

Fig 4.7-3.3: Temperature plots for thermocouples E and F for measured and modelled values

The difference in the measured and modelled trends for thermocouples E and F can again be explained by:

E: The exact height of the matte in the mould was very difficult to control exactly and therefore it is very difficult to confirm the exact thermocouple tip position relative to the ingot top surface. It is therefore unclear exactly what caused the rapid drop in temperature in the first hour of cooling (dark green line). For the modelled temperature (light green) the thermocouple tip position was just above the matte surface and therefore the rapid temperature increase during the first 3 hours before the cooling started.

F: The thermocouple on the top of the lid showed a relatively small temperature increase (~80 – 100°C) vs. the modelled thermocouple reaching ~800°C. This is due to the modified thermal conductivity used for the lid and the assumption that there are no slots cut into the lid. The data for thermocouple F is only shown in this graph Fig 4.7-3.3 but was excluded for the correlation data.

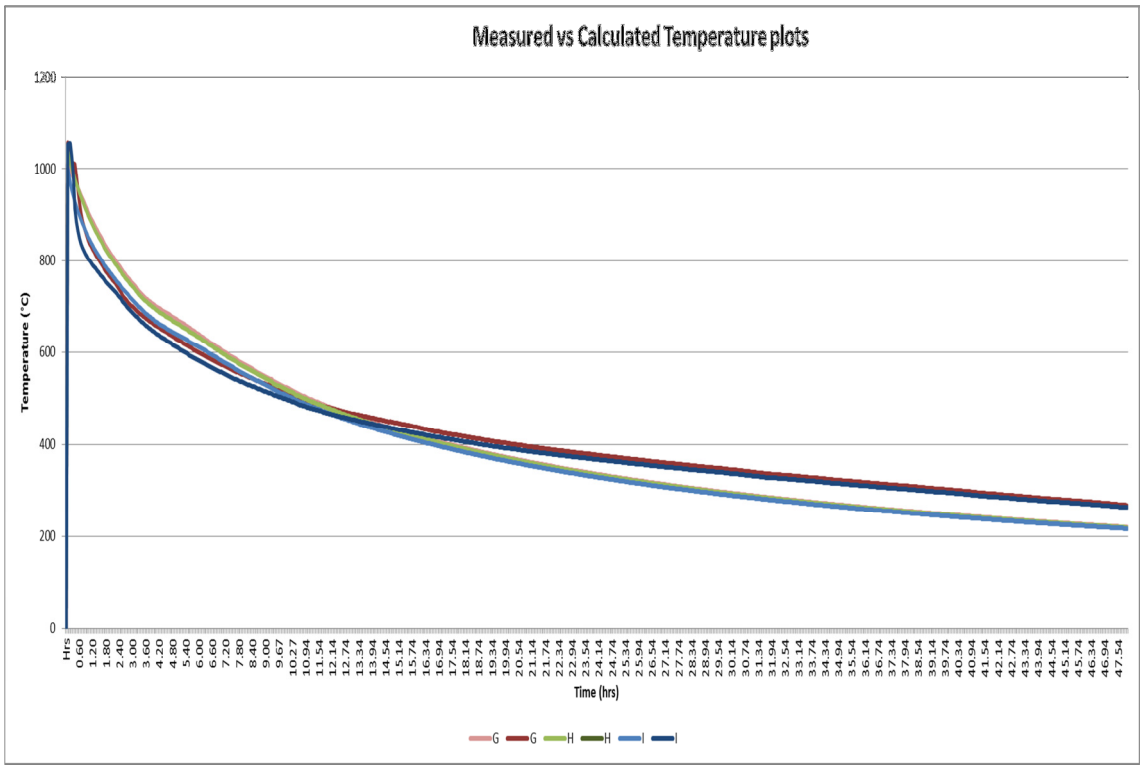

Fig 4.7-3.4: Temperature plots for thermocouples G to I for measured and modelled values

The modelled and measured values for thermocouples G and I as shown in Figure 4.7-3.4 follows almost exactly the same cooling profile over the cooling period and ended ~50°C apart after 48 hours. The data correlations G and I shows a R^2>0.99 as per Table 4.7-3.1.

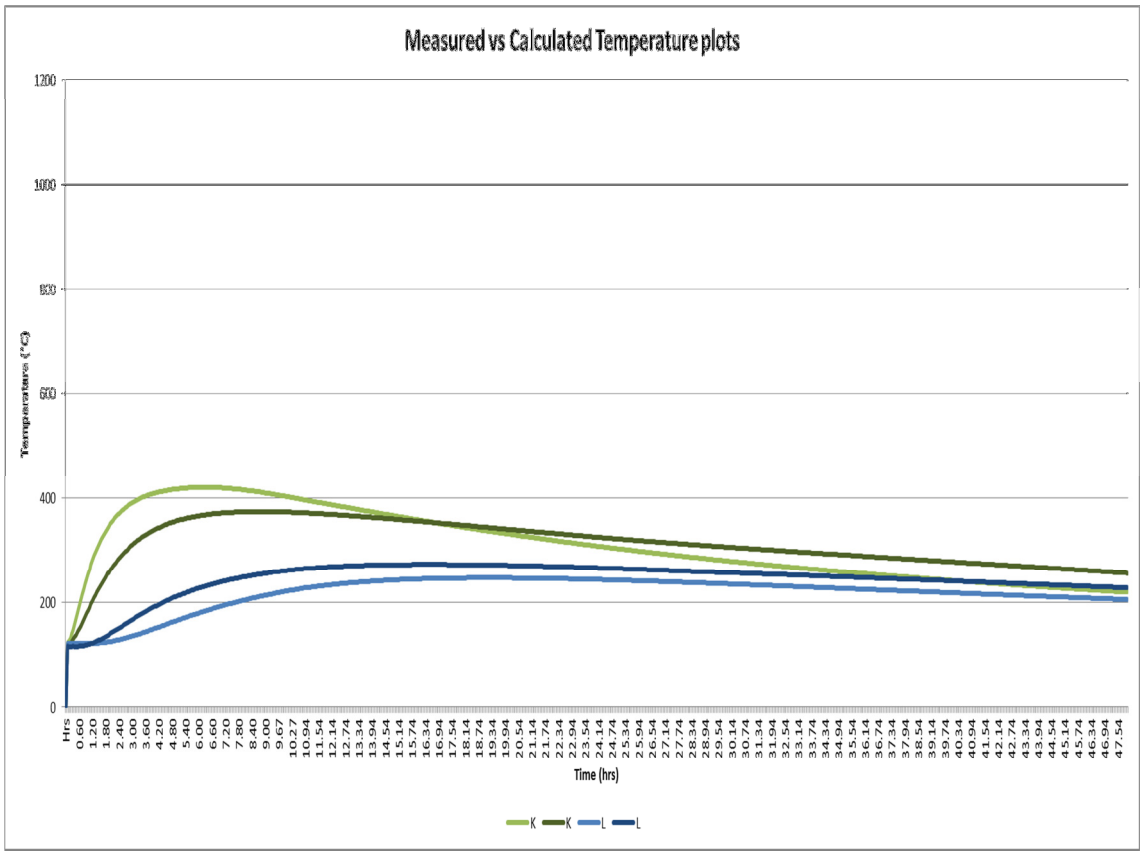

Fig 4.7-3.5: Temperature plots for thermocouples K and L for measured and modelled values

The data for the two thermocouples as shown in Fig 4.7-3.5 within the refractory correlated relatively well with R^2 = 0.86 and 0.96 respectively for K and L. Comparing the modelled and measured temperatures the conclusion can be made that the thermal conductivity used during the modelling for the inner refractory materials used might have been slightly higher than the actual at high temperatures.

Table 4.7-3.1: 5t ingot C, Test 2, data correlation for the modelled temperature data with the measured thermocouple temperatures with all the data and then also with the data excluding the data for the first hour of cooling (Problematic thermocouples: A & H which did not record properly and D & J not installed because of the small ingot - data was excluded from any analysis).

Correlation Geom 3_2_48hrs

	A Surf Mon 1	B Surf Mon 2	C Surf Mon 3	D Surf Mon 4	E Surf Mon 5	G Surf Mon 7	H Surf Mon 8	I Surf Mon 9	J Surf Mon 10	K Surf Mon 11	L Surf Mon 12
A Measured Value											
B Measured Value		0.991006									
C Measured Value			0.997847								
D Measured Value											
E Measured Value					0.770697						
G Measured Value						0.995186					
H Measured Value											
I Measured Value								0.995145			
J Measured Value											
K Measured Value										0.858642	
L Measured Value											0.960558

Correlation Variance Geom 3_2_48hrs_after 1hr

	A Surf Mon 1	B Surf Mon 2	C Surf Mon 3	D Surf Mon 4	E Surf Mon 5	G Surf Mon 7	H Surf Mon 8	I Surf Mon 9	J Surf Mon 10	K Surf Mon 11	L Surf Mon 12
A Measured Value											
B Measured Value		0.996243									
C Measured Value			0.997798								
D Measured Value											
E Measured Value					0.9718						
G Measured Value						0.99877					
H Measured Value											
I Measured Value								0.998448			
J Measured Value											
K Measured Value										0.869956	
L Measured Value											0.958778

The contour temperature profile plots for the 5 t ingot, showing the modelled temperature contours at different time intervals are graphically shown in Figures 4.7-3.6 to 4.7-3.11. The temperature scale was varied for the contour plots as the temperature zones were more clearly visible, but for completeness the same contour plots with a fixed temperature scale are also shown in Appendix 6, Figure 7.6-2.1 to 7.6-2.6.

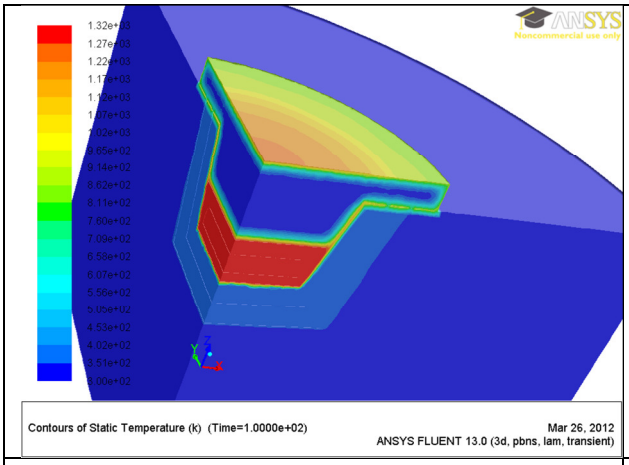

Figure 4.7-3.6: Static temperature profile showing the 5t ingot C, Test 2 after - 1min

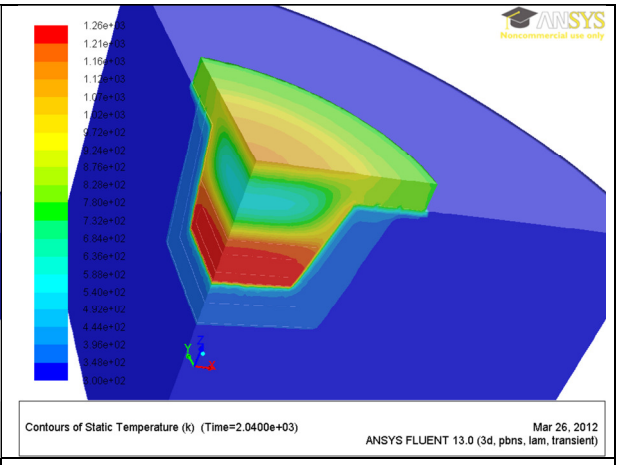

Figure 4.7-3.7: Static temperature profile showing the 5t ingot C, Test 2 after - 1hr

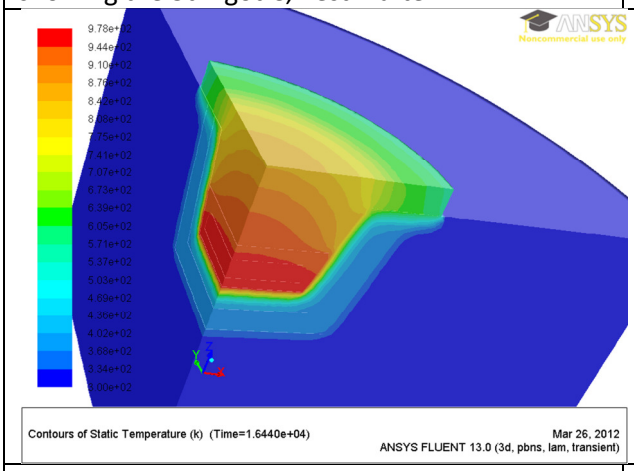

Figure 4.7-3.8: Static temperature profile showing the 5t ingot C, Test 2 after - 5hrs

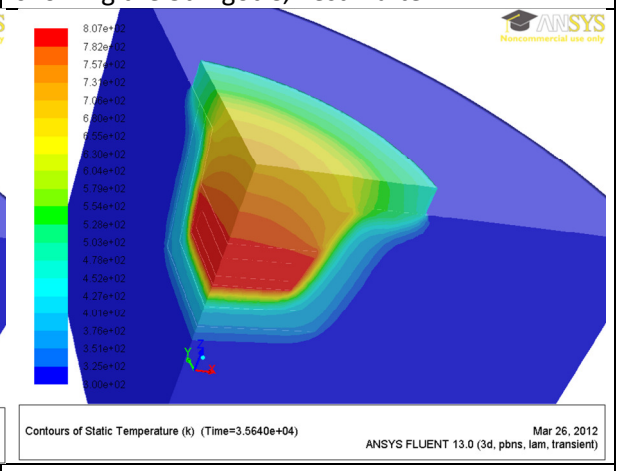

Figure 4.7-3.9: Static temperature profile showing the 5t ingot C, Test 2 after - 10hrs

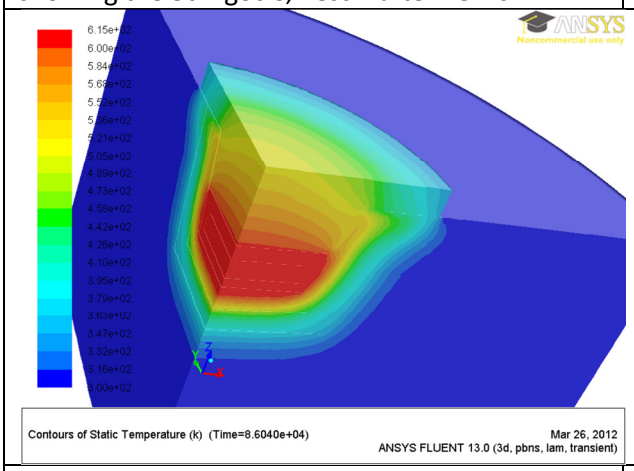

Figure 4.7-3.10: Static temperature profile showing the 5t ingot C, Test 2 after - 24hrs

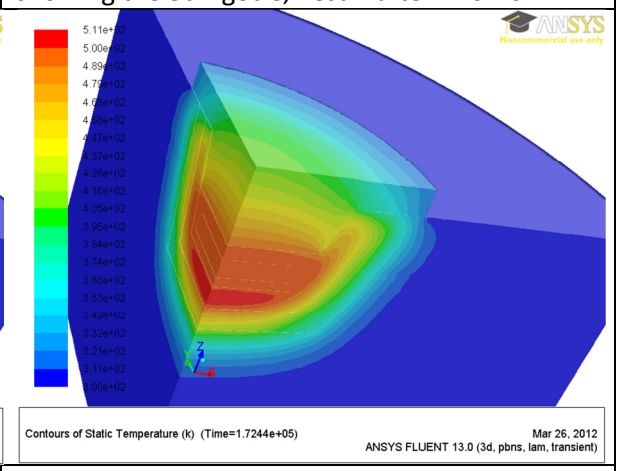

Figure 4.7-3.11: Static temperature profile showing the 5t ingot C, Test 2 after - 48hrs

4.7-4 **Temperature data analysis – Test 3, Ingot A, 15t:**

The thermocouple layout for Test 3 is shown in Figure 4.7-4.1, and the temperature trends with both the measured and modelled cooling profiles are shown in four separate graphs in Figure 4.7-4.2 to 4.7-4.5 where the thermocouples are grouped together based on location within the ingot.

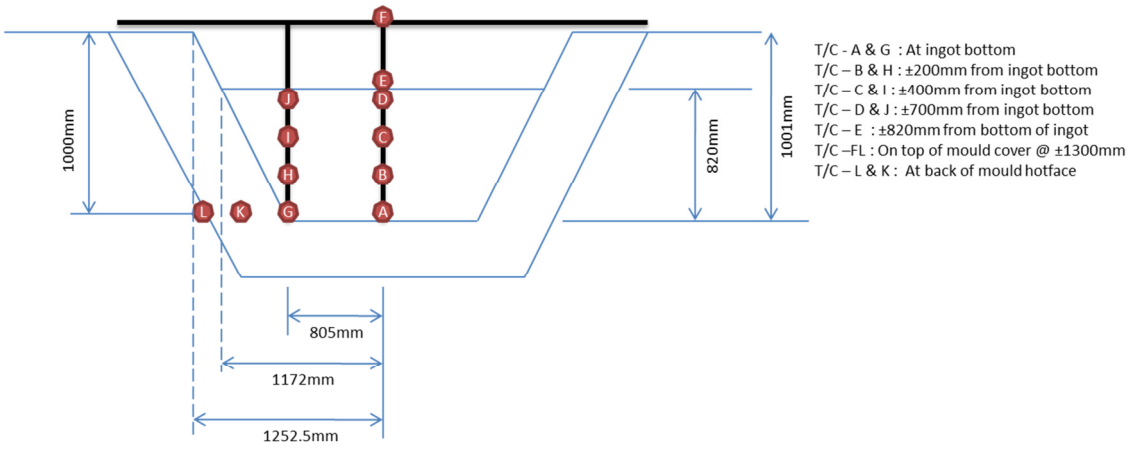

Figure 4.7-4.1: Test 3 – Ingot A, 15t thermocouple layout

The cooling of the 15 ton ingot was extremely rapid during the first two hours of cooling as shown in Figures 4.5-3, 4.5-5 and 4.5-6. After the first two hours the cooling profile followed a slightly faster but similar cooling profile as obtained from Test 1 and 2.

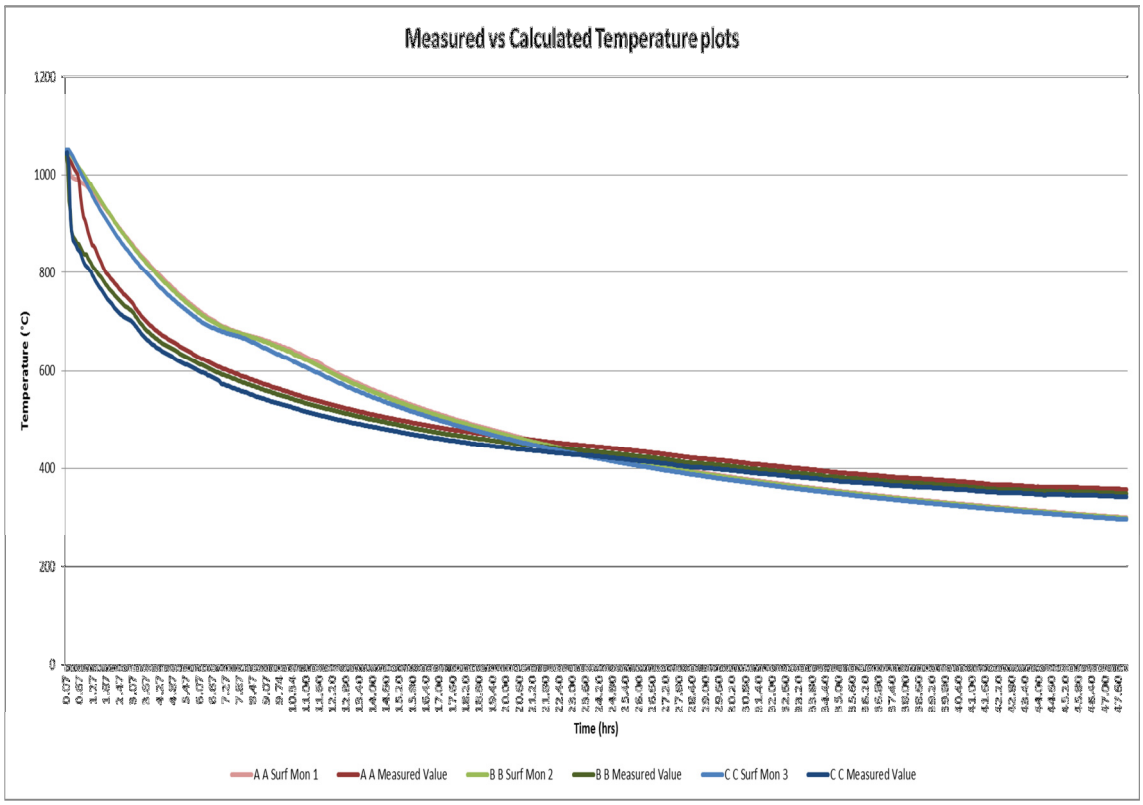

Fig 4.7-4.2: Temperature plots for thermocouples A to C for measured and modelled values

In all the temperature profile graphs the lighter colour refers to the surface monitor data which was created at a specific point within the Fluent model which corresponds to the approximate position of the actual thermocouple tip used during measurement. The darker colour each time shows the actual measured temperature profile for each thermocouple. The modelled cooling profile for the centre thermocouples (A to C as plotted in Figure 4.7-4.2) shows a slight slowdown in the cooling rate between 700 – 600°C as a result of the phase transformations taking place towards the eutectic point as calculated in Appendix 3, Figure 7.3-3. The modelled cooling profile is slightly slower than the actual cooling profile measured and ends ~100°C below the actual temperatures after 48 hours of cooling. The data correlation for all three thermocouples shown in Figure 4.7-4.2 have a R^2>0.98 as shown in Table 4.7-4.1 with a slightly better correlation excluding the data for the first hour of cooling.

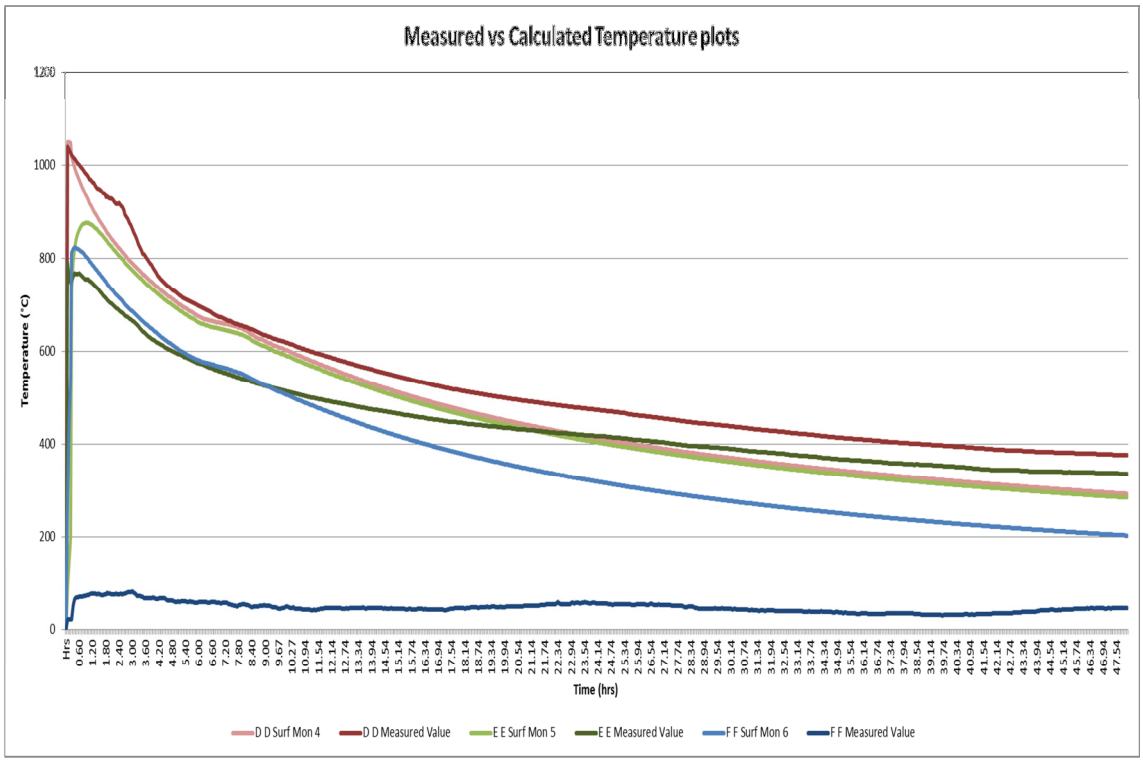

Fig 4.7-4.3: Temperature plots for thermocouples D to F for measured and modelled values

The modelled (light red) and measured (dark red) cooling profiles in Figure 4.7-4.3 for thermocouple D are fairly similar for the first 10 hours of cooling and then starts to diverge to end ~100°C apart after 48 hours of cooling. The R^2 for D was 0.99 as shown in Table 4.7-3. From the measured temperatures for thermocouple E (dark green), it is clear that the thermocouple tip was well above the WCM surface and therefore only reached a maximum of 800°C before the cooling started.

Thermocouple F on the top of the lid showed a relatively small temperature increase (~80 – 100°C) vs. the modelled thermocouple reaching ~800°C after 1 hour. This was due to the fact that the model assumed a modified thermal conductivity for the lid and which also included the assumption that there were no slots cut into the lid. The data for thermocouple F is only shown in this graph Fig 4.7-4.3 but was excluded for the correlation data.

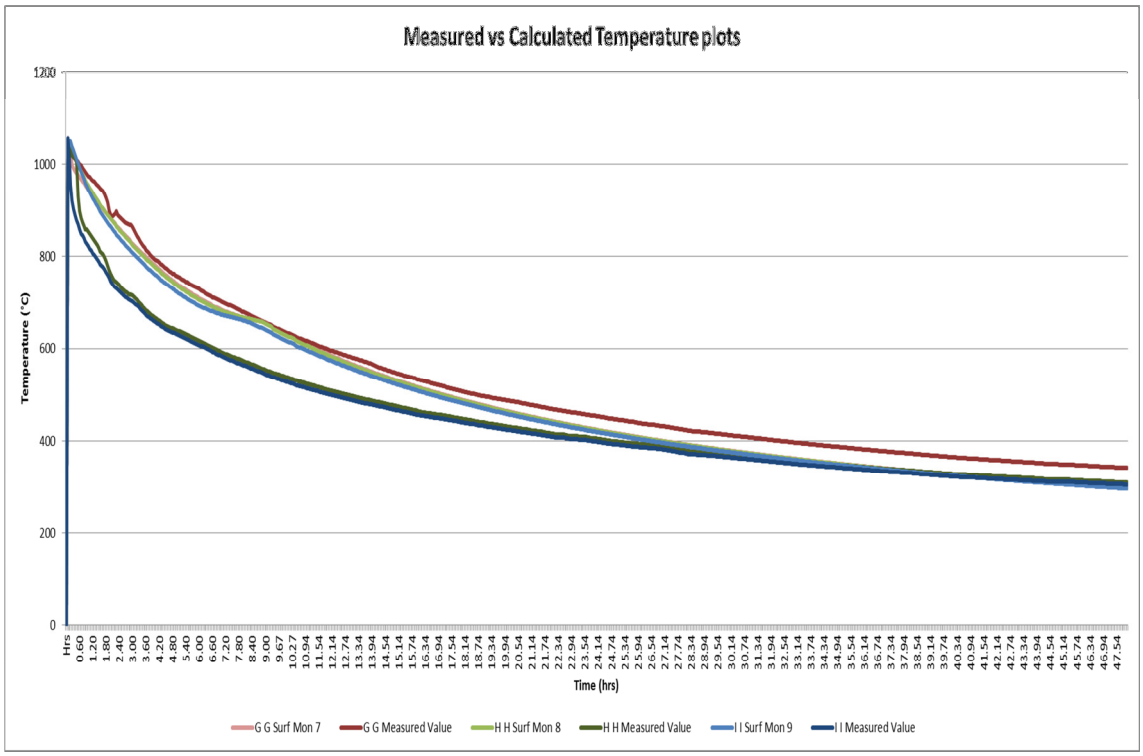

Fig 4.7-4.4: Temperature plots for thermocouples G to I for measured and modelled values

Interestingly enough the measured temperature on thermocouple G (dark red, Figure 4.7-4.4) also follows the modelled temperature very closely for the first 10 hours of cooling before diverging slightly to end up only ~50°C apart after 48hours of cooling. Thermocouples H and I follow very much the same profile as described for thermocouples A to C but ends up only ~20°C apart after 48 hours. The data correlation between measured and modelled data had a R^2>0.99 for all three thermocouples over the 48 hour period as shown in Table 4.7-4.1.

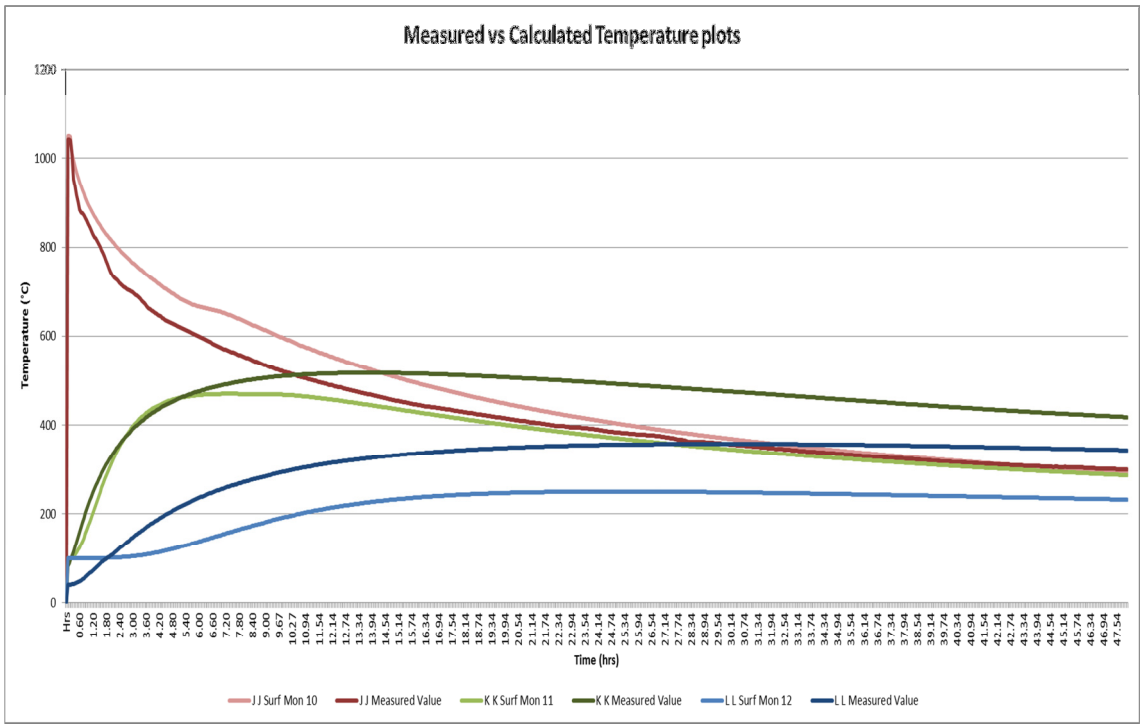

Fig 4.7-4.5: Temperature plots for thermocouples J to L for measured and modelled values

The measured (dark red) and modelled (light red) temperatures for thermocouple J as shown in Fig 4.7-4.5 follows the same trend as D, which is positioned at a similar depth, and ends up <50°C apart after 48 hours. The two refractory thermocouples shows a different comparative temperature trend than observed in the first two tests with the measured values (dark green) for thermocouple K being slightly higher for the first 3 hours than the modelled values (light green) and also only for this test reaches 500°C. The modelled (light blue) and measured (dark blue) temperature for thermocouple L is also much further apart and the measured values much higher than observed in the other two tests. This was due to the fact that the thermocouples in the refractory for test 3 were positioned slightly closer to the hot-face compared to the other two tests.

Test 3 data shows the best set of R^2 numbers of all the correlations done with all being > 0.83. If thermocouples K and L are excluded (in the refractory) the lowest R^2 is > 0.974 which is an excellent validation for the model as shown below.

Table 4.7-4.1: 15t ingot A, Test 3, data correlation for the modelled temperature data with the measured thermocouple temperatures with all the data and then also with the data excluding the data for the first hour of cooling.

Correlation Geom 3_18_48hrs

	A Surf Mon 1	B Surf Mon 2	C Surf Mon 3	D Surf Mon 4	E Surf Mon 5	G Surf Mon 7	H Surf Mon 8	I Surf Mon 9	J Surf Mon 10	K Surf Mon 11	L Surf Mon 12
A Measured Value	0.980115										
B Measured Value		0.992016									
C Measured Value			0.989346								
D Measured Value				0.993273							
E Measured Value					0.939451						
G Measured Value						0.998705					
H Measured Value							0.991776				
I Measured Value								0.996022			
J Measured Value									0.99333515		
K Measured Value										0.7738982	
L Measured Value											0.960275

Correlation Variance Geom 3_18 after 1hr

	A Surf Mon 1	B Surf Mon 2	C Surf Mon 3	D Surf Mon 4	E Surf Mon 5	G Surf Mon 7	H Surf Mon 8	I Surf Mon 9	J Surf Mon 10	K Surf Mon 11	L Surf Mon 12
A Measured Value	0.993241										
B Measured Value		0.996485									
C Measured Value			0.995695								
D Measured Value				0.991889							
E Measured Value					0.995567						
G Measured Value						0.99862					
H Measured Value							0.997224				
I Measured Value								0.997994			
J Measured Value									0.99523625		
K Measured Value										0.6984949	
L Measured Value											0.9707284

The contour temperature profile plots for the 15 ton ingot, showing the modelled temperature contours at different time intervals are graphically shown in Figures 4.7-4.6 to 4.7-4.11. The temperature scale was varied for the contour plots as the temperature zones were more clearly visible, but for completeness the contour plots with a fixed temperature scale are also shown in Appendix 6, Figure 7.6-3.1 to 7.6-3.6.

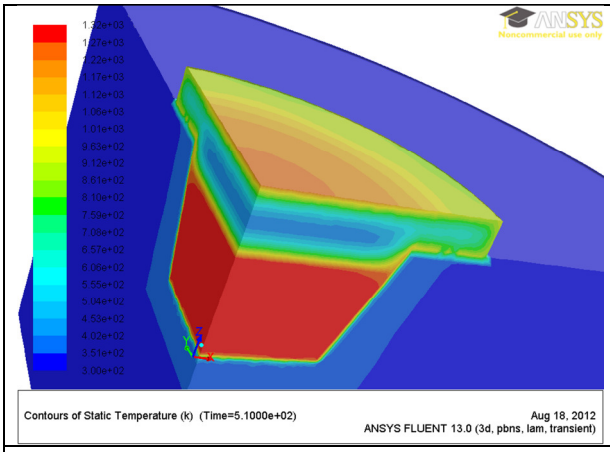

Figure 4.7-4.6: Static temperature profile showing the 15t ingot A, Test 3 after - 30min

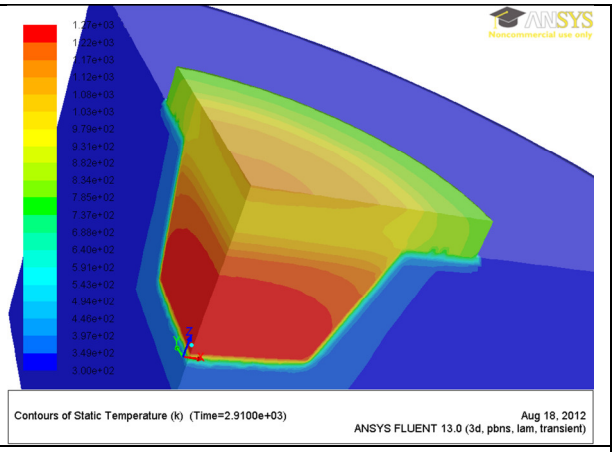

Figure 4.7-4.7: Static temperature profile showing the 15t ingot A, Test 3 after - 1hr

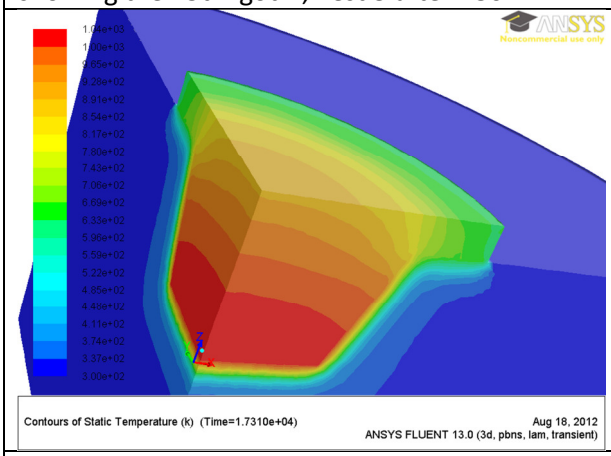

Figure 4.7-4.8: Static temperature profile showing the 15t ingot A, Test 3 after - 5hrs

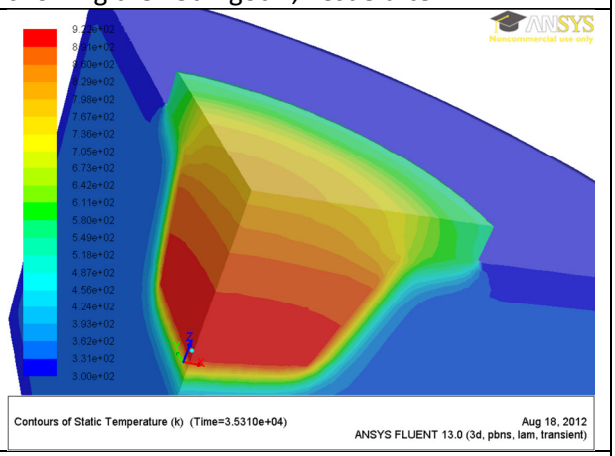

Figure 4.7-4.9: Static temperature profile showing the 15t ingot A, Test 3 after - 10hrs

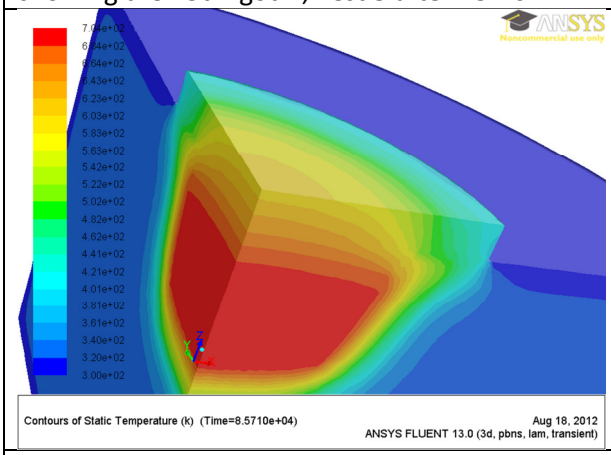

Figure 4.7-4.10: Static temperature profile showing the 15t ingot A, Test 3 after - 24hrs

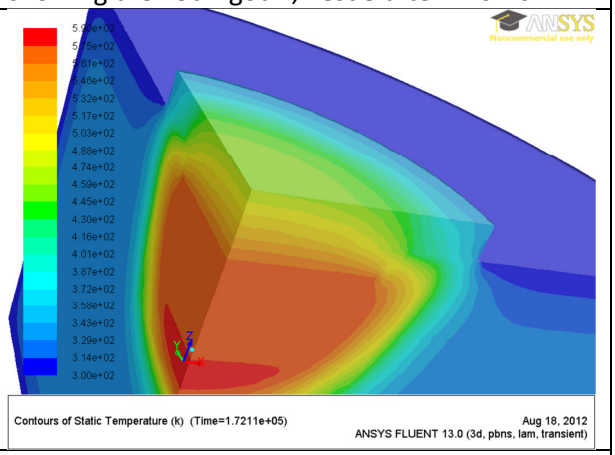

Figure 4.7-4.11 : Static temperature profile showing the 15t ingot A, Test 3 after - 48hrs

Both point and surface monitors were also selected as part of the model and some of the point monitors are visible in Figure 4.7- 1.1, indicated by the small crossed circles in black. These point monitors were set up in similar positions to the thermocouple tips as discussed in Section 3. Similar to the point monitors, surface monitors were used to calculate the heat losses through the outer surfaces (top, bottom and side circumference) of the various WCM ingot geometries over time. The trends for the calculated heat losses over time are shown in Appendix 5, Figures 7.5-1.5, 7.5-2.5 and 7.5-3.5. The cumulative heat losses over time are shown in Appendix 5, Figures 7.5-1.6, 7.5-2.6 and 7.5-3.6, for the three tests respectively.

From the heat loss data it was calculated the bulk of the heat lost from the ingots is through the top surface as shown per illustration for the 15 t ingot case in Table 4.7-4.2. After the first 12 hours approximately 89% of the heat lost from the ingot is via the top surface and this increases to 96% after 24 hours. It can therefore be concluded that the cooling rates of the ingots can be easily manipulated by changing the thermal insulation of the lid that is placed over the ingot after casting.

Table 4.7-4.2: Heat losses as a % of total heat loss, calculated over time for the modelled 15t ingot geometry

	Instantaneous heat loss per surface			Cumulative heat loss per surface		
	Top Surface	Side surface around the circumference	Bottom surface	Top Surface	Side surface around the circumference	Bottom surface
Start of cooling	58%	21%	21%	58%	21%	21%
After 12 hours	75%	18%	7%	89%	9%	3%
After 24 hours	80%	15%	5%	96%	4%	1%

4.8 Slow-cool Capacity

The slow-cool aisle, where the WCM ingots are cast and cooled, consists of a total of 108 moulds that are used for the slow-cool process. Each mould used for casting and cooling of an ingot is therefore utilised depending on the converter throughput and WCM production. The slow-cool aisle capacity was calculated with the assumptions:

- 10% of the moulds not available, due to repair or refurbishing purposes
- Average tap size of 16.2t, from a normal blow size of 60t and matte fall of 27% (as summarized in Table 4.8-1)
- Cooling times in the moulds of 72 hours and four hours for mould preparation between casts

Assumptions for calculation		
Blow Size	60	t
Matte Fall	27%	
WCM Production	16.2	t
Number of moulds in aisle	108	
Mould in repair (%)	10%	
Number of moulds available in aisle	98	
Mould under repair	10	

Table 4.8-1: Summary of assumptions made to calculate the slow-cool aisle capacities

The current practice on the operation is to cast an ingot and place the lid over the ingot for 52 hours, then remove the lid and allow further cooling for another 20 hours before the ingot is removed from the mould (totalling 72 hours in the mould as described in detail in Section 3.1.2). The slow-cool capacity shortfall is plotted versus converter feed rate in Figure 4.8-1 in an attempt to show the slow-cool capacity constraint with increased federate for a given mould size. The converter slow-cool isle becomes a bottleneck if the capacity shortfall >0 (shown in brown and on the secondary Y axis).

The calculated capacity with the current 10t mould volume is 38tph continuous converter feed (brown dotted line). If the continuous feed rate is increased to 45tph then the maximum available cooling time per ingot in the mould decreases to 59hrs to ensure moulds available for casting when operating the converter continuously. For a further increase to 60tph continuous converter feed the available cooling time in the moulds will decrease to only 31hrs as indicated by the dotted blue line in Figure 4.8.1. If the available time for cooling is kept constant it results in a capacity shortfall as is illustrated by the red dotted line for the current slow-cool isle configuration with the 10 moulds.

If the mould size in the slow-cool aisle would be increased to 20t and the number of moulds kept at 108 (as currently) the slow-cool isle mould capacity will increase and allow continuous operation of the converter at 76tph, if the cooling time of 72hrs is maintained, resulting in a doubling of the current capacity. This is graphically illustrated by the solid brown and blue lines respectively in Figure 4.8-1. This will allow for a single mould being used for each tap that will not only increase the slow aisle capacity but also benefit the logistics in the area with:

- Shorter casting times will be achieved because the bottom caster ladle will not have to be moved between mould during each cast
- The number of ingots lifted from the moulds will be halved and similarly the ingots handled to/in the crushing plant
- A significant cost saving is expected from the reduction in the usage of hanger bars and refractory material

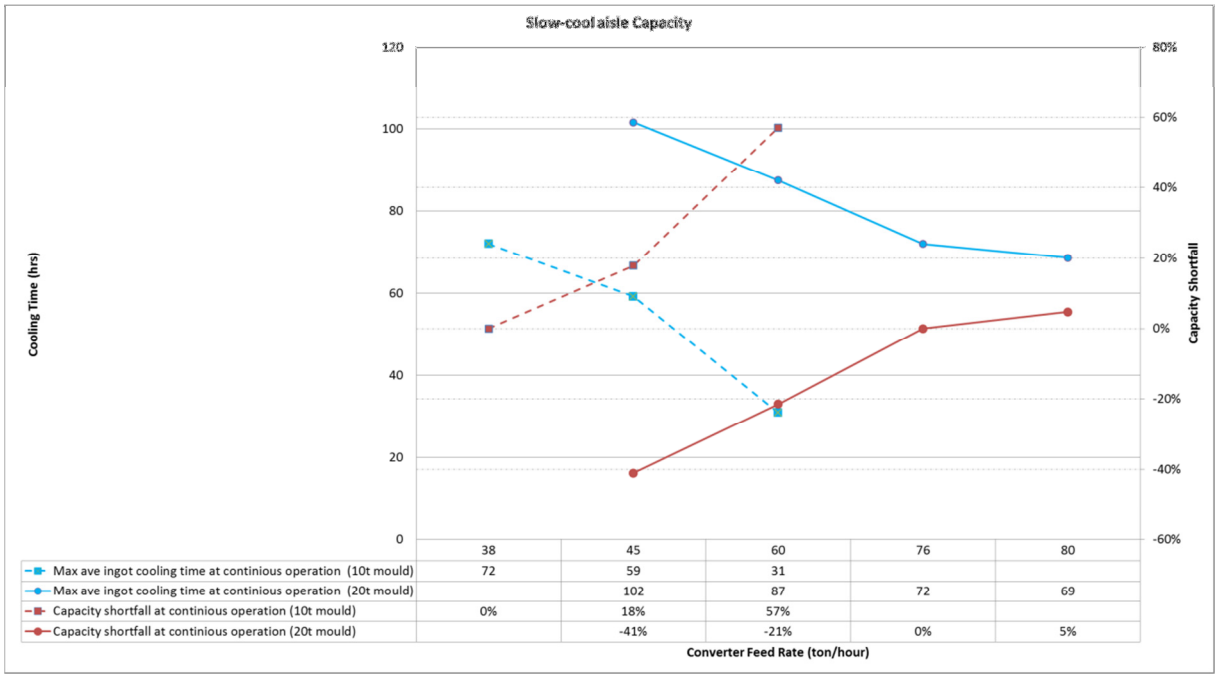

Figure 4.8-1: The slow-cool aisle capacity presented for a range of converter feed rates, illustrating the opportunity for capacity increase by increasing the slow-cool mould size from 10t to 20t.

5. Conclusions

A Fluent model was developed to simulate the transient slow cooling of WCM. The accuracy of the calculated temperature data from the model (for the available data) was validated with statistical correlations against the actual measured temperature data. The statistical data correlations for the cool down curves between the modelled and measured values produced a R^2>0.99 and it was therefore concluded that the data fit was representative.

The important input parameters to the model were calculated based on the chemical and mineralogical data obtained from samples taken from drill cores, which facilitated the development of a detailed mineralogical/chemical map of the various ingots (Fig. 4.2-1 to 3). The observations from the mineralogical zoning of the ingots concluded that the larger 15t ingot had a substantial higher BMA+Pt content (up to 5% higher) in the core (Ingot section 1), compared to the 10t ingot despite the faster cooling rate. It also then resulted in a slightly lower Heazlewoodite concentration (between 1.5-3.8% lower) in Ingot section 1. However, the higher concentration of total BMA, for the 15t ingot, was predicted from the % theoretical alloy as calculated in Table 4.1-1 from the chemical analysis data because of the slightly lower %S and %Fe.

The cooling rate of the 15t ingot was more than double at 0.54°C/min compared to that of the 10t ingot at 0.24°C/min (as shown in Figure 4.5-5 for thermocouple A at the base of the ingots) between the defined critical temperatures of 920°C – 520°C. From the literature it would have been expected that more finely grained dispersed alloy platelets (<25µm) with abundant sulphide-plate intergrowths, would be present in the 15t ingot because of the Ni/Cu ratio <1.5 and the rapid cooling rate. Alloy platelets smaller than 25µm are considered eutectic and normally do not recover well because it cannot be properly liberated during the milling process.

From the quantitative analysis done on the platelet sizing for the centre core of each of the three ingots, it was however shown that the 15t ingot had the least amount of fine alloy platelets (<25µm). Comparing the platelet size distributions for the bottom 3 sections (Sections B1-1 to B1-3 and A1-1 to A1-3) of the cores of the 10t and 15t ingots, it is evident that the 10t ingot has a substantial higher amount of -25µm platelets of 37% versus the 19% of the 15t ingot. Comparing the data for the complete core of each ingot, the larger 15t ingot, in test 3, has the lowest number of <25µm platelets (21%) and also the largest amount of >400µm platelets at 14% >400µm platelets. The platelets in the 10t ingot core, with the lowest cooling rate, had 25% of -25µm platelets and 7% >400µm platelets. The smallest 5t ingot, in test 2, had the largest amount of <25µm particles at 27% and also the lowest amount of >400µm platelets at 4%. This observation is significant and may indicate that sufficient the platelet size growth can be obtained at even faster cooling rates.

Due to the rapid rate of cooling (compared to previous tests performed and reported in the literature) that was measured and observed during the three tests conducted, the actual phase changes were not distinctly visible on the measured cooling curves as was the case in previous work done by Bruwer, 1995 and shown in Figure 4.5-4. The faster rate of cooling can be explained by the different lid design and type of insulation currently in use on the lids that are used to cover the ingots after casting. From the initial quantitative work done on platelet sizing, the faster cooling rates measured during the test work did not have a negative effect on the WCM quality, therefore from the cooling rates and mineralogical data obtained from the experiments it seems to provide evidence that the cooling rate of the ingots in the slow-cool process are possibly less important than previously thought. This was derived from the fact that

the 5t and 15t ingots cooled down 3 and 4 times faster respectively than the 10t ingot, but from the alloy formation and platelet size data, there were no significant difference in the final WCM quality. This still needs to be verified via magnetic separation test work, but falls outside the scope of this work.

In all the modelling the initial rate of cooling between ~1050°C and ~900°C for the centre line of thermocouples was slightly lower than the measured values. This is likely to be as a result two factors:

1. In practice the lid is only placed over the ingot after ~40min from the completion of the cast, therefore resulting in no thermal barrier above the ingot during the initial stages of cooling whereas in the model it was assumed that the ingot was covered from time zero.

2. The assumption was made that no convective heat transfer takes place within the ingot after casting, but in practice it is well known that the first solids only start forming at ~ 920°C, with final solidification only taking place below ~600°C, depending on the exact WCM chemical composition. Convection within the initial period of cooling can contribute significantly to the heat transfer to the ingot surfaces, especially to the top surface. From the modelling work the rate of heat transfer to the top surface is likely to be the heat transfer rate limiting step during this period. Therefore for future work an effective thermal conductivity can be applied "k^{eff}" to compensate for this unknown as a function of temperature.

The equilibrium model in FactSage® v6.2 was used to calculate the Cp curves for the various sections in the ingots, so as to describe the energy release taking place during the phase changes for solidification whilst cooling.

The thermal conductivity calculated and used in the model of 84.3 – 151.4 W/m-k simulates the cooling profile well down to a temperature of ~500°C after which the cooling rate slows and it would seem that the thermal conductivity is closer to the values used during the prior modelling done by the CSIR as shown in Table 2.6-3, and is in the order of between 7 and 11 W/m-k. There are no empirical or experimental data available to verify these numbers and this must definitely be a subject of future study in order to better the understanding of the slow-cool process.

The modelled heat losses as calculated show that over 90% of the heat lost during the slow cooling process is through the ingot top surface (and therefore the lid). This is because of the very low thermal conductivity of refractory material, thermally insulating the sides and bottom of the ingot very effectively. Therefore the rate of cooling can be controlled and/or manipulated by the insulation of the lid and the size of the holes for the hanger bars in the lid.

From the data obtained it is recommended that the ingot size can be increased to 20t without increasing the cooling times or inventory and without any detrimental effect on WCM quality, assuming the desired chemical composition persists. It can be stated with relative certainty that all solidification of the ingot in the 20t mould would have taken place within the 52 hours of cooling with the lid on. It must furthermore be noted that if the change is made to the larger ingots, the time between casting and placing the lid will be reduced because only one ingot (two ingots currently) needs to be cast, which will reduce the initial heat losses during the process. This can only be advantageous to the process.

6. Future Work

From the experimental and modelling work it is clear that quite a number of aspects regarding the slow-cool process are not fully understood and must be studied in more detail going forward. This can be summarised with the following general proposals:

- The thermal properties i.e. thermal conductivity and linear expansion, of the WCM are not well understood and must be studied and/or measured for future optimisation of the actual/modelled cooling rates.

- Modelling can be attempted to simulate the fractional crystallisation process and rate of alloy platelet growth with varying matte compositions and cooling rates.

- Test work can continue with different mould lid designs to manipulate and optimise the slow-cool process. Once the optimum cooling rates are determined, permanent thermocouples can then be placed in the mould sidewall refractory that can then be used to optimally control the ingot cooling rates depending on composition and required cooling rates by manipulating the heat loss via the lid.

- Controlled cooling rate tests can be conducted with different chemical compositions i.e.: Cu/Ni ratios, %Fe and %S to further the understanding the effect of chemistry on the slow-cool process. Although this was attempted by Bruwer, 1998 on laboratory scale which was not successful due to the complexity of the fractional crystallisation, these experiments can be repeated on plant scale by cooling down ingots with similar composition at different rates.

Appendices

7. Appendix 1: Core drill Layout for Chemical and Mineralogical Analysis

Figure 7.1-1 -Test1 – Ingot B

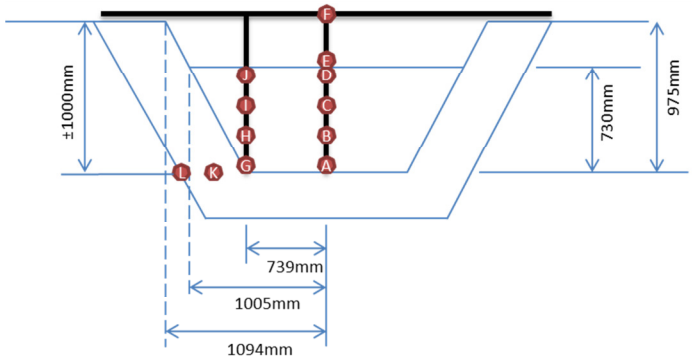

T/C - A & G : At ingot bottom (±970mm from top)
T/C – B & H : 200mm from ingot bottom (±770mm from top)
T/C – C & I : 400mm from ingot bottom (±570mm from top)
T/C – D & J : 700mm from ingot bottom (±270mm from top)
T/C – E : ±760mm from bottom of ingot (±201mm from top)
T/C – F : On top of mould cover @ ±1300mm
T/C – K & L : At back of mould hotface (K = ±960mm & L = ±920mm)

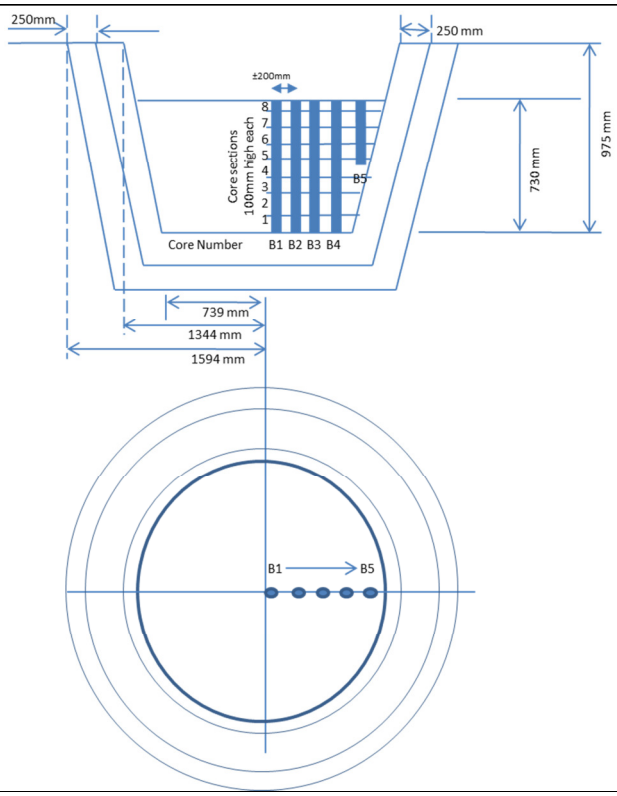

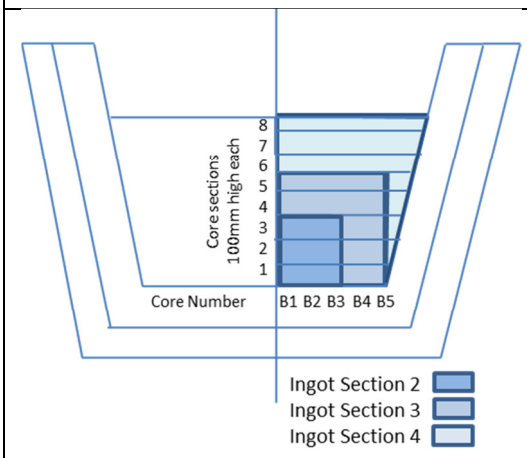

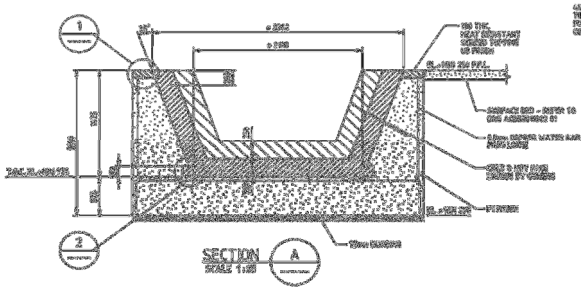

Figure 7.1-2 -Test2 – Ingot C

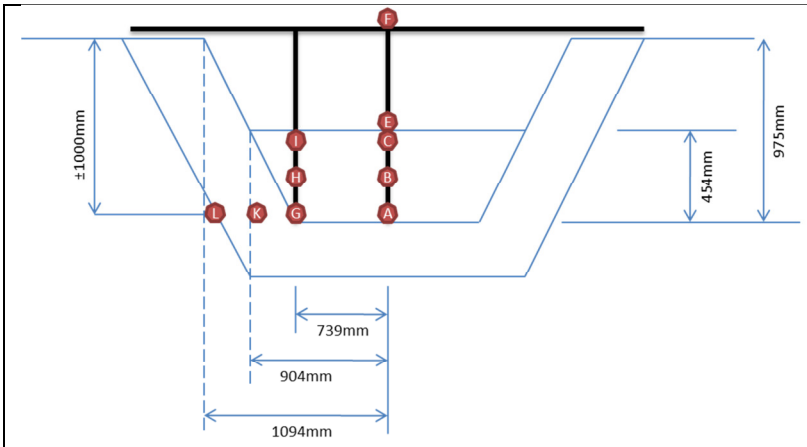

T/C - A & G : At ingot bottom
T/C – B & H : ±200mm from ingot bottom
T/C – C & I : ±400mm from ingot bottom
T/C – E : ±421mm from bottom of ingot
T/C – F : On top of mould cover @ ±1300mm
T/C – L & K : At back of mould hotface

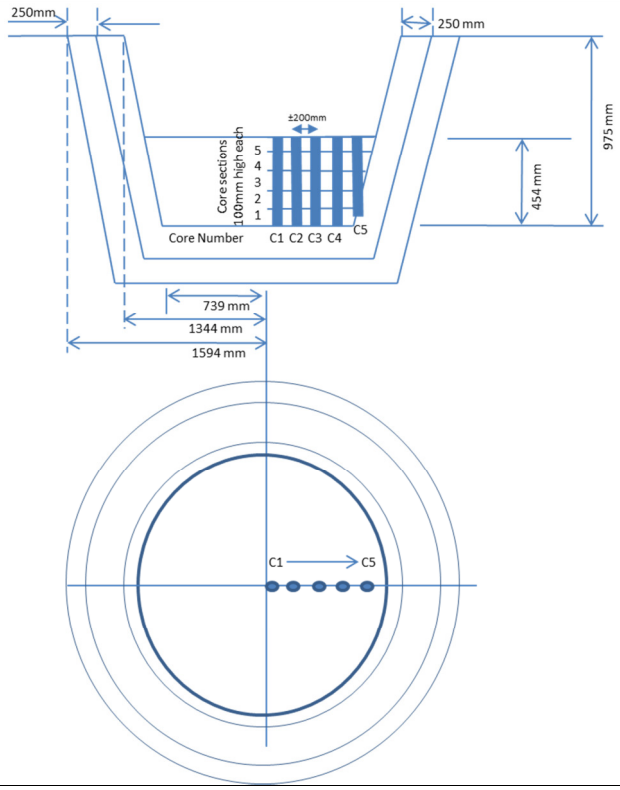

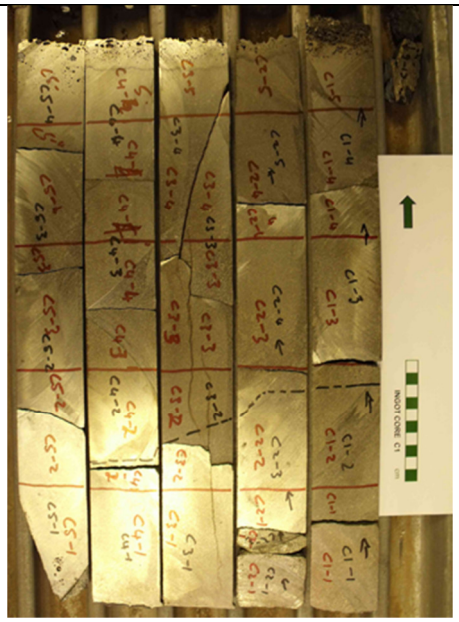

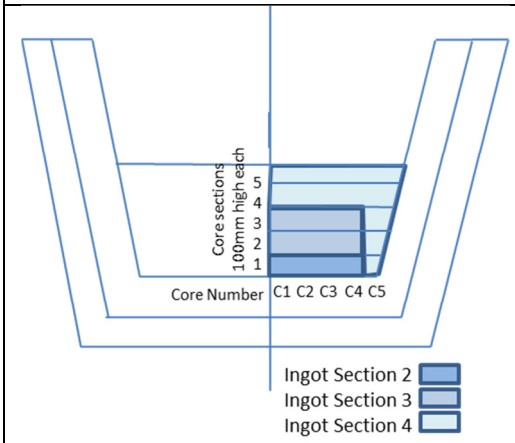

Figure 7.1-3 - Test3 – Ingot A

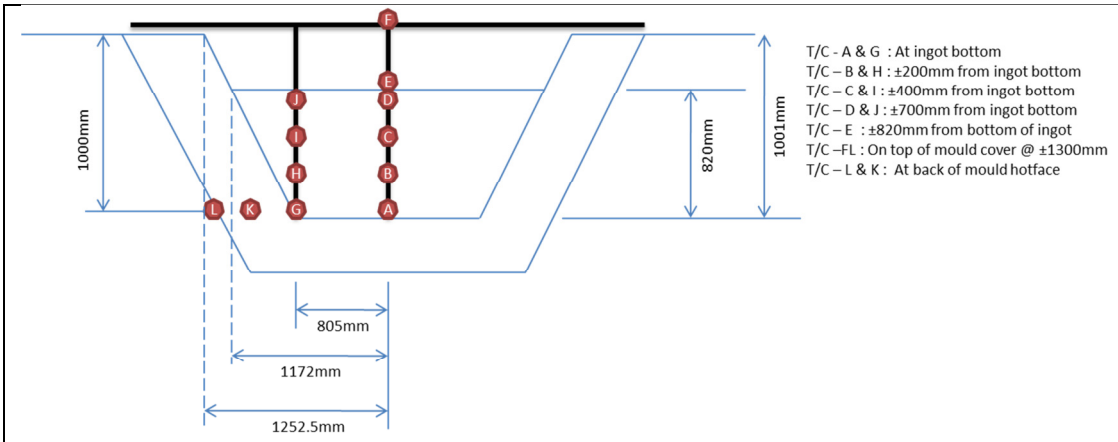

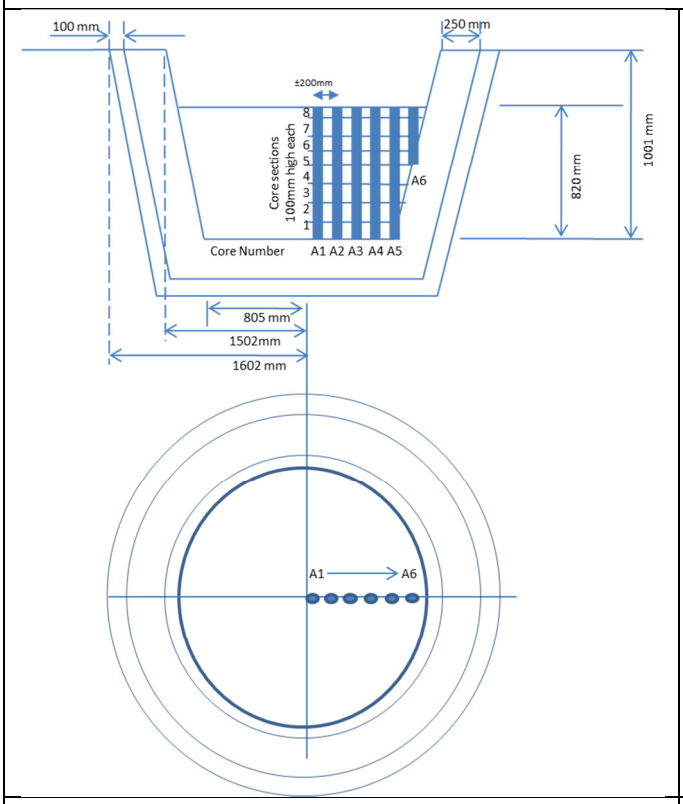

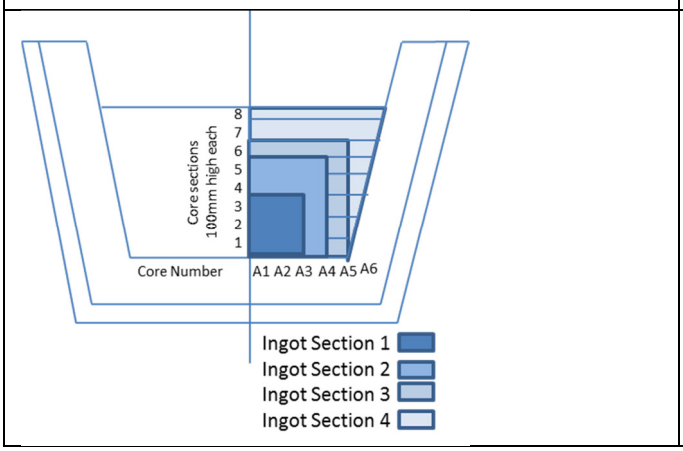

7. Appendix 2: Mineralogical Data

Figure 7.2-1 - Test 1, Ingot B, 10t

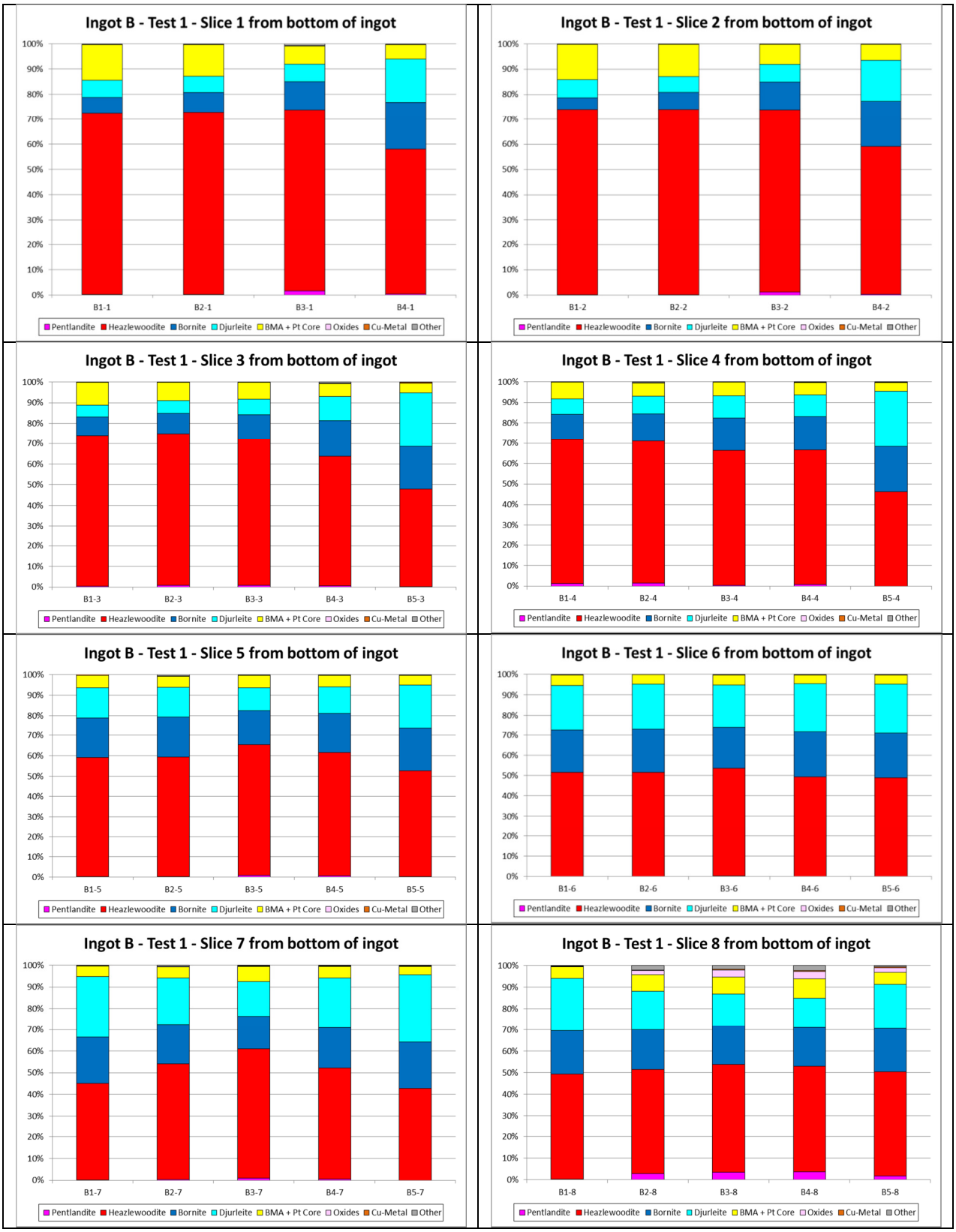

Figure 7.2-2 - Test 2, Ingot C, 5t

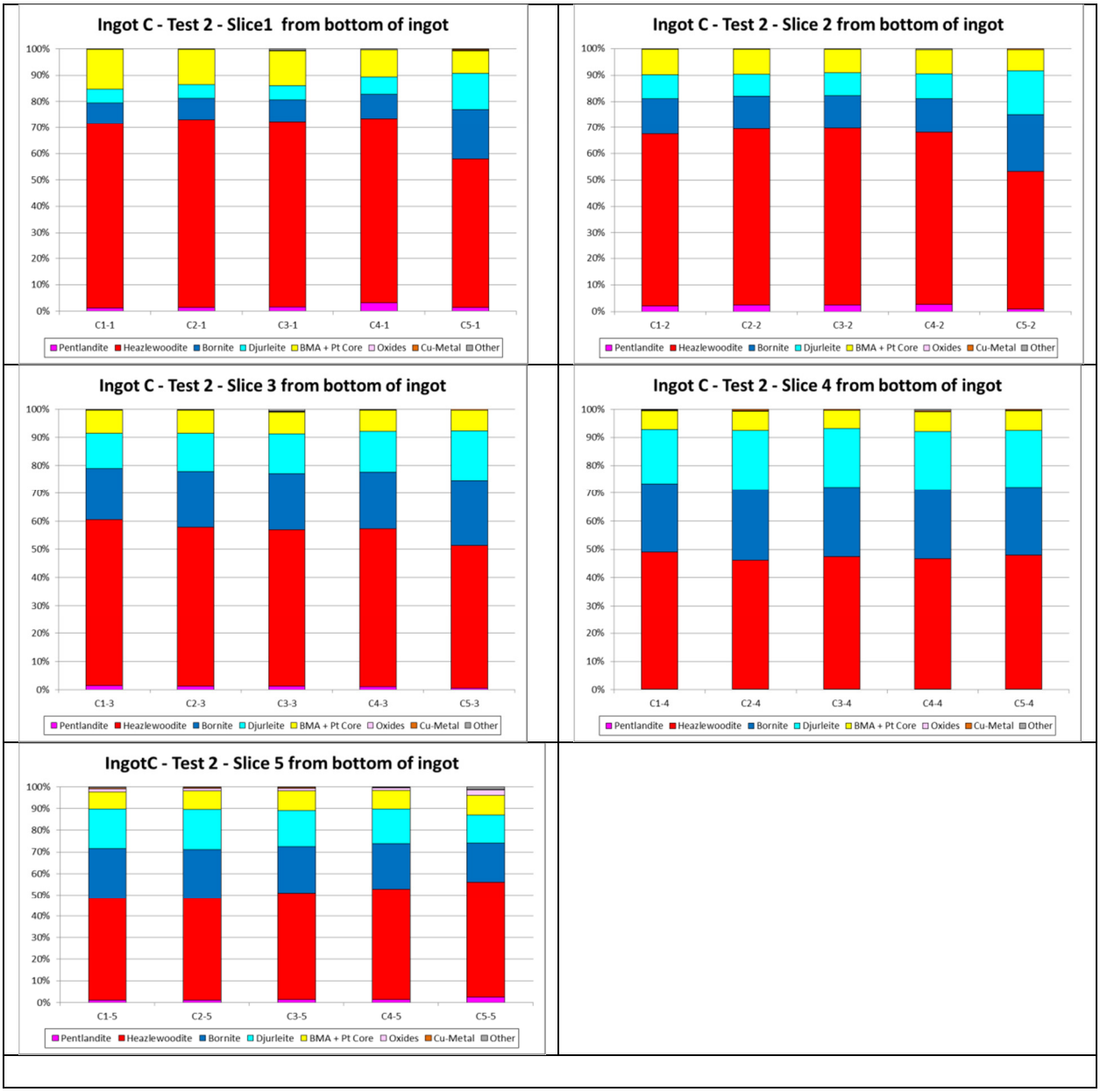

Figure 7.2-3 - Test 3, Ingot A, 15t

7. Appendix 3: FactSage® data

Figure 7.3-1 - Test 1:

Bulk Analysis for Factsage modelling - Sec 2	Pt	Pd	Au	Rh	Ir	Ru	Cu	Fe	Ni	S	Cu,Ni, Co sum
	ppm	ppm	ppm	ppm	ppm	ppm	%	%	%	%	
B1-1 to B3-1, B1-2 to B1-3, B3-1 to B3-3	1265.8	1568.8	151.7	354.8	38.9	459.3	13.0	2.4	59.9	22.8	98.0

Factsage Data - Test 1- Matte Section 2

(Multiplied x10 for 100g - 1Kg)

Equil amount - Mass Fraction (100g)

Temp (K)	Temp (C)	Cp (J/K)	Cp (J/K/kg)	H (J)	H (J/kg)	BLiq(Matte/ Metal)#1	Cu9S5 Digenite#1	Digenite#2	fcc#1	Hazelwood ite Beta-Ni3S2
1323	1050	70.2	702.2	19 668	196 680	100	0	0	0	0
1273	1000	69.4	694.2	16 178	161 782	100	0	0	0	0
1223	950	68.7	686.6	12 726	127 260	100	0	0	0	0
1173	900	67.9	679.4	9 311	93 114	100	0	0	0	0
1123	850	67.7	677.3	5 931	59 313	100	0	0	0	0
1073	800	66.6	666.1	2 584	25 840	100	0	0	0	0
1023	750	66.0	660.0	-731	-7 307	100	0	0	0	0
1000	727	65.7	657.3	-2 217	-22 165	100	0	0	0	0
973	700	78.5	784.5	-4 392	-43 916	98.3	1.6	0.0	0.0	0.0
967	694	78.1	781.3	-4 834	-48 340	98.1	1.9	0.0	0.0	0.0
923	650	126.6	1265.6	-12 061	-120 607	50.6	5.8	0.0	0.0	43.7
903	630	109.4	1093.9	-14 453	-144 530	38.8	6.8	0.0	0.0	54.4
900	627	84.1	841.2	-18 210	-182 100	0.0	8.5	0.0	3.7	87.7
873	600	83.9	839.4	-20 400	-204 000	0.0	9.1	0.0	4.1	86.7
823	550	83.5	834.7	-24 620	-246 200	0.0	10.2	0.0	4.9	84.9
773	500	82.8	828.2	-28 780	-287 800	0.0	11.3	0.0	5.7	83.0
723	450	82.1	820.9	-32 900	-329 000	0.0	12.4	0.0	6.4	81.2
673	400	82.0	820.0	-37 032	-370 320	0.0	13.4	0.0	7.2	79.4

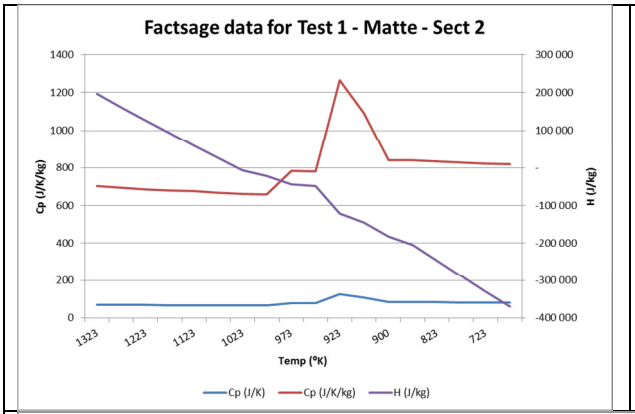

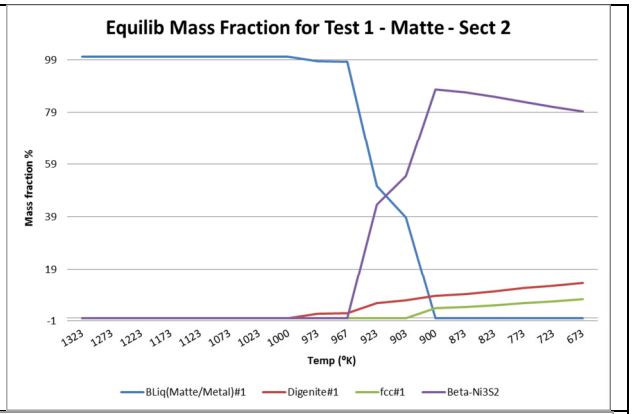

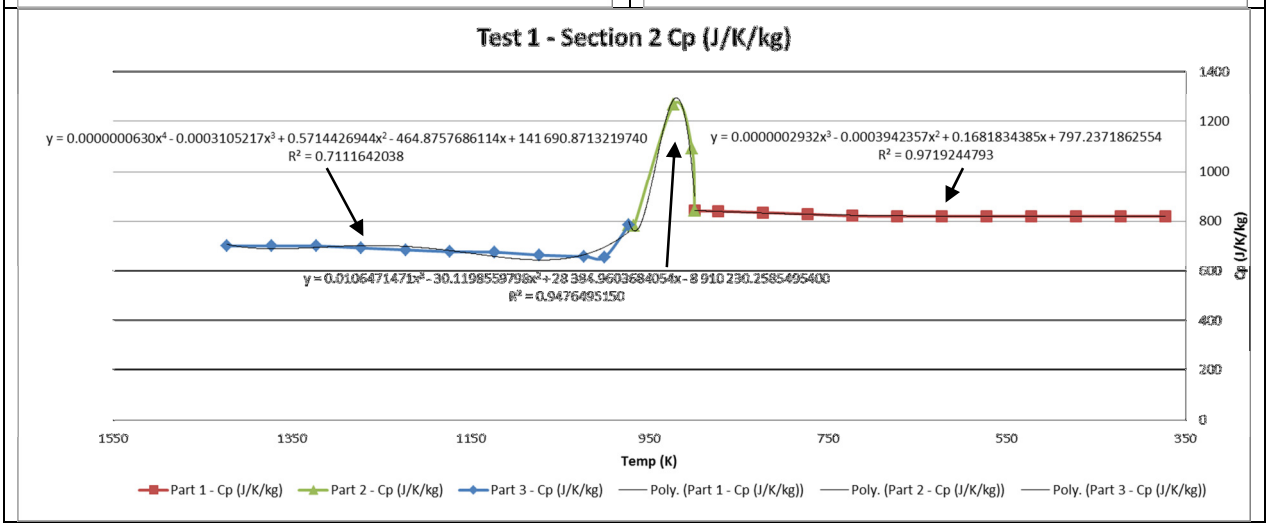

Bulk Analysis for Factsage modelling - Sec 3	Pt	Pd	Au	Rh	Ir	Ru	Cu	Fe	Ni	S	Cu,Ni, Co sum
	ppm	ppm	ppm	ppm	ppm	ppm	%	%	%	%	
B1-4 to B1-5, B2-4 to B2-5, B3-4 to B3-5, B4-1 to B4-5	1411.0	691.8	52.2	185.8	81.1	317.2	22.6	2.9	50.1	23.5	99.1

Factsage Data - Test 1 - Matte Section 3

(Multiplied x10 for 100g - 1Kg)

Equil amount - Mass Fraction (100g)

Temp (K)	Temp (C)	Cp (J/K)	Cp (J/K/kg)	H (J)	H (J/kg)	BLiq(Matte/ Metal)#1	Cu9S5 Digenite#1	Digenite#2	fcc#1	Hazelwood ite Beta-Ni3S2
1323	1050	69.7	696.8	19 846	198 460	100	0.0	0.0	0.0	0.0
1273	1000	68.9	689.2	16 381	163 810	100	0.0	0.0	0.0	0.0
1223	950	68.2	682.2	12 953	129 528	100	0.0	0.0	0.0	0.0
1202	929	67.9	679.4	11 557	115 568	100	0.0	0.0	0.0	0.0
1173	900	89.4	893.9	8 871	88 712	97	2.9	0.0	0.0	0.0
1123	850	84.7	847.2	4 523	45 232	93	7.2	0.0	0.0	0.0
1073	800	81.0	810.1	383	3 831	89	10.7	0.0	0.0	0.0
1023	750	78.0	779.6	-3 589	-35 891	86	13.7	0.0	0.0	0.0
1004	731	76.9	769.4	-5 038	-50 380	85.3	14.7	0.0	0.0	0.0
973	700	164.8	1648.3	-11 854	-118 544	37.2	18.6	0.0	0.0	44.2
923	650	93.1	930.8	-17 782	-177 819	7.6	21.0	0.0	0.0	71.4
906	633	86.2	862.5	-19 332	-193 321	3.5	21.5	0.0	0.0	75.1
905	632	81.3	812.7	-19 682	-196 817	0.0	21.6	0.0	0.3	78.0
873	600	81.0	809.8	-22 298	-222 981	0.0	22.3	0.0	0.8	77.0
823	550	80.4	804.1	-26 333	-263 334	0.0	23.2	0.0	1.5	75.3
773	500	79.7	797.0	-30 337	-303 368	0.0	24.2	0.0	2.2	73.7
723	450	80.1	800.5	-34 304	-343 037	0.0	25.1	0.0	2.8	72.1
673	400	78.2	782.1	-38 254	-382 536	0.0	25.9	0.0	3.5	70.6

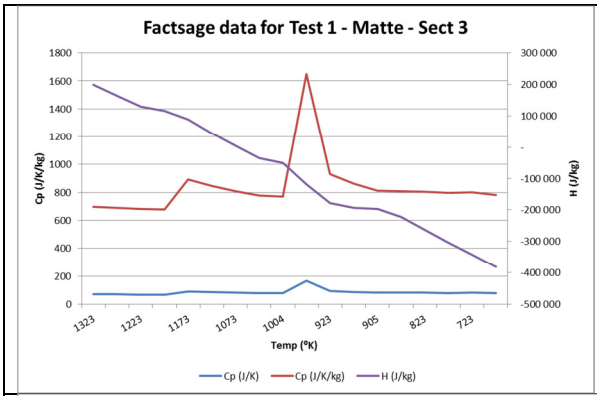

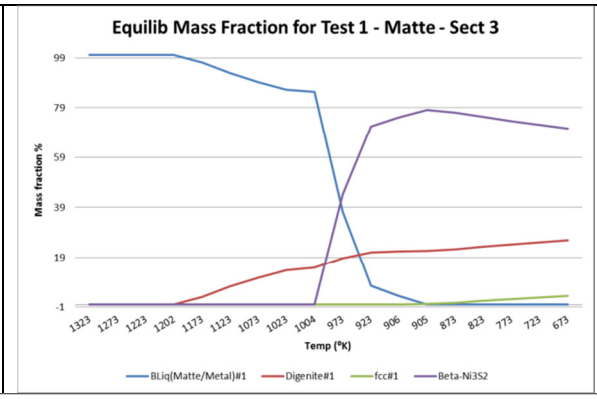

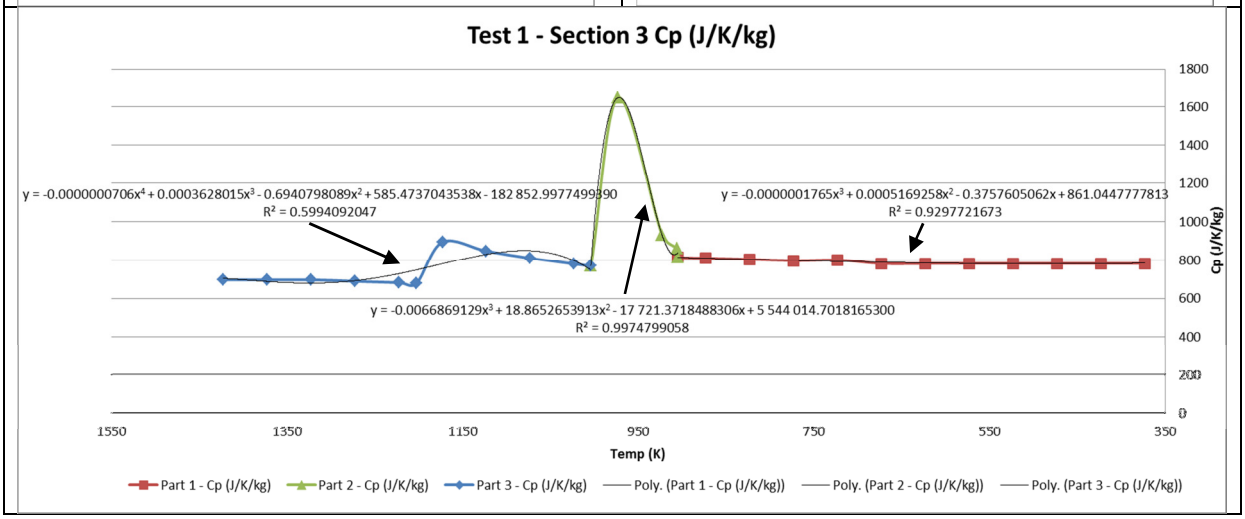

Bulk Analysis for Factsage modelling - Sec 4	Pt	Pd	Au	Rh	Ir	Ru	Cu	Fe	Ni	S	Cu,Ni, Co sum
	ppm	ppm	ppm	ppm	ppm	ppm	%	%	%	%	
B1-6 to B1-8, B2-6 to B2-8, B3-6 to B6-8, B4-6 to B4-8, B5-3 to B5-8	1133.7	568.1	44.0	154.0	65.3	244.2	32.0	4.0	39.4	22.7	98.1

Factsage Data - Test 1 - Matte Section 4

(Multiplied x10 for 100g - 1Kg)

Equil amount - Mass Fraction (100g)

Temp (K)	Temp (C)	Cp (J/K)	Cp (J/K/kg)	H (J)	H (J/kg)	BLiq(Matte/ Metal)#1	BLiq(Matte/ Metal)#2	Cu9S5 Digenite#1	Digenite#2	fcc#1	Hazelwood ite Beta-Ni3S2
1323	1050	82.4	824.1	20 617	206 165	90.4	9.6	0.0	0.0	0.0	0.0
1273	1000	81.2	812.1	16 526	165 259	85.9	14.1	0.0	0.0	0.0	0.0
1223	950	80.0	800.0	12 495	124 952	82.1	17.9	0.0	0.0	0.0	0.0
1213	940	79.8	797.5	11 659	116 586	81.3	18.7	0.0	0.0	0.0	0.0
1201	928	84.8	847.9	9 759	97 590	82.5	0.0	17.5	0.0	0.0	0.0
1173	900	82.3	823.0	7 460	74 598	80.3	0.0	19.7	0.0	0.0	0.0
1123	850	78.7	787.1	3 439	34 386	77.0	0.0	23.0	0.0	0.0	0.0
1075	802	76.1	761.3	-313	-3 135	74.3	0.0	25.7	0.0	0.0	0.0
1073	800	85.2	851.7	-441	-4 414	74.2	0.0	25.5	0.3	0.0	0.0
1023	750	84.4	844.2	-4 685	-46 849	70.7	0.0	21.8	7.5	0.0	0.0
1014	741	84.2	842.2	-5 350	-53 501	70.2	0.0	21.5	8.3	0.0	0.0
1007	734	174.4	1744.3	-8 067	-80 668	49.0	0.0	29.6	0.0	0.0	21.4
973	700	115.3	1153.5	-12 879	-128 789	24.9	0.0	31.6	0.0	0.0	43.5
923	650	84.6	845.7	-17 704	-177 037	9.6	0.0	33.0	0.0	0.0	57.5
921	648	84.1	840.8	-17 850	-178 503	9.3	0.0	33.0	0.0	0.0	57.7
919	646	78.0	779.7	-18 977	-189 771	0.0	0.0	33.4	0.0	1.0	78.0
873	600	77.4	773.5	-22 512	-225 115	0.0	0.0	34.2	0.0	1.5	64.3
823	550	76.6	766.3	-26 361	-263 611	0.0	0.0	35.1	0.0	2.0	62.8
773	500	75.9	758.8	-30 174	-301 736	0.0	0.0	36.0	0.0	0.0	61.4
723	450	75.5	755.2	-33 971	-339 706	0.0	0.0	36.8	0.0	3.1	60.1
673	400	74.2	741.5	-37 713	-377 126	0.0	0.0	37.5	0.0	3.7	58.8

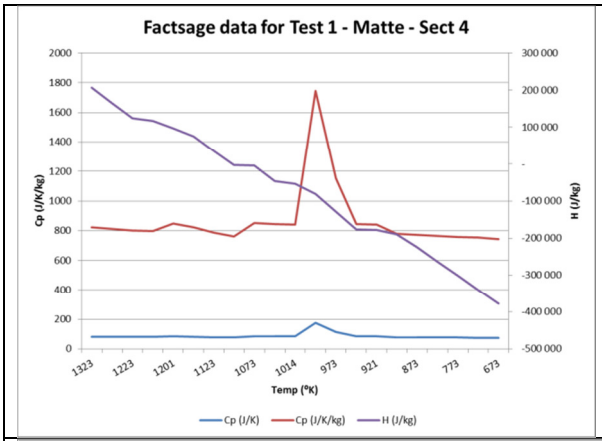

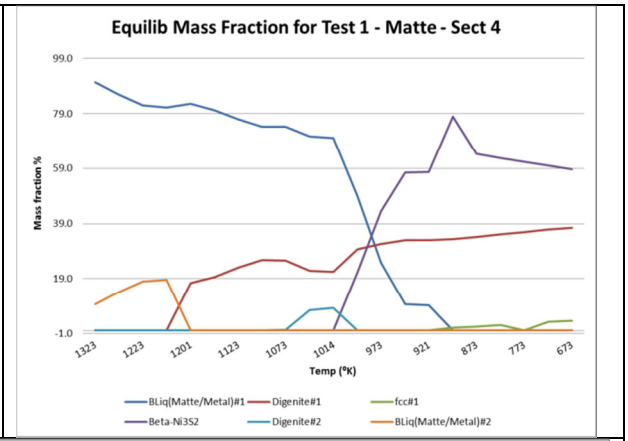

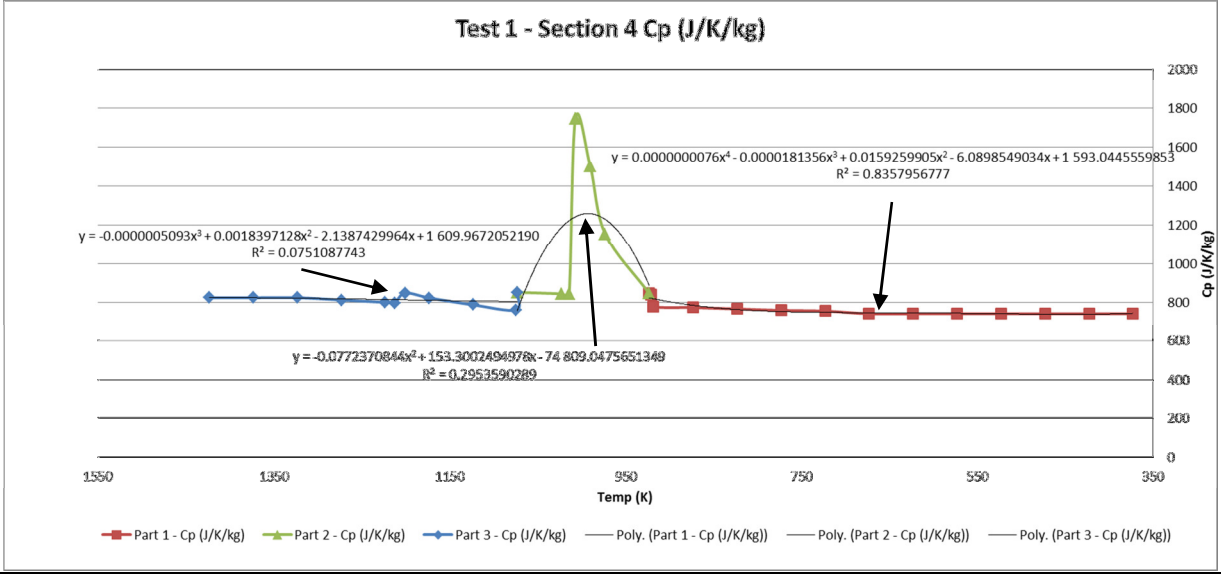

Figure 7.3-2 - Test 2

	Pt	Pd	Au	Rh	Ir	Ru	Cu	Fe	Ni	S	sum
Bulk Analysis for Factsage modelling -Sec 2	ppm	ppm	ppm	ppm	ppm	ppm	%	%	%	%	
C1-1, C2-1, C3-1, C4-1	1491.9	1082.6	108.5	318.1	58.6	493.6	11.8	3.1	58.6	23.3	96.8

Factsage Data - Test 2- Matte Section 2

(Multiplied x10 for 100g - 1Kg)

Equil amount - Mass Fraction (100g)

Temp (K)	Temp (C)	Cp (J/K)	Cp (J/K/kg)	H (J)	H (J/kg)	BLiq(Matte/ Metal)#1	Cu9S5 Digenite#1	Digenite#2	fcc#1	Hazelwood ite Beta-Ni3S2
1323	1050	70.9	708.8	17 964	179 635	100	0	0	0	0
1273	1000	70.1	700.7	14 440	144 398	100	0	0	0	0
1223	950	69.3	693.1	10 955	109 554	100	0	0	0	0
1173	900	68.6	685.8	7 508	75 082	100	0	0	0	0
1123	850	67.9	678.9	4 096	40 964	100	0	0	0	0
1073	800	67.2	672.3	718	7 185	100	0	0	0	0
1023	750	66.6	666.0	-2 627	-26 272	100	0	0	0	0
998	725	66.3	662.9	-4 291	-42 914	100	0	0	0	0
989	716	172.2	1721.8	-5 931	-59 314	88.8	0.0	0.0	0.0	11.2
973	700	199.6	1996.1	-9 522	-95 221	62.7	2.1	0.0	0.0	35.2
923	650	107.9	1078.6	-16 637	-166 367	20.8	5.6	0.0	0.0	73.6
905	632	97.5	975.4	-18 476	-184 755	14.3	6.2	0.0	0.0	79.5
904	631	85.8	858.1	-19 892	-198 918	0.0	6.9	0.0	1.4	91.7
873	600	85.6	855.7	-22 521	-225 213	0.0	7.6	0.0	1.9	90.5
823	550	85.0	850.3	-26 787	-267 871	0.0	8.8	0.0	2.7	88.5
773	500	84.3	842.9	-31 021	-310 207	0.0	10.0	0.0	3.5	86.6
723	450	83.5	834.9	-35 215	-352 145	0.0	11.0	0.0	4.3	84.7
673	400	82.8	827.8	-39 401	-394 006	0.0	12.1	0.0	5.1	82.8

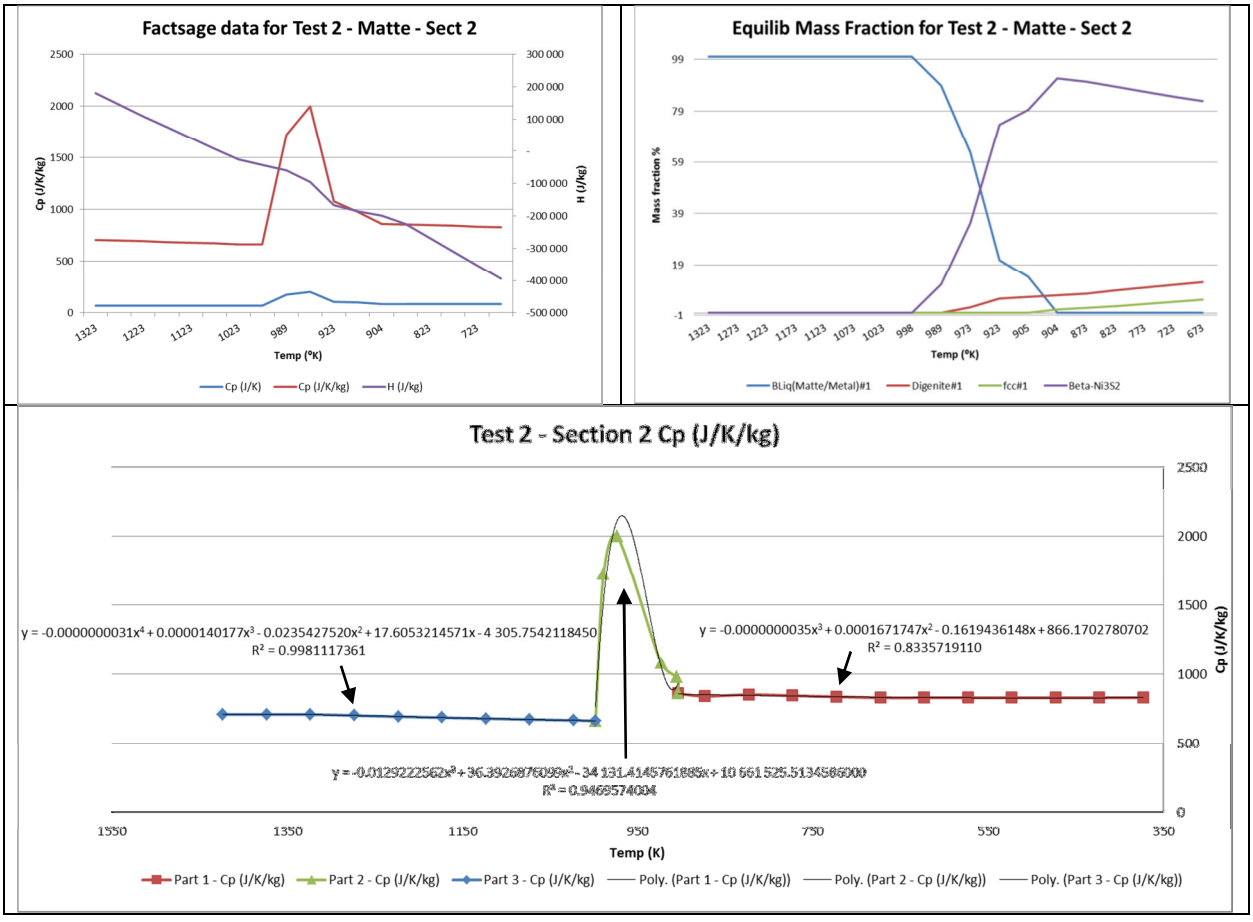

Bulk Analysis for Factsage modelling -Sec 3	Pt	Pd	Au	Rh	Ir	Ru	Cu	Fe	Ni	S	sum
	ppm	ppm	ppm	ppm	ppm	ppm	%	%	%	%	
C1-2 to C1-3, C2-2 to C2-3, C3-2 to C3-3, C4-2 to C4-3	1619.6	739.1	61.6	233.5	75.0	402.6	21.5	3.5	49.3	22.7	97.0

Factsage Data - Test 2 - Matte Section 3

(Multiplied x10 for 100g - 1Kg)

						Equil amount - Mass Fraction (100g)					
								Cu9S5			Hazelwood ite
Temp (K)	Temp (C)	Cp (J/K)	Cp (J/K/kg)	H (J)	H (J/kg)	BLiq(Matte/ Metal)#1		Digenite#1	Digenite#2	fcc#1	Beta-Ni3S2
1323	1050	69.6	696.4	20 685	206 852	100		0.0		0.0	0.0
1273	1000	68.9	688.9	17 222	172 221	100		0.0		0.0	0.0
1223	950	68.2	681.8	13 796	137 956	100		0.0		0.0	0.0
1195	922	67.8	678.0	11 903	119 032	100		0.0		0.0	0.0
1173	900	88.8	887.7	9 910	99 097	98		2.1		0.0	0.0
1123	850	84.3	843.0	5 587	55 875	94		6.3		0.0	0.0
1073	800	80.7	807.4	1 464	14 642	90		9.8		0.0	0.0
1023	750	77.8	778.0	-2 498	-24 976	87		12.8		0.0	0.0
1001	728	76.6	766.4	-4 203	-42 027	86.1		13.9		0.0	0.0
973	700	156.7	1566.6	-9 316	-93 156	55.7		16.5		0.0	27.8
923	650	101.0	1010.2	-15 488	-154 883	25.8		19.0		0.0	55.2
912	639	95.7	957.1	-16 558	-165 577	22.2		19.4		0.0	58.4
908	635	81.4	813.7	-18 946	-189 456	0.0		20.4		2.2	77.3
873	600	81.0	810.2	-21 825	-218 245	0.0		21.2		2.7	76.1
823	550	80.4	804.1	-25 861	-258 609	0.0		22.2		3.4	74.4
773	500	79.7	796.9	-29 864	-298 639	0.0		23.2		4.0	72.8
723	450	80.1	801.1	-33 846	-338 456	0.0		24.1		4.7	71.2
673	400	78.2	781.7	-37 798	-377 984	0.0		25.0		5.3	69.6

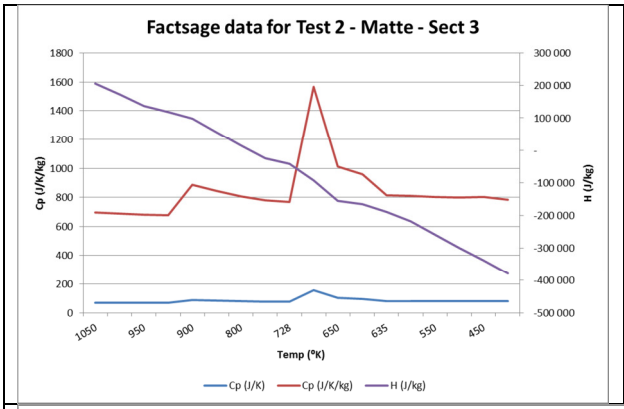

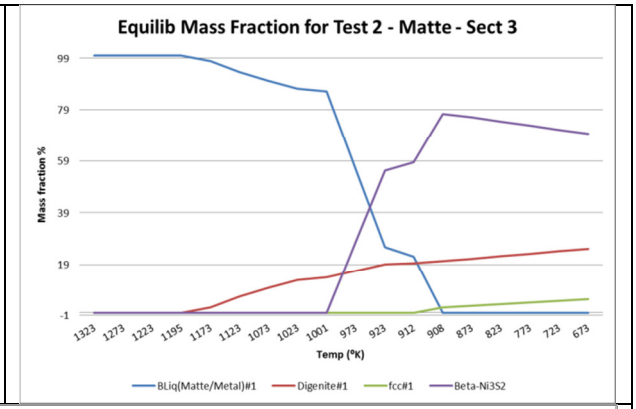

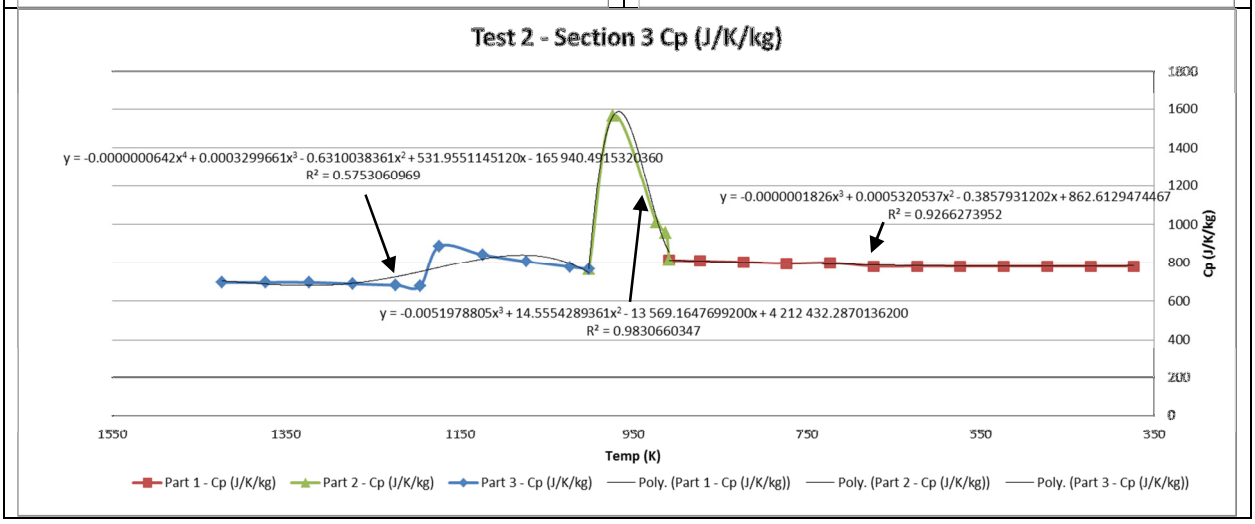

Bulk Analysis for Factsage modelling -Sec 4	Pt	Pd	Au	Rh	Ir	Ru	Cu	Fe	Ni	S	sum
	ppm	ppm	ppm	ppm	ppm	ppm	%	%	%	%	
C1-4 to C1-5, C2-4 to C2-5, C3-4 to C3-5, C4-4 to C4-5, C5-1 to C5-5	2124.2	624.3	50.2	199.9	144.4	337.2	30.8	4.2	39.3	22.6	96.9

Factsage Data - Test 2 - Matte Section 4

(Multiplied x10 for 100g - 1Kg)

Equil amount - Mass Fraction (100g)

Temp (K)	Temp (C)	Cp (J/K)	Cp (J/K/kg)	H (J)	H (J/kg)	BLiq(Matte/Metal)#1	BLiq(Matte/Metal)#2	Cu9S5 Digenite#1	Digenite#2	fcc#1	Hazelwoodite Beta-Ni3S2
1323	1050	82.4	824.1	20 617	206 165	90.4	9.6	0.0	0.0	0.0	0.0
1273	1000	81.2	812.1	16 526	165 259	85.9	14.1	0.0	0.0	0.0	0.0
1223	950	80.0	800.0	12 495	124 952	82.1	17.9	0.0	0.0	0.0	0.0
1213	940	79.8	797.5	11 659	116 586	81.3	18.7	0.0	0.0	0.0	0.0
1201	928	84.8	847.9	9 759	97 590	82.5	0.0	17.5	0.0	0.0	0.0
1173	900	82.3	823.0	7 460	74 598	80.3	0.0	19.7	0.0	0.0	0.0
1123	850	78.7	787.1	3 439	34 386	77.0	0.0	23.0	0.0	0.0	0.0
1075	802	76.1	761.3	-313	-3 135	74.3	0.0	25.7	0.0	0.0	0.0
1073	800	85.2	851.7	-441	-4 414	74.2	0.0	25.5	0.3	0.0	0.0
1023	750	84.4	844.2	-4 685	-46 849	70.7	0.0	21.8	7.5	0.0	0.0
1015	742	84.2	842.2	-5 350	-53 501	70.2	0.0	21.5	8.3	0.0	0.0
1007	734	174.4	1744.3	-8 067	-80 668	49.0	0.0	29.6	0.0	0.0	21.4
973	700	115.3	1153.5	-12 879	-128 789	43.5	0.0	31.6	0.0	0.0	24.9
923	650	84.6	845.7	-17 704	-177 037	9.6	0.0	33.0	0.0	0.0	57.5
921	648	84.1	840.8	-17 850	-178 503	9.3	0.0	33.0	0.0	0.0	57.7
919	646	78.0	779.7	-18 977	-189 771	0.0	0.0	33.4	0.0	1.0	65.6
873	600	77.4	773.5	-22 512	-225 115	0.0	0.0	34.2	0.0	1.5	64.3
823	550	76.6	766.3	-26 361	-263 611	0.0	0.0	35.1	0.0	2.0	62.8
773	500	75.9	758.8	-30 174	-301 736	0.0	0.0	36.0	0.0	2.6	61.4
723	450	75.5	755.2	-33 971	-339 706	0.0	0.0	36.8	0.0	3.1	60.1
673	400	74.2	741.5	-37 713	-377 126	0.0	0.0	37.5	0.0	3.7	58.8

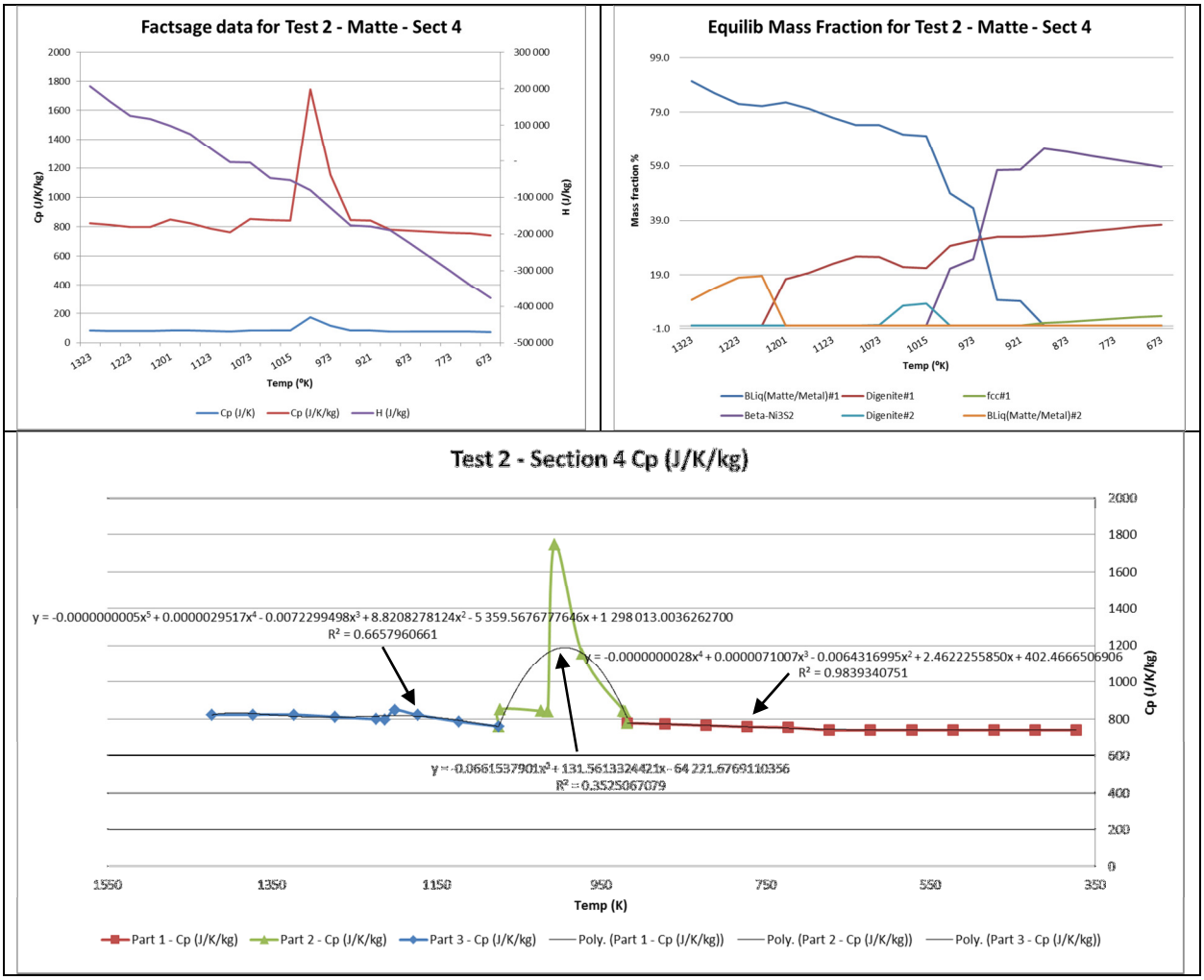

Figure 7.3-3 - Test 3

Bulk Analysis for Factsage modelling- Sec 1	Pt	Pd	Au	Rh	Ir	Ru	Cu	Fe	Ni	S	sum
	ppm	ppm	ppm	ppm	ppm	ppm	%	%	%	%	
A1-1 to A1-3, A2-1 to A2-3, A3-1 to A3-3	478	1302	138	294	4	361	11.6	1.6	61.6	21.9	96.7

Factsage Data - Test 3 - Matte Section 1

(Multiplied x10 for 100g - 1Kg)

Equil amount - Mass Fraction (100g)

Temp (K)	Temp (C)	Cp (J/K)	Cp (J/K/kg)	H (J)	H (J/kg)	BLiq(Matte/ Metal)#1		Cu9S5 Digenite#1	Digenite#2	fcc#1	Hazelwood ite Beta-Ni3S2
1323	1050	69.9	699.3	20 508	205 078	100		0		0	0
1273	1000	69.1	691.1	17 032	170 320	100		0		0	0
1223	950	68.3	683.4	13 596	135 959	100		0		0	0
1173	900	67.6	676.1	10 197	101 972	100		0		0	0
1123	850	66.9	669.2	6 834	68 339	100		0		0	0
1073	800	66.3	662.6	3 505	35 046	100		0		0	0
1023	750	65.6	656.3	207	2 073	100		0		0	0
973	700	65.0	650.4	-3 059	-30 593	100		0		0	0
960	**687**	64.9	648.9	-3 904	-39 038	100		0		0	0
941	**668**	77.0	769.7	-5 375	-53 752	99.0		1.0		0	0
923	650	148.5	1485.5	-8 361	-83 613	77.5		2.7		0.0	20
898	625	119.4	1193.7	-11 680	-116 796	57.3		4.4		0.0	38.3
895	**622**	83.6	836.0	-16 965	-169 654	0		6.9		5.5	87.7
873	600	83.5	834.9	-18 799	-187 988	0		7.3		5.7	86.9
823	550	83.1	831.0	-22 964	-229 640	0		8.4		6.6	85.0
773	500	82.5	825.3	-27 106	-271 056	0		9.5		7.4	83.1
723	450	81.8	818.1	-31 214	-312 143	0		10.5		8.2	81.3
673	400	74.9	749.3	-32 863	-328 627	0		11.5		9.0	79.5

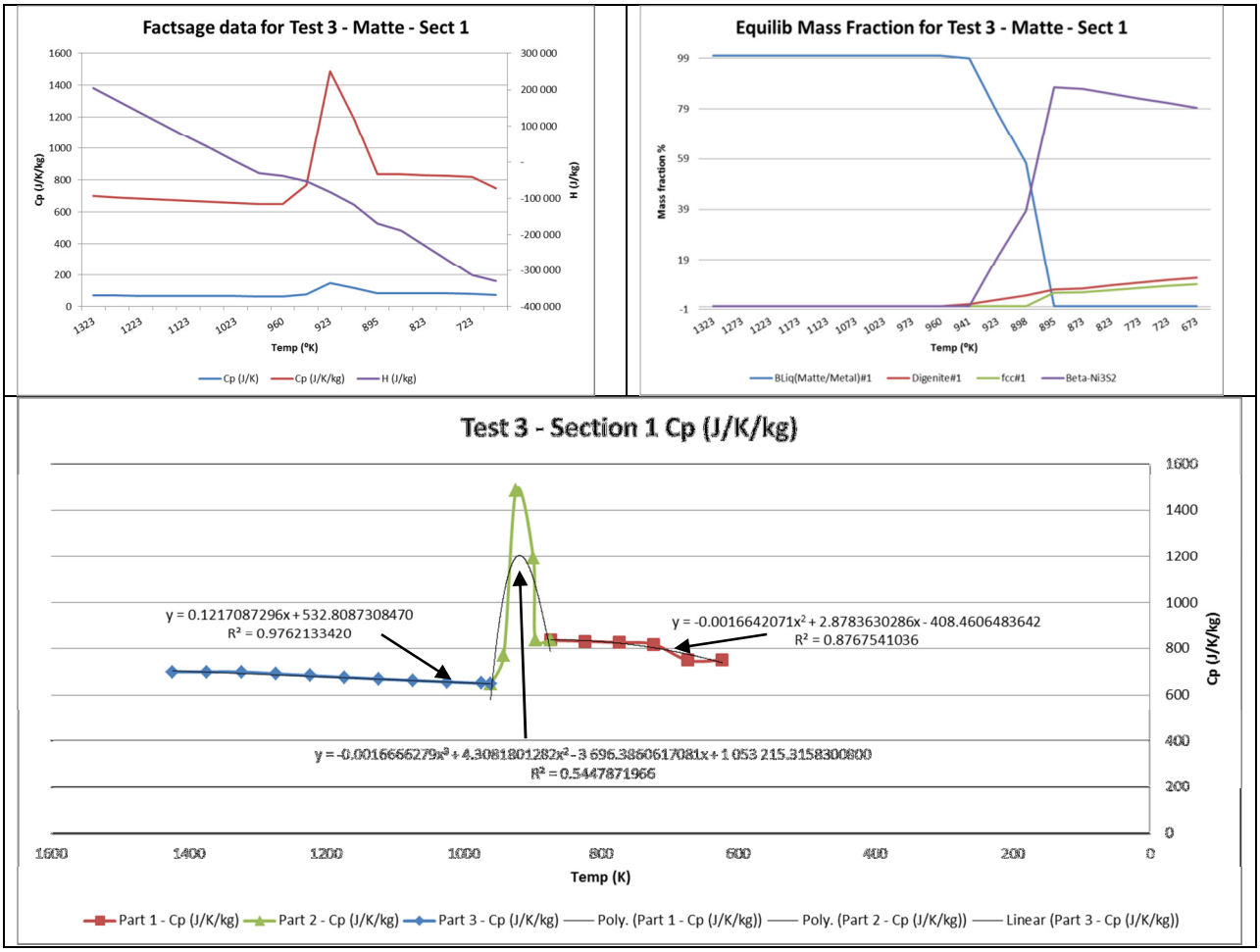

Bulk Analysis for Factsage modelling- Sec 2	Pt	Pd	Au	Rh	Ir	Ru	Cu	Fe	Ni	S	sum
	ppm	ppm	ppm	ppm	ppm	ppm	%	%	%	%	
A1-4 to A1-5, A2-4 to A2-5, A3-4 to A3-5, A4-1 to A4-5	1600	735	63	190	87	280	24.0	2.1	49.5	22.3	97.8

	Factsage Data - Test 3 - Matte Section 2										
	(Multiplied x10 for 100g - 1Kg)					Equil amount - Mass Fraction (100g)					
								Cu9S5			Hazelwood ite
Temp (K)	Temp (C)	Cp (J/K)	Cp (J/K/kg)	H (J)	H (J/kg)	BLiq(Matte/ Metal)#1		Digenite#1	Digenite#2	fcc#1	Beta-Ni3S2
1323	1050	68.9	689.0	21 850	218 496	100.0		0.0		0.0	0.0
1273	1000	68.2	681.7	18 422	184 220	100.0		0.0		0.0	0.0
1230	957	67.6	675.8	15 517	155 173	100.0		0.0		0.0	0.0
1223	950	93.3	932.9	14 843	148 425	99.2		0.8		0.0	0.0
1173	900	87.6	876.3	10 326	103 259	94.3		5.7		0.0	0.0
1123	850	83.2	832.4	6 058	60 580	90.3		9.7		0.0	0.0
1073	800	79.7	796.9	1 987	19 873	86.8		13.2		0.0	0.0
1023	750	76.7	767.2	-1 921	-19 213	84.0		16.0		0.0	0.0
973	700	74.2	741.8	-5 693	-56 927	81.5		18.5		0.0	0.0
969	696	74.0	740.0	-5 971	-59 710	81.3		18.7		0.0	0.0
923	650	113.0	1130.4	-12 662	-126 624	40.3		22.0		0.0	37.7
903	630	99.4	993.6	-14 772	-147 720	31.1		22.8		0.0	46.2
900	627	79.1	791.2	-17 821	-178 210	0.0		24.1		3.0	72.9
873	600	78.9	789.2	-19 951	-199 510	0.0		24.6		3.3	72.0
823	550	78.4	784.5	-23 886	-238 860	0.0		25.5		3.9	70.5
773	500	78.9	788.5	-27 794	-277 940	0.0		26.3		4.6	69.0
723	450	77.2	772.1	-31 670	-316 700	0.0		27.2		5.3	67.5
673	400	77.0	770.3	-35 550	-355 499	0.0		28.1		5.9	66.0

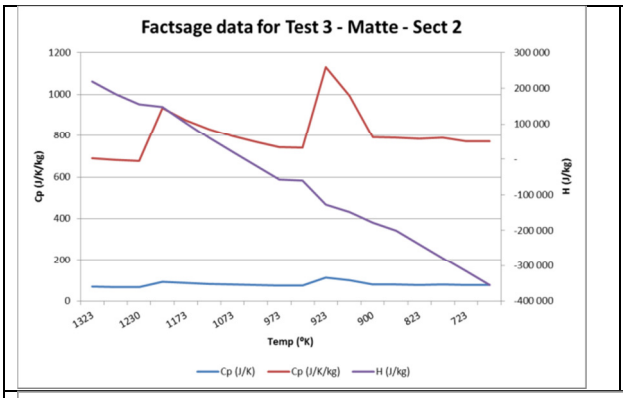

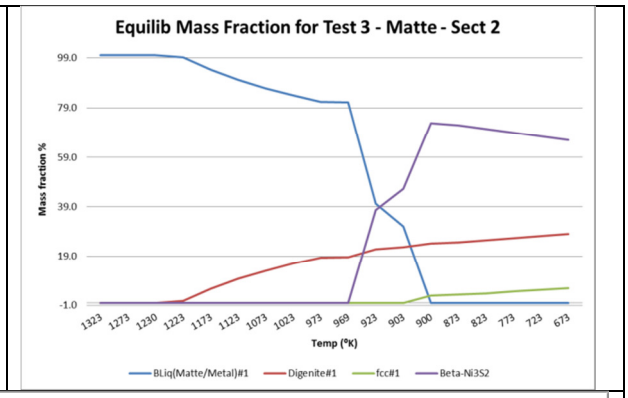

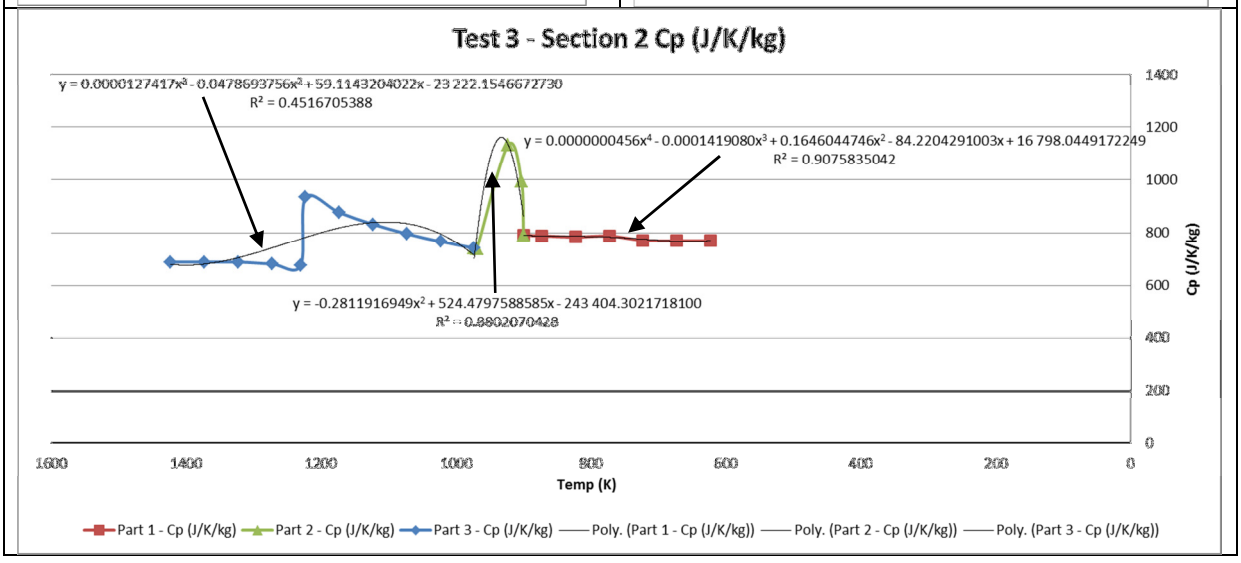

Bulk Analysis for Factsage modelling- Sec 3	Pt	Pd	Au	Rh	Ir	Ru	Cu	Fe	Ni	S	sum
	ppm	ppm	ppm	ppm	ppm	ppm	%	%	%	%	
A1-6, A2-6, A3-6, A4-6, A5-1 to A5-6	1382	797	64	208	67	303	33.8	2.2	40.6	22.0	98.6

Factsage Data - Test 3 - Matte Section 3

(Multiplied x10 for 100g - 1Kg)

Equil amount - Mass Fraction (100g)

Temp (K)	Temp (C)	Cp (J/K)	Cp (J/K/kg)	H (J)	H (J/kg)	BLiq(Matte/Metal)#1	BLiq(Matte/Metal)#2	Cu9S5 Digenite#1	Digenite#2	fcc#1	Hazelwood ite Beta-Ni3S2
1323	1050	81.5	815.1	2 200	22 001	87.9	12.1	0.0		0.0	0.0
1273	1000	80.3	803.0	17 955	179 549	83.8	16.2	0.0		0.0	0.0
1262	989	80.0	800.2	17 066	170 658	83.0	17.0	0.0		0.0	0.0
1256	983	89.5	894.9	15 475	154 754	84.0	0.0	16.0		0.0	0.0
1223	950	85.7	856.7	12 575	125 750	80.9	0.0	19.1		0.0	0.0
1173	900	81.2	811.7	8 409	84 090	76.9	0.0	23.1		0.0	0.0
1123	850	77.7	776.9	4 440	44 403	73.7	0.0	26.3		0.0	0.0
1073	800	74.9	748.7	628	6 281	71.0	0.0	29.0		0.0	0.0
1023	750	72.5	725.1	-3 055	-30 552	68.7	0.0	31.3		0.0	0.0
976	703	70.6	705.6	-6 449	-64 490	66.9	0.0	33.1		0.0	0.0
973	700	152.5	1524.5	-6 842	-68 416	64.7	0.0	33.3		0.0	2.0
923	650	100.1	1000.9	-12 982	-129 821	33.5	0.0	35.8		0.0	30.6
908	635	92.5	924.6	-14 407	-144 065	28.2	0.0	36.3		0.0	35.5
903	630	74.1	740.8	-17 380	-173 796	0.0	0.0	37.5		2.8	59.7
873	600	74.7	747.0	-19 657	-196 569	0.0	0.0	38.0		3.1	58.9
823	550	74.2	741.8	-23 379	-233 790	0.0	0.0	38.7		3.6	57.7
773	500	73.6	735.9	-27 073	-270 734	0.0	0.0	39.4		4.2	56.4
723	450	73.1	730.6	-30 738	-307 380	0.0	0.0	40.1		4.7	55.2
673	400	72.6	726.3	-34 411	-344 109	0.0	0.0	40.8		5.2	54.0

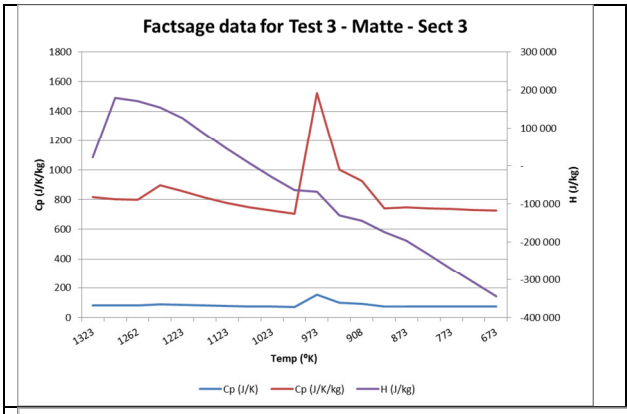

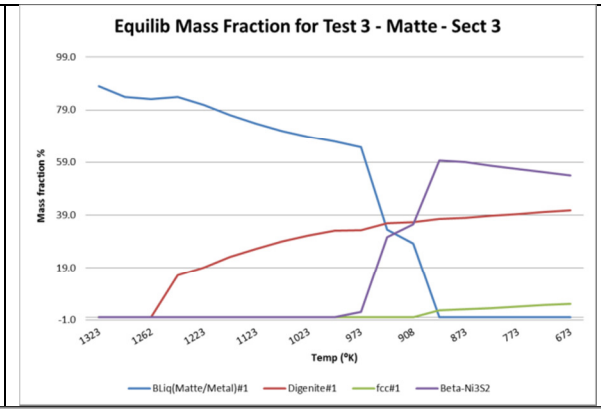

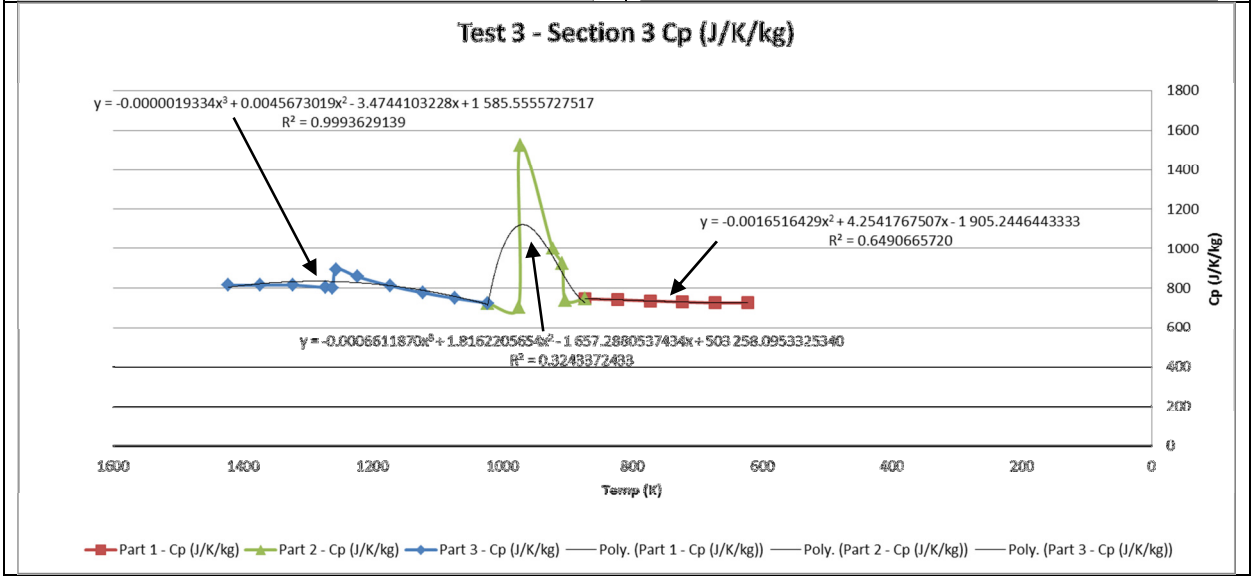

Bulk Analysis for Factsage modelling- Sec 4	Pt	Pd	Au	Rh	Ir	Ru	Cu	Fe	Ni	S	sum
	ppm	ppm	ppm	ppm	ppm	ppm	%	%	%	%	
A1-7 to A1-8, A2-7 to A2-8, A3-7 to A3-8, A4-7 to A4-8, A5-7 to A5-8, A6-5 to A6-8	1376	603	49	160	84	229	39.3	4.2	32.1	20.8	96.4

Factsage Data - Test 3 - Matte Section 4

(Multiplied x10 for 100g - 1Kg)

Equil amount - Mass Fraction (100g)

Temp (K)	Temp (C)	Cp (J/K)	Cp (J/K/kg)	H (J)	H (J/kg)	BLiq(Matte/Metal)#1	BLiq(Matte/Metal)#2	Cu9S5 Digenite#1	Digenite#2	fcc#1	Hazelwood ite Beta-Ni3S2
1323	1050	79.3	793.1	22 473	224 725	71.9	28.1	0.0		0.0	0.0
1273	1000	78.1	781.2	18 536	185 364	68.9	31.1	0.0		0.0	0.0
1271	998	78.1	780.7	18 381	183 810	68.8	31.2	0.0		0.0	0.0
1262	989	81.5	815.4	15 891	158 910	70.2	0.0	29.8		0.0	0.0
1223	950	78.3	782.5	12 771	127 711	67.4	0.0	32.6		0.0	0.0
1173	900	75.1	750.5	8 942	89 418	64.4	0.0	35.6		0.0	0.0
1123	850	72.7	726.8	5 251	52 511	61.9	0.0	38.1		0.0	0.0
1073	800	70.9	709.4	1 662	16 625	59.9	0.0	40.1		0.0	0.0
1070	797	70.8	708.5	1 430	14 303	59.8	0.0	40.2		0.0	0.0
1023	750	79.3	792.7	-2 300	-22 997	57.3	0.0	36.0	6.7	0.0	0.0
941	667.9	76.6	766.2	-8 708	-87 081	53.3	0.0	33.8	12.8	0.0	0.0
940	666.6	212.2	2121.7	-11 629	-116 293	0.0	0.0	44.4	0.0	2.7	26.9
924	651	72.7	727.3	-41 871	-418 714	0.0	0.0	45.7	0.0	5.6	48.7
923	650	72.7	727.1	-15 599	-155 991	0.0	0.0	45.7	0.0	5.6	48.7
873	600	71.9	719.1	-19 214	-192 140	0.0	0.0	46.4	0.0	6.0	47.6
823	550	71.2	712.0	-22 791	-227 913	0.0	0.0	47.1	0.0	6.4	46.5
773	500	70.7	707.2	-26 337	-263 374	0.0	0.0	47.8	0.0	6.8	45.4
723	450	70.7	706.6	-29 913	-299 130	0.0	0.0	48.5	0.0	7.2	44.3
673	400	69.1	691.0	-33 406	-334 057	0.0	0.0	49.1	0.0	7.5	43.3

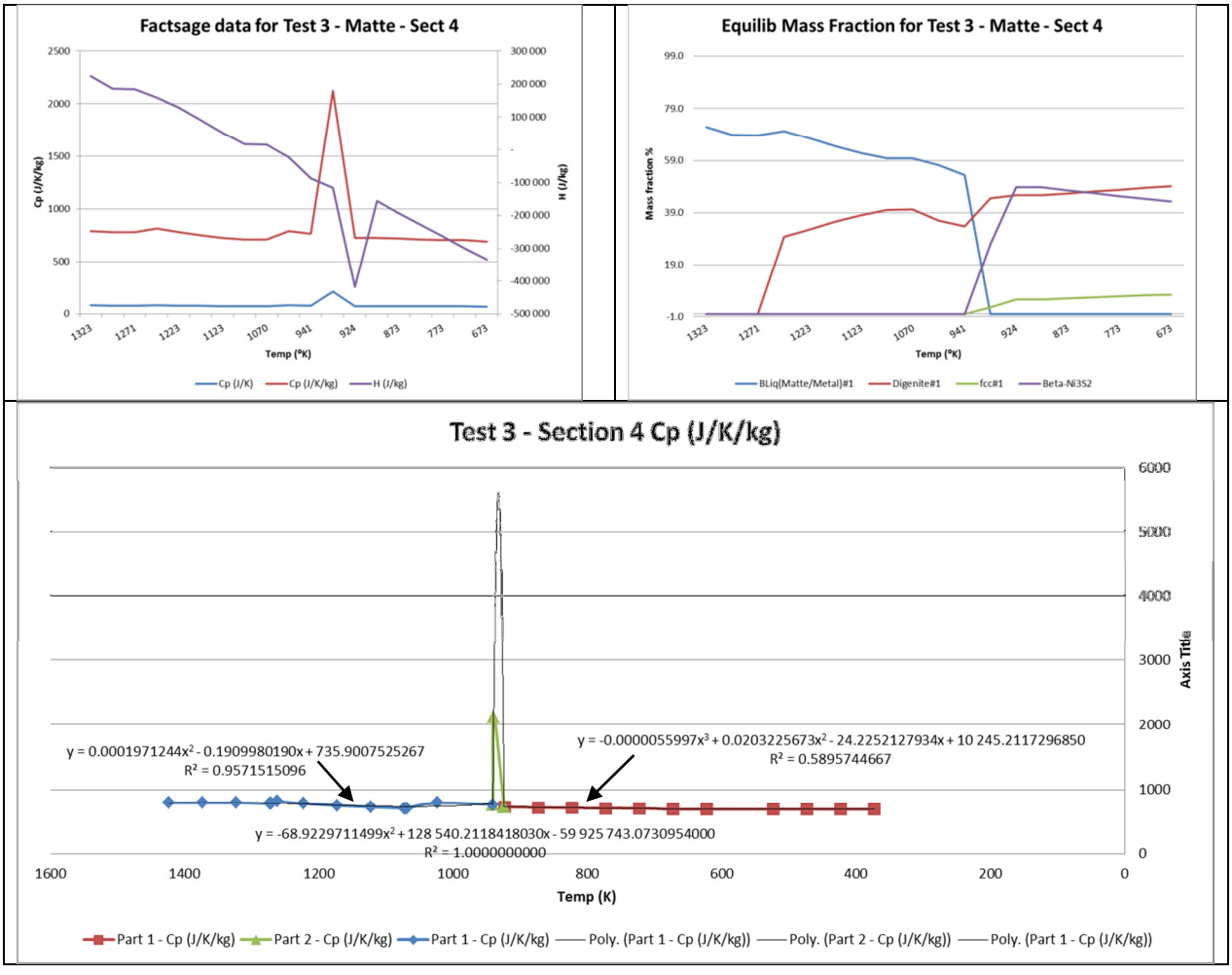

7. Appendix 4: Boundary conditions and material properties for CFD modelling

7.4-1: Table 1 Initial Temperatures	°C	K
Bulk temp of surroundings	27	300
Inner Refractory	100*	373
WCM	1050*	1323
* Initial temperatures used from actual measurements for each test		

7.4-2: Table 2 : Physical Properties of Materials

	Density kg/m^3	Specific heat Cp j/kg-k	Thermal Conductivity w/m-k	Viscosity kg/m-s	External Emissivity	Internal Emissivity	Heat transfer Coefficient (w/m2-k)	Wall Thickness (m)
Air	1.225	1006.46	0.0242	0.000017894				
Solids								
***Low density structural concrete	670	900	0.21					
Inner Refractory	2225	880	PWL					
Outer Refractory	2220	880	PWL					
WCM Sect 1	5695	PWP	Table 7.4-4					
WCM Sect 2	5695	PWP	Table 7.4-4					
WCM Sect 3	5695	PWP	Table 7.4-4					
WCM Sect 4	5695	PWP	Table 7.4-4					
Steel Plate Cover	8030	502	16.27		0.3	0.96	12	0.05

** PWP or PWL ~ Piece wise linear or polynomial functions calculated for the Cp curve of a given composition matte over the range of cooling temperatures.
***Hollman p654

7.4-3: Table 3 Refractory Thermal Conductivity

Temp (°C)	Temp (K)	Inner Refractory (W/mK)	Outer Refractory (W/mK)
100	373	0.49	0.49
200	473	0.57	0.57
300	573	0.66	0.66
400	673	0.74	0.74
500	773	0.82	0.82
600	873	0.9	0.9
700	973	0.98	0.98
800	1073	1.05	1.0
900	1173	1.05	1.0
1000	1273	1.05	1.0

** Source – Vereeniging Refractories A5 brick (Values below 400°C extrapolated)

7.4-4: Table 4 : Ingot Thermal Conductivities			
Ingot Sections	Test 1: Thermal Conductivity: W/m-k	Test 2: Thermal Conductivity: W/m-k	Test 3: Thermal Conductivity: W/m-k
Section 1			85.8
Section 2	87.9	84.3	114.0
Section 3	109.0	107.0	136.4
Section 4	131.3	128.6	151.4
** Thermal conductivities calculated based on the molar fractions calculated from the chemical analysis of elements (Cu, Ni, Fe and S)			

7.4-5: Table 5 : Approximate thermocouple positions and point monitor positions in ingot and refractory						
	Smaller Mould - Test 1 & 2			Larger Mould - Test 3		
Thermocouple Position (m)	X plane	Y Plane	Z Plane	X plane	Y Plane	Z Plane
Zero Position - Top centre of mould	0	0	0	0	0	0
A	0	0	-0.970	0	0	-1.000
B	0	0	-0.770	0	0	-0.800
C	0	0	-0.570	0	0	-0.600
D	0	0	-0.270	0	0	-0.300
E	0	0	-0.210	0	0	-0.208
F	0	0	0.300	0	0	0.300
G	0.739	0	-0.970	0.860	0	-1.000
H	0.739	0	-0.770	0.860	0	-0.800
I	0.739	0	-0.570	0.860	0	-0.600
J	0.739	0	-0.270	0.860	0	-0.300
K	0.864	0	-0.96	0.991	0	-0.950
L	0.989	0	-0.92	1.155	0	-0.950

7. Appendix 5: Data correlations

Figure 7.5-1 - Test 1 – Ingot B, 10t

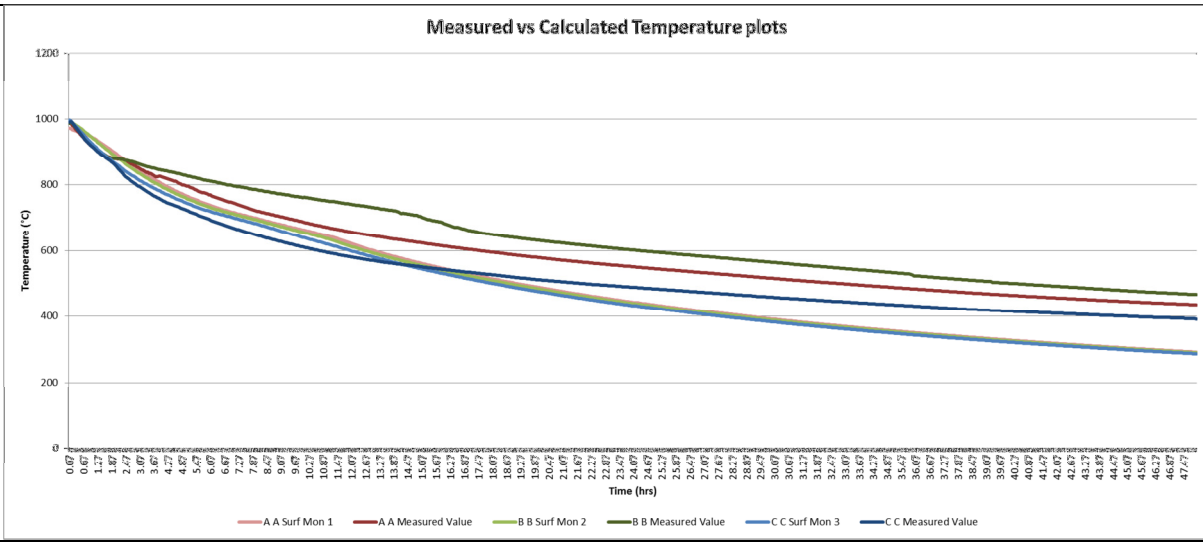

Fig 7.5-1.1 : Temperature plots for thermocouples A to C for measured and modelled values

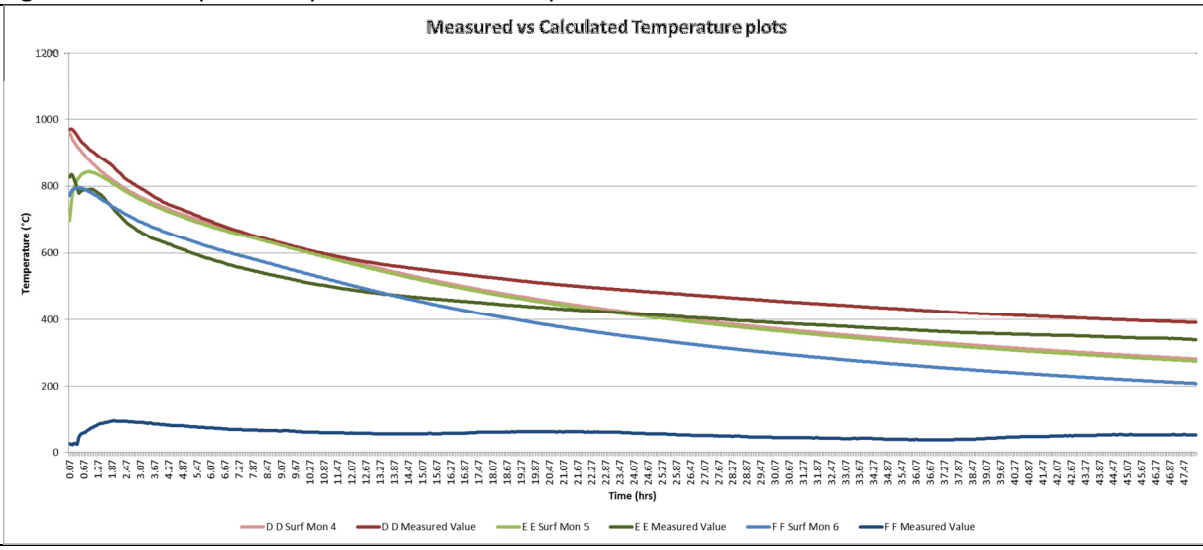

Fig 7.5-1.2 : Temperature plots for thermocouples D to F for measured and modelled values

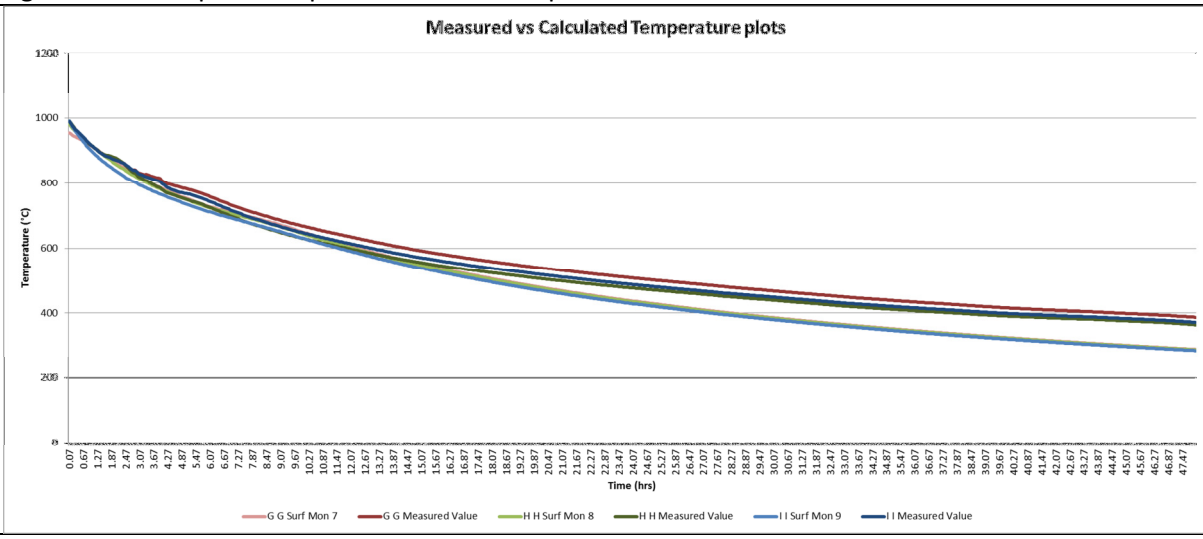

Fig 7.5-1.3 : Temperature plots for thermocouples G to I for measured and modelled values

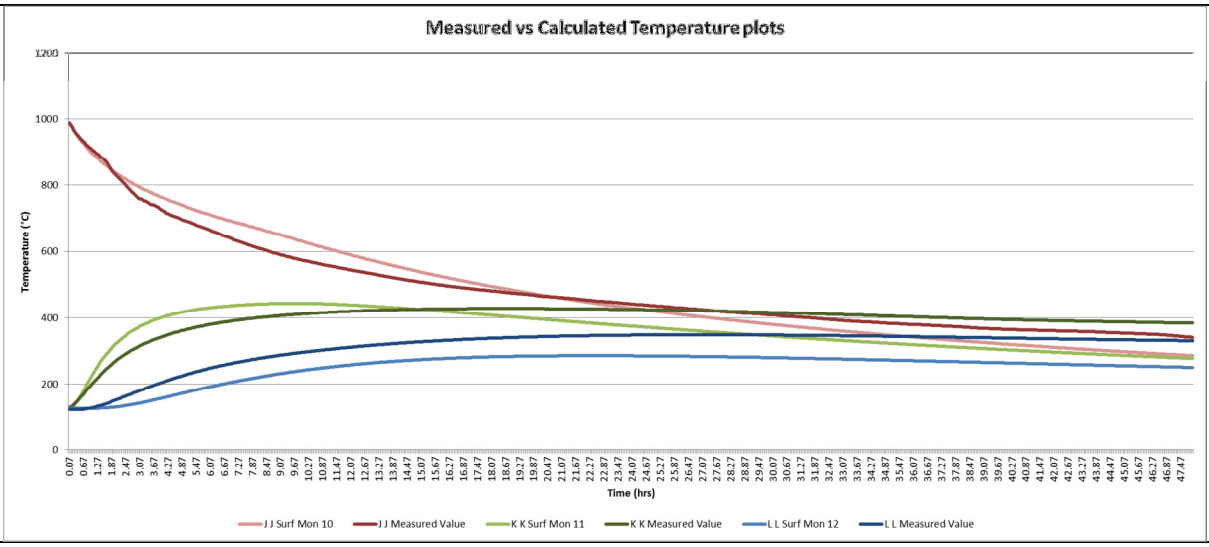

Fig 7.5-1.4 : Temperature plots for thermocouples J to K for measured and modelled values

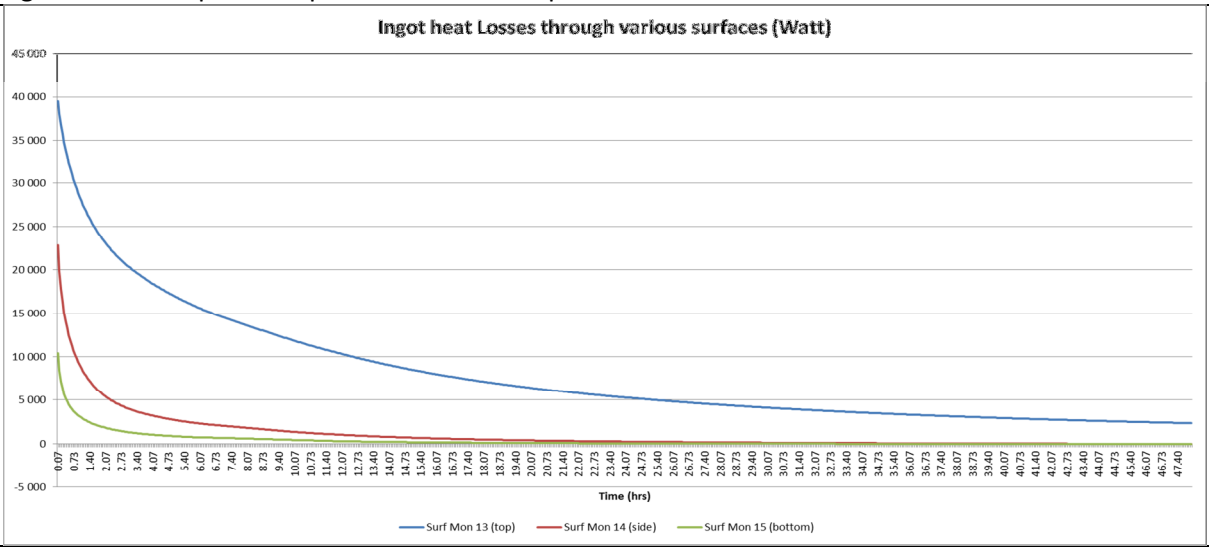

Fig 7.5-1.5 : Heat loss calculated through the various outer surfaces of the ingot: upper surface, bottom surface and side circumference

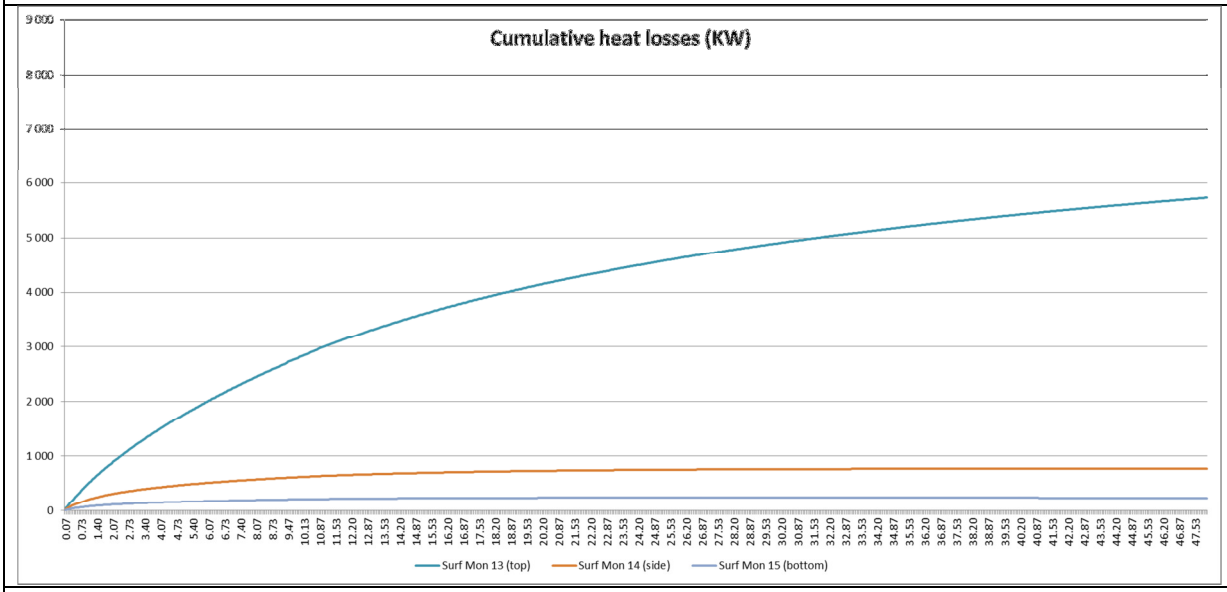

Fig 7.5-1.6 : Cumulative heat loss calculated through the various outer surfaces of the ingot: upper surface, bottom surface and side circumference

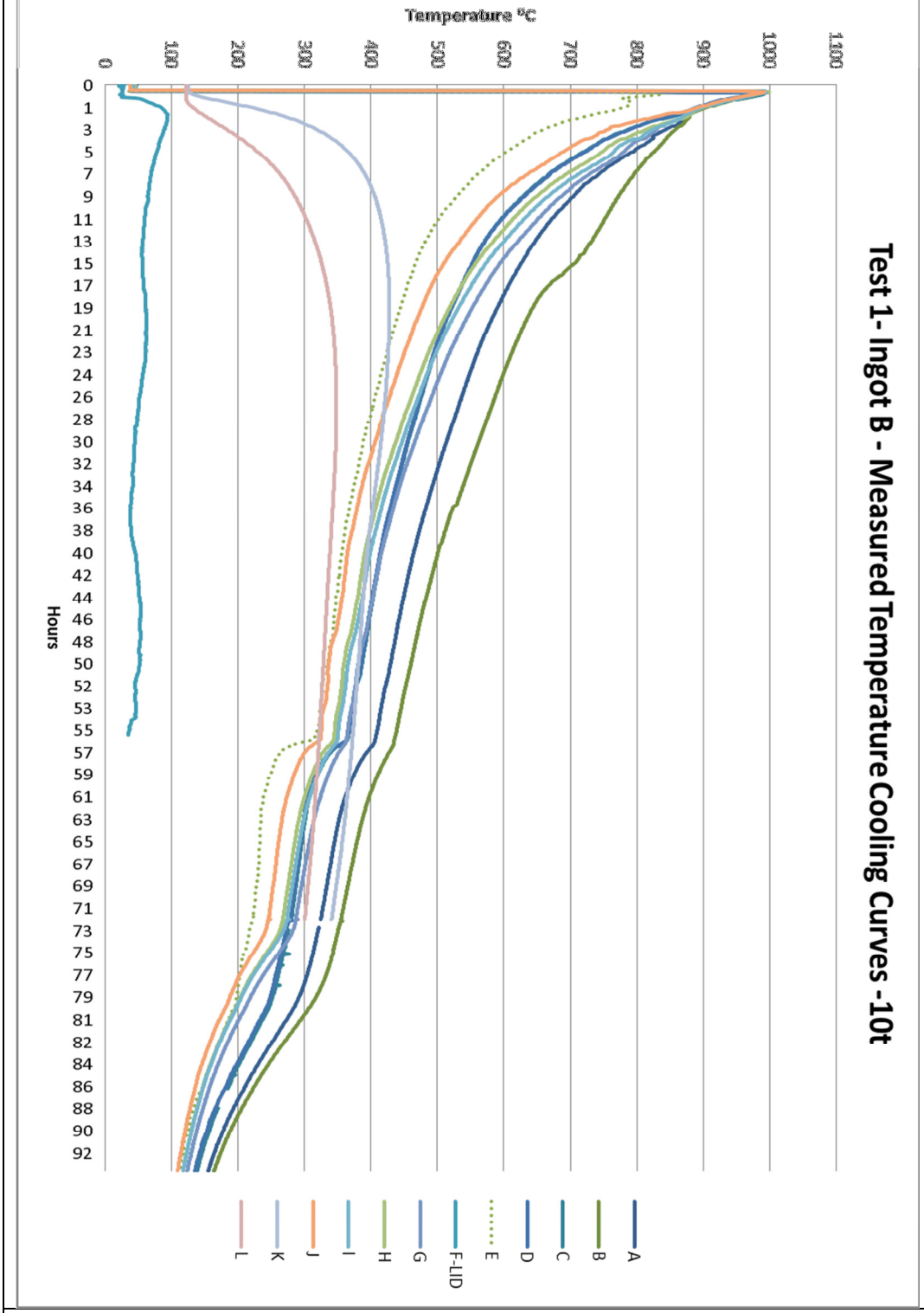

Fig 7.5-1.7 : Measured cooling curves for test 1, 10t ingot B.

Figure 7.5-2 - Test 2 – Ingot C, 5t

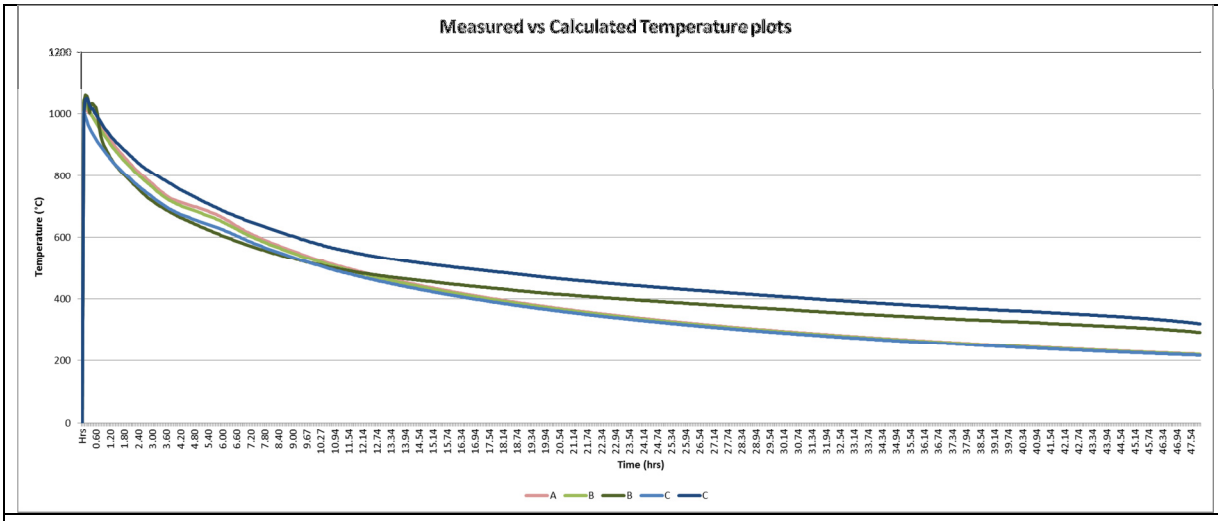

Fig 7.5-2.1 : Temperature plots for thermocouples A to C for measured and modelled values

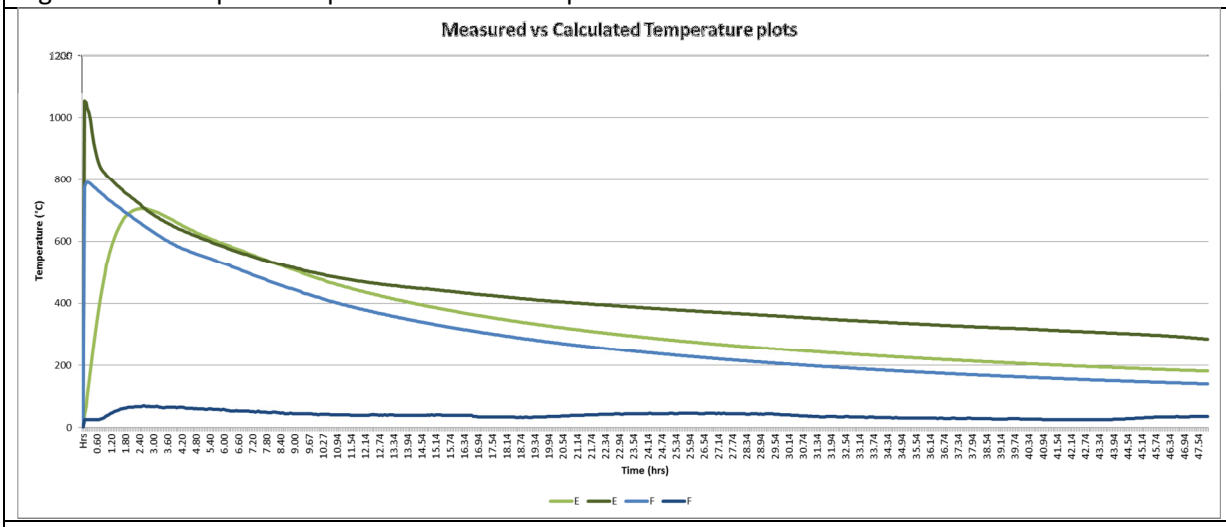

Fig 7.5-2.2 : Temperature plots for thermocouples D to F for measured and modelled values

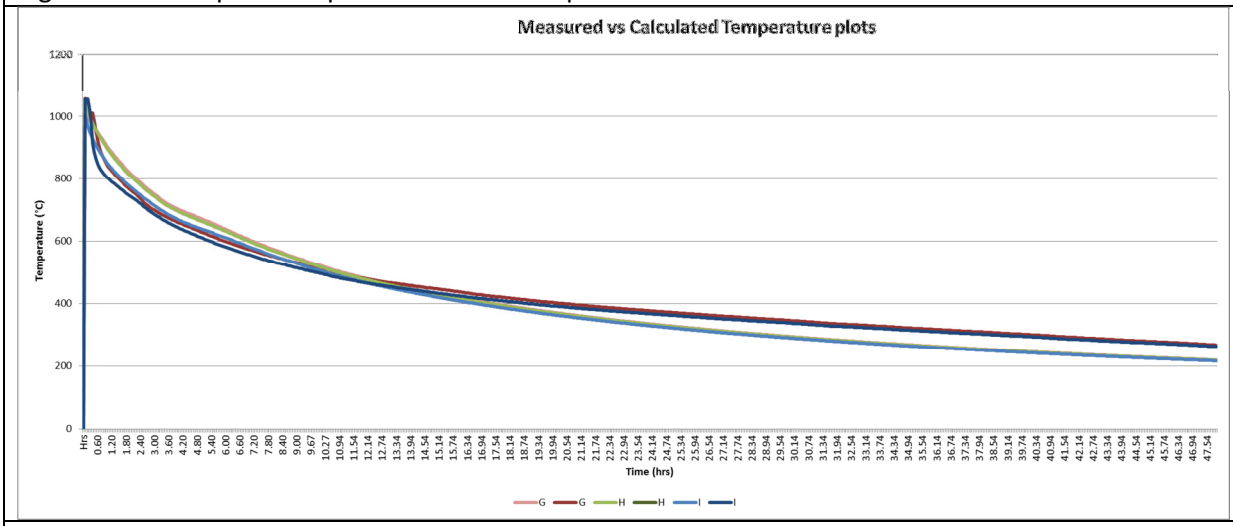

Fig 7.5-2.3 : Temperature plots for thermocouples G to I for measured and modelled values

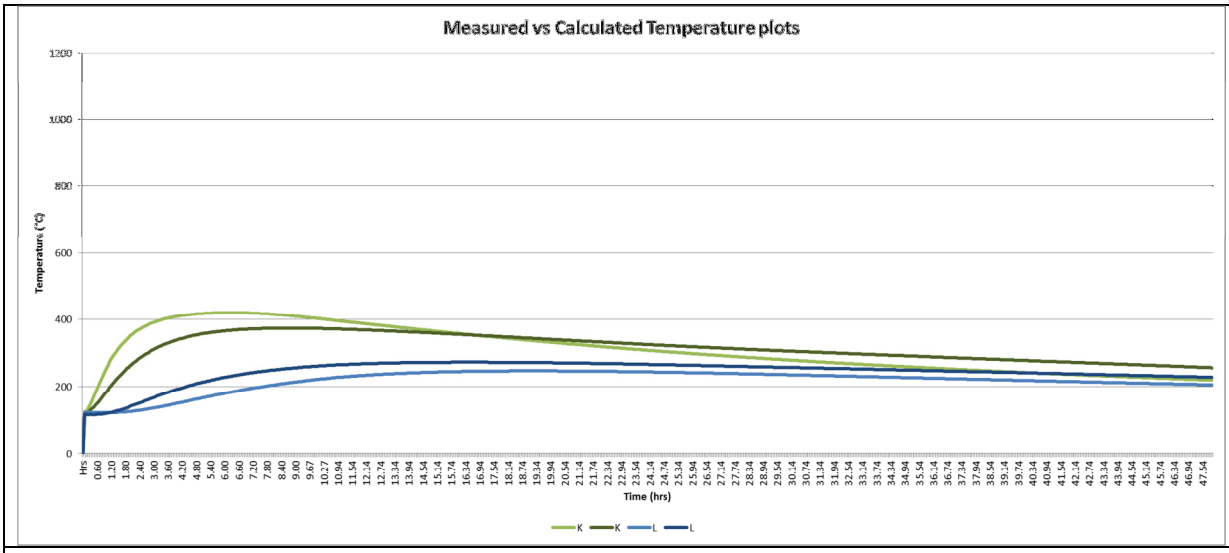

Fig 7.5-2.4 : Temperature plots for thermocouples J to K for measured and modelled values

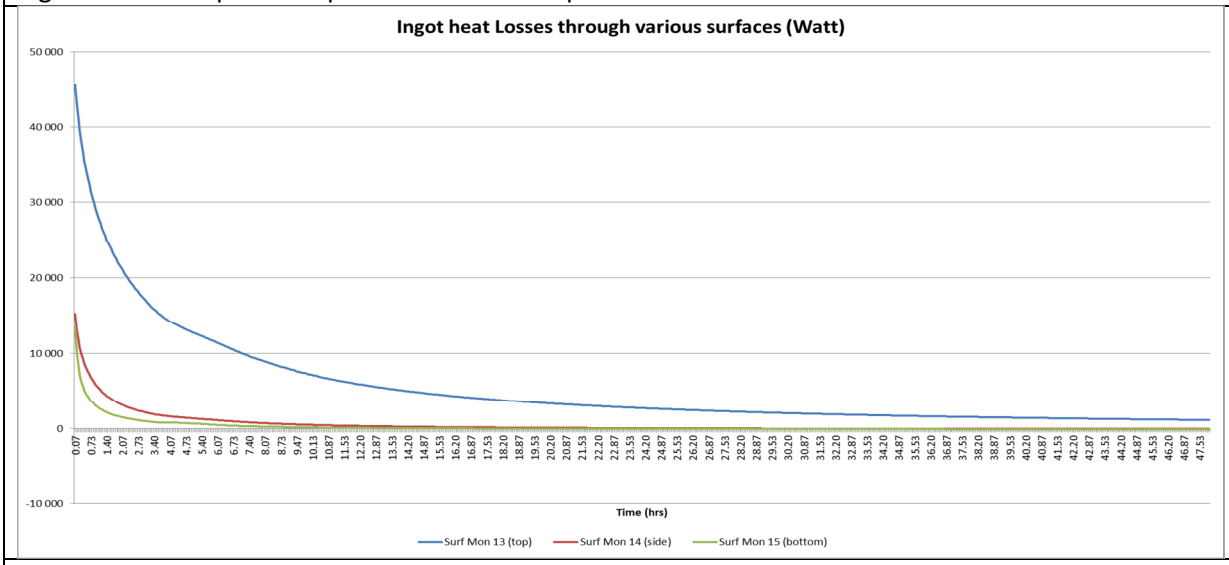

Fig 7.5-2.5 : Heat loss calculated through the various outer surfaces of the ingot: upper surface, bottom surface and side circumference

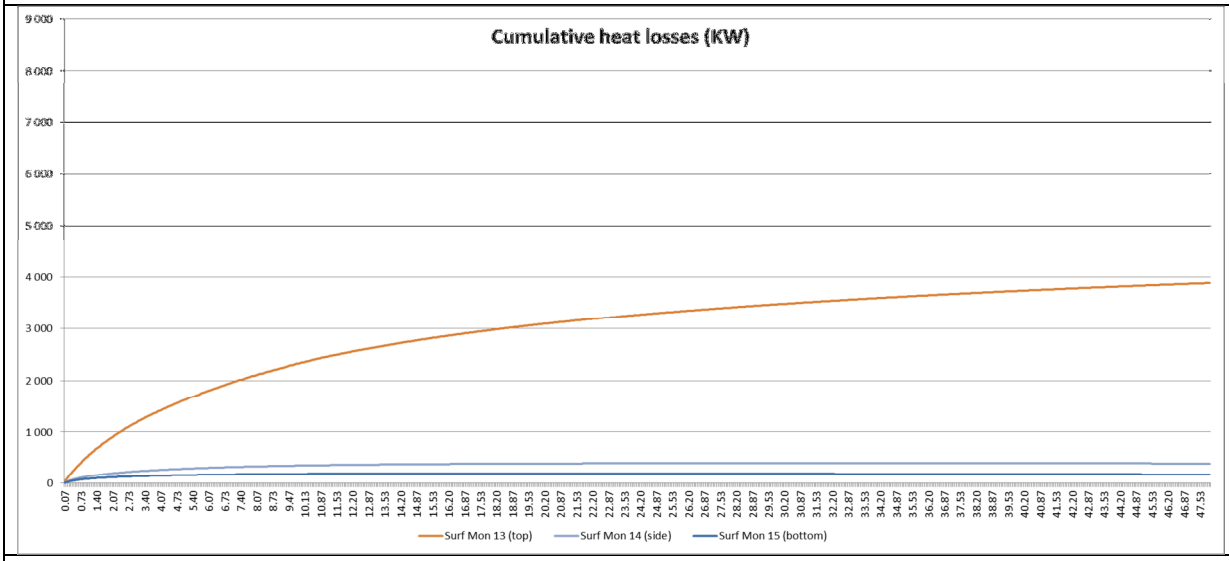

Fig 7.5-2.6 : Cumulative heat loss calculated through the various outer surfaces of the ingot: upper surface, bottom surface and side circumference

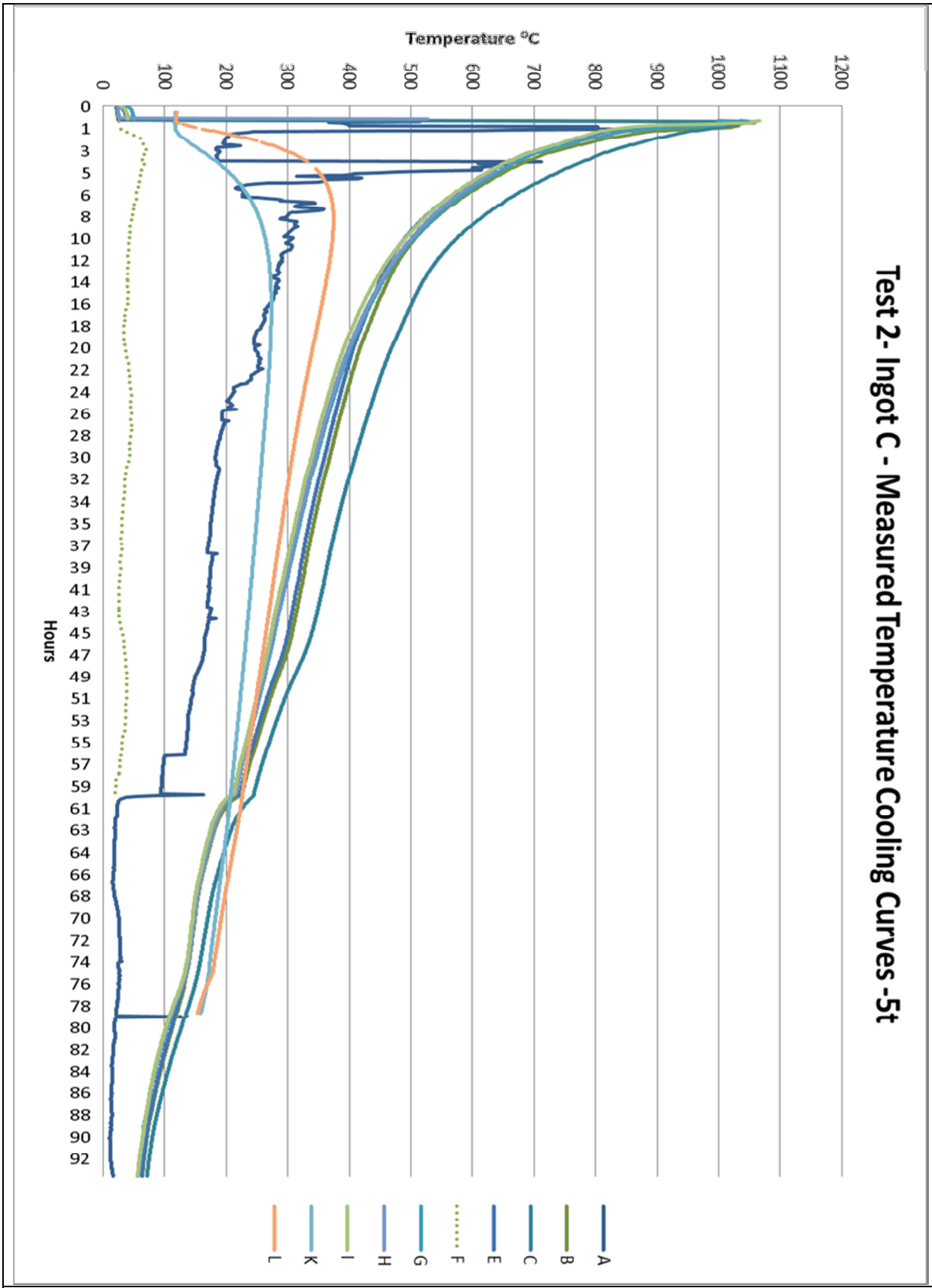

Fig 7.5-2.7: Measured cooling curves for test 2, 5t ingot C. Problematic thermocouples: A, D, H, J which did not record properly and the data was excluded from any analysis

Figure 7.5-3 - Test 3 – Ingot A, 15t

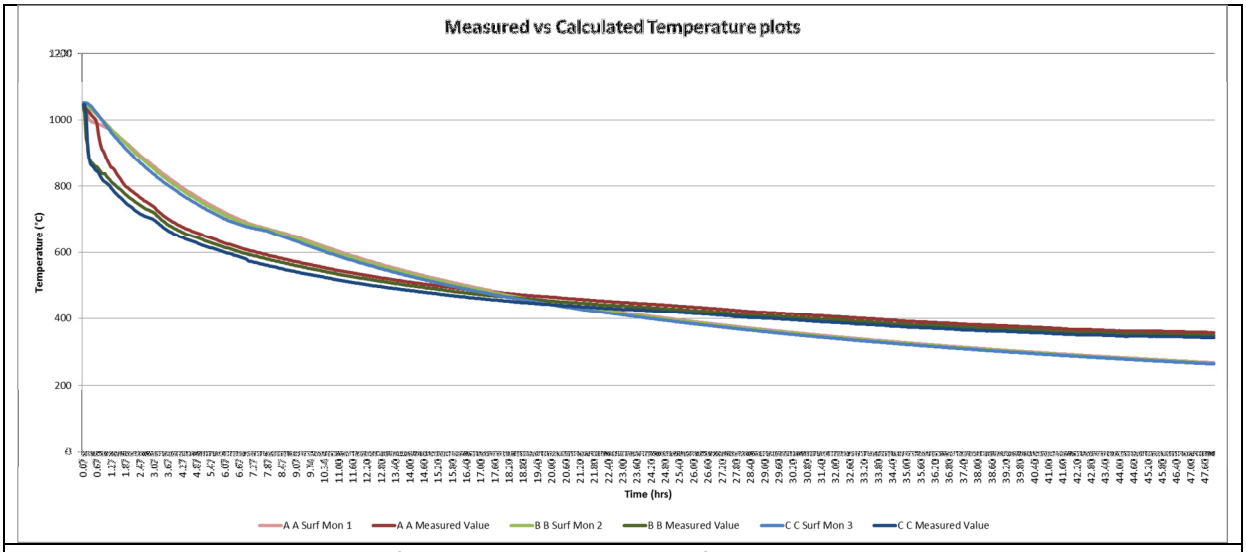

Fig 7.5-3.1 : Temperature plots for thermocouples A to C for measured and modelled values

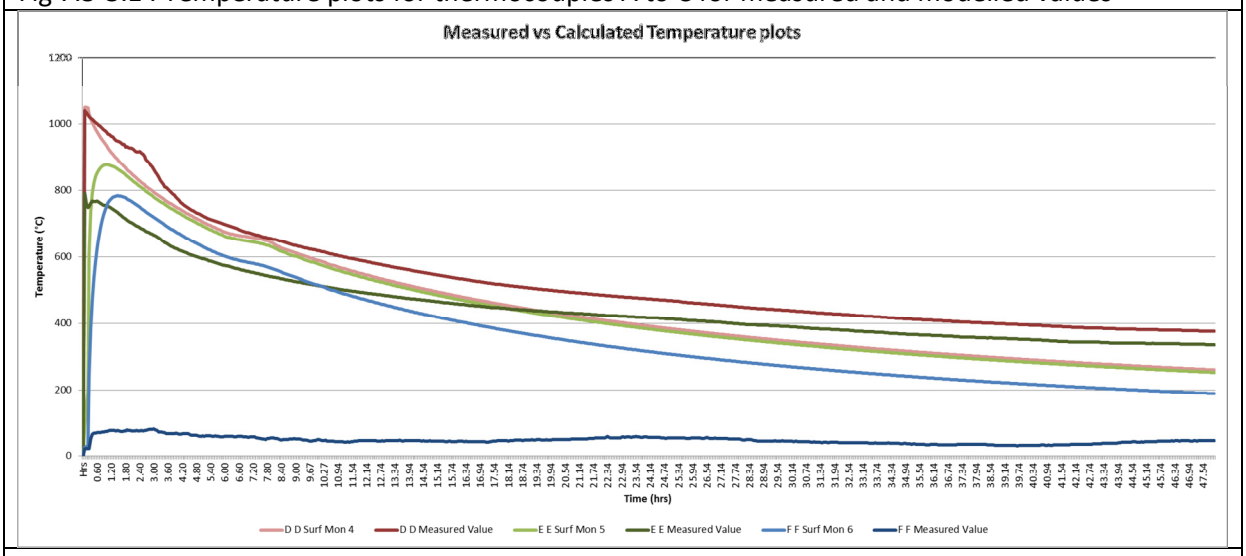

Fig 7.5-3.2 : Temperature plots for thermocouples D to F for measured and modelled values

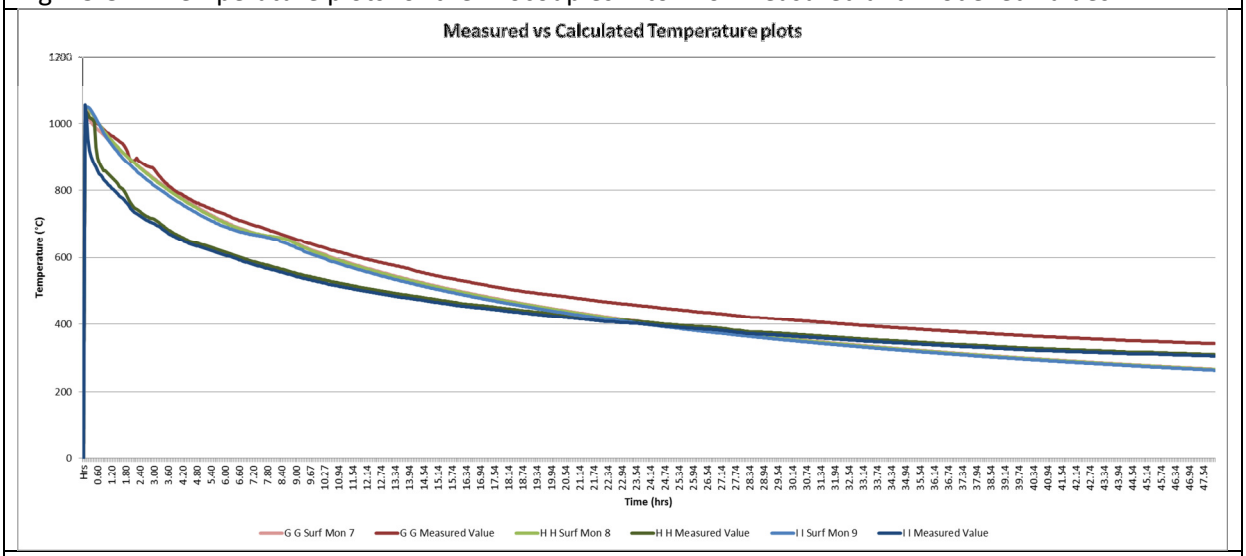

Fig 7.5-3.3 : Temperature plots for thermocouples G to I for measured and modelled values

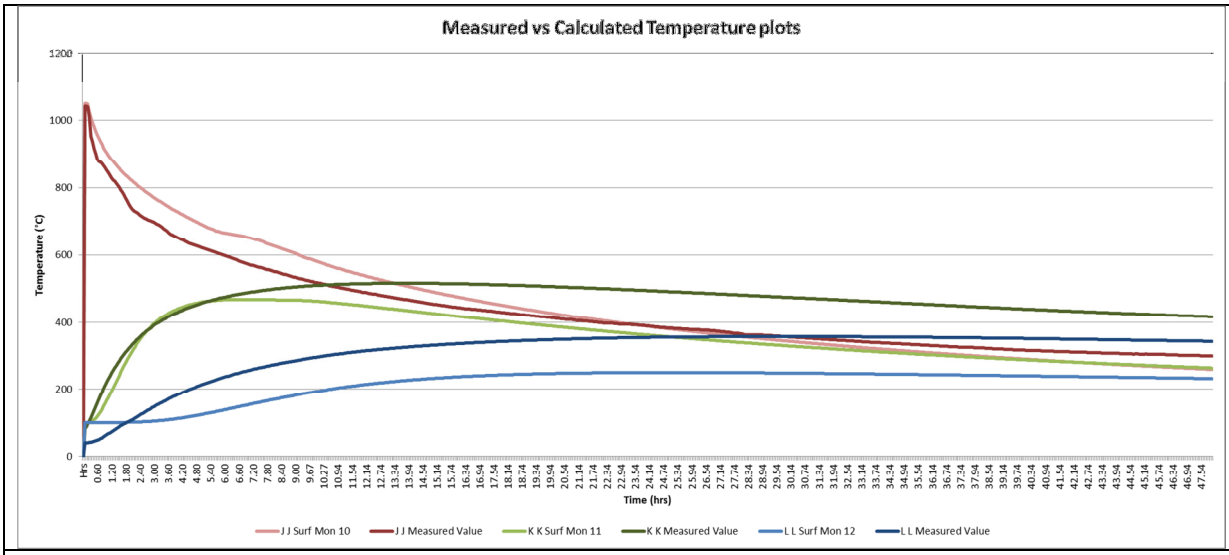

Fig 7.5-3.4 : Temperature plots for thermocouples J to L for measured and modelled values

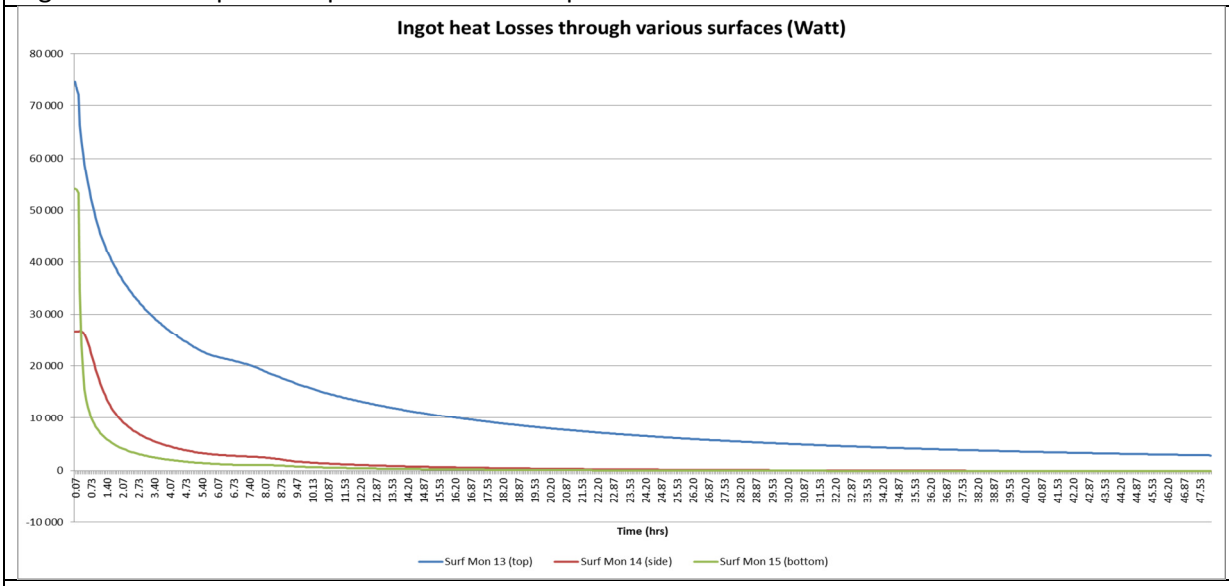

Fig 7.5-3.5 : Heat loss calculated through the various outer surfaces of the ingot: upper surface, bottom surface and side circumference

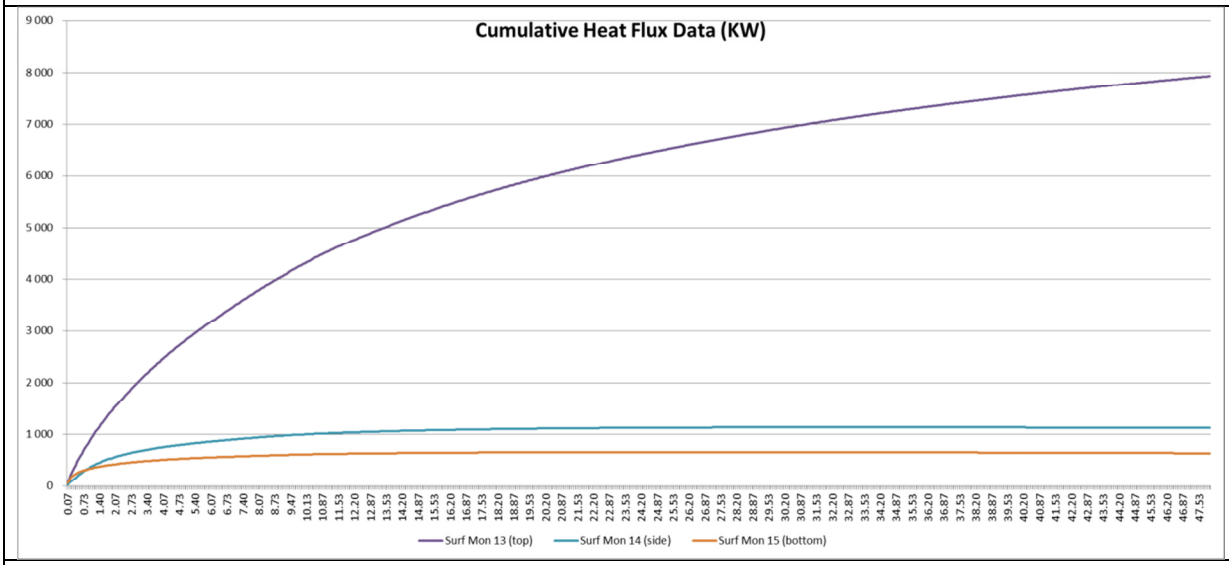

Fig 7.5-3.6 : Cumulative heat loss calculated through the various outer surfaces of the ingot: upper surface, bottom surface and side circumference

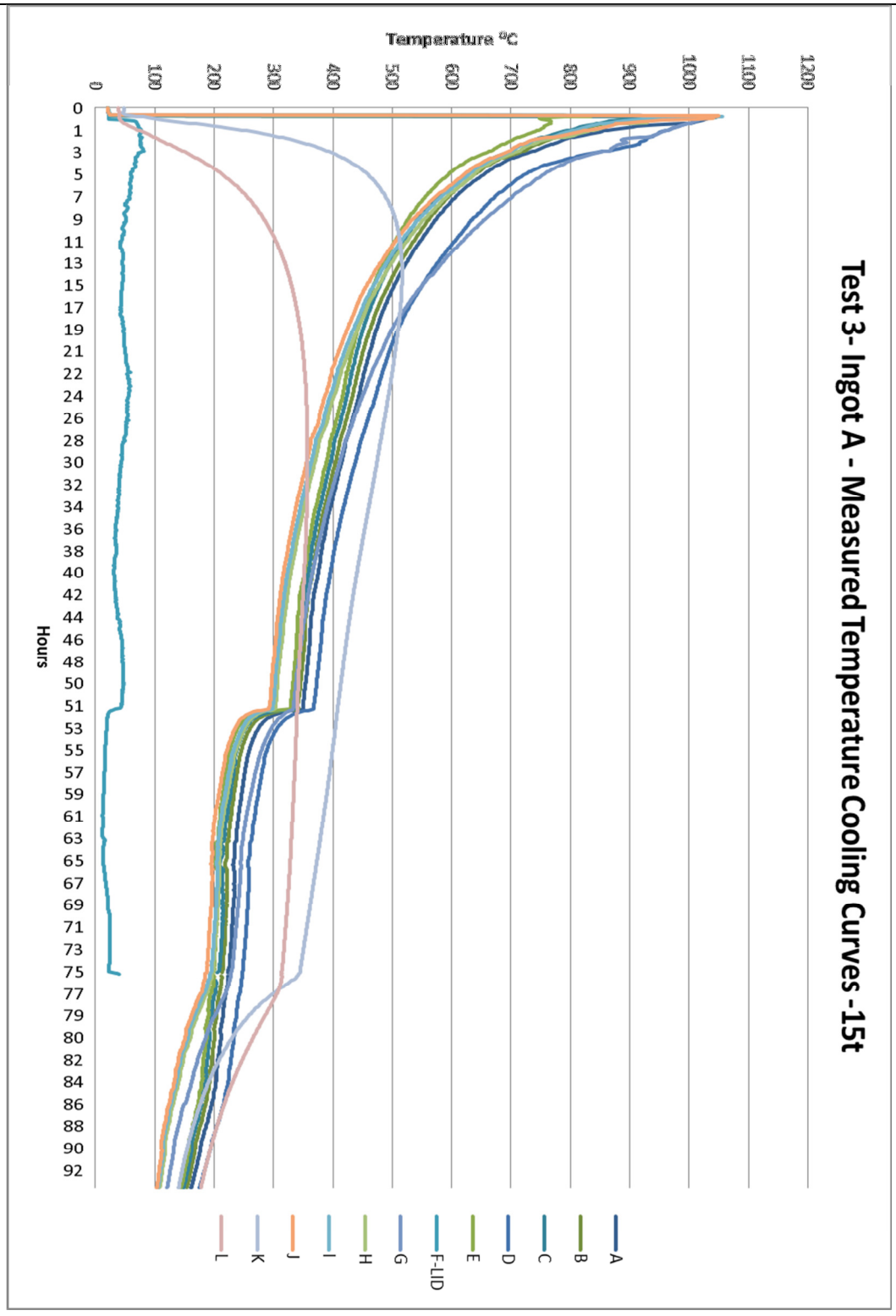

Fig 7.5-3.7 : Measured cooling curves for test 3, 15t ingot A.

7. Appendix 6: Contour temperature profiles with a constant temperature scale for Test 1 to 3

7.6-1: Contour temperature profile with a constant temperature scale showing the cooling down of a 10t Ingot B, Test 1

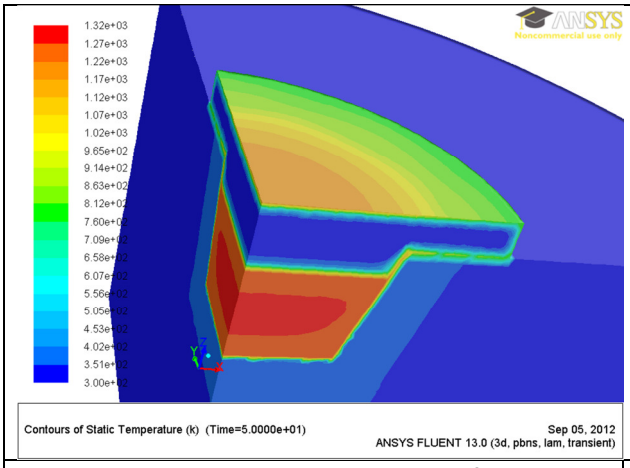

Figure 7.6-1.1: Static temperature profile showing the 10t ingot B, Test 1 after - 1min

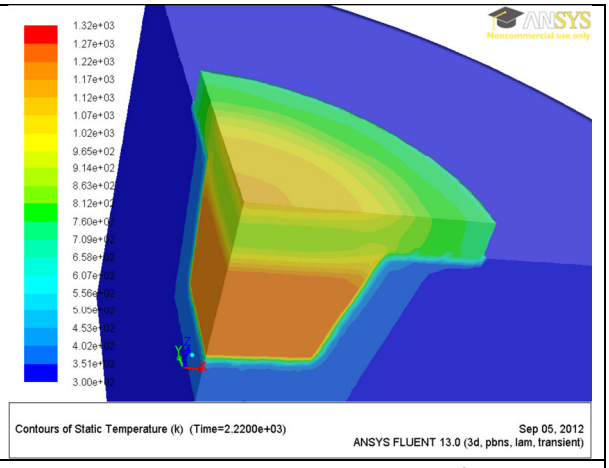

Figure 7.6-1.2: Static temperature profile showing the 10t ingot B, Test 1 after - 1hr

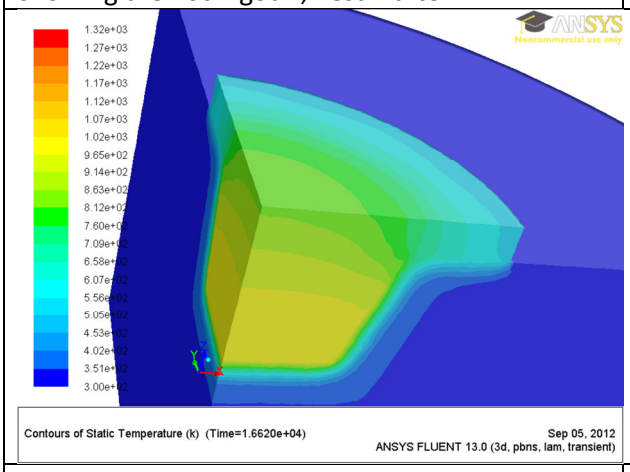

Figure 7.6-1.3: Static temperature profile showing the 10t ingot B, Test 1 after - 5hrs

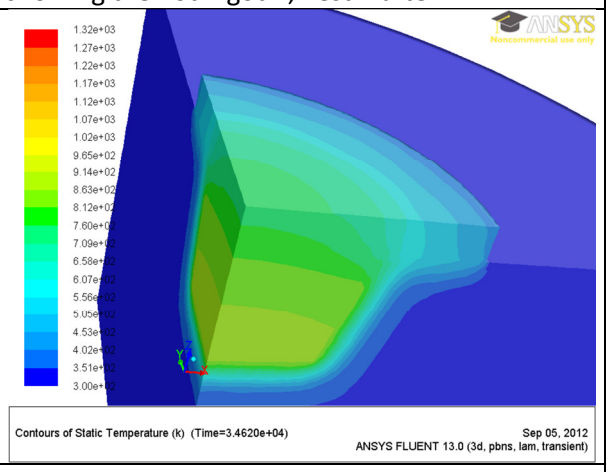

Figure 7.6-1.4: Static temperature profile showing the 10t ingot B, Test 1 after - 10hrs

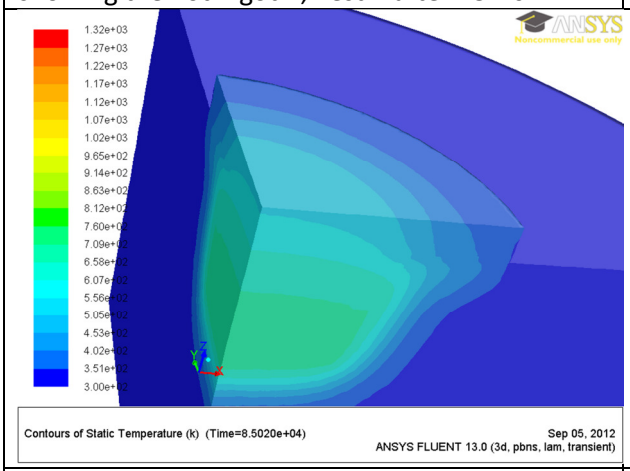

Figure 7.6-1.5: Static temperature profile showing the 10t ingot B, Test 1 after - 24hrs

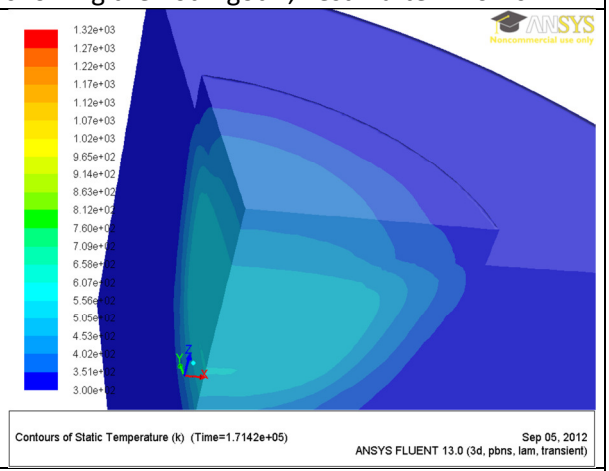

Figure 7.6-1.6: Static temperature profile showing the 10t ingot B, Test 1 after - 48hrs. (showing specifically a wider zoom to include the complete meshed section)

7.6-2 Contour temperature profile with a constant temperature scale showing the cooling down of a 5t Ingot C, Test 2

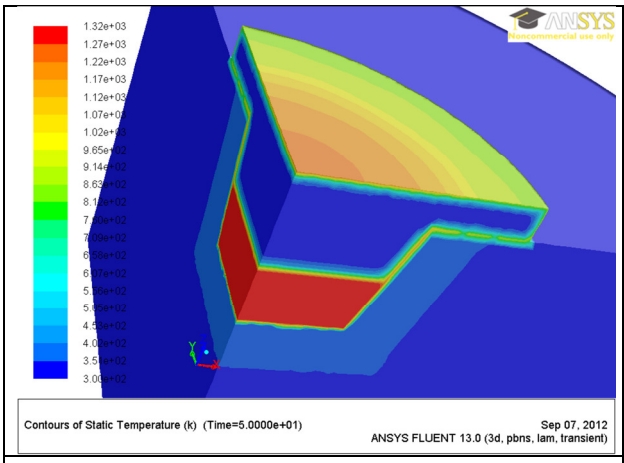

Figure 7.6-2.1: Static temperature profile showing the 5t ingot C, Test 2 after - 1min

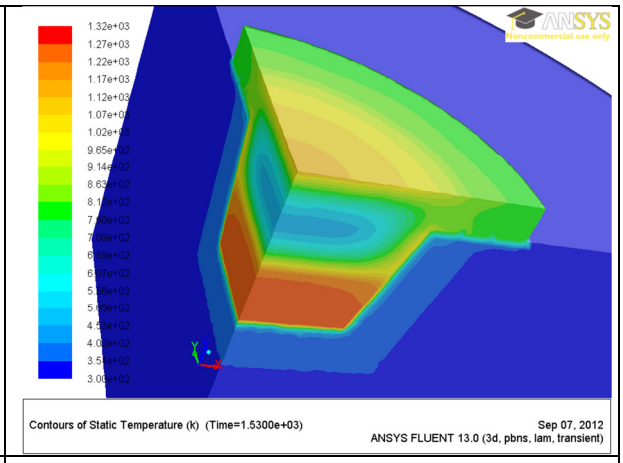

Figure 7.6-2.2: Static temperature profile showing the 5t ingot C, Test 2 after - 1hr

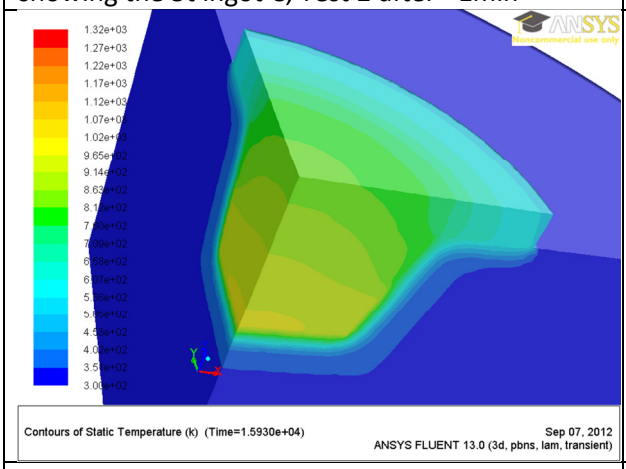

Figure 7.6-2.3: Static temperature profile showing the 5t ingot C, Test 2 after - 5hrs

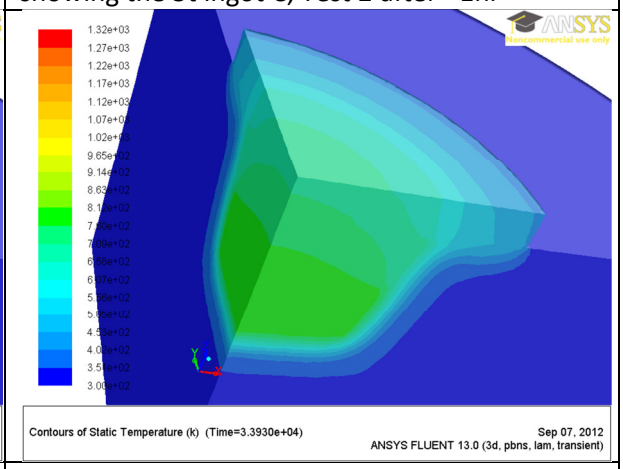

Figure 7.6-2.4: Static temperature profile showing the 5t ingot C, Test 2 after - 10hrs

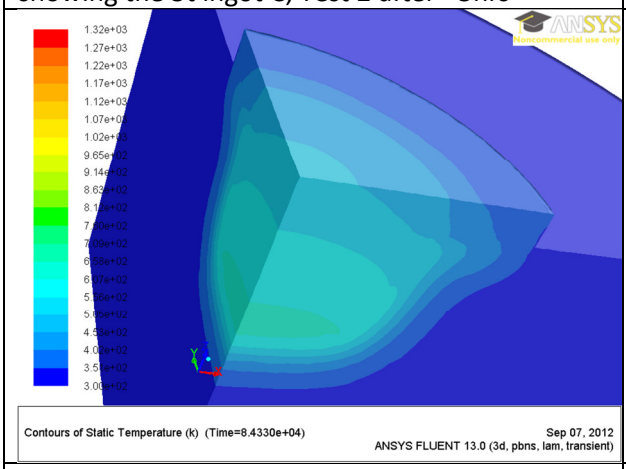

Figure 7.6-2.5: Static temperature profile showing the 5t ingot C, Test 2 after - 24hrs

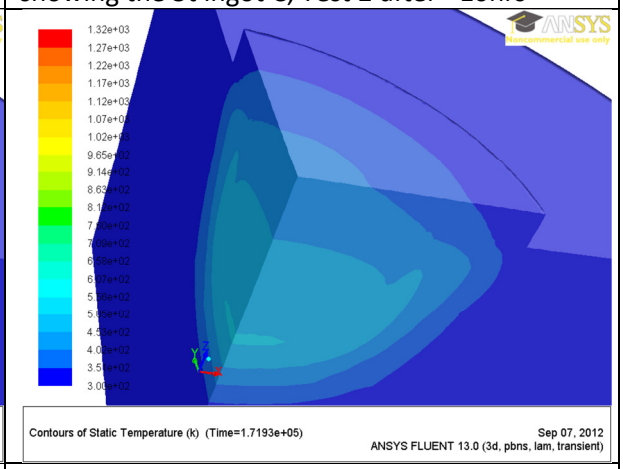

Figure 7.6-2.6: Static temperature profile showing the 5t ingot C, Test 2 after - 48hrs

7.6-3:Contour temperature profile with a constant temperature scale showing the cooling down of a 15t Ingot A, Test 3

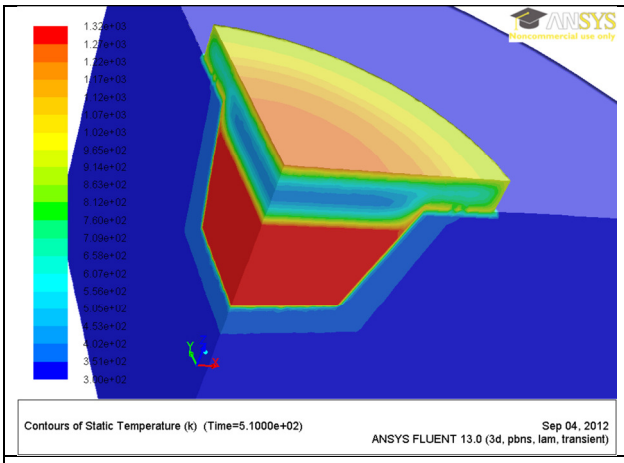

Figure 7.6-3.1: Static temperature profile showing the 15t ingot A, Test 3 after - 30min

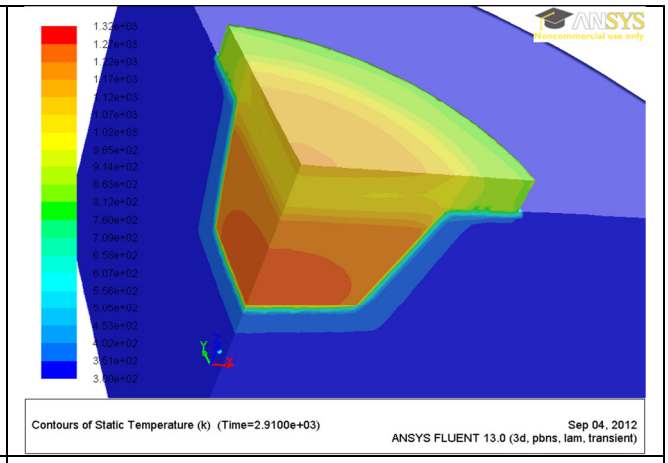

Figure 7.6-3.2: Static temperature profile showing the 15t ingot A, Test 3 after - 1hr

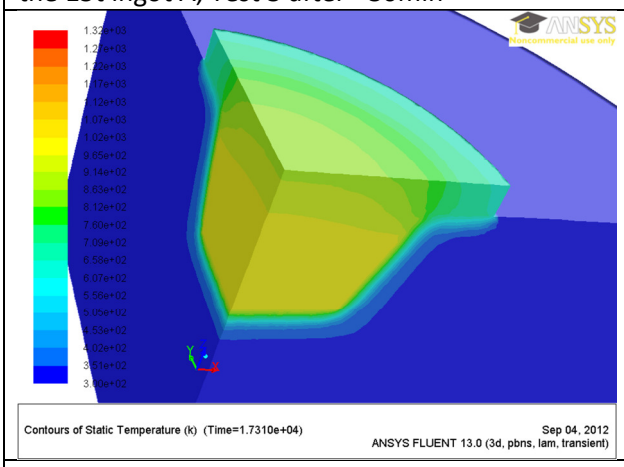

Figure 7.6-3.3: Static temperature profile showing the 15t ingot A, Test 3 after - 5hrs

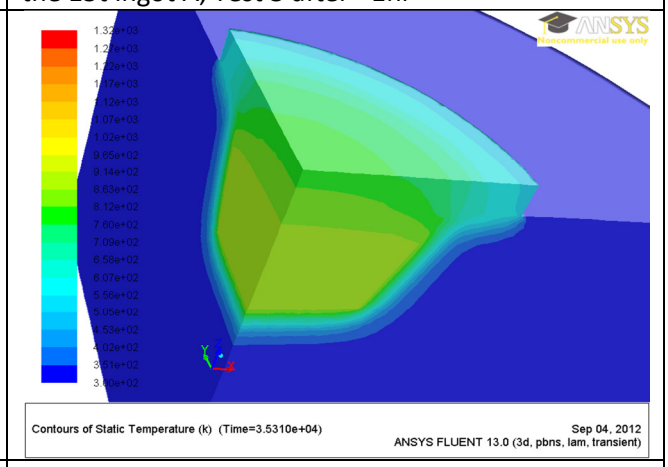

Figure 7.6-3.4: Static temperature profile showing the 15t ingot A, Test 3 after - 10hrs

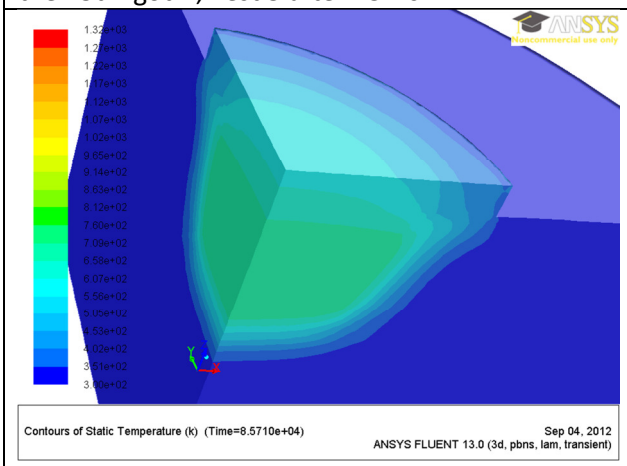

Figure 7.6-3.5: Static temperature profile showing the 15t ingot A, Test 3 after - 24hrs

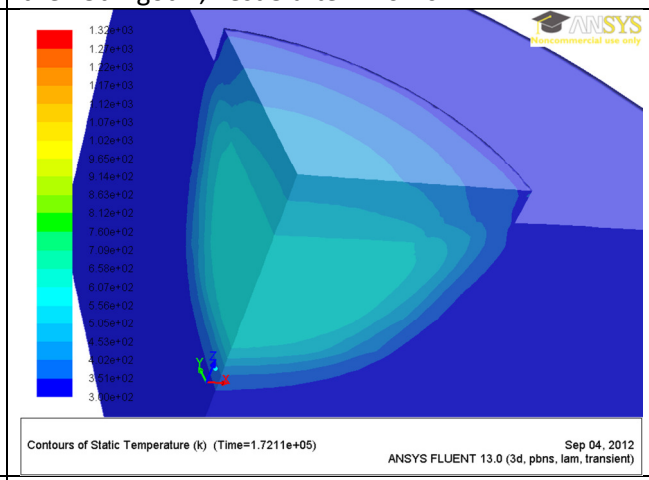

Figure 7.6-3.6: Static temperature profile showing the 15t ingot A, Test 3 after - 48hrs

8. Reference

1. Anglo Platinum Limited Annual Safety and Sustainability Report 2010

2. ANSYS® Software 13.0 help files

3. Badcock, R.F.W. (1993). 129 Process – 20 years on.

4. R., Wicks,J., (1997) Slow-cooled matte process review team – Internal Report

5. Badcock, R.F.W. (1998). *A review of the future nickel: copper ratio of WCM*, Memorandum to J.M. Hallhead, 16 February

6. Barton, P.B.J. (1973) Solids solutions in the system Cu-Fe-S. Part 1. The Cu-S and CuFe-S joins. Economic Geology 68, 455-465.

7. Bruwer, J.S. (1998). Optimisation of Key pyro-metallurgical processes: Slow cooling of AMPLATS converter matte

8. Bruwer, J.S. (1998). *Experimental investigation of the phase relations of the system Cu-Ni-S in the temperature range 1200 to 700°C*, M.Sc. thesis (unpub.), Pretoria University, 157pp

9. Bruwer, J.S and Merkle, R.K.W. (1998) Experimental investigation of the liquidus isotherms in the system Cu-Ni-S from 1200°C to 700°C. In Proceedings of the 5th International Congress on Applied Mineralogy in the Mineral Industry (ICAM '96), Warsaw, Poland, Edited by A. Niedbalska, A. Szymanski and A. Wiewiora, Subdan Druk s.c. Warsaw, Poland, 130-135.

10. Bruwer, J.S. (1998). Slow cooling of converter matte : Project update and results to date, Amplats Research Centre, Research Report

11. Chakrabarti, D.J. and Laughlin, D.E. (1983) Cu-S. Bulletin of Alloy Phase Diagrams 4, 953-957.

12. Chang, Y.A, Neumann, J.P., and Choudary, U.V. (1979) Phase diagrams and thermodynamic properties of ternary copper-sulphur-metal system. INCRA Monograph VII. 7. The International Copper Research Association, Inc. New York.

13. Clark, L.A. and Kullerud, G. (1963) The sulfur-rich portion of the Fe-Ni-S system. Economic Geology 58, 853-885.

14. Crocket, J.H., Fleet, M.E. and Stone, W.E. (1997) Implication of composition for experimental partitioning of platinum-group elements and gold between sulphide liquid and basalt melt: The significance of nickel content. Geochimica et Cosmochimica Acta, 61, 4139-4149.

15 Davenport, W.G., King, M., Schlesinger, M., Biswas, A.K., Extractive Metallurgy of Copper, Fourth Edition, 2000

16. Dinham, P. (1999). *Mineralogical investigation into the possible causes of extended copper leaching times in the Secondary Pressure Leach and high selenium levels at RBMR during August/September 1998*, Min. Rep. No. M/99/02, 13pp

17. Dinham, P., Schouwstra, R.P. (2002). Preliminary findings on silica in WCM, M/02/108, 5pp

18. Dinham, P. (2003a). *Microscopic scanning results – ALR/PTLG/FIC production samples*, Min Memo. M/03/61, 3 pp

19. Dinham, P. (2003b). *Mineralogy of ALR/PTL and FIC production samples*, Min. Rep. M/03/61, 8pp

20. Dinham, P. (2003c). Pt losses in three NCM samples, Min. Memo. M/03/85, 4pp

21. Dinham, P. (2003d). *Samples from problematic leach period, June 2003, MC Plant, RBMR,* M/03/54, 6pp

22. Dinham, P. (2003e). *Investigation of WCM ingot samples covering the June-July 2003 period*, (in preparation)

23. Dinham, P, Reinecke, P.M. (2002a). *Mineralogical and metallurgical comparison of several small ingots produced at Waterval Smelters*. Min. Rep. No. M/01/68, 21 pp

24. Distler, V.V., Malevskiy, A.Yu., Laputina, I.P. (1977). Distribution of platinoids between pyrrhotite and pentlandite in crystallization of a sulphide melt. Trans. From *Geokhimiya*, 11, pp. 1646-1657

25. Ebel, D.S. and Naldrett, A.J. (1996a) Fractional crystallization of sulphide ore liquids at high temperature. Economic Geology, 91, 607-621.

26. Eric, R.H., (2004), Slag properties and design issues pertinent to matte smelting electric furnaces, VII International conference on molten slags fluxes and salts, South African Institute of Mining and Metallurgy.

27. FactSage® databases and help files contained in the FactSage® v6.2 software, www.FactSage.com

28. Fleet, M.E. and Pan, Y. (1994) Fractional crystallization of anhydrous sulphide liquid in the system Fe-Ni-Cu-S, with application of magmatic sulfide deposits. Geochimica et Cosmochimica Acta 58, 3369-3377.

29. Fleet, M.E. and Stone, W.C. (1991) Partitioning of platinum-group elements in the Fe-Ni-S system and their fractionation in nature. Geochimica et Cosmochimica Acta 55, 245-253.

30. Fleet, M.E., Crocket, J.H., Liu, M. and Stone, W.E. (1999) Laboratory partitioning of platinum-group elements (PGE) and gold with application to magmatic sulphide-PGE deposits. Lithos, 47, 127-142.

31. Fleet, M.E., Stone, W.E. (1991). Partitioning of platinum-group elements in the Fe-Ni-S system and their fractionation in nature. *Geochem. Cosmochim. Acta.,* 55, pp. 245-253

32. Hill, J. Report on investigations into the 129process, April 1995

33. Holman, J.P., Heat transfer, tenth edition, Mc Graw Hill Publishers, 2010

34 Jacobs, Waterval Smelter Induction Material, 2006

35. Kongoly, F., Dessureault, Y. and Pelton, A.D. (1998) Thermodynamic modelling of liquid Fe-Ni-Cu-Co-S mattes. Metallurgical and Materials Transactions B, 29B, 591-601.

36. Koster W., and Mulfinger W. (1940) Die Systeme Kupfer-Nickel-Schwefel und Kupfer-Nickel-Arsen. Zeitschrift fur Electrochemie, vol 46, no.3, pp 135

37. Kullerud, G., Yund, R.A., and Moh, G.H. (1969) Phase relations in the Cu-Fe-S, Cu-Ni-S, and Fe-Ni-S systems. Wilson, H.D.B. (editor) Economic Geology Monograph. Magmatic Ore Deposits. 4. 343 p

38. Kullerud, G. (1963). *The Fe-Ni-S system*, Carnegie Inst. Wash. Year Book 62, pp. 175-189

39. Mackey, P.J., (1982) The physical chemistry of copper smelting slags – a review, Canadian Metallurgical Quarterly. Vol.21. No.3 pp 221-260

38. Mathew, S., ACP Furnace Reduction, Internal Presentation, 2009

40. Metskill (PTY) LTD, ACP Converter Operations Manual, 2007

41. Miodownik, A.P. (1977). *Report on the magnetic properties of nickel-iron-copper alloys in the region* $Ni_{0.8}(Fe_xCu_{1-x})_{0.2}$

42. Pain, A., (997), Thermal analysis of slow cooling Cu/Ni Matte process, CSIR project report (Project number 4600/4770/MTC40)

43. Peyeri, W. (1979). *Mineralogical examination of an extremely low iron WCM ingot from Waterval operation No. 1442 (Cast 9.8.1979)*. Min. Report. No. M/79/132. 5

44. Poushkarova, M., (2001). Thermal analysis of slow cooling process of WCM ingots cast in moulds of different sizes.

45. Scharneck, Y., Bramdeo, S., Alloy Sizes in ingot samples, May 2012, Internal Memeo Ref M/11/200

46. Schouwstra, R.P. (1996). *The slow-cooling process: A mineralogical perspective – A report for discussion,* Min. Rep. M/96/19, 53 pp

47. Schcouwstra, R.P. (1997) *Milling tests performed on WCM to determine the possibility of producing material for QEM*SEM particle analysis*, Slow-Cool Project: Stage 1, 11 pp

48. Schouwstra, R.P., Rixom, P.M. & Roberts, J.R.D. (1998) The effect of cooling rates on converter matte alloy microstructures: a laboratory study. In 8th international Platinum Symposium, Abstracts 8th International Platinum Symposium, Abstracts, Geological Society of South Africa and The South African Institute of Mining and Metallurgy, Johannesburg, Symposium Series S18, 363-366.

49. Schouwstra, R.P. (1999). *Formation of large alloy plates in WCM ingots during March/April '99 – cause and effect – A mineralogical study*, Min. Rep. M/99/16, 15 pp

50. Schouwstra, R. P. (2000a). The slow-cooling process: a mineralogical perspective, *CIM Bulletin*, 93, No. 1036, pp 168-171

51. Schouwstra, R. P. (2000a). The slow-cooling process: The a mineralogical perspective, *CIM Bulletin*, 93, No. 1036, pp 168-171

52. Schouwstra, R.P. (2000b). *Mineralogical investigation of an ACP test ingot produced at the ACP pilot plant facility (ARC)*, Min. Rep. M/00/78, 7 pp

53. Schouwstra, R.P., (2001). *Mineralogical and metallurgical investigation of a FIC-enriched ACP ingot*, Min. Rep. M/01/54, 13 pp

54. Schouwstra, R.P. (2002), *WCM Quality – Controlling factors*, Min. Rep. M/02/13, 9 pp

55. Schouwstra, R.P. (2003). *Quality of stockpiled WCM matte (WCM 560, 591, 614 and 617),* Min. Memo. M/03/75, 5 pp

56. Schouwstra, R.P., Andrews, L. (2000). *A summary of a SIMS and Micro-PIXE investigation into the deportment of platinum and palladium in converter matte*, Min. Rep. M/00/37, 9 pp

57. Schouwstra, R.P., Reinecke, P.M. (2001a) *Mineralogical and metallurgical investigation of four palladium-enriched ACP ingots*, Min. Rep. M/01/47, 17 pp

58. Schouwstra, R.P., Reinecke, P.M. (2001b). *Mineralogical investigation of four palladium-enriched ACP ingots*, Min. Rep. M/01/07, 12 pp

59. Schouwstra, R.P., Rixom, P.M. (1997). *The effect of the cooling profile on the microstructure of alloy*, Slow-Cool Project: Stage 3, 23 pp

60. Schouwstra, R.P., Rixom, P.M. (1998). *The effect of the nickel to copper ratio on the microstructure of alloy,* Slow-Cool Project: Stage 4, 17 pp

61. Sheng, Y.Y., Irons, G.A., Tisdale, D.G., (1998), Transport Phenomena in electric smelting of Nickel matte: part II. Mathematical modelling, Metallurgical and material transactions volume 29B, Feb 1998.

62. Singiresu, S.R., The finite element method in engineering, fourth edition, Elsevier Butterworth – Heinemann publishers, 2005

63. Sploure K, Harcourt G.A. and Renzoni L.S. (1960) Treatment of Nikel-copper matte. Journal of Metals, March, pp214-219.

64. Stahleisen, M. B. H., Slag Atlas, 1981

65. Taylor, J.R. (1995). *Comments on a memorandum on control of WCM alloy content*. 2 pp

66. Taylor, J.R. (1997). Aspects of the 129 process, November 1997

67. Taylor, J.R. (2000). *Calculation methods for the deportment of Pd in slow-cooled ingots*. Tech. Memo.

68. Taylor, J.R. Control of 129 processes (internal memo)

69. Thyse, E.L., et al. Towards understanding nickel converter matte solidification. Miner. Eng. (2013)

70. Thyse, E.L., et al. Partitioning of PGEs in nickel converter matte phases: Direct Observations by electron microscopy and electron probe microanalysis.

71. Thyse, E.L., et al. 3D insights into nickel converter matte phases: Direct observations via TEM and FIB SEM tomography. Miner. Eng. (2013.

72. Thyse, E.L., et al. The effect of changes in iron-endpoint during Peirce-Smith converting on PGE–containing nickel convert matter mineralization.

73. Tredoux, M., Lindsay, N.M., Davies, G. & McDonald, I. (1995). The fractionation of platinum-group elements in magmatic systems, with the suggestion of a novel causal mechanism. *S. Afr. J. Geol*. 98(2), pp. 157-167

74. Ueckermann, H. (2002). *Partioning of platinum-group elements between metal and sulphide melt in the Cu-S and Ni-S systems*, M.Sc thesis (unpub.), Pretoria University, 146 pp

75. Van der Merwe, C. (2003). *WCM Quality parameters – document for discussion*, 2 pp

76. Wright, G M. 129 Process feed parameters, April 1998 – Ref 2